Selective Laser Melting of Duplex Stainless Steels

Karl Davidson

A thesis submitted to
Auckland University of Technology in fulfilment of the
requirement for the degree of Doctor of Philosophy

December 2017

School of Engineering, Computer and Mathematical Sciences

Abstract

Duplex stainless steels are a special class of alloys characterised by the equal amounts of austenite and ferrite in the microstructures, achieved through a balanced composition of the alloying elements. The dual phase structure makes them strong, tough and resistant to corrosion in extreme environments, combining the good properties of both the constituent phases. As a result, duplex steels became very useful and important in a wide range of applications including oil and gas, food and beverages, civil construction and architecture, and medical devices and implants.

While the dual phase structure is essentially the reason for all the useful attributes of duplex steels, the same may also act as a hindrance to their performance, during and after the application of secondary processes. Thermo-mechanical interactions might lead to a loss of the equal phase duplex structures and machinability attributes are not often encouraging due to work hardening and formation of strong and continuous chips. Considering the significant properties and the applications, and problems associated with the secondary processing, the material system kept the challenges of improving existing methods and finding alternative ways of manufacturing alive.

The past decade saw a tremendous growth in the additive manufacturing technologies, as a few of the more promising techniques grew beyond the simple rapid prototyping solutions. In particular with the metal powders, the selective laser melting process became a strong contestant in terms of the near net shape consolidation and higher densities. At the time this research project started, there was no evidence of any *a priori* data related to the laser based processing of duplex stainless steel powder through a layer-wise consolidation. This was the research gap identified and the research proposal was developed to answer the questions that will arise encompassing the possible immediate responses of duplex steels to laser melting conditions, process-structure-property relationships and abnormalities if any that may arise from the structures altered significantly due to the non-equilibrium conditions.

Experimental plans were then drawn, appropriate equipment identified and the proposed research was conducted as planned, achieving the set objectives. Duplex stainless steels were proved to be suitable for processing by selective laser melting. Structural distortions were noted to arise due to the laser interactions, but post-process heat treatment procedures were observed to be effective in rectifying the problems to varying degrees. The maximum bulk density levels reached were at around 95%, while the mechanical and other properties showed no significant losses. The transformation of the duplex stainless steels from the hard to the soft magnetic states as a result of the structural alterations induced by selective laser melting is an additional research outcome. Further, the machinability of the material in the as-built state was found to be better than in the wrought case. As far as the published literature commonly available goes, the initial experimental trials conducted as part of this research were the first to apply selective laser melting to duplex steel powders. Other original contributions include the establishment of the ensuing metallographic and mechanical attributes of the samples printed with varying conditions and establishment of the anomalous magnetic responses and the unexpected improvement in the machinability responses.

Table of Contents

Abstract II

List of Publications IX

List of Figures X

List of Tables XVIII

List of terms and Abbreviations XIX

Attestation of Authorship XXI

Acknowledgments XXII

Chapter 1 Introduction 1

1.1 Background 1

1.2 Alloying elements, structural sensitivity, and processing limitations 2

1.3 The additive processing realm 4

1.4 Research gap, questions and hypothesis 5

1.5 Objectives, methods and critical achievements 6

Chapter 2 Literature review, research gaps, questions, and objectives 8

2.1 Duplex stainless steels 8

2.1.1 The chronology of development of duplex stainless steels 8

2.1.2 Metallurgy of duplex stainless steels 11

2.1.3 Properties 14

2.2 Applications 17

2.2.1 Pulp and paper 17

2.2.2 Oil and Gas 18

2.2.3 Construction 19

2.2.4 Desalination 21

2.2.5 Food and Beverage 22

2.2.6 Medical and Orthodontic 23

2.3 Traditional Processing methods and issues 24

2.3.1 Casting 25
2.3.2 Hot / Cold forming 27
2.3.3 Machining 30
2.3.4 Powder metallurgy 33
2.4 Powder additive manufacturing in metals 37
2.4.1 Laser engineered net shaping (LENS) 37
2.4.2 Electron beam melting (EBM) 40
2.4.3 Selective laser melting (SLM) 42
2.5 Research gaps, hypothesis and questions 45
2.6 Objectives and the organisation of the thesis 51
Chapter 3 Methodology 54
3.1 Critical factors of selective laser melting 54
3.1.1 Process parameter settings and sample printing 54
3.1.2 Scan Strategy Settings 57
3.1.3 Support Structure Design 59
3.1.4 Build Design and Job Setting 60
3.2 Duplex stainless steel powder material 63
3.3 The laser melting system 65
3.3.1 Pre-build preparations 65
3.3.2 Post-build tasks and Sample Removal 66
3.4 Physical Properties 67
3.4.1 Dimensional accuracy 67
3.4.2 Density Analysis 67
3.5 Metallography 68
3.5.1 Sample Preparation 68
3.5.2 Void fraction / Porosity measurements 70
3.5.3 Etching for metallography 70
3.5.4 Grain Size measurements 73

3.5.5 EBSD preparation for SEM 73
3.5.6 XRD preparation for SEM 74
3.5.7 Feritscope 75
3.6 Mechanical properties 77
3.6.1 Hardness Evaluation 77
3.6.2 Tensile testing 80
3.7 Surface roughness 82
3.8 Magnetic properties 84
3.9 Machinability studies 85
3.9.1 Sample preparation and machine tools 86
3.9.2 Drill tools and inserts 88
3.9.3 Dynamometer 91
3.9.4 Temperature measurement 91
3.9.5 Insert analysis 92
3.10 Solution Annealing Heat treatment conditions 93
3.11 Summary of methodology 95
Chapter 4 Preliminary experiments 97
4.1 Evaluation of a new material for selective laser melting 97
4.2 Single layer samples 97
4.3 Multilayer cubic samples 100
4.3.1 Dimensional stability 102
4.3.2 Metallographic observations 103
4.3.3 Void fraction and density evaluation 108
4.3.4 Micro-hardness measurements 111
4.4 Laser scan speed influence on void fraction 113
4.5 Post-process solution annealing 117
4.6 Summary of the preliminary laser melting trials 118

Chapter 5 Metallographic and mechanical characterisations 120

5.1 Roles of process parameters 120

5.2 Metallographic evaluation 120

5.2.1 Epitaxial ferrite crystals growth and the precipitation of austenite ..121

5.2.2 Widmanstätten austenite growth 126

5.2.3 Location on the build plate 127

5.2.4 The role of the scan strategy 130

5.2.5 Fine cellular grain growth 132

5.2.6 CrN precipitation 134

5.2.7 Fusion zones and lack of fusion defects 136

5.2.8 Density analysis 140

5.2.9 Micro-hardness evaluation 142

5.3 Alternative scan strategies 144

5.3.1 Scan strategy vs density 145

5.4 Mechanical characterisation 147

5.4.1 Structure-property relationships 148

5.4.2 Tensile tests and results 151

5.4.3 Fracture surfaces and modes 156

5.5 Summary of Metallographic and Mechanical characterisation 165

Chapter 6 Magnetic characteristics of selective laser melted duplex stainless steels 166

6.1 Magnetic Characterisation 166

6.2 Ferrite to Austenite Ratios 168

6.3 Magnetic Hysteresis Loops 170

6.3.1 Saturation Magnetism 170

6.3.2 Coercivity 172

6.3.3 Anisotropic Features 174

6.4 Summary of the magnetic responses 176

Chapter 7 Machining and machinability of laser melted duplex stainless steels .. 177

7.1 Non-equilibrium structures and the anomalies 177

7.2 Mechanism of machining and metallographic responses 178

7.2.1 Wrought vs SLM samples 179

7.2.2 The role of the varying laser energy density 190

7.2.3 As-built vs solution annealing 193

7.3 Mechanics of machining 200

7.3.1 Comparative assessment of SLM and Wrought duplex steels 201

7.3.2 Varying laser energy density 208

7.3.3 The solution annealing effects on the machinability 212

7.4 Surface roughness responses 216

7.5 Chipping and breakage of cutting edges 219

7.6 Summary of the machinability studies 223

Chapter 8 Conclusions 225

8.1 Objectives and Achievements 225

8.2 General Conclusions 227

8.3 Quantitative Conclusions 231

8.4 Future Scope 234

References 235

Appendices 251

Appendix I: Powder Conformity Certificate 251

List of Publications

Journal Articles:

Davidson, K. and Singamneni, S., *Selective Laser Melting of Duplex Stainless Steel powders: An investigation.* Material and Manufacturing Processes, 2016. **31**(12): p. 1543-1555.

Davidson, K. and Singamneni, S., *Magnetic Characterization of Selective Laser-Melted Saf 2507 Duplex Stainless Steel.* JOM, 2017. **69**(3): p. 569-574.

Davidson, K. P. and Singamneni, S. B., *Metallographic evaluation of duplex stainless steel powders processed by Selective Laser Melting.* Rapid Prototyping Journal, 2017. **23**(6): p. 1146-1163.

Davidson, K. P. and Singamneni, S. B., *Mechanism of machining selective laser melted duplex stainless steels.* To be communicated at the time of submission.

Davidson, K. P. and Singamneni, S. B., *Mechanics of machining selective laser melted duplex stainless steels.* To be communicated at the time of submission.

List of Figures

Fig. 2-1 3D duplex stainless steel phase diagram (from Pohl et al. [10]) 11
Fig. 2-2 Pseudo-binary duplex stainless steel phase diagram (from Hoffmeister and Mundt [11]) 12
Fig. 2-3 Austenite forms. (Adapted from Yang et al. [14]) 13
Fig. 2-4 Cr_2N precipitation along ɣ-austenite/α-ferrite grain boundaries (from Ramirez [20]) 14
Fig. 2-5 σ-phase precipitation in SAF 2205 duplex stainless steel (from Chen and Yang [21]) 14
Fig. 2-6 Kraft pulp mill made from SAF 2205 (from Tigerstrand [44]) 18
Fig. 2-7 Duplex stainless steel tubed umbilical (from Sandvik [46]) 19
Fig. 2-8 Construction applications (a) Stonecutters Bridge, (b) Doha International Airport (Adapted from Outokumpu [49]) 20
Fig. 2-9 Multi stage flash evaporator made from SAF 2205 and LDX 2101 duplex stainless steel (from McManus [52]) 21
Fig. 2-10 Winery tanks made from LDX 2101 (from Chater [53]) 22
Fig. 2-11 Bionator made from SEW 410 Nr. 14517 duplex stainless steel wire (from Filho et al. [59]) 24
Fig. 2-12 σ-phase precipitation in cast duplex stainless steel (from Martins and Forti [65]) 27
Fig. 2-13 Shrinkage cavities in cast duplex stainless steel (from Haušild et al. [68]) 27
Fig. 2-14 Alligator cracking in hot rolled duplex stainless steel (from Subramanian and Chandramohan [71]) 29
Fig. 2-15 Hot deformed duplex stainless steel showing cracking at α-ferrite/α-ferrite grain boundaries (from Reis et al. [73]) 29
Fig. 2-16 α'-martensite precipitation in cold rolled SAF 2507 duplex stainless steel (from Hättestrand et al. [76]) 30
Fig. 2-17 Stagnation zone and α-ferrite agglomeration in SAF 2507 machining (Adapted from Nomani et al. [80]) 32
Fig. 2-18 BUE and Adhesion wear in a drill after machining SAF 2507 (from Nomani et al. [90]) 32
Fig. 2-19 Micro-hardness variation from machined surface (from Bordinassi et al. [87]) 33

Fig. 2-20 Sintered duplex stainless steel sample showing precipitates and constituents (from Martín [94])....36
Fig. 2-21 Porosity and microstructure of 750 MPa 300s duplex stainless steel sample (from Martín [94])....36
Fig. 2-22 Oxide formation on porosity in sintered duplex stainless steel (from Bautista [101])....36
Fig. 2-23 LENS Schematic (from Shin et al. [111])....38
Fig. 2-24 LENS processing of a turbine blade (from Gill [107])....39
Fig. 2-25 LENS manufactured duplex stainless steel microstructure (from Palmer [108])....39
Fig. 2-26 EBM schematic (from Arcam [123])....41
Fig. 2-27 EBM melting process (from Hiemenz [124])....41
Fig. 2-28 Precipitates formed during EBM processing of 316L (from Zhong et al. [114])....42
Fig. 2-29 SLM process schematic (from Kempen et al. [137])....44
Fig. 2-30 SLM of a dental crown (from EOS [138])....44
Fig. 2-31 Porosity in a high density SLM 316L sample (from Sun et al. [132])....44
Fig. 2-32 Columnar grain growth in SLM 316L (from Ma et al. [134])....45
Fig. 2-33 Equiaxed subgrain microstructure in SLM 1Cr18NiTi (from Ma et al. [134])....45
Fig. 2-34 Laser welded showing columnar ferrite grains, grain boundary austenite and Widmanstätten needles (from Liu et al. [145])....50
Fig. 2-35 Corrosion pits in ferrite of the laser weld fusion zone (from Yang et al. [14])....50
Fig. 2-36 Tensile test results of laser surface heat treated and non-treated (NT) laser welded SAF 2205 (from Liu et al. [145])....51
Fig. 2-37 The research plan....53
Fig. 3-1 SLM build flowchart....56
Fig. 3-2 Linear scan strategy and step numbers (dimensions in µm)....57
Fig. 3-3 Checkerboard scan strategy showing steps 1-10 (dimensions in µm)....58
Fig. 3-4 Meander scan strategy showing steps 1-4 and 67° rotation between layers (dimensions in µm)....59
Fig. 3-5 Support structure consisting of internal wall supports and a single contour support....59

Fig. 3-6 Build layout for cubic samples; (a) Naming convention, (b) Build dimensions (dimensions in mm) 61
Fig. 3-7 Tensile sample build layout (dimensions in mm)..... 62
Fig. 3-8 Build layout for drill samples; (a) Naming convention, (b) Build dimensions (dimensions in mm) 62
Fig. 3-9 Duplex stainless steel powder morphology (from Davidson and Singamneni [155])..... 64
Fig. 3-10 Powder size distribution (from Davidson and Singamneni [155])..... 64
Fig. 3-11 Renishaw AM250 SLM machine (from AUT 3D Printing Lab[156])..... 65
Fig. 3-12 Archimedes density experimental setup..... 68
Fig. 3-13 Sample mountings; (a) Cut Sample, (b) PolyFast Resin, (c) ClaroFast Resin 69
Fig. 3-14 Olympus BX51 M optical microscope..... 70
Fig. 3-15 Electrochemical etching setup..... 72
Fig. 3-16 Hitachi SU-70 SEM..... 73
Fig. 3-17 FEI Quanta 200 scanning electron microscope (from the University of Glasgow [164])..... 74
Fig. 3-18 Xpert Pro Panalytical XRD (from James Hutton Institute [165])..... 75
Fig. 3-19 Fischer Fischerscope MMS (a) with an EGAB1.3-FE probe (b) (Adapted from Helmut Fischer [167])..... 76
Fig. 3-20 Feritscope testing locations (dimensions in mm)..... 76
Fig. 3-21 Leco LM800AT Vickers micro-hardness tester..... 77
Fig. 3-22 Micro-hardness testing locations on preliminary multi-layer samples (dimensions in mm) 78
Fig. 3-23 Micro-hardness test area on sample cross-section for metallographic characterisation samples..... 79
Fig. 3-24 Lyric HR-150A hardness tester..... 80
Fig. 3-25 Drill sample hardness test locations (dimensions in mm)..... 80
Fig. 3-26 Tinius Olsen H50KS tensile testing machine..... 81
Fig. 3-27 Tensile test sample dimensions (dimensions in mm)..... 81
Fig. 3-28 Taylor Hobson Talysurf 50 stylus profilometer..... 83
Fig. 3-29 Drill test surface roughness measurement locations 83
Fig. 3-30 Lake Shore 3900 VSM (from Lake Shore Cryotronics used for magnetic characterisation [177]) 85
Fig. 3-31 Fanuc Tape Drill and dynamometer setup..... 87
Fig. 3-32 Thermocouple hole locations and depth (dimensions in mm) 88

Fig. 3-33 Iscar indexable head drill and insert (a)-(b) and Sandvik solid carbide drill (c)-(d) 89
Fig. 3-34 Kistler drill dynamometer setup; (a) Dynamometer, (b) Charge Amplifier 91
Fig. 3-35 Thermocouple data logger 92
Fig. 3-36 Olympus SZX9 stereo microscope 93
Fig. 3-37 Abar Ipsen HR-50 vacuum furnace 94
Fig. 3-38 Solution annealing heat treatment cycle - (a), First 500°C cooling - (b) 95
Fig. 4-1 Single layer trials build layout (dimensions in mm) 98
Fig. 4-2 Single layer laser melted duplex samples. (a) 28.2 J/mm^3: (b) 56.5 J/mm^3; (c) 84.7 J/mm^3; (d) 113 J/mm^3 laser energy density samples 99
Fig. 4-3 Multi-layer test pieces on the substrate plate and laser energy density settings 101
Fig. 4-4 113 J/mm^3 sample showing discolouration of top surface and sintered powder line on LHS wall 102
Fig. 4-5 Percentage error in; (a) width and length, (b) height with increasing laser energy density; 103
Fig. 4-6 Photomicrographs of cross sections of multi-layer samples in order of build position. (a)-(e), 49.4-77.7 J/mm^3; (f)-(j), 84.7-113 J/mm^3 105
Fig. 4-7 Void fraction vs laser energy density at a fixed scan speed of 590mm/s 108
Fig. 4-8 Pore morphology of samples with increasing laser energy density; (a) 49.4 J/mm^3, (b) 77.7 J/mm^3 and (c) 105.9 J/mm^3 110
Fig. 4-9 Part density vs laser energy density with the scan speed fixed at 590mm/s ... 111
Fig. 4-10 Micro-hardness vs laser energy density with the scan speed fixed at 590mm/s 112
Fig. 4-11 Void fraction for 290, 390, 490 and 790 mm/s 115
Fig. 4-12 Void fraction variation with scan speed (a) 74.8 J/mm^3 390mm/s, (b) 76.5 J/mm^3 490mm/s and (c) 79.1 J/mm^3 790mm/s 115
Fig. 4-13 Void fraction of 290-490 mm/s samples with images at; (a) 85 J/mm^3 490mm/s, (b) 128.2 J/mm^3 390mm/s and (c) 215.5 J/mm^3 290mm/s 116
Fig. 4-14 Photomicrographs of solution annealed samples; (a) 105.9 J/mm^3, and (b) 113 J/mm^3 118
Fig. 5-1 Photomicrographs of the cross sections of laser melted duplex stainless steel samples with varying energy densities 123
Fig. 5-2 (a) XRD pattern of the sample produced at 300W and 119.9 J/mm^3, (b) XRD pattern obtained from a slow scan in the 2Θ range of 38 to 48° 124

Fig. 5-3 Average grain aspect ratio at corresponding laser energy densities 125
Fig. 5-4 EBSD orientation map and inverse pole figures of the sample produced at 400 W and 141 J/mm^3 126
Fig. 5-5 Samples produced with 91.7 and 119.9 J/mm^3 at 300 and 325 W respectively 128
Fig. 5-6 EBSD orientation map and inverse pole figures of the sample produced at 300 W and 91.7 J/mm^3 129
Fig. 5-7 The 350 W sample at 134 J/mm^3 showing widened columnar grain at the double scanned centreline 130
Fig. 5-8 The 400 W sample at 141 J/mm^3 showing columnar grains around the outer contour 131
Fig. 5-9 Sample at 141 J/mm^3 and 375 W showing densely packed intersecting Widmanstätten growth 132
Fig. 5-10 SEM images of 91.7 and 141 J/mm^3 samples at 300 and 400 W 133
Fig. 5-11 SEM image of 112.8 J/mm^3 sample at 300 W showing cellular grain growth 134
Fig. 5-12 CrN precipitate formation in the 141 J/mm^3 sample at 300 W 135
Fig. 5-13 Fusion zones of the 91.7 J/mm^3 sample at 300 W at (a) 2000x and (b) 6000x magnification 137
Fig. 5-14 Lack of fusion defects in samples produced at (a) - 105.8 J/mm^3 375 W and (b) - 91.7 J/mm^3 350 W, (c) - higher magnification of (a) 138
Fig. 5-15 Sample produced at 91.7 J/mm^3 and 400 W showing impinged columnar grain growth between lack of fusion defects 139
Fig. 5-16 Bulk densities of samples at laser energy densities 140
Fig. 5-17 Bulk density variation with laser power and energy density 141
Fig. 5-18 Variation of density with respect to scan speed at 350 and 400 W 142
Fig. 5-19 Micro-hardness variation along part contour, bulk and centre with increasing laser energy density 143
Fig. 5-20 Bulk density of meander and checkerboard samples with varying laser power and speed 146
Fig. 5-21 Highest density values and corresponding parameters 147
Fig. 5-22 Cross-sectional microstructures of samples produced at 154.8 J/mm^3 150
Fig. 5-23 Wrought rolled plate SAF 2507 150
Fig. 5-24 Average tensile strength of SLM and wrought duplex stainless steels 152
Fig. 5-25 Average elongation of SLM and wrought duplex stainless steel 153

Fig. 5-26 Tensile results for a select As Built and Annealed samples at orientations; (a) - 0°, (b) - 45°, (c) - 90° 155
Fig. 5-27 Underside surface of sample produced at 178.6 J/mm^3 and 0°, showing defects in between supports 156
Fig. 5-28 Fracture angle in; (a) 0°, (b) 45° and (c) 90° samples at 178.6 J/mm^3 157
Fig. 5-29 Rippling in 45° sample at 154.8 J/mm^3. (a) Ripples along underside, (b) Ripple on thickness, (c) Ripple on width, and respective location image 158
Fig. 5-30 Fracture surfaces of samples produced at 154.8 J/mm^3 159
Fig. 5-31 Fracture surface of 0° samples at 5000x magnification 160
Fig. 5-32 Fracture surface of 45° samples at 5000x magnification 162
Fig. 5-33 Fracture surface of 90° samples at 5000x magnification 163
Fig. 5-34 High magnification of Fig. 5-32(f) showing micro-cracking on fracture surface 164
Fig. 5-35 High magnification of Fig. 5-33-(c) showing CrN precipitation on fracture surface 165
Fig. 6-1 Photomicrograph of a SLM sample built at 98.9 J/mm³ 169
Fig. 6-2 Ferrite content vs LED 170
Fig. 6-3 Saturation Magnetism results SLM samples produced at varying Laser Energy Densities 172
Fig. 6-4 Coercivity results with SLM samples produced at varying Laser Energy Densities 174
Fig. 6-5 Hysteresis loops for the 91.8 J/mm^3 sample with grains; perpendicular (a) and parallel (b) to the direction of vibration. Inset: microstructure orientation. Detail of graph intersection and coercivity. 175
Fig. 7-1 Microstructural images of wrought and SLM samples at a feed of 0.025 mm/rev 181
Fig. 7-2 Microstructural images of wrought and SLM samples at a feed of 0.05 mm/rev 182
Fig. 7-3 Grain elongation and deformation kinks in wrought duplex stainless steel machined at 20 m/min and 0.025 mm/rev 183
Fig. 7-4 Plastic deformation of austenite grains in wrought (a) and SLM (b) samples machined at 20m/min and 0.05 mm/rev 184
Fig. 7-5 Micro-hardness results from wrought (a)-(b) and SLM (c)-(d) samples 186
Fig. 7-6 Chip images of Wrought and SLM samples at a feed of 0.025 mm/rev 188
Fig. 7-7 Chip images of Wrought and SLM samples at a feed of 0.05 mm/rev 189

Fig. 7-8 Microstructural images of SLM samples at four LED's and wrought duplex stainless steel at Vc – 60 m/min, f – 0.025 mm/rev 191
Fig. 7-9 Bulk hardness of SLM samples with varying LED and wrought SAF 2507 .. 192
Fig. 7-10 Microstructural images of SLM samples in the as-built and solution annealed condition 194
Fig. 7-11 Micro duplex grain structure in as-built and solution annealed samples at 100 m/min 196
Fig. 7-12 High magnification images of as-built and solution annealed samples drilled at 100 m/min 197
Fig. 7-13 Austenite whiskers formed in the drilling of the as-built sample at 60 m/min 198
Fig. 7-14 As-Built and Solution Annealed SLM samples drilled at 100 and 140 m/min, showing discoloured plastic deformation 199
Fig. 7-15 Micro-hardness readings for SLM samples in the (a) as-built and (b) solution annealed condition 200
Fig. 7-16 Drilling torque variation while machining (a) wrought and (b) SLM samples 202
Fig. 7-17 Thrust force variation while machining (a) wrought and (b) SLM samples . 203
Fig. 7-18 Temperature traces of wrought and SLM samples at a feed of 0.025mm/rev 206
Fig. 7-19 Temperature traces of wrought and SLM samples at a feed of 0.05mm/rev 207
Fig. 7-20 Drilling torque - (a) and thrust force - (b) for SLM samples of varying LED produced at; Vc – 60 m/min, f- 0.025 mm/rev 209
Fig. 7-21 Drilling temperature traces for SLM samples at varying LED and Wrought SAF 2507 211
Fig. 7-22 Drilling torque - (a) and thrust force - (b) for SLM samples in the as-built and solution annealed conditions (feed 0.025 mm/rev) 213
Fig. 7-23 Average maximum temperatures in drilling as-built and solution annealed SLM duplex stainless steel 213
Fig. 7-24 Drilling temperature traces for SLM samples in the as-built and the solution annealed conditions 215
Fig. 7-25 Surface Roughness of (a) wrought and (b) SLM samples 217
Fig. 7-26 Average surface roughness for SLM samples at varying LED and Wrought SAF 2507 218

Fig. 7-27 Surface roughness for SLM samples in the as-built and solution annealed condition.....219
Fig. 7-28 Drill insert damage in the SLM samples at varying LED and Wrought SAF 2507 220
Fig. 7-29 Drill damage in the as-built SLM sample.....222
Fig. 7-30 Solution annealed SLM sample drill wear 223

List of Tables

Table 2-1 Processing issues with duplex stainless steels 25
Table 3-1 Design of the study 55
Table 3-2 Support structure parameters 60
Table 3-3 Drill sample build parameter layout 63
Table 3-4 Chemical composition of SAF 2507 super duplex stainless steel powder 64
Table 3-5 Micro-hardness testing locations of metallographic characterisation samples 79
Table 3-6 Surface roughness test parameters 83
Table 3-7 Process parameter settings for the Machinability studies 86
Table 3-8 Insert and Drill body allocation SLM vs Wrought SAF 2507 trials and LED evaluation 90
Table 3-9 Solid carbide drill allocation for SLM as built vs solution anneal trials 90
Table 4-1 Multilayer cubic sample build parameter layout 100
Table 4-2 Laser scan speed influence on void fraction cubic sample build parameter layout 114
Table 4-3 Post process solution anneal cubic sample build parameter layout 117
Table 5-1 Metallographic evaluation cubic sample build parameter layout 121
Table 5-2 Scan strategy evaluation sample build parameter layout 145
Table 5-3 Tensile test result summary 148
Table 6-1 Magnetic characterisation sample build parameter layout 168
Table 6-2 Magnetic saturation values of comparable duplex stainless steels 172
Table 6-3 Coercivity values of comparable duplex stainless steels 174
Table 7-1 Machinability condition window 178
Table 7-2 SLM processing parameters 179

List of terms and Abbreviations

γ: Austenite

γ_2: Secondary Austenite

α / δ: Ferrite

α': Martensite

σ: Sigma Phase

AM: Additive Manufacturing

B: Magnetic Flux Density

BUE: Built-Up Edge

CNC: Computer Numerical Control

CPT: Critical Pitting corrosion Temperature

Cr_2N /CrN: Chromium Nitrides

DED: Direct Energy Deposition

EBM: Electron Beam Melting

EBSD: Electro Backscatter Diffraction

EDM: Electro Discharge Machining

EDS: Electro Dispersive Spectrometry

EN: European standard

FSW: Friction Stir Welding

Fx / Fy: Drill side Forces

Fz: Drill Thrust Force

GTAW: Gas Tungsten Arc Welding

H: Magnetic Field Strength

HAZ: Heat affected zone

Hc: Coercivity

HIP: Hot Isostatic Pressing

HRC: Rockwell Hardness C

HSS: High Speed Steel

HV: Hardness Vickers

LED: Laser Energy Density

LENS: Laser Engineered Net Shaping

Mr: Remnant Magnetism

Ms: Saturation Magnetism

Mz: Drilling Torque

PREN: Pitting Resistance Equivalent Number

SLM: Selective Laser Melting

SLS: Selective Laser Sintering

UAM: Ultrasonic Additive Manufacturing

UNS: Unified numbering system

UTS: Ultimate Tensile Strength

VSM: Vibrating Sample Magnetometer

W-DED: Wire Direct Energy Deposition

XRD: X-Ray Diffraction

Attestation of Authorship

I hereby declare that this submission is my own work and that, to the best of my knowledge and belief, it contains no material previously published or written by another person (except where explicitly defined in the acknowledgments), nor material which to a substantial extent has been submitted for the award of any other degree or diploma of a university or other institution of higher learning.

Karl Davidson – 15/11/2017 Signature: 

Acknowledgments

I would like to express my utmost gratitude to those who have assisted me in the completion of this thesis, who without their support this would not be possible. I wish to express my profound gratitude to my primary supervisor Assoc. Professor Sarat Singamneni for his valuable support, financial assistance, wealth of knowledge and supervision through this project for which I am greatly indebted. I wish to further acknowledge my secondary supervisor Professor Thomas Neitzert for his supplementary assistance in this project.

I wish to acknowledge to the Additive Manufacturing Research Centre including its scholars both past and present, for providing a platform to conduct this research and who's assistance in the doctoral process I have valued greatly.

This thesis and research work contained would not be possible without the facilities and expertise of the 3D Printing Lab including technicians Ross Jacobs and Jenna Makgill who have welcomed and supported me in the operation of the laser melting machine.

I further wish to recognize AUT University mechanical engineering technical staff; Mark Masterton, Thomas Jones and Patrick Conor, and science technicians Yan Wang and Dr Chris Pook for providing me with equipment and knowledge to conduct the experiments presented.

In specific cases, facilities were required outside of AUT University for which I would like to thank the staff who accommodated me and the facility location; Dr Christian Ohneiser at the University of Otago, Michael Sanders of Optimech International Ltd, Catherine Hobbis at the University of Auckland, Adam Walmsley of Heat Treatments Ltd and E. Nandha Kumar at the Indian Institute of Technology in Madras.

This PhD journey would not have been possible without the endless support and motivation of my friends who made it all the more enjoyable through shared experiences.

Lastly, I wish to express my sincere appreciation and love to my family including my sister Amy and her partner Stephen, and my grandmother Wendy. I am especially indebted to my parents, Peter and Carolyn for their continual guidance, love and encouragement, and who without, this thesis would be but a dream.

Chapter 1
Introduction

1.1 Background

Duplex stainless steels are a family of alloy grades combining good attributes of both austenitic and ferritic stainless steels and exhibiting excellent corrosion resistance and strength qualities. All duplex stainless steels have chloride stress corrosion cracking resistance and strength qualities significantly greater than those of the austenitic stainless steels, while also possessing good ductility and toughness. Furthermore, they are also much cheaper compared to the most popular Ti-6Al-4V alloy. The lower overall costs and excellent properties make duplex stainless steels promising candidates for a wide range of applications. Fabrication techniques as used with other stainless steels are also applied to duplex stainless steels, but considering the high strength and sensitive metallographic aspects, careful considerations are often necessary depending on the nature of the process.

The main benefits of using duplex stainless steels include high strength, almost double that of the austenitic counterparts together with high pitting and crevice corrosion resistance properties. This led to the possibility of thinner and lighter components in oil and gas and desalination installations. The same attributes allowed duplex steels to make great strides towards the applications in the biofuels, food and beverage, and the architectural industries. The umbilicals for the oil and gas, large storage tanks for biofuel, food or wine storage tanks in the food and beverage, and structural components of bridges or roof panels in the civil construction and architecture industries are notable examples.

Duplex stainless steel is over 30 times cheaper than the popular engineering alloy Ti-6Al-4V. This makes duplex stainless steels a lucrative metal for the manufacture of patient specific medical implants also. When electrochemically corroded in salt and synthetic bio-fluidic solutions, duplex stainless steels did not show signs of pitting and resisted

localised corrosion. Additionally *in vivo* pins made of 2507 DSS were implanted with a PTFE sleeve into test subject animals and did not show any signs of corrosion. The annual turnover of medical device companies worldwide runs into several billion dollars, a large portion of which comes from artificial knees, fracture repair fasteners and artificial hips. The lower overall cost and promising properties of duplex stainless steels make them cheaper candidates for medical implants.

While all these attributes find an important place for duplex steels in the manufacturing realm, the added benefits over the other stainless steel counter parts also come with additional shortcomings. The essential attributes of duplex steels stem from the equal ratios of ferrite and austenite in the dual phase microstructures. Maintaining this balance is often quite sensitive during secondary processing, which makes it relatively difficult to apply processing methods such as machining. Powder metallurgy methods have been used to achieve consolidation of duplex steel powders into products. However, these are limited by shape, size, and also often suffer from porosities. Considering the application potentials, it is important to look for possible new avenues for processing these exciting stainless steel alloy grades. Additive manufacturing is a recent development as a viable means of producing near net shape objects from powder metals, based on the digital product data. It is interesting to evaluate how duplex steels and additive manufacturing can be brought together and this thesis is the result of experimental research conducted towards this goal.

1.2 Alloying elements, structural sensitivity, and processing limitations

Early development of duplex steels began with the use of chromium, nickel, and molybdenum, and the so-called first generation duplex stainless steels helped reduce the inter-granular corrosion problems in the then austenitic stainless steels. However, welded structures suffered from lack of corrosion resistance and toughness, as the heat affected zones were predominantly turned into ferrite. Nitrogen was found to resolve this issue as the second generation duplex stainless steels are alloyed with nitrogen, to help maintain

the toughness and the corrosion resistance of the heat affected zones in welding. Considering the specific roles of these essential alloying elements, chromium helps improve the corrosion resistance by means of generating a passive film. It also promotes the body centered cubic ferrite formation. Nickel is then necessary to help promote the face centered cubic structure and acts as an austenite stabiliser. Therefore, the relative amounts of these two ingredients are critical in achieving the balanced equal ratio austeno-ferritic structures, characteristic of the duplex steels. Molybdenum and nitrogen play roles increasing the pitting and the crevice corrosion resistances respectively.

Duplex stainless steels are strong and the equally balanced dual phase structures are very sensitive to thermomechanical interactions during secondary processing stages. The yield stress is twice and they also work harden at almost the same rates as that of the austenitic grades. Hot forming is done with duplex steels, but depending on the temperature used, it is often common that cracks may generate in the ferrite regions. Cold forming could lead to much higher spring-back due to higher strength and work hardening characteristics. While machining, formation of continuous chips often leads to difficulties as these are strong and subject the tool faces to significant wear and tear. Consequently, most duplex grades of steels are more difficult to machine compared to the austenitic steels. The weldability is generally high due to the higher ferrite contents compared to the austenitic steels, but post-welding performance problems are common in the heat affected zones. Loss of the duplex structures due to non-equilibrium heating and cooling rates in the heat affected zones could lead to loss of corrosion resistance and toughness, apart from possible post-weld cracking.

Powder metallurgy techniques were used effectively to sinter duplex powders into solid forms. The raw powder metals could be made of the duplex alloys or mixtures of austenitic and ferritic stainless steel constituents. The mechanical characteristics of the sintered parts were noted to be as expected of duplex steels, but insufficient sintering and associated porosity are often shortcomings associated with the powder metallurgy methods. Also, the final forms achieved are often confined to those of the sintering tools employed. The additive processing methods, while allowing for powder consolidation in similar lines as the solid state sintering mechanisms in the powder metallurgy routes, will

also bring the benefits of liquid state sintering and possibly offer promising new processing options for duplex stainless steels.

1.3 The additive processing realm

In the recent past, the additive processing methods progressed by leaps and bounds, evolving from the mere prototyping solutions into the direct digital manufacturing options. While all different material systems including polymers, metals, ceramics and their composites are involved in the progression towards additive manufacturing, the possibility of converting metal powders directly into final three dimensional forms of relatively more complex shapes opened up a plethora of opportunities both for research and practical applications. Electron beam melting, laser engineered net shaping, and selective laser melting are the three most important technologies that saw considerable growth and establishment in the past decade. In particular, the selective laser melting is the most popular choice, as the basic systems are comparatively cheap and are more commonly made available for experimental research. The efforts of the past decade established around five different metal systems as commercially viable options for selective laser melting (SLM), while the extensive research exploring other options is widely happening around the world.

By far, titanium and its alloys are the most popular materials researched for selective laser melting, considering their attractive properties including high strength to mass ratio, corrosion resistance and low ion formation in aqueous conditions. Considerable research interest and progress followed, establishing the possible metallographic variations emanating from the thermo-physical process conditions and the process-structure and property relationships. Apart from further investigation of influences of varying process parameters on micro hardness, phase composition, and fatigue responses, considerable growth is also evident in the integration of the material and process combination to the requirements of the medical field. Selective laser melting of pure titanium attracted significant research attention in terms of evaluating specimen density, microstructure and wear performance. Biomedical applications of SLM parts produced from pure titanium

powder and applications of bioactive Ti structures as human cancellous bone replacements are other significant developments. Experimental research also established the selective laser melting process as the most suitable for fabricating the biomedical scaffolds of controlled porosities.

Other metals investigated for SLM include aluminium alloys and different grades of stainless steels. Aluminium alloys such as AlSi10Mg, austenitic stainless steel 316L, and precipitation hardened martensitic stainless steel 17-4 PH are the common alloys evaluated based on selective laser melting as the processing route. Effects of laser power, scanning speed, layer thickness and energy density were considered independently and in combinations, in order to establish properties such as tensile strength, density, and surface quality. While all these efforts and the science progress constitute a new wave of knowledge and technological progress in the advanced manufacturing of metals, the whole endeavour is still in its infancy, as many metal and alloy systems are yet to be evaluated for processing by selective laser melting. In particular, the dual-phase duplex stainless steels have attained very little or no attention in the context of SLM. Considering the processing difficulties associated with duplex steels, predominately due to the bi-phasic internal structures and the sensitive interactions of the meta-stable phases to thermomechanical processing, it is interesting and important to experimentally evaluate duplex steels for processing by selective laser melting.

1.4 Research gap, questions and hypothesis

Evidently, duplex stainless steel powders are amenable for processing by sintering, but there was hardly any evidence of scientific research conducted applying selective laser melting, particularly at the time this project had started. This was the research gap identified and the research proposal was to undertake this task through experimental investigations, targeting a thorough evaluation of the response of the material system to varying laser melting process conditions. The overarching research question highlights as to how the duplex steel material responds overall to the point-by-point consolidation by the laser energy input. Further questions followed around the possible implications on the

internal structures, methods of regaining the structural alterations, the process-structure-property relationships, and the possible after-effects of the critical structural variations on specific responses if any. Based on the literature reviewed in a parallel but related field, laser welding, the hypothesis that selective laser melting can be applied to duplex steels and structural alterations if any can be regained through suitable solution annealing processes was formulated.

1.5 Objectives, methods and critical achievements

Experimental research has been planned for implementation in two stages. The first stage was to evaluate the basic responses of duplex stainless steels to selective laser melting under simple and preliminary processing conditions. Once the suitability of the material and process combination was established, the second stage experimentation would commence, considering deeper analyses of the microstructures, mechanical properties, and the process-structure-property relationships. The second stage also included evaluation of the outstanding property variations if any, arising out of the possible changes in the microstructures as a result of the laser interactions. The overall objective is to experimentally establish how duplex stainless steels respond to the laser melting conditions and if structural alterations resulting can be eliminated by a suitable heat treatment process. Beyond this, the research also aims at a deeper understanding of the metallographic aspects, the mechanical properties, and other structure property relations and responses including magnetic and machinability attributes.

Experimental evaluations are the central theme of the research methodology employed. A Renishaw AM250 laser melting system was the test bed for all the laser melting trials. The scan strategies considered include the conventional linear hatch, cross hatch, contour and the use of a multi scan process for each layer. Optical and scanning electron microscopy were used for the metallographic evaluations. The Archimedes method was used for the density evaluations. Measurements based on a ferritscope allowed to assess the relative amounts of ferrite and austenite in the microstructures. Critical mechanical properties are established by means of the standard materials testing equipment. Vibration

sample magnetometer studies led to the establishment of the magnetic properties. Machinability tests were done based on a CNC machining centre, using a Kistler dynamometer, and a data logger for recording the temperature profiles.

The research began with a comprehensive literature review understanding the behaviour of metallic materials processed by SLM and the metallurgy of duplex stainless steel. This was followed by initial trials involving SLM of selected grades of duplex stainless steels to develop the *a priori* data. Once the process-parameter window was established, the experimental design for further evaluation of the microstructures and mechanical characterisations were developed and executed. Considering the observations that the processed materials turned into predominantly ferritic structures, variations in the magnetic responses were established next. The same structural variations also led to the evaluation of the machining responses of the laser melted duplex materials in the as-built and the solutions annealed states compared to the wrought steels.

The experimental results from the initial stage clearly elucidated that the duplex powders can be processed by selective laser melting, achieving densities at above 90%. The microstructures were distorted completely as high amounts of ferrite were noted, but a solution annealing treatment was noted to bring the results back to almost equal amounts of ferrite and austenite, though with some restraints in the grain size and growth. The physical and mechanical property data were in accordance with the micro structures in the as-built and the solution annealed states. The magnetic behaviour in the as-built state was an anomaly, as the normally hard duplex steel was turned into a promising soft magnetic material. It was also an interesting and useful finding that the machinability actually improved in the as-built state in spite of the structural complications. Within the limits of the experimental conditions, the maximum density obtained with the laser melted duplex samples as at almost 95%. This is promising, considering the fact that the process parameters can further be optimised during the course of building the material file for commercial applications.

Chapter 2
Literature review, research gaps, questions, and objectives

2.1 Duplex stainless steels

Combining equivalent ratios of face centred cubic austenite and body centred cubic ferrite, duplex stainless steels possess beneficial properties induced from both grades with high mechanical strength, corrosion and chloride stress corrosion cracking resistance. By default, they contain more than 13 wt% chromium with different grades tailored by adding varying amounts of molybdenum, tungsten, and nitrogen. Higher mechanical and chemical properties together with good welding characteristics led to the widespread use of duplex steels in different fields of application; oil and gas, construction, desalination, food and beverage, etc. Though in existence for over 80 years, more significant adoption of these steels only began actively in 1980's but there has been an increasing use ever since [1]. Duplex stainless steels are chosen for the current research and the aim is to integrate them with the rapid developments taking place in the additive processing technologies in the recent past. A brief review of the relevant literature is presented in the following sections, contextualising the history of development, metallography, application potential, processing methods and associated shortcomings of duplex steels. The research gaps, questions, and the hypothesis will be formulated based in this review.

2.1.1 The chronology of development of duplex stainless steels

The foundation of stainless steels was laid in 1913 with the discovery of a 12.8% chromium and 0.24% carbon steel to be devoid of rusting by Harry Brearley [2]. No more than 14 years after this discovery, Bain and Griffith published their work on the ferritic-austenitic (duplex) structures [3]. Further research was carried out in Europe including the French patent granted to J. Holtzer Steelworks for the duplex alloy 21Cr-7Ni-2.5Mo. However, Scandinavia led the development of duplex stainless steels, with the production

of two grades 453E & 453S by Avesta Steelworks in Sweden [4]. Further advances were made in the following years, including the establishment of the promising resistance to chloride stress corrosion cracking of duplex steels in the 1950's. A shortage of nickel in the next two decades (60's and 70's) further promoted the use of duplex stainless steels, while an increase in the offshore oil mining warranted the extensive application of the steels [4, 5].

Certain advances in the steel casting techniques were made during the 1970's, minimising process related oxidation and compositional changes. Nitrogen impartation and a reduction in carbon content showed to improve corrosion resistance and high temperature stability attributes [5]. The addition of nitrogen promoted commercial use of stainless steels in welded structures, as the nitrogen was found to restore the HAZ of the weld and also to improve the pitting corrosion resistance of the weld [4]. These advances in the composition yielded the second generation of duplex stainless steels, including the popular SAF 2205 (EN 1.4462, UNS 31803/32205) grade with a composition of 22Cr-5Ni-3Mo-0.16N, which took up almost 85% of the volume of duplex stainless steel produced [5, 6].

The high alloyed 25Cr series duplex stainless steels were re-introduced in the mid-1980's as super duplex stainless steels (SAF 2507, EN 1.4410, UNS S32750) with increased molybdenum and nitrogen contents giving rise to higher pitting corrosion resistance. At the same time, lean duplex stainless steel grades emerged with reduced nickel and increased manganese and nitrogen contents to lower the overall material costs (SAF 2304, EN 1.4362, UNS S32304) [4]. Recent years have seen considerable interest and increase in the production of both lean and super grades of duplex stainless steels. The lean grade is promoted as a possible successor to the popular austenitic stainless steel grades 304 and 316, assisted by a reduced material cost [7]. All the while, superduplex grades have seen increasing alloying elements and evolved as hyper-duplex grades such as SAF 2707HD (UNS S32707), 2906, and the more recent addition 3207HD (UNS 33207), to promote welds without the precipitation of the intermetallic phases [4]. The identification codes of duplex stainless steel grades follow their Sandvik trade name e.g. SAF 2507. In specific cases the Outokumpu trade name is used e.g. LDX 2101. Identification codes in

the brackets above represent the European standard (EN) and Unified numbering system (UNS) standard respectively.

Classification of duplex stainless steel grades

Commonly, duplex stainless steels are ranked based on their pitting corrosion resistance. The unit-less Pitting Resistance Equivalent Number (PREN) is defined by the constituent alloy quantities as weight percentages [1].

$$PREN = \%Cr + 3.3(\%Mo + 0.5\%W) + 16\%N \quad \text{(Eq. 2.1)}$$

The PREN numbers of the five common grades of duplex stainless steels are as follows:

- Lean duplex - Reduced nickel content and no molybdenum addition, PREN between 23 and 29, e.g. SAF 2304
- Standard duplex – Greatest production numbers (80% of Duplex production) e.g. SAF 2205 with a PREN between 31 and 38 [8]
- 25Cr duplex – 25% chromium e.g. 255 with a PREN less than 40
- Superduplex – 25-26% chromium, increased molybdenum and nitrogen content over 25Cr grade with a PREN between 40 and 45, e.g. SAF 2507
- Hyper-duplex – High alloy content, PREN over 45 , e.g. SAF 2707 [1]

Sandvik's SAF 3207HD has the maximum stated PREN number of 50. However, there have been detrimental responses noted in steels with very high PREN numbers. Liljas observed that duplex stainless steels with a PREN number in excess of 50 exhibit increased risk of intermetallic phase formation [4, 9].

2.1.2 Metallurgy of duplex stainless steels

The bi-phasic microstructure comprising of ferrite and austenite is unique to the duplex grade stainless steels, with austenite contents ranging from 45 to 60% by volume [3]. The chemical composition and the annealing temperature are to be critically controlled in order to achieve the characteristic duplex structures as depicted in the three dimensional complex Fe-Cr-Ni phase diagram of Fig. 2-1. The duplex phase transformation occurs at the centre trisection as shown in Fig. 2-2 [3].

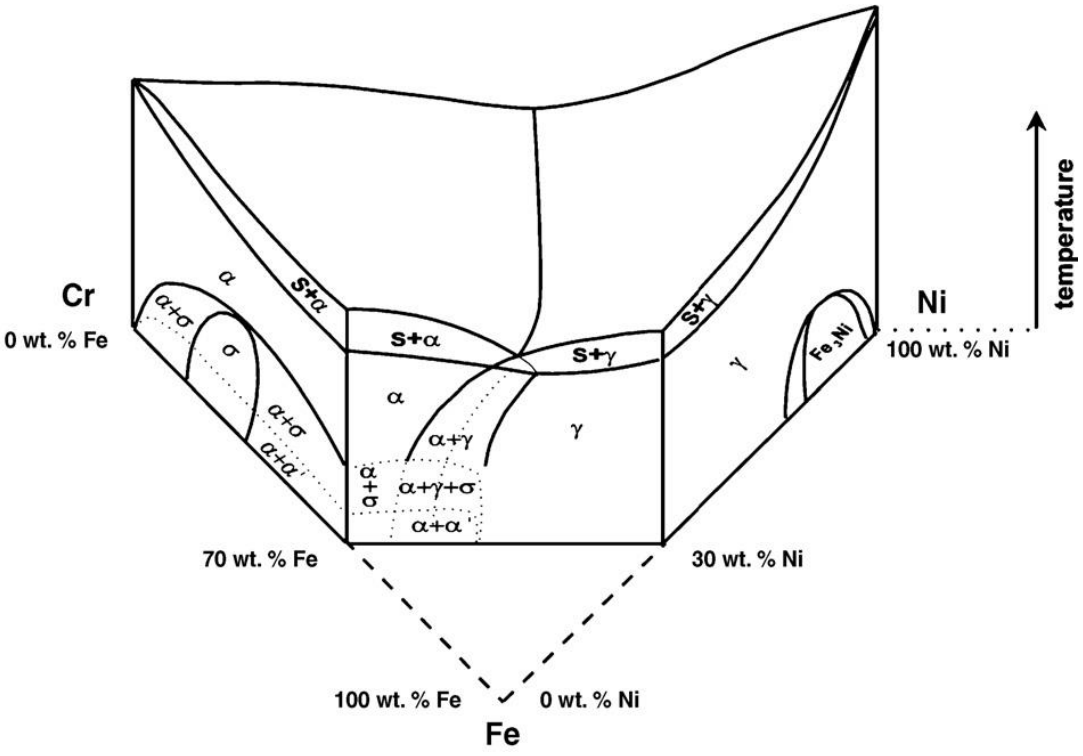

Fig. 2-1 3D duplex stainless steel phase diagram (from Pohl et al. [10])

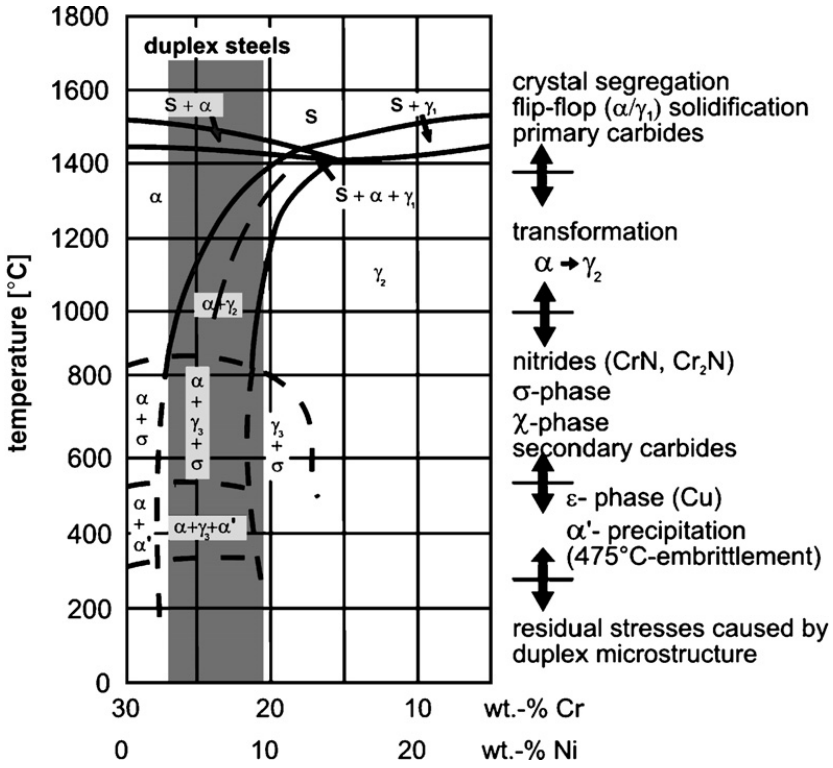

Fig. 2-2 Pseudo-binary duplex stainless steel phase diagram (from Hoffmeister and Mundt [11])

Solidification process

Conversion of α-ferrite to γ-austenite is principal to the formation of the duplex microstructure. It can commence in two different ways; decomposition of the solidified α-ferrite phase and direct solidification as austenite from the liquid state through an ordered sequence of solidification [12]. Further to the formation of austenite below the solidus line, the orientation and shape of austenite grains depend on the cooling rates. Ogawa *et al.* observed the solid state phase transformation of ferrite to austenite to occur based on three characteristic mechanisms; as grain boundary allotriomorphs along prior ferrite grain boundaries, plate-like growth with Widmanstätten morphology, and intragranular precipitation with a fine acicular morphology. The three forms of austenite formation are depicted in the photomicrograph of Fig. 2-3 [13].

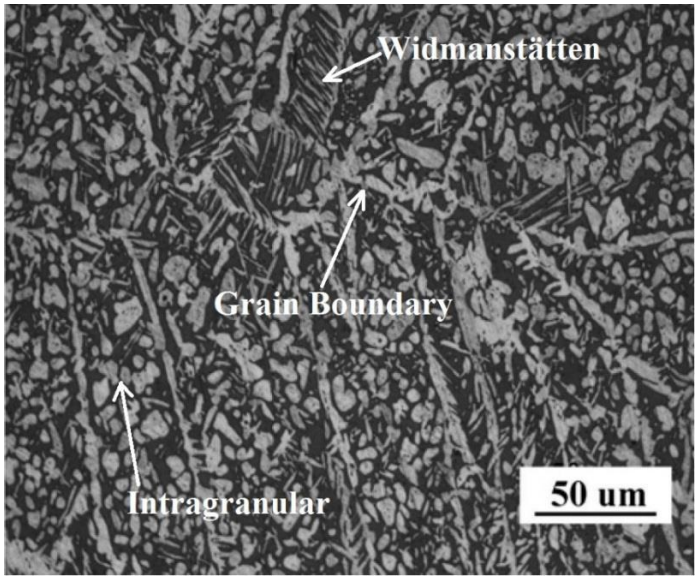

Fig. 2-3 Austenite forms. (Adapted from Yang et al. [14])

Formation of γ-austenite occurs below the solidus, between 1150-1250 °C, preferentially along grain boundaries, and commonly under slow cooling rates [13]. Comparatively, Widmanstätten austenite laths are noted by Ohmori *et al.* to precipitate between 1000-1100 °C under rapid cooling rates while similar observations were also made with intragranular austenite by Ramirez *et al.* [15, 16]. Precipitation of deleterious phases including nitrides (Cr_2N, CrN) along α-ferrite/γ-austenite grain boundaries as seen in Fig. 2-4 may also result from the rapid cooling rates. Liao *et al.* noted that cooling rates in excess of 20 K/s can result in nitride precipitation due to insufficient nitrogen absorption in the α-ferrite, leading to super-saturated precipitates [17]. Slow cooling rates are equally detrimental to the bi-phase microstructure with the decomposition of α-ferrite into σ phase as seen in Fig. 2-5. Precipitation of σ-phase is reported by Pohl *et al.* to form between 600-1000 °C, for which Sieurin *et al.* note a cooling rate greater than 0.23 K/s is sufficient in restricting σ phase precipitation to no more than 1% of the microstructure [10, 18]. Additionally, Murr *et al.* reports ferrite to form by two means as noted by; δ-ferrite from the melting point at 1537 °C to approximately 1390 °C and as α-ferrite below 910 °C [19]. The less documented higher temperature δ-ferrite differs from α-ferrite by an enlarged lattice constant of ~9.93-2.87 Å and is less common than α-ferrite in duplex stainless steels.

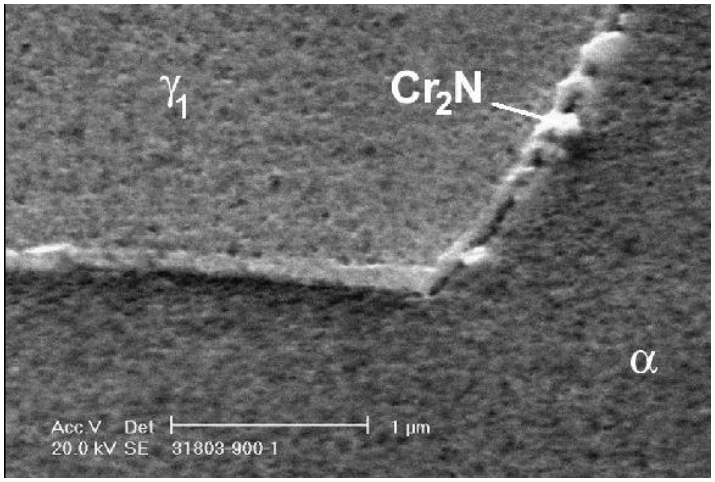

Fig. 2-4 Cr_2N precipitation along γ-austenite/α-ferrite grain boundaries (from Ramirez [20])

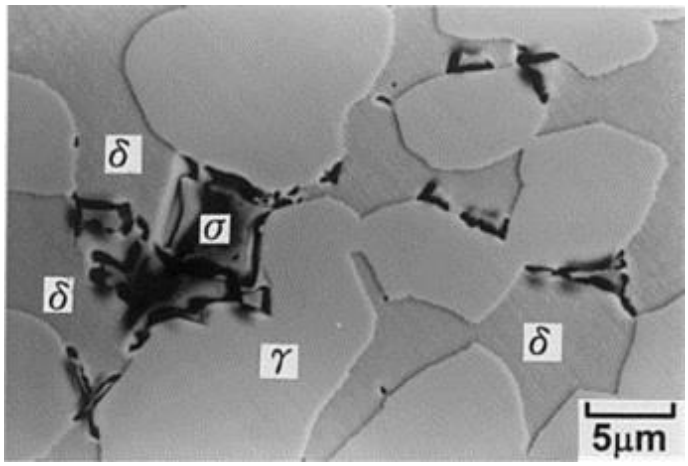

Fig. 2-5 σ-phase precipitation in SAF 2205 duplex stainless steel (from Chen and Yang [21])

2.1.3 Properties

Processing under the ideal cooling rates results in the equal ratio of α-ferrite to γ-austenite, allowing duplex stainless steels to possess excellent mechanical and corrosion properties, as reported by Davison *et al.* to exceed those of α-ferrite and γ-austenite stainless steel grades separately [22].

Mechanical Properties

The combination of α-ferrite and γ-austenite in duplex stainless steel results in a microstructure promoting both strength and ductility. As noted by Nilsson, α-ferrite is stronger than austenite for identical interstitial content but with a trade-off in ductility [23]. Smaller grain size is the main contributor to the high tensile strength in duplex stainless steels. However, Floreen and Hayden found that α-ferrite controlled tensile strength in a 60% α-ferrite : 40% γ-austenite duplex stainless steel, irrespective of the grain-size influence [24]. Similarly, Gadelrab *et al.* found α-ferrite to be the harder phase from nano-indentation tests on a SAF 2205 duplex stainless steel, though the yield strength was similar for both phases [25]. Conversely, γ-austenite was reported by Moverare and Odén as the harder phase with greater yield strength in duplex stainless steels containing nitrogen contents above 0.12wt% [26]. This was attributed to nitrogen stabilising the γ-austenite phase and promoting planar glide of the microstructure, which is further assisted by chromium and molybdenum contributing to the solid solution strengthening [23, 26].

The increased strength of duplex stainless steels over their constituent phase counterparts, lends them to be more resistant to fatigue. High fatigue crack resistance and the crack propagation that is predominantly ductile are features of duplex stainless steel, as reviewed by Charles [7]. Stolarz and Foct noted the crack propagation to initiate in the α-ferrite and γ-austenite grains with grain boundaries observed as barriers to crack propagation [27]. Conversely, Balbi *et al.* observed micro crack propagation in γ-austenite/α-ferrite and α-ferrite/α-ferrite grain boundaries in low cycle fatigue testing of a SAF 2205 duplex stainless steel. They also noted persistent slip bands control the growth and nucleation of micro-cracks and were observed to form at the aforementioned grain boundaries [28]. Furthermore, crack propagation predominance was given to the more brittle α-ferrite phase in high cycle fatigue tests as noted by Mateo *et al.* [29]. In low cycle fatigue testing nitrogen addition assists the fatigue strength by increasing γ-austenite content, which is seen by Vogt *et al.* to prevent cracks propagating from α-ferrite to γ-austenite in a 70:30 γ-austenite:α-ferrite duplex stainless steel [30].

Toughness properties of duplex stainless steels are influenced predominantly by the presence of γ-austenite. Cleavage fracture of α-ferrite was observed by Floreen and Hayden to be stunted by the addition of γ-austenite [24]. Fracture toughness mechanism was observed by Devillers –Guerville *et al.* to follow three stages; cleavage fracture in the α-ferrite phase due to embrittlement of this phase, growth of formed cavities resulting from plastic deformation of γ-austenite, and coalesce of cavities forming a defect [31]. Toughness of the duplex stainless steel is very sensitive to the precipitate formation as exemplified by Topolska and Labanowski, as 200 J of energy was lost in impact testing from a duplex stainless steel containing less than 4% of σ-sigma phase [32].

Corrosion Resistance

The best feature of duplex stainless steel is its resistance to various forms of corrosion including; pitting, crevice, and inter granular corrosion, and stress corrosion cracking. This is attributed to the dual phase microstructure, grain size and constituent element composition. The constituents of high importance for corrosion resistance are; chromium, molybdenum, nitrogen and nickel [33]. Guo *et al.* observed chromium and molybdenum to stabilise the ferrite phase, whilst nitrogen and nickel were seen to stabilise the austenite phase [34]. As is evident in the duplex stainless steel classification section above, nitrogen is strongly influential as a corrosion inhibiter by improving pitting and crevice corrosion resistance [35]. Nitrogen's most influential impact is on pitting corrosion and the PREN number (defined in Section 2.1.1). As explained by Merello *et al*, the PREN number in duplex stainless steels depends solely on the PREN of the weaker phase, which in low nitrogen content grades (<0.18% N) is austenite, as chromium and molybdenum enrich α-ferrite. However, in high nitrogen grades, the element forms in austenite due to ferrite solubility limitations, leading to an equal or greater PREN of austenite [36].

More commonly, corrosion is observed along grain boundaries as noted by Nilsson, due to the precipitation of deleterious phases including σ-sigma, χ-chi, Cr_2N and $M_{23}C_6$ [23]. Magnabosco observed σ-sigma phase growth in an isothermally aged SAF 2205 duplex stainless steel, consuming α-ferrite along the grain boundaries due to the diffusion of chromium into the boundaries [37]. In a critical pitting corrosion temperature (CPT) test on a SAF 2507 duplex stainless steel, Nilsson and Wilson observed a 20°C reduction in

CPT for 1.9% volume of the sigma phase [38]. Similarly, Cr_2N precipitates within α-ferrite and along α/γ grain boundaries were observed by Liou *et al.* to act as nucleation sites for pitting corrosion in a SAF 2205 duplex stainless steel [39]. Furthermore, secondary austenite (γ_2) precipitates were reported by Pardal *et al.* as potential nucleation sites for pitting corrosion due to their reduced nitrogen, chromium and molybdenum contents [40]. As stress corrosion cracking resistance relates directly to both the pitting resistance and mechanical strength, the formation of precipitates is equally detrimental. The ratio of α-ferrite in the microstructure was recounted by Baldo to have the greatest influence on stress corrosion cracking resistance due to its increased strength and higher chromium and molybdenum contents [41].

2.2 Applications

As with the majority of stainless steels, applications pertaining to duplex stainless steel reflect the advantageous corrosion and strength properties of the material. The reduced nickel content and its associated cost in duplex stainless steels, promoted their use above the popular austenitic grade 316L [5]. While commonly used in large scale applications, duplex stainless steels have been applied to various small scale components as well.

2.2.1 Pulp and paper

The highly corrosive environment in various papermaking equipment contributed to the pulp and paper industry being one of the first applications for duplex stainless steel [42]. The highly alkaline conditions and high temperatures between 150-180 °C in pulp digesters were reported by Liljas and Sjöholm to result in a greater potential for stress corrosion cracking [42]. Duplex and super duplex grades (SAF 2205 and F255) were highlighted in the case study by Bendall on the long term service life of duplex stainless steels in a Kraft mill such as the one shown in Fig. 2-6 [43]. Duplex stainless steel was used in various locations along the paper line including the hot stack where a SAF 2205 duplex stainless steel replaced carbon steel lasting twice as long as 8-9 years in a heated chloride environment. Super duplex stainless steel F255 was used as a replacement to

316L austenitic stainless steel in a recovery furnace fan containing SO_2 and SO_3 chloride gases, extending the life of the fan by more than 4 years [43].



Fig. 2-6 Kraft pulp mill made from SAF 2205 (from Tigerstrand [44])

2.2.2 Oil and Gas

The most popular application for duplex stainless steel is in the oil and gas industry, which in turn has driven the development of specific grades of duplex stainless steel. In addition to the salt water corrosion attributed to offshore mining, CO_2 and H_2S levels in extracted oil and gas were high as explained by Liljas and Sjöholm [42]. Duplex stainless steels were used in; flow-lines, umbilicals, separators, process piping systems and pumps [1]. Low pressure in flow-lines connecting subsea equipment to surface units can result in water condensation leading to chloride and H_2S formation increasing corrosion potential, hence the use of duplex stainless steel [42]. Umbilicals such as the ones shown in Fig. 2-7 are used to transport service lines including hydraulic fluid, power, lubrication fluid

and process chemicals from the wellhead to the platform and require the strength and corrosion resistance of duplex stainless steels [42]. With the ever increasing demand for deeper mining, the need for stronger and more corrosion resistant duplex stainless steels also increased [1]. Sandvik AB developed the hyper duplex grade, SAF 3207 HD for umbilical applications and Chai *et al.* reported yield strengths 20% higher than SAF 2507 and the ability to work in saltwater conditions up to 90 °C. The increased strength and ductility of SAF 3297 HD led to a reduced umbilical weight and the consequent extension of the length to more than 2500m for ultra-deep well applications [45].



Fig. 2-7 Duplex stainless steel tubed umbilical (from Sandvik [46])

2.2.3 Construction

More recently, duplex stainless steels are being used in the construction industry as a strong and long lasting lustrous alternative to both carbon and austenitic stainless steels. Duplex stainless steels are particularly suited in the manufacture of bridges, in part to their high strength, corrosion resistance and low maintenance [1, 42]. As noted by Zahurul Islam and Young, duplex stainless steel was implemented in the manufacture of foot and vehicle bridges in Spain, Sweden, Singapore, Norway, Slovenia, Italy, USA and the 1596m long Stonecutters bridge in Hong Kong as shown in Fig. 2-8-(a) [47]. The low cost lean duplex stainless steel grade LDX 2101 is commonly used in the manufacture of foot bridges and small road bridges, whilst the additional corrosion resistance and

strength of SAF 2205 is required in the manufacture of large bridges in harsh environments [47].

UNS S32003 duplex stainless steel has also been used for building applications such as the roof of the Doha International Airport in Qatar, shown in Fig. 2-8-(b) [1]. Further, duplex stainless steels are used as concrete reinforcement bars in beams prone to chloride attack, common in bridge columns [42]. A mechanical performance comparison between two duplex stainless steel reinforcement bars (SAF 2304, SAF 2001), the austenitic stainless steel (304) and the conventional carbon steel (B500SD) as reinforcement bars was conducted by Medina *et al.* [48]. Hot rolled duplex stainless steels showed increased ductility over the conventional reinforcement bar carbon steel, leading to the advantageous applications in seismic structural components [48].



Fig. 2-8 Construction applications (a) Stonecutters Bridge, (b) Doha International Airport (Adapted from Outokumpu [49])

2.2.4 Desalination

Desalination is the transformation of salt water to fresh potable water, which occurs by evaporating the salt water in flash chambers or vent chambers. This leads to a highly corrosive environment which is best handled by duplex stainless steels. Halling reported that, multi stage flash desalination plants commonly use SAF 2205 and LDX 2101 duplex stainless steels grades together, as a Dual-Duplex system in flash chambers as exemplified in Fig. 2-9 [50]. The lean duplex grade LDX 2101 is further used in storage tanks due in part to low maintenance associated to its corrosion resistance [50]. Oxygen leakage into the plant during shut down cycles promotes corrosion, which led to thinner gauges of duplex stainless steels replacing mild steels. Similarly, duplex stainless steels are used in vent systems in multi effect distillation and multi-stage flash systems for boiling water, thus requiring the pitting and stress corrosion cracking resistance of SAF 2205 and SAF 2507 duplex stainless steel grades [42]. Pitting and crevice corrosion resistivity and high strength, are the properties required by pipelines in reverse osmosis desalination plants. High pipe pressures up to 80 bar require the use of the high strength super duplex grade SAF 2507 and Olsson and Snis highlighted its implementation as a cheaper alternative to austenitic grade 254 SMO [42, 51].



Fig. 2-9 Multi stage flash evaporator made from SAF 2205 and LDX 2101 duplex stainless steel (from McManus [52])

2.2.5 Food and Beverage

Cost, strength to weight ratio, and corrosion resistance qualities of lean grades of duplex stainless steels have promoted their use in the food and beverage industries. Food and beverage environments with high levels of corrosivity including; wine making, vinegar making, cheese, honey and sauce making are some situations requiring the use of duplex stainless steels [53, 54]. The lean duplex grade LDX 2101 as used for the tanks in Fig. 2-10 is the most common material for the manufacture of situation tankers, storage and fermentation tanks and heat exchangers [53]. Continual advancements in food safety has been met with the implementation of regulations around alloying elements leeching into food products. A recent study by Mazinanian *et al.* on the element leeching in 2.4 pH citric acid and 7.5 pH tap water concluded that LDX 2101 duplex stainless steels emitted the lowest amount of Fe ions compared to austenitic grades and satisfied the guidelines of the European Council [55].



Fig. 2-10 Winery tanks made from LDX 2101 (from Chater [53])

2.2.6 Medical and Orthodontic

Duplex stainless steels have been tested as a future material alternative for *in vivo* medical applications and orthodontic brackets. The superior corrosion resistance of duplex stainless steel 25Cr-7Ni-4Mo-0.3N proved the application potential of the alloy in both *in vitro* and *in vivo* tests by Cigada *et al.* [56]. No localised corrosion was observed on the duplex stainless steel pins subjected to *in vivo* tests in rabbits, contrasting the pitting and crevice corrosion observed in AISI 304 and AISI 316L austenitic stainless steel samples under identical conditions [56]. However, the magnetic properties of duplex stainless steels were observed by Gregorutti *et al.* to complicate their adoption in medical applications. Cast duplex stainless steels were observed to have soft magnetic characteristics and magnetically saturate at 1T, which may be disadvantageous, as magnetic resonance imaging (MRI) machines conventionally operate with a field strength of 1.5T, leading to heating of the implants [57].

Orthodontic applications for duplex stainless steels have seen greater potential, due to the increased corrosion resistance and strength over austenitic stainless steels, enabling for lighter components for an equivalent strength. Platt *et al.* also summarised that hypersensitivity reactions to nickel were potentially reduced due to the lower content of the alloy in duplex stainless steels. Potentio-dynamic polarization tests conducted by the authors, concluded that the SAF 2205 duplex stainless steel performed better in simulated oral fluid corrosion, compared to the austenitic 316L grade [58]. Cold drawn duplex stainless steel wire produced by Filho *et al.* as shown in the Bionator in Fig. 2-11 was observed to conform to orthodontic implant standards BS 3507:1976 and ISO 5832-1, showing ductility and malleability for orthodontic prostheses [59].

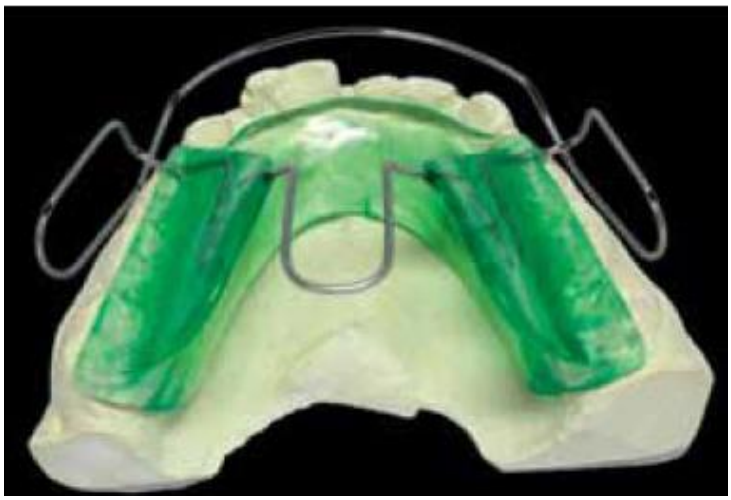

Fig. 2-11 Bionator made from SEW 410 Nr. 14517 duplex stainless steel wire (from Filho et al. [59])

2.3 Traditional Processing methods and issues

The wide range of applications utilising duplex stainless steels requires the metal to be manufactured and fabricated into forms specific for each application. The thermally sensitive microstructure and high mechanical strength lead to difficulties in processing duplex stainless steels by conventional manufacturing means. A summary of issues related to the processing of duplex stainless steel is presented in Table 2-1 below, with the complexities discussed hereafter.

Table 2-1 Processing issues with duplex stainless steels

Processing Method	Associated Problems
Casting	• Grain size variance • Precipitation of deleterious σ-sigma phase • Need for solution annealing • Shrinkage porosity
Hot / Cold forming	Hot Forming • Edge/Alligator cracking • Precipitation of σ-sigma phase and Cr_2N • Need for solution annealing heat treatment Cold Forming • Limitation to reduction % • α'-martensite transformation
Machining	• Work hardening • Built up edge (BUE) • High tool wear rate • Coolant requirement in drilling • Surface hardening
Powder Metallurgy	• Precipitate formation • Solution annealing requirement • High porosity

2.3.1 Casting

While commonly researched and developed duplex stainless steel grades are in the wrought state, cast grades are also popular in the manufacture of pump and valve systems [60]. Cast duplex stainless steel grades are compositionally comparable to the wrought grades however, differences lie in their liquid corrosion service 'C' grade designation e.g. CD3MN, CE3MN [1, 61]. Microstructurally, cast duplex stainless steels are seen by Pineau and Besson to be characterised by big α-ferrite grains ~10mm in size oriented in the direction of cooling or randomly in cases where no specific cooling direction exists. As cooling progresses ɣ-austenite grains of ~1 mm size form inside the α-ferrite,

eventually leading to the austeo-ferritic network, in each of the three characteristic forms; along grain boundaries, intragranularly and as Widmanstätten laths [62]. Fine equiaxed grains were observed at the extremities of the casting with Widmanstätten austenite growth, whilst in the centre columnar grains were observed in the centre of the casting, leading to a hardness decrease of ~20.3 HV and ~4 HV for the γ-austenite and α-ferrite phases respectively [63].

Ferrite content was observed to decrease with increasing nitrogen content and thickness castings by Glownia *et al.*, with the greatest α-ferrite variation observed in the W8 casting with 0.2% nitrogen, corresponding to a 24.1% decrease in ferrite between the 20 and 110 mm sections [64]. More significantly, Martins *et al.* observed the σ-phase formation (Fig. 2-12) in the cast microstructure of a CD3MCuN sand cast super duplex stainless steel [65]. They further noted that this formation was common for duplex castings, with a thickness greater than 125mm due to σ-phase precipitation between 700-1020 °C [65-67]. Thus, for cast duplex stainless steels a solution annealing heat treatment process consisting of heating between 1135-1162 °C and rapidly quenched in water as detailed by Johnson *et al.*, is required to return the microstructure to an equilibrium state and restore its mechanical and corrosion resistance properties [67]. During the casting of thick sections, the metal is particularly prone to shrinkage cavities, seen in Fig. 2-13, resulting from insufficient flow of liquid metal into the mould. Haušild *et al.* estimated an average of 15% of shrinkage pores in a 110 mm think CF8M duplex stainless steel casting, leading to the initiation of tearing in the weaker γ-austenite phase and propagation to adjacent pores [68].

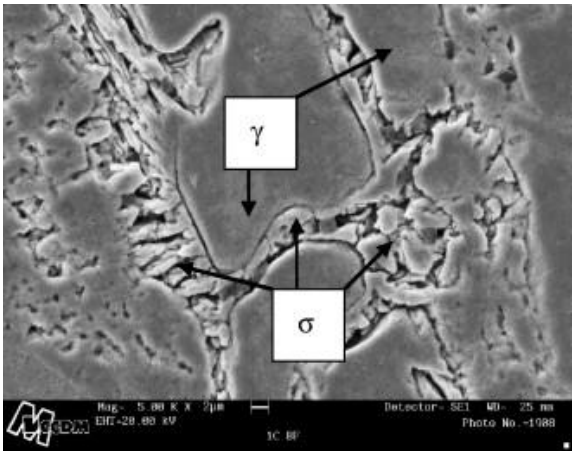

Fig. 2-12 σ-phase precipitation in cast duplex stainless steel (from Martins and Forti [65])

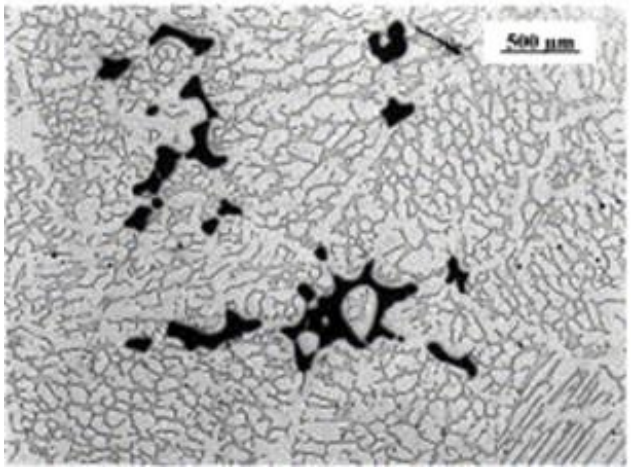

Fig. 2-13 Shrinkage cavities in cast duplex stainless steel (from Haušild et al. [68])

2.3.2 Hot / Cold forming

As with casting, hot and cold forming operations disturb the duplex stainless steel microstructures. Forming operations impart strong grain anisotropy in addition to modifying the grain morphology, phase volume fraction, and grain orientations. As summarised by Gutierrez and Iza-Mendia, hot forming leads to α-ferrite formed as equiaxed grains at steady state and polygonised under high deformations, whilst γ-austenite will be present as smaller sub-grains due to the weaker degree of recovery [69]. Mao *et al.* reported that after hot deformation of a 0Cr17Mn14Mo2N duplex stainless steel casting the spheroid morphology of α-ferrite phase coarsened when heated at 1050

°C and elongated at temperatures above 1150 °C with fine equiaxed γ-austenite grain formation from recrystallisation [70].

Further, the α-ferrite:γ-austenite ratio within duplex stainless steel has a large influence on the metal due to the differing recovery rates during hot deformation. In the hot rolling process of two duplex stainless steels (0.22% nitrogen and 0.18% nitrogen), Subramanian and Chandramohan observed an increase in α-ferrite content from 47% to 76% in the 0.22% nitrogen alloy and from 46% to 54% in the 0.18% nitrogen alloy. The formation of σ-phase was observed in the 0.22% nitrogen duplex stainless steel in addition to alligator cracking seen in Fig. 2-14 when reduced in thickness by more than 15%, thus suggesting the requirement for a solution annealing heat treatment after processing [71]. The influences of the composition of LDX 2101 and SAF 2205 duplex stainless steel grades on hot rolling responses was evaluated by Feng *et al.* [72]. Increased manganese and nitrogen content and reduced nickel content in lean duplex LDX 2101 were found to reduce the stacking fault energy of γ-austenite and coarsen the grain formation. The difference in hardness of both the α-ferrite and γ-austenite phases was influenced by the manganese and nitrogen content which limits the strain transformation to occur between α-ferrite and γ-austenite grain boundaries. This leads to restricted recrystallisation softening and crack propagation. Additionally the authors observed Cr_2N precipitation in the α-ferrite grains after hot rolling LDX 2101, which remained in the microstructure in lesser quantities and at a smaller size after solution annealing [72]. Similarly, Reis *et al.* observed crack propagation to result from the γ-austenite and its increased strength and reduced ductility restricting plastic deformation and imparting work hardening behaviour, leading to cavity formation and crack propagation along the α-ferrite/α-ferrite grain boundaries as seen in Fig. 2-15 [73].

Comparable microstructural features were observed to influence the cold forming ability of duplex stainless steels. An increase in strain hardening and greater affinity for recrystallisation of the γ-austenite phase over the α-ferrite phase was observed in the cold rolling of SAF 2205 duplex stainless steel by Reick *et al.* [74]. In addition to strong grain alignment along the rolling direction of a cold rolled SAF 2205 duplex stainless steel, Pramanik *et al.* observed the formation of α'-martensite which increased in quantity with rolling deformation. The increase in rolling deformation also led to an increase in the hardness and grain refinement of the microstructure, although at the expense of γ-austenite, transforming into α'-martensite [75]. The formation of α'-martensite

potentially results in embrittlement of the alloy, which was observed in Fig. 2-16 by Hättestrand *et al.* in the cold worked and aged SAF 2507 duplex stainless steel [76]. Further, Baldo and Mészáros established a near complete α-ferrite and α'-martensite alloy formation from a lean duplex stainless steel, at a thickness reduction of 80% [77]. A solution annealing process is required after cold forming to restore the microstructure to equilibrium.



Fig. 2-14 Alligator cracking in hot rolled duplex stainless steel (from Subramanian and Chandramohan [71])

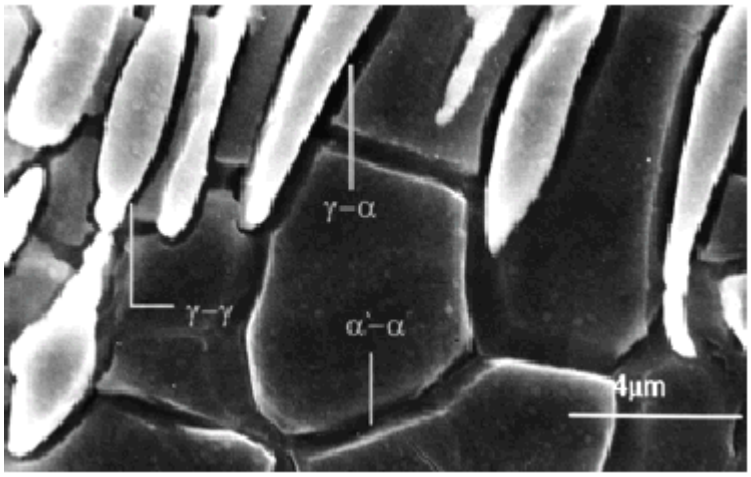

Fig. 2-15 Hot deformed duplex stainless steel showing cracking at α-ferrite/α-ferrite grain boundaries (from Reis et al. [73])

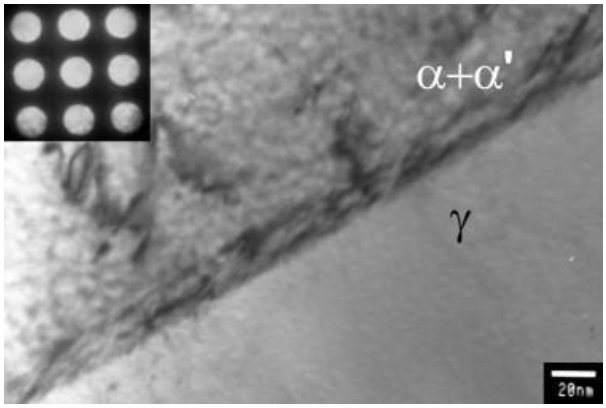

Fig. 2-16 α'-martensite precipitation in cold rolled SAF 2507 duplex stainless steel (from Hättestrand et al. [76])

2.3.3 Machining

The bi-phase microstructure of duplex stainless steels adversely influences the machinability characteristics. The work hardening rate, high toughness, high fracture toughness and low thermal conductivity are commonly attributed to the poor machinability of duplex stainless steels [78]. The work hardening nature of the γ-austenite phase was noted by Dolinšek to occur from the tendency of the phase to deform due to larger numbers of sliding planes, resulting in an increase in the hardness and the strength of the phase. The author further noted the mechanism of chip formation in AISI 321 austenitic stainless steel to be based on a plastic deformation process rather than the common mode of shear during drilling [79].

The machinability of duplex stainless steels is additionally worsened by the formation of the built-up edge (BUE) on the tool rake face. The agglomeration of α-ferrite bands in the stagnation zone of chips led by the greater plasticity of γ-austenite was observed by Nomani *et al.* to be the potential cause of BUE formation in duplex stainless steels, as depicted in Fig. 2-17 [80]. BUE formation and the chip-tool interface conditions were observed by Krolczyk and Legutko while machining with coated carbide inserts to significantly deteriorate the surface roughness. This was further accentuated by increasing the cutting speed and the lack of coolant [81].

Drill tests on duplex stainless steel specimens with a coolant allowed Nomani *et al.* to observe that the BUE causes adhesion wear on the flank face of the drill as shown in Fig. 2-18 [79]. The International Molybdenum Association recommends the use of coolants in duplex stainless steel machining to alleviate machinability issues and was also validated by Koyee *et al.*, while turning SAF 2507 and SAF 2205 duplex stainless steels. Wet cutting showed a reduction in specific effective cutting power of 18.81% and 10.82% respectively with SAF 2507 and SAF 2205 [1, 82]. In contradiction, Krolczyk *et al.* observed a 65% tool life reduction when turning SAF 2205 duplex stainless steels with a mineral oil coolant [1, 83].

Compositional variation between duplex stainless steel grades was also seen to significantly influence the machinability. The low-alloyed lean duplex stainless steels e.g. 2304 were noted by Hariharan to impart improved machinability compared to the austenitic grades 316 and 317 [84]. Renaudot *et al.* went further, developing a grade of lean duplex stainless steel with increased copper and nickel content over the popular LDX2101 grade, resulting in reduced tool wear rates in turning, due to the reduction in the strain hardening of the chips [85]. The addition of sulphur to super duplex stainless steel containing rare earth elements was observed by Jeon *et al.* to result in a substantial increase in tool life. Manganese sulphide precipitates adhered to the tool surface, forming a thin film which acted as a lubricant during the machining process [86]. Microstructural variations resulting from different duplex stainless steel production methods also have considerable effects on tool wear. The machinability differences of duplex stainless steels produced by casting and by powder metallurgy with subsequent hot isostatic pressing (HIP) treatment were presented by Paro *et al.* [78]. Despite the greater tendency for built up edge formation in the cast A890 1A duplex stainless steel, the powder metallurgical Duplok 27 exhibited an 8min reduction in tool life at 60m/min cutting speed due to the hard oxide particles present in the microstructure [78].

In addition to tool wear and machinability issues, surface integrity and other changes were also observed on the machined surfaces. Krolczyk *et al.* and Bordinassi *et al.* have both studied the hardness variation of the machined duplex stainless steel surfaces. Although no microstructural variations were detected, Bordinassi *et al.* observed a decrease in the hardness of the α-ferrite and a minor decrease of the ɣ-austenite phase from the machined

surface as shown in Fig. 2-19 [87]. These findings were validated by Krolczyk *et al.* who further investigated hardness responses of SAF 2205 with varying cutting speeds in both dry and wet conditions. They found that increasing cutting speed results in a decrease in the maximum hardness of both phases, but contributes to an increased depth of hardness. A reduction in the depth of hardness was observed by machining in the wet condition [88]. More significantly, surface micro-cracking was observed by Jiang *et al.*, while grinding HIP SAF 2205 and SAF 2507 duplex stainless steels, contributed to a decrease in surface roughness and cutting forces compared to HIP austenitic 316L. Work hardening was attributed to the micro-crack formation with the differences in deformability of the α-ferrite and γ-austenite phases proposed as the plausible mechanisms [89].

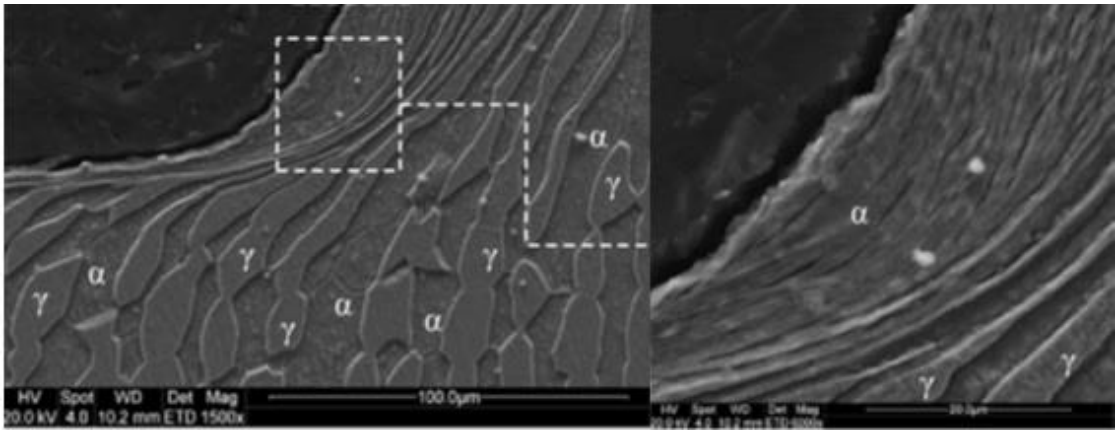

Fig. 2-17 Stagnation zone and α-ferrite agglomeration in SAF 2507 machining (Adapted from Nomani et al. [80])

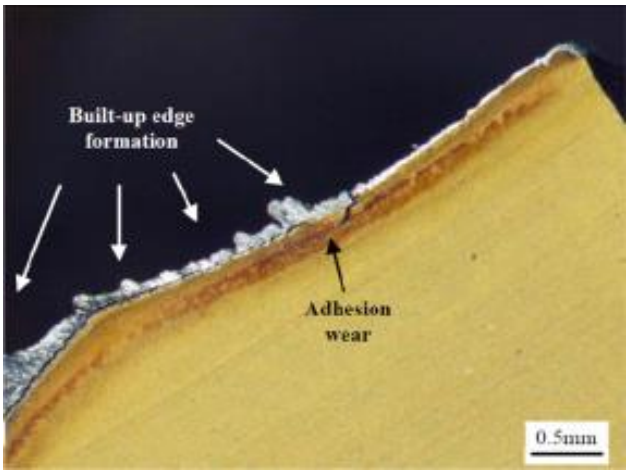

Fig. 2-18 BUE and Adhesion wear in a drill after machining SAF 2507 (from Nomani et al. [90])

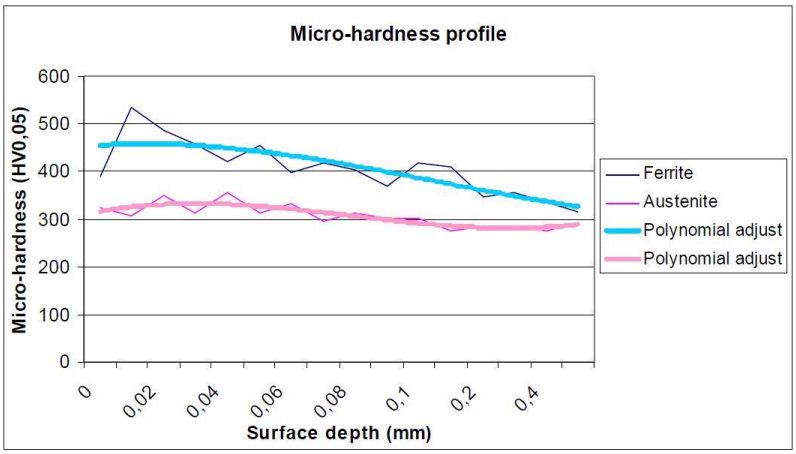

Fig. 2-19 Micro-hardness variation from machined surface (from Bordinassi et al. [87])

2.3.4 Powder metallurgy

Powder metallurgy has gained momentum in recent years due to its ability to manufacture components from a range of alloys with near-net shape characteristics, reducing both material consumption and tooling costs. These features are particularly advantageous in the manufacture of duplex stainless steel components when compared to the aforementioned processing routes. Duplex stainless steel powder is commonly produced either by elemental composition [91], mixing austenitic and ferritic grades [92] or from pre-alloyed powder mechanically mixed in a ball mill [93]. The mixing aspect of powder metallurgy facilitates tailored development of duplex stainless steel grades with varying ratios of austenite and ferrite as demonstrated by Martín *et al.* [94]. Austenitic 316L was mixed in 25, 50 and 75% by volume with ferritic 430L and compacted at varying pressures, sintered at 1250°C in nitrogen and subjected to furnace, water, or gas cooling conditions. The cooling condition contributes most significantly to the mechanical properties. Slow cooling resulted in a high volume of lamellar constituents and precipitates, which worsened with decreasing ferrite volume as seen in Fig. 2-20. However, furnace cooled samples exhibited greater tensile strength and elongation than water cooled samples [94].

The formation of Cr_2N precipitates was observed by Mariappan *et al.* while sintering mixed austenitic-ferritic duplex stainless steel powders in a nitrogen environment. The nitrogen gas environment led to the lamellar formation of the constituents and Cr_2N

precipitation along the grain boundaries of ferrite. Interestingly, the tensile strength and elongation were found to increase with the Cr_2N precipitation [95]. Wear resistance is also greatly influenced by the lamellar constituent formation as observed by Mariappan *et al.* in the sintering of mixed duplex stainless steel in both argon and nitrogen environments. The nitrogen environment resulted in better wear resistance than argon, due to the hard Cr_2N precipitates as well as greater volumes of lamellar constituents, despite greater pore volumes observed [96]. The lamellar constituents formed in the sintering of a mixed duplex stainless steel in a nitrogen environment was studied by García *et al.* via metallurgical analysis techniques. Through quantification of the sintered precursor powders, the lamellar constituents in the duplex stainless steel were determined to consist of M_6C and M_7C carbides, intermetallics of CrNiFe and FeCrMo, Cr_2N nitrides and α'-martensite [97]. Electrochemical corrosion tests conducted by Garcia *et al.* concluded that sintered duplex stainless steel samples responded poorly due to the lamellar constituents and the precipitates. However, post-sintering annealing heat treatment was found to alleviate the problems [98].

Pore formation was commonly attributed to powder metallurgical sintering of duplex stainless steels due to powder packing characteristics and sintering conditions. Porosity was observed by Martin *et al.* to be affected primarily by powder compaction pressure and time in the green state. Duplex stainless steel components made from austenitic and ferritic powder in a range of mixes were compacted at 650 and 750 MPa between 60-600s before sintering at 1250 °C in nitrogen. As observed in Fig. 2-21 a compaction pressure of 750 MPa and time of 300 s were found by the authors to result in the lowest porosity of 8.97% with an equal austenitie:ferrite powder ratio, with no observed variance when cooled at differing rates [94]. Mariappan *et al.* noted that porosity levels in argon gas sintered duplex stainless steel were less than those sintered under nitrogen environment, due to Cr_2N precipitation consuming the nitrogen gas and reducing the diffusion rate [95].

Vacuum sintering was noted by García *et al.* to result in greater shrinking and sintered densities than in a nitrogen environment for comparable duplex powder mixes [97]. Densification could be improved by the addition of elements acting as catalysts in the sintering process. The addition of copper to mixed duplex stainless steel powder by Dobrzanski *et al.* was seen to assist the sintering characteristics by speeding up the mass

transport through the formation of a liquid phase [99]. Alternatively, boron was added to AISI 329A duplex stainless steel powder by Coccia *et al.* to slow down the α-ferrite to γ-austenite transition during sintering, but the densities could not be improved. They further researched the influence of the sintering temperature on density with the result that density increases with sintering temperature from a density of 94.5% at 1120 °C to a maximum of 98.75% at 1150 °C before reaching a plateau [100].

Increasing porosity was observed to negatively influence tensile strength of samples regardless of compositional variances. Dobrzánski *et al.* prepared five samples of varying duplex stainless steel compositions with the greatest tensile strength and elongations observed in the rapidly cooled samples with a porosity range of 7.06-7.34% [99]. Duplex stainless steel's response to oxidation at elevated temperature was determined by Bautista *et al.* to be significantly influenced by the porosity. A range of austenitic-ferritic powder mixes were tested for their oxidation resistances at 900 °C. The formation of open pores seen in Fig. 2-22 during sintering allowed air to enter and accelerate the oxidation process, further accelerated with mixes containing greater ratios of austenite due to the formation of nickel oxides which increase oxidation susceptibility [101]. Similarly, Utrilla *et al.* linked porosity to the poor corrosion response of sintered duplex stainless steel. Pore formation was seen to break up the passive layer promoting localised corrosion [102].

By far, the powder metallurgy route was considered the most suitable to process duplex stainless steel powders. Yet, metallurgical irregularities and densification issues during sintering have limited its applicability. Further, the need for use of specific dies will restrict the forms that can be generated by the powder metallurgy method. Powder bed additive manufacturing (AM) processes are an alternative approach, considering the localised and dynamic melting and point-by –point consolidation. It will be interesting to evaluate how duplex stainless steel powders respond to processing by the additive methods. A brief review of the technologies and their applications to specific steels are presented next so as to identify the research gaps.

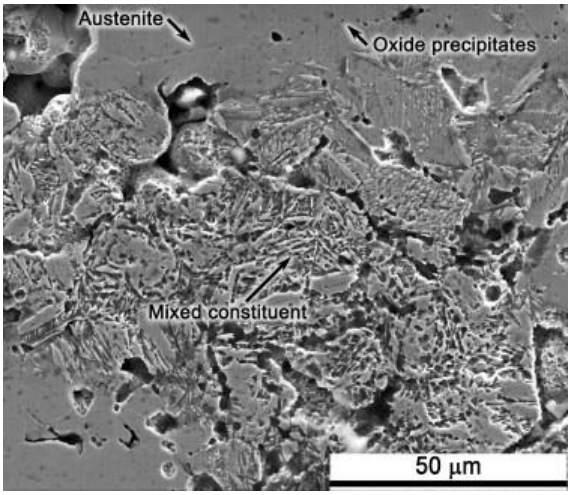

Fig. 2-20 Sintered duplex stainless steel sample showing precipitates and constituents (from Martín [94])

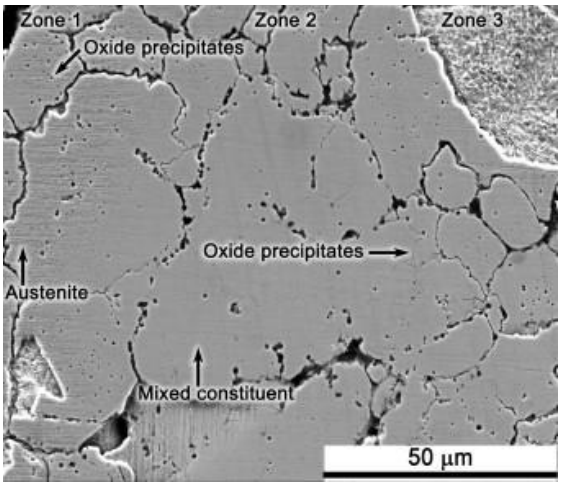

Fig. 2-21 Porosity and microstructure of 750 MPa 300s duplex stainless steel sample (from Martín [94])

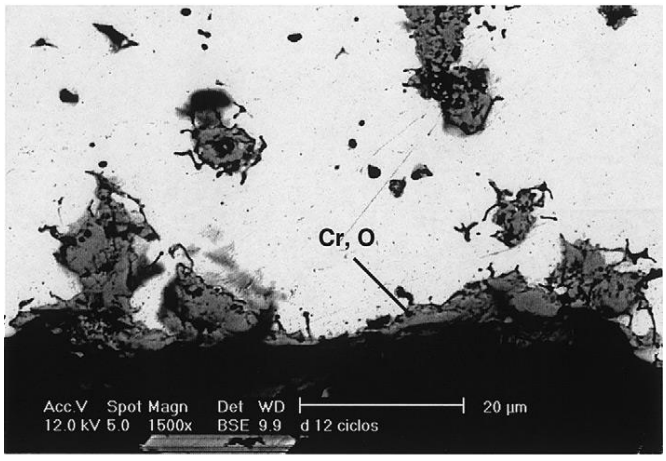

Fig. 2-22 Oxide formation on porosity in sintered duplex stainless steel (from Bautista [101])

2.4 Powder additive manufacturing in metals

As with their polymer counter parts, metal AM has seen rapid growth and development in recent years with considerable industrial interest as a replacement of the casting and machining technologies. Metal AM methods are separable by their feedstock and consolidation methods. Powder is the most common feedstock being used in the powder bed fusion systems; selective laser melting (SLM) and electron beam melting (EBM) as well as the laser engineered net shaping (LENS). Less common alternatives are wire, used as a feedstock in direct energy deposition (W-DED) systems and as metal strips in ultrasonic additive manufacturing (UAM). A review of the more popular powder AM systems is presented next, with a focus on the possible consolidation of duplex stainless steels.

2.4.1 Laser engineered net shaping (LENS)

Initially developed by Jeantette *et al.* at Sandia National Laboratories in 1996, LENS belongs to the direct energy deposition (DED) family of AM processes which utilises a concentrated heat source (laser or electron beam) to melt metal powder or wire in a focused location on a substrate building it up into a 3D object [103, 104]. Fundamental to LENS is the laser beam which melts the target surface forming a small melt pool and melts the deposited powder above the melt pool. Powder deposition is via a nozzle which as seen in Fig. 2-23 surrounds the laser beam directing the powder into the melt pool. The metal processing occurs in an inert environment, either by filling in the chamber directed at the melt pool zone [105]. The high energy directed consolidation mechanism of LENS enables it to near-net shape manufacturing of components as in Fig. 2-24 in various orientations via 3-5 axis machine gantries or robotic arms. This flexibility is further enhanced with the implementation on a CNC machining centre, aiding hybrid additive-subtractive manufacturing that allows laser cladding and repair [103]. Laser cladding processes can be conducted with hard wearing alloys forming functionally gradient components while, LENS nozzle systems with up to five separate powder feeds have been developed for additive manufacturing of multi grade components [106].

LENS is commonly used with high alloyed and high temp alloys including; Inconel 625 and 718, Ti-6Al-4V, H13 and numerous hard facing and cladding alloys [105, 107]. Stainless steels are also processed via LENS including austenitic (304 & 316), martensitic (410, 420) and precipitation hardened (17-4PH) grades [105]. While there is no evidence in published literature of the processing of duplex stainless steel by LENS, a recent presentation by Palmer in the processing of SAF 2205 concluded that consolidation in a 100% argon environment resulted in an equilibrium phase balance as observed in Fig. 2-25. Furthermore, austenite ratios were elevated with increasing nitrogen environment to a maximum of 61.1% austenite in a 7% nitrogen, 93% argon gas environment [108].

In general, LENS literature has been focused on the processing of 316L stainless steel although microstructures have not been completely austenitic. In the research by Ziętala *et al.*, δ-ferrite precipitation was observed on the subgrain boundaries which were rich in chromium and molybdenum [109]. Although LENS has proven the ability to freeform manufacture near net shape components from duplex stainless steel, Ruan *et al.* notes undesirable features of the system including; poor surface roughness and geometrical accuracy and the inability to create overhanging geometry and support structures [110]. The powder bed processing techniques may resolve these issues and are seen as preferable alternatives.

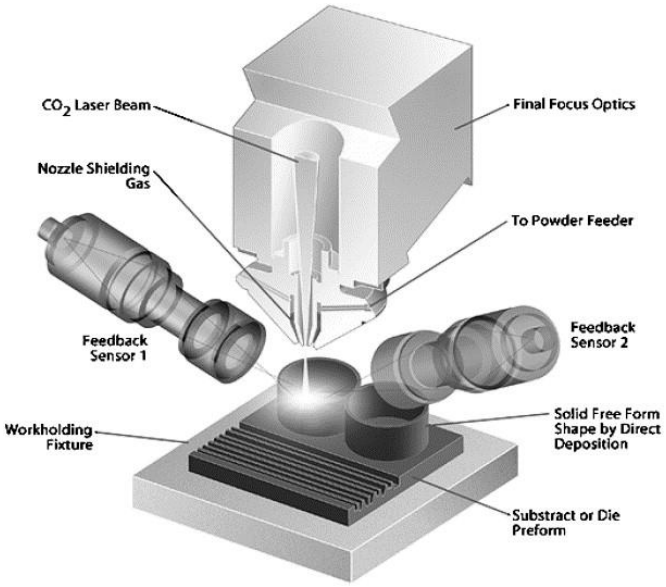

Fig. 2-23 LENS Schematic (from Shin et al. [111])

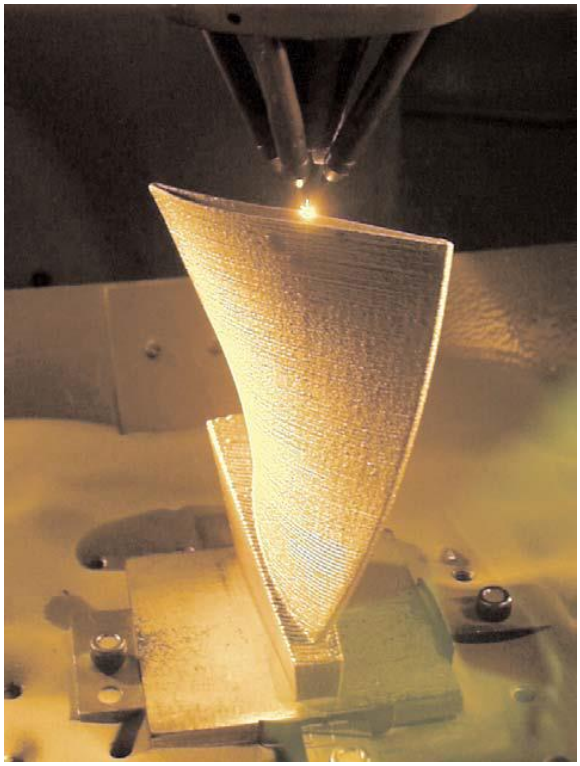

Fig. 2-24 LENS processing of a turbine blade (from Gill [107])

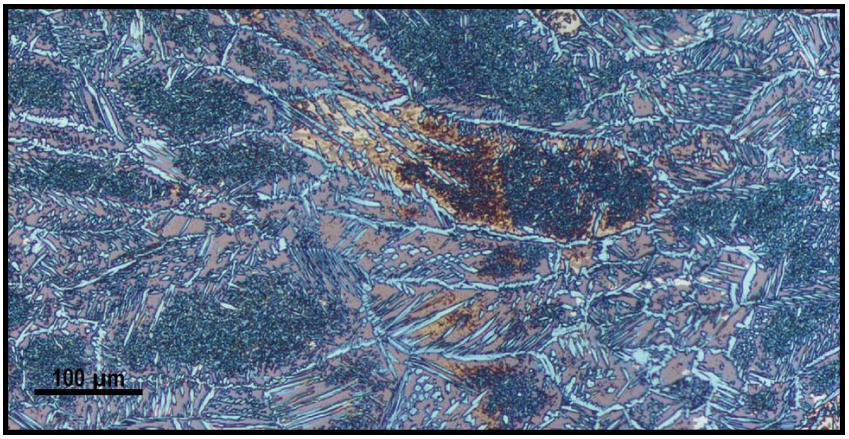

Fig. 2-25 LENS manufactured duplex stainless steel microstructure (from Palmer [108])

2.4.2 Electron beam melting (EBM)

Originally patented by Larson in 1998, EBM uses an electron beam as shown in Fig. 2-26 to melt a 50-120μm layer of spherical powder atop each other in a layer-wise fashion at rapid beam speeds [112, 113]. Consolidation is done in a vacuum and prior to forming each layer, the electron beam preheats the layer maintaining the build envelope at an elevated temperatures in excess of 700°C as in Fig. 2-27 [114]. The result of which is the reduced volume of support structure during building and a denser and more continuous microstructure with similarities to casting [115]. Arcam's (Arcam AB, SE) exclusivity of the EBM technology restricts the range of alloys processed commercially to titanium grades (Ti6Al4V and commercially pure Ti), cobalt chrome F75 and Ni-base superalloy Inconel 718 [116]. At a research level further titanium and Ni-base super alloys of Ti48Al2Cr2Nb, Inconel 625 and Rene 142 have been processed by EBM, in addition to H13 tool steel, aluminium alloys and niobium [113, 117-120].

Although there is no literature on the processing of duplex stainless steels by EBM, pure iron powder and the popular austenitic grade 316L have been successfully processed. A dual phase microstructure containing δ-ferrite platelets in a α-ferrite matrix was observed by Murr *et al.* in the EBM processing of pure iron powder [19]. Early research in austenitic 316L stainless steel by Qi *et al.* focused on the mix ratio of gas atomised and water atomised powders processed by EBM. The spherical gas atomised powder particles consolidated into a single track, while the irregular water atomised powder particles resulted in balling. A 40-60% gas atomised powder mixture was seen as the ideal mixture for EBM consolidation [121]. More recently, Zhong *et al.* processed 316L via EBM, producing samples of 99.8% density and with strong columnar grain growth. Ferrite growth was contained to 0.1%, but, prolonged cooling was suggested to result in precipitate formation along grain boundaries and dispersed within the matrix (Fig. 2-28) inducing brittle fracture during tensile testing. Additionally, crescent shaped pores were formed probably from the thick powder layers, further hampering the tensile results [114]. Certain complexities arise in EBM as noted by Larsson *et al.*; Both the vacuum and the electron beam systems are complex and require appropriate maintenance to prevent damage. More intriguing aspect is the emission of x-rays during operation which require appropriate shield to prevent the operator harm [122].

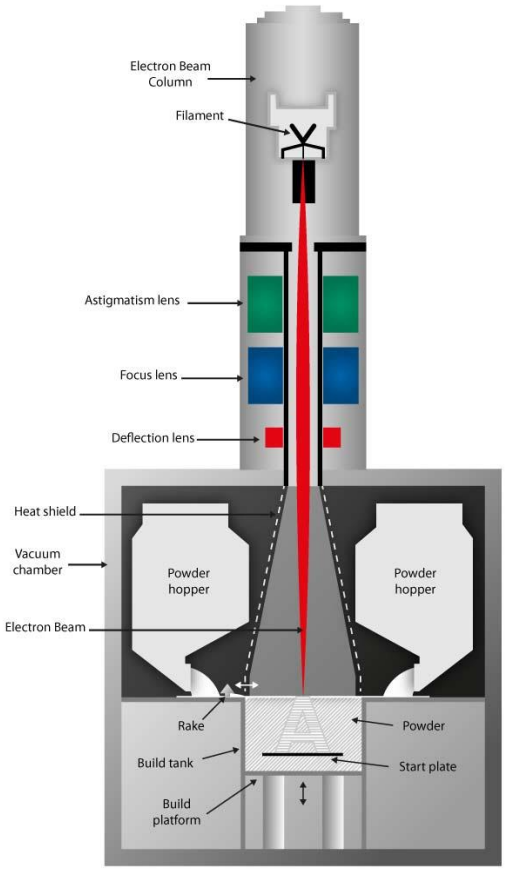

Fig. 2-26 EBM schematic (from Arcam [123])



Fig. 2-27 EBM melting process (from Hiemenz [124])

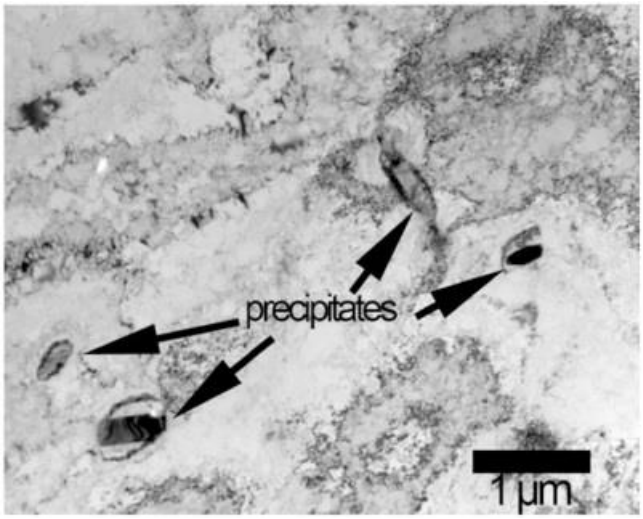

Fig. 2-28 Precipitates formed during EBM processing of 316L (from Zhong et al. [114])

2.4.3 Selective laser melting (SLM)

Conceptualised within Carl Deckard's breakthrough selective laser sintering (SLS) patent in 1988, Fraunhofer IPT developed in 1995 that a system to selectively laser melt single metal alloys e.g. 316L austenitic stainless steels [125, 126]. In the years following, SLM has become the most popular metal additive manufacturing system due to design freedom, relatively lower cost and lesser process complexities. The SLM process shown in Fig. 2-29 consists of a fibre or solid state Nd:YAG laser focused to melt metallic powder particles layer-by-layer, with layer thicknesses varying from 20 to 100µm and the powder consolidation as shown in Fig. 2-30 [127]. Powder metal is spread atop a heated substrate of an equivalent alloy grade, acting as both a heat sink and a build anchor for components. The substrate is contained within a build envelope, surrounded by recirculated nitrogen or argon gas to prevent oxidation and remove powder nano-particulates. A wide range of metals and alloys have been researched and are commercially available including; titanium, Inconel, cobalt-chrome, aluminium, magnesium, tool steels, tungsten, gold, amorphous alloys, rare earth alloys, steel and stainless steels [127-129].

At the time of commencement of this project there was no literature on processing duplex stainless steel by SLM, but considerable research was done on the austenitic, precipitation

hardened and martensitic stainless steels. A maximum density of 99.64% was recorded by Cherry *et al.* in the SLM of austenitic 316L stainless steel, comparable to Zhao *et al.*'s density of 99.95% in SLM of martensitic 420 stainless steel [130, 131]. Optimal processing of 316L stainless steel by Sun *et al.* resulted in the formation of tiny spherical porosity observed in Fig. 2-31, likely formed from gas trapped in the powder [132]. In the SLM of 316L stainless steel porosities below 0.1% were reported by Carlton *et al.* to result in comparable fracture mechanics to 0.004% porous wrought material. However, ultimate tensile strength (UTS) of the SLM samples were 125MPa greater than the wrought 316L due to anisotropic microstructural effects [133]. Strong columnar grain growth through multiple layers in SLM of 1Cr18NiTi was observed by Ma *et al.* in Fig. 2-32 to impart high UTS values exceeding 700MPa when tested perpendicular to the layer formation. Furthermore, fine equiaxed subgrains (Fig. 2-33) formed at a powder layer thickness of 60μm resulted in microhardness readings 25HV greater than ASTM wrought standard [134].

Compositionally, Rafi *et al.* observed rapid cooling conditions of SLM processing of 17-4 PH precipitation hardened stainless steel to induce a predominantly martensitic microstructure with retained austenite formation volume influenced by envelope atmosphere. Comparable ratios of martensite and austenite were observed in samples processed in a nitrogen environment due to the austenite stabilising characteristics of nitrogen whereas, an argon environment resulted in a martensite dominated microstructure [135]. An austenite dominated microstructure was observed by Sun *et al.* in the SLM of austenitic 316L stainless steel however, retained acicular δ-ferrite was observed to precipitate randomly within the matrix [132]. Saeidi *et al.* further observed the retained δ-ferrite in SLM 316L stainless steel to increase in volume creating a duplex microstructure after heat treatment at 1100 and 1400 °C for 6min and furnace cooling [136].

As is evident from the literature above, stainless steels have been successfully processed by SLM and ferrite growth within an austenite matrix was achieved by tailoring the processing conditions and heat treatment cycles. However, the response of an equilibrium phase duplex stainless steel to SLM has not attained much attention.

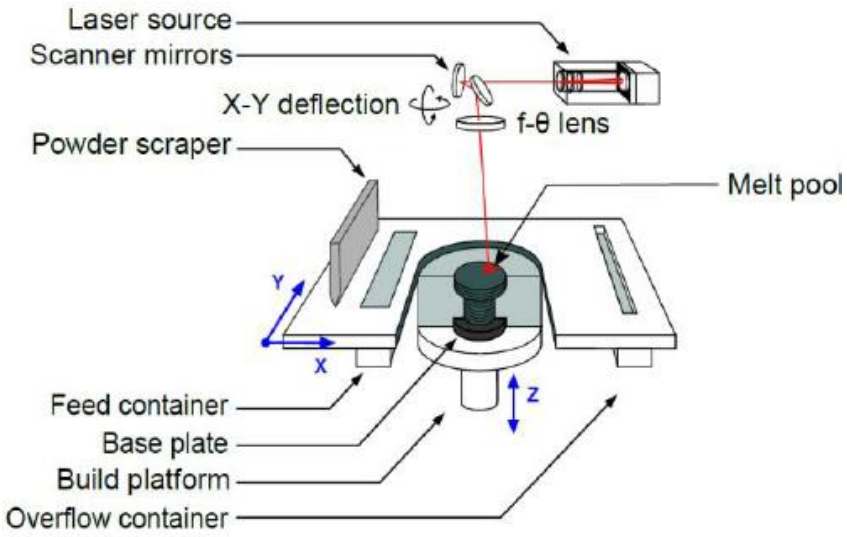

Fig. 2-29 SLM process schematic (from Kempen et al. [137])



Fig. 2-30 SLM of a dental crown (from EOS [138])

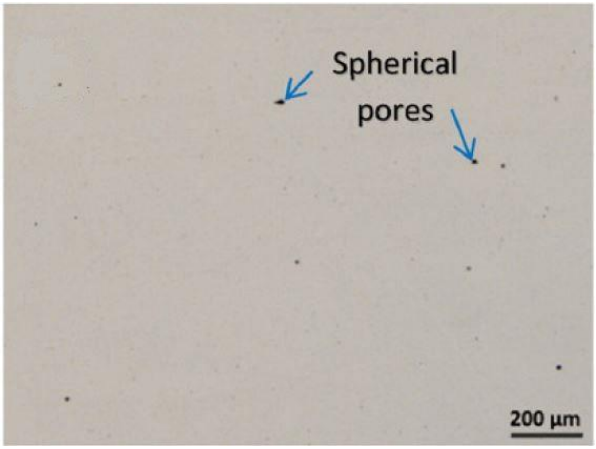

Fig. 2-31 Porosity in a high density SLM 316L sample (from Sun et al. [132])

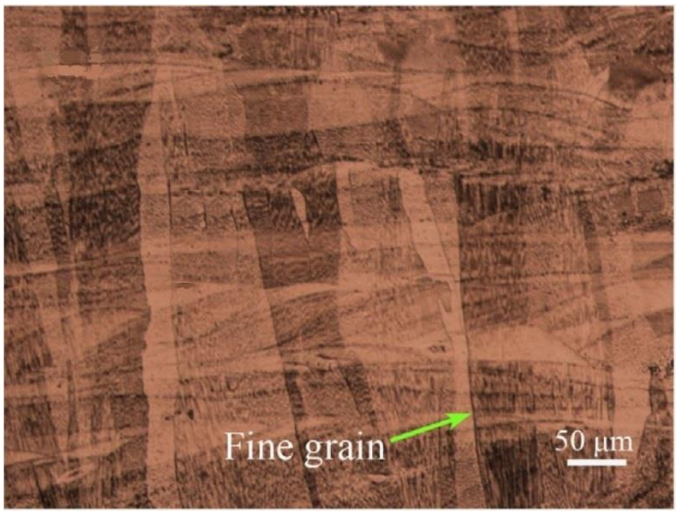

Fig. 2-32 Columnar grain growth in SLM 316L (from Ma et al. [134])

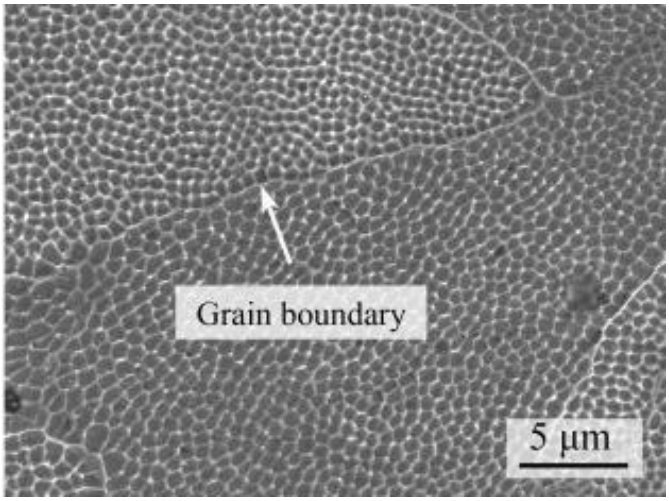

Fig. 2-33 Equiaxed subgrain microstructure in SLM 1Cr18NiTi (from Ma et al. [134])

2.5 Research gaps, hypothesis and questions

Based on the literature reviewed above, it is clearly evident that the bi-phase austeno-ferritic microstructure of duplex stainless steels allows for much better properties compared to the ferritic or the austenitic counterparts; high strength, ductility, fatigue resistance, pitting and stress corrosion cracking resistance [7, 23, 35, 36]. This has led to the widespread promotion and use of the duplex steels over the austenitic stainless steels, encompassing application areas such as pulp and paper mills [43], oil and gas [45], bridge

and building construction [1, 47], desalination plants [50], food and beverage storage [53], and also as a replacement metal for medical and orthodontic implants [59]. However, maintaining the balance within the dual phase structures is often difficult during the secondary processing stages. Challenges such as the precipitation of the deleterious phases in casting and forming [65, 76], cracking in hot forming operations [71], work hardening and built-up-edge formation leading to excessive tool wear in machining [78, 81], and both precipitation and porosity issues in powder metallurgy sintering [94, 97] have generally been reported as issues with the microstructural intricacies of these alloy grades. Considering the extremely useful properties the duplex steels and the wide-spread application potentials, there has been an ever increasing research interest, targeting better results with the conventional processing routes as well as exploring alternative ways for better control.

Additive processing technologies gained a great momentum in the recent years as the technology gradually evolved and matured and being accepted as a viable manufacturing method for metals. Layered manufacturing based on powder metals is currently drawing significant research attention through proven technologies such as the Laser Engineered Net Shaping (LENS) [103], Electron Beam Melting (EBM) [113] and Selective Laser Melting (SLM) [127]. In particular, the selective laser melting became a popular choice, considering the possibility to apply to a wide spectrum of metal systems. The literature review showed a wide spread interest and progress addressing the application of the laser melting method to process different alloy steel systems. Notable examples are the reports evaluating the critical responses while applying selective laser melting to process steels of martensitic [131], precipitation hardened [135], and austenitic [132] grades. However, there was no evidence of any research report attempting the application of the laser melting method to process duplex stainless steel powders, at the time of the start of this project. This has been identified as a clear research gap and the research hypothesis and questions are framed to address this gap. The research gap proposed to be filled in through this research and the questions to be addressed are as follows:

The Research Gap

While additive manufacturing and in particular the selective laser melting process appear to be viable solution to achieve near net shapes with a wide variety of metal systems in powder form, the possible application of the method to process the duplex stainless steel systems has not drawn specific research attention yet.

Research Questions

The Overarching Research Question:

How do duplex stainless steels respond to processing by Selective Laser Melting?

Sub-questions:

1. *What mechanisms and mechanics of material consolidation signify selective laser melting of duplex stainless steels?*
2. *What will be the possible influences of the point-by point laser interaction on the microstructural balance that is typical of duplex stainless steels?*
3. *What are the laser beam parameters for the best inter-particle and inter-layer coalescence while laser sintering duplex stainless steel powders?*
4. *What are the influences of critical process parameters such as composition, grain size, raster path pattern, together with the laser beam settings on specific responses?*

Considering the nature of these questions and how the outputs of the experimental investigations undertaken addressing them unfold, the research may be considered to be carried out in two distinct stages as detailed in the flowchart at the end of this chapter in Fig. 2-37. The first stage addresses first two sub questions, while the later part goes on searching for answers to the last two questions. Hypothetically, selective laser melting can be applied to any metal powder system. However, with the duplex stainless steel system, the first two questions stated above will become critical, as failure to achieve

positive responses while addressing these research questions might lead to the termination of the project at the first stage itself as optimum process conditions and critical responses will be meaningless if the basic attributes of the metal system cannot be assured. In order to ascertain that the research framework proposed is feasible, inferences are drawn based on the literature reported on the application of laser welding process. Laser welding is seen to be comparable to SLM from a material processing standpoint, due to its localised fast moving heat source and rapid cooling conditions. Furthermore, laser welding has been successful in joining duplex stainless steels of varying grades including; LDX 2101, SAF 2205, SAF 2507 [139-141]. A brief review of the developments in the laser welding of duplex stainless steels is essential now, before the hypothesis for the current research can be articulated.

Laser welds are characterised by their deep penetration and low heat input which ensures a small fusion zone and narrow heat affected zone (HAZ) without the requirement for the filler metal [141]. However, the low heat input and corresponding rapid cooling rates result in a distorted non equilibrium duplex microstructure as shown in Fig. 2-34. Ferrite content up to 89% was observed by Pekkarinen and Kujanpää in the laser welding of LDX 2101 lean duplex stainless steel, with more than 98% ferrite approximated in SAF 2205 duplex stainless steel [142]. Columnar ferrite grain growth in the fusion zone was observed by El-Batahgy *et al.* to stem from the fine grain growth at the edge of the HAZ, directed toward the weld centre and with austenite precipitation resulting from solid state phase transformations [139].

In the laser welding of SAF 2507 Dengiz observed austenite growth primarily along the grain boundaries. Widmanstätten needles were observed within grains with increasing heat input, contributing to an increase in the Widmanstätten austenite quantity [141]. Of higher importance is the formation of deleterious precipitates during the solidification of the laser weld. The carbide precipitate $M_{23}C_6$ is observed by Liu *et al.* in the weld fusion zone resulting in a chromium depleted zone within the ferrite phase of the weld [143]. chromium nitride (Cr_2N) precipitation is more commonly affiliated to rapid cooling processes and was observed by Yang *et al.* as needle-like laths within the α-ferrite of the fusion zone. Further, the Cr_2N precipitation was detrimental to the critical pitting corrosion temperature of the weld, reducing it by 14°C in comparison to the base metal

as a result of the chromium depleted zone formed by Cr_2N in α-ferrite as evidenced in Fig. 2-35 [14]. A 77-95 MPa reduction in UTS and 14.8-19.1% loss in elongation compared to the base metal was observed by Amigó *et al.* in the laser welded rolled SAF 2205 plate, resulting from the distorted microstructure. However, a comparable result to the base metal was achieved in the laser welding of sintered duplex stainless steel, due to the fracture propagating in the base metal adjacent to the HAZ of the weld [144].

However, solution annealing or laser surface heat treatments were attempted to restore the equilibrium phase distribution in laser welds and revive the corrosion resistance and other mechanical properties. Pitting corrosion resistance of laser welded SAF 2205 was restored by Yang *et al.* through the application of a short-duration solution annealing process. The optimised solution annealing conditions for the decomposition of Cr_2N precipitates were noted to be holding at 1080°C and rapidly quenching in water [14]. Liu *et al.* applied laser surface heat treatment using 4, 6 and 8kW of power to different samples, promoting secondary austenite growth within the weld as Widmanstätten needles and by coarsening of the grain boundary austenite [145]. Schwarz *et al.* further observed a 12% reduction in ferrite after the laser surface heat treatment of the welded zone of a laser welded SAF 2507 duplex stainless steel specimen [146]. Based on the results shown in Fig. 2-36, Liu *et al.* reported that a 6 kW laser treatment led to a UTS higher by 30 MPa and percent elongation increased by 5% compared to the untreated welds [145].

Evidently, laser welding is a possible method of processing duplex stainless steels without thermal cracking or porosity. However, the thermal variations emanating from the cooling conditions result in a distorted duplex microstructure, favouring the excessive ferrite growth. Further research also evidenced that a suitable solution annealing or laser surface heat treatment processes can bring the duplex structures back to the equilibrium states and restore the properties. Based on the strength of these arguments, the following hypothesis is proposed as the basis of the current research

The hypothesis

Additive processing methods based on the selective laser melting can be applied to process duplex stainless steels in the powder form though the point-by-point laser consolidation may lead to structural distortions. While the structural variations may give rise to unexpected property responses, a suitable post-process heat treatment method can be developed to alleviate the issues with the structural concerns.

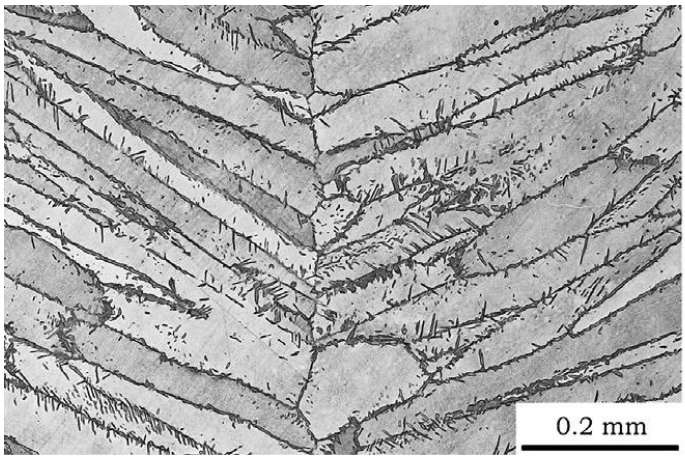

Fig. 2-34 Laser welded showing columnar ferrite grains, grain boundary austenite and Widmanstätten needles (from Liu et al. [145])

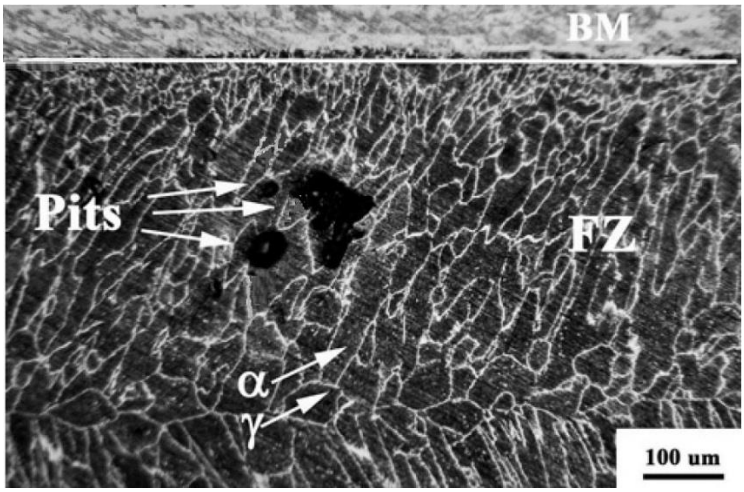

Fig. 2-35 Corrosion pits in ferrite of the laser weld fusion zone (from Yang et al. [14])

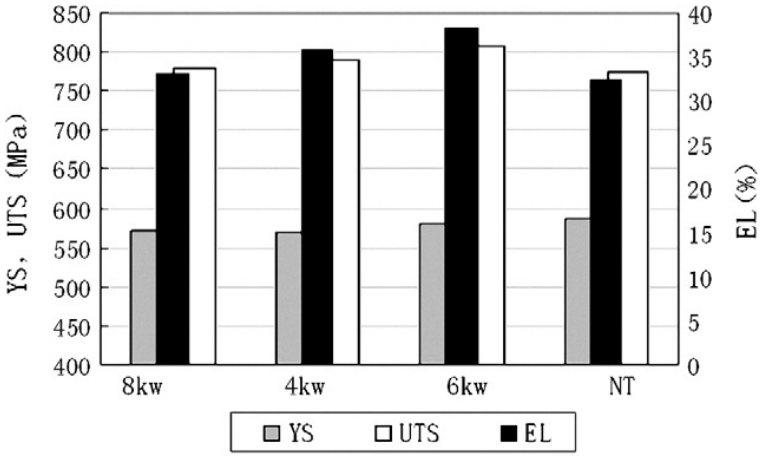

Fig. 2-36 Tensile test results of laser surface heat treated and non-treated (NT) laser welded SAF 2205 (from Liu et al. [145])

2.6 Objectives and the organisation of the thesis

The principal aim of the current research is to evaluate the responses of a selected duplex stainless steel alloy to processing by selective laser melting with varying conditions. The first stage is to conduct preliminary experiments leading to the proof of concept. Once this is achieved, further research has to be undertaken evaluating the internal structures resulting from the laser melting process more intricately. The process, structure, and property relationships must be established next. It will also be essential to evaluate the possible effects of the structural variations resulting from the laser melting process on the specific attributes of the alloy system. The following are the broad objectives set for the experimental research planned to prove the hypothesis:

- Conduct initial experiments applying selective laser melting to a selected grade of duplex stainless steel and establish the possible changes to the internal micro structures.
- Evaluate a possible post-process heat treatment option and ascertain, if the structures can be brought back to the equilibrium states
- Experimentally evaluate the process-structure relationships more intricately
- Identify the more favourable ranges of laser process parameters and build test pieces to evaluate and establish the process-structure-property relationships

- Considering the presumably ferritic structures, identify significant changes if any in the magnetic nature of the printed duplex steels
- Finally, evaluate the possible roles of laser melting and the ensuing structural alterations on the machinability responses of the samples printed with varying laser melting and machining process conditions

Experimental research is planned and executed as part of this research, in order to achieve these objectives. The methodology, details of the instrumentation and other experimental facilities, and the material and process conditions employed are presented in Chapter 3. The initial laser melting trials, the single layer and cubic samples produced with simple process parameter combinations and microstructures resulting are detailed in the fourth chapter. Chapter 5 includes a more detailed analysis and discussion of the resulting microstructures and the process- structure relationships. The physical and mechanical property results and their relationships to the process and structure combinations are also presented in this chapter. The magnetic responses of the laser melted duplex samples in the as-built states are examined in the sixth chapter. Chapter 7 is dedicated to evaluating the machinability responses of the laser melted duplex stainless steels with varying experimental conditions and comparing to the wrought and the solution annealed states. Finally, the significant qualitative and quantitative conclusions drawn from the experimental results are consolidated in the conclusions Chapter 8.

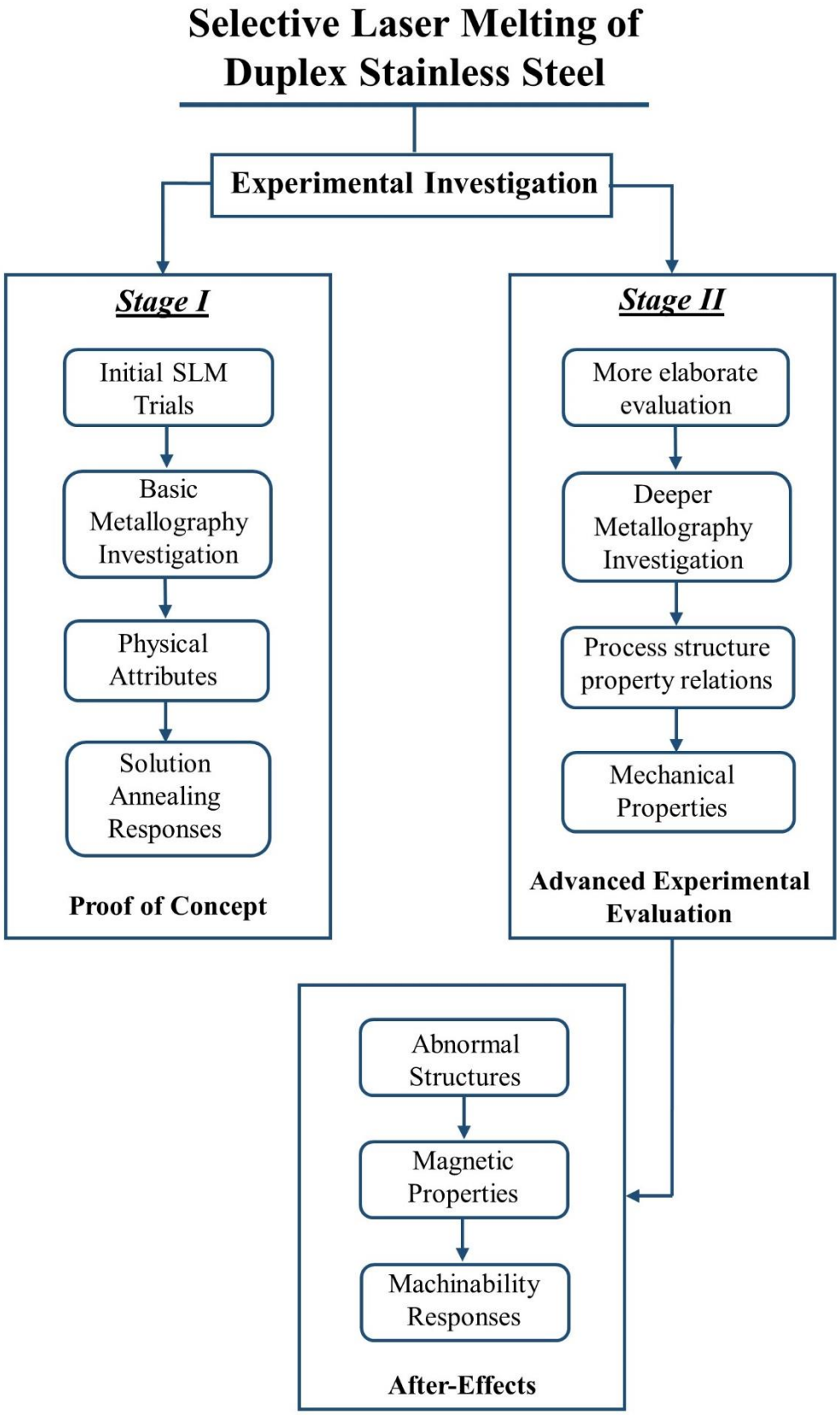

Fig. 2-37 The research plan

Chapter 3
Methodology

3.1 Critical factors of selective laser melting

The complex thermomechanical process of selective laser melting is influenced by multiple laser and mechanical parameters. The wide range of parameters influencing laser-powder interaction are commonly condensed to the most important factors of; laser power (P) [W], laser scan speed (v) [mm/s], scan line spacing (h) [mm] and powder layer thickness (t) [mm]. These parameters are universally represented as a single engineering parameter, laser energy density (LED), calculated via Equation 3.1 below.

$$LED = \frac{P}{v \cdot h \cdot t} \quad (J/mm^3) \qquad \text{(Eq. 3.1)}$$

Where, P represents laser power in W, v is the laser scan speed in mm/s, h is the spacing between scan lines in mm and t is the powder layer thickness in mm.

The laser energy density equation is used as a basis for the experiments with the laser power (P) and laser scan speed (v) set as controlled variables in conducted experiments. A powder layer thickness (t) of 50 μm is used in all tests, ensuring consistent powder packing. The coalescence zone of 20 μm is obtained by setting the scan line spacing to 120 μm for all scan strategies employed. These two settings were based on the optimised values provided by Renishaw PLC, GB, for similarly sized 316L austenitic stainless steel powder particles.

3.1.1 Process parameter settings and sample printing

The parametric combinations used for different experimental trials targeting different responses are listed in Table 3-1. Fig. 3-1 is a consolidated depiction of the overall design of the experimental work done in the two stages, to achieve the targets set for the current research. The actual process parameter settings with each of the experimental evaluations

undertaken will be discussed in the respective chapters that follow next. It may be noted that all test pieces for all the experiments in both Stage I and II are printed in multi-layers, other than the first attempt in Stage I noted as single layer trials.

Table 3-1 Design of the study

Test Name	Sample Config	Build Sets (Samples)	LED (J/mm^3)	Laser Power (W)	Laser Scan Speed (mm/s)	Scanning Strategy
Single Layer Trials (Chapter 4)	Flat Rectangle	1 (15)	Dependant 14.1-113 Inc - 7.1	50-400 Inc - 25	590	Linear
Preliminary Multi-layer Trials (Chapter 4)	Cubic	1 (20)	Dependant 49.4-113 Inc - 7.1	175-400 Inc – 25	590	Linear
Solution Annealed Trials (Chapter 4)	Cubic	1 (8)	Dependant 105.9-113 Inc - 7.1	375-400 Inc – 25	590	Linear
Laser Scan Speed variation (Chapter 4)	Cubic	2 (40)	36.9-229.2 Dependant	175-400 Inc – 25	290, 390, 490, 790	Linear
LED Microstructure Analysis (Chapter 5)	Cubic	2 (40)	91.7-141 Inc - 7.1	300-400 Inc – 25	354.5-727.3 Dependant	Linear
Scan Strategy Evaluation (Chapter 5)	Cubic	2 (30) Checker Board	125-222.2 Dependant	300-400 Inc – 25	300, 350, 400	Checker Board / Meander
		2 (30) Meander				
Tensile Testing (Chapter 5)	Flat Tensile Samples	2 (18) As built	135.5	325	400	Checker Board
			154.8	325	350	
		2 (18) Annealed	178.6	375	350	
Magnetic Characteristics (Chapter 6)	Cubic	1 (10)	49.4-113 Inc - 7.1 Dependant	175-400 Inc – 25	590	Linear
Machinability Studies (Chapter 7)	Vertical Rectangle	5 (64)	135.5	325	400	Linear
			154.8	325	350	
			178.6	375	350	
			194.4	350	300	

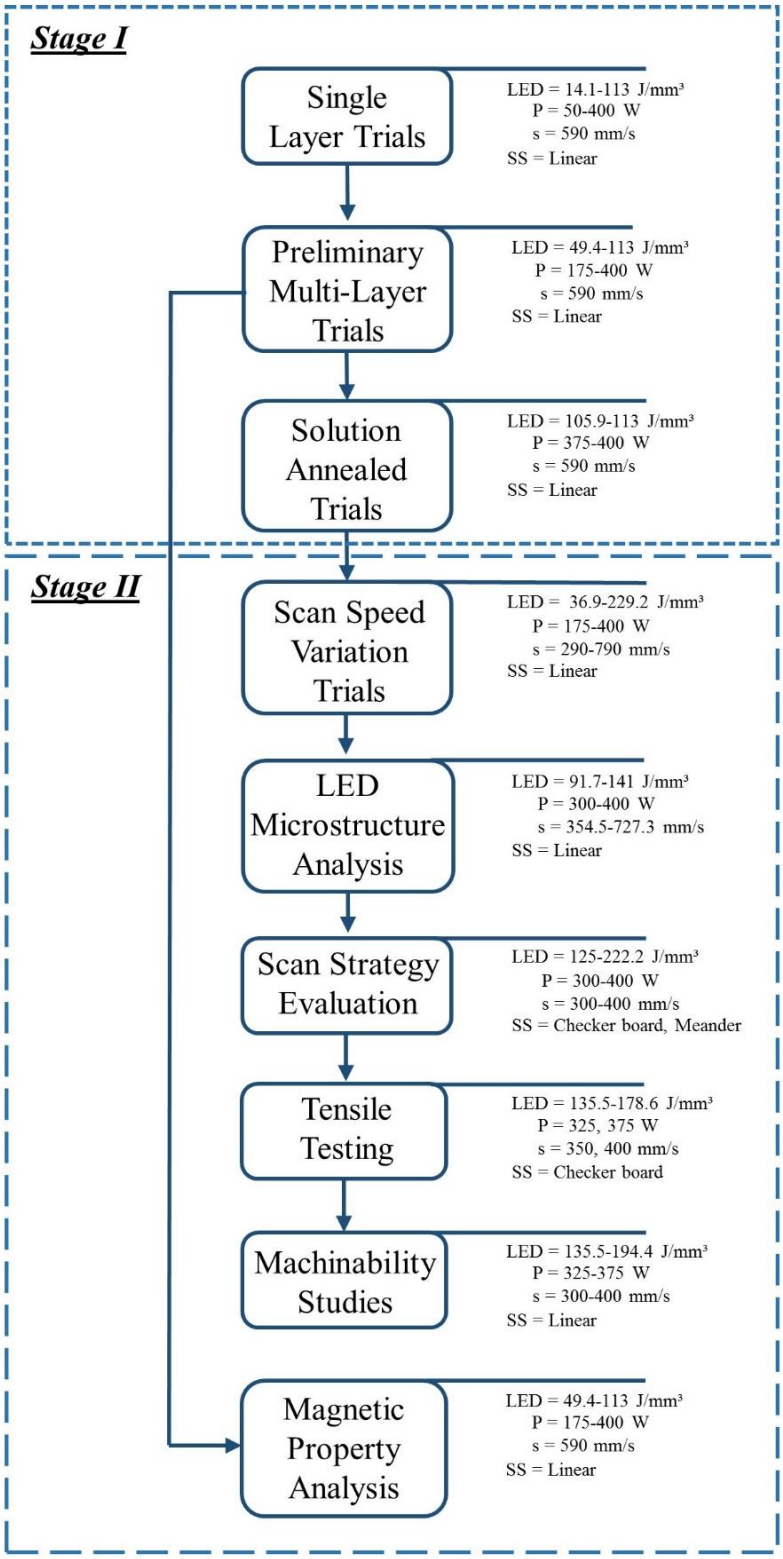

Fig. 3-1 SLM build flowchart

3.1.2 Scan Strategy Settings

Laser scan strategy selection has a profound influence on the internal stresses and the distortion of components produced by SLM as it can be tailored to control the cooling rate of the component. Three scan strategies; linear, checkerboard and meander were used in this study for density and microstructural evaluation purposes. The linear scan strategy was used predominantly for most samples reported in Chapter 4, to Chapter 7, as it allows consolidation simplification to better understand the process-structure-property relationships. The linear scan strategy consists of two sections, whereby, each section starts from the centre of the sample and extends to the border following the raster paths identified as 1 and 2 in Fig. 3-2. A final border scan line was traced clockwise around the profile at 100 µm from the consolidated powder, for the cubic samples as well as the test pieces used for machinability studies based on the drilling tests.

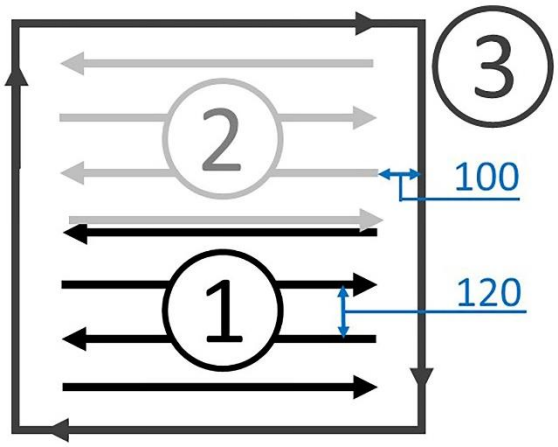

Fig. 3-2 Linear scan strategy and step numbers (dimensions in µm)

The checkerboard and meander scan strategies used for specific tests presented in Chapter 5 were selected from the pre-set options available in the Renishaw AutoFab (Marcam Engineering GmbH, DE) SLM build software. The shorter scan lengths in the checkerboard scan strategy implemented by Zhang *et al.* was seen to result in retaining the heat in small sections for greater lengths of time, due to rapid scanning between tracks [147]. Individual checker size was noted by Lu *et al.* to result in a maximum density of 99.1% with a checkerboard scan strategy at either 5X5 or 7X7 mm checkers [148]. The checkerboard scan strategy used in this study (Fig. 3-3) consists of four 5X5 mm checkers which were chose by virtue of their uniform fit within the confines of a 10X10mm cubic sample, simplifying consolidation effects. Each checker contains either vertical or

horizontal scan lines, alternating adjacent to each other, followed by a single border scan, spaced at 100 μm from the consolidated tracts following steps 1-10 as depicted in Fig. 3-3. Scan lines in each checker starts from the centre and terminates at the border with each layer starting at the bottom left checker with corresponding checkers consolidated clockwise as per the steps in Fig. 3-3. The scan lines for each checker reverse after each pass similar to the linear strategy above and are spaced by 120 μm. The (n+1) layer scan lines are rotated 90° to the $(n+1)^{th}$ layer, as shown.

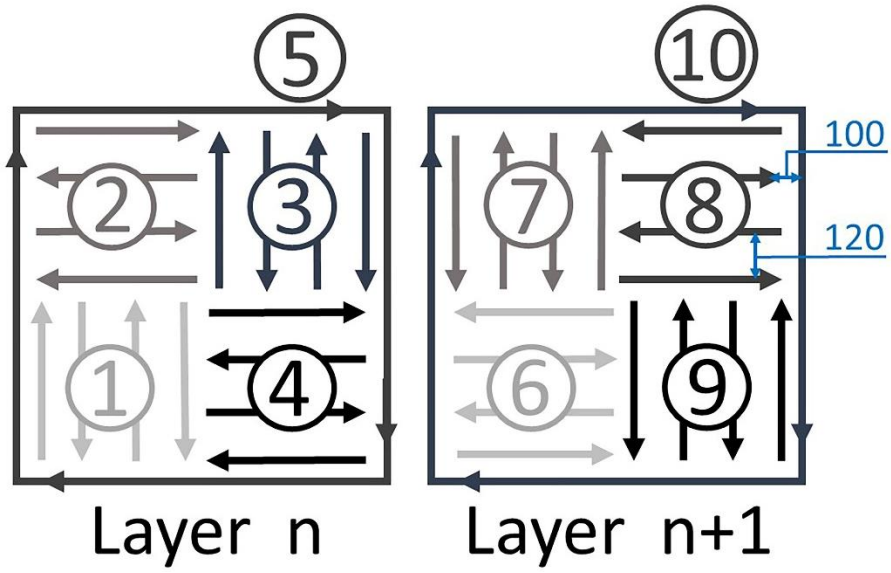

Fig. 3-3 Checkerboard scan strategy showing steps 1-10 (dimensions in μm)

A reduction of thermal stresses and promotion of fine grained microstructure was stated by Zhou *et al.* as defining factors in the implementation of a meander scan strategy with 67° scan line rotation between layers [149]. This produces samples with no preferred grain orientation, preventing the formation of a strong texture and only partial re-melting as noted by Casati *et al.* [150]. The meander scan strategy as used in Chapter 5 consists of 120 μm spaced scan lines travelling back and forth from the top of the cross section similar to the linear scan strategy. As observed in Fig. 3-4, the orientation of the scan lines rotates clockwise by 67° after each successive layer, and bound by a border scan 100 μm from the end of the scan tracts.

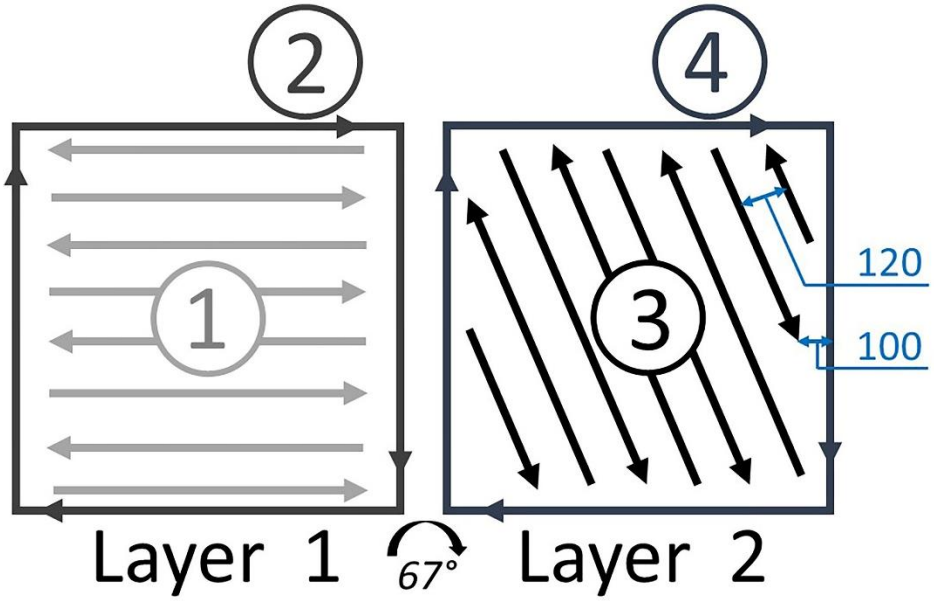

Fig. 3-4 Meander scan strategy showing steps 1-4 and 67° rotation between layers (dimensions in µm)

3.1.3 Support Structure Design

Support structure requirement is significant as Hussein *et al.* notes, that they support complex, overhanging geometries during the SLM process and act as heat sinks [151]. All support structures used throughout this study consist of multiple wall supports in the bulk of the sample at 45° from the long edge of the sample and a single contour support use to define the edge of the sample as observed in Fig. 3-5. The SLM processing parameters used for the support structures are listed in Table 3-2, while a constant scan line spacing and a powder layer thickness of 120 and 50 µm respectively were used.

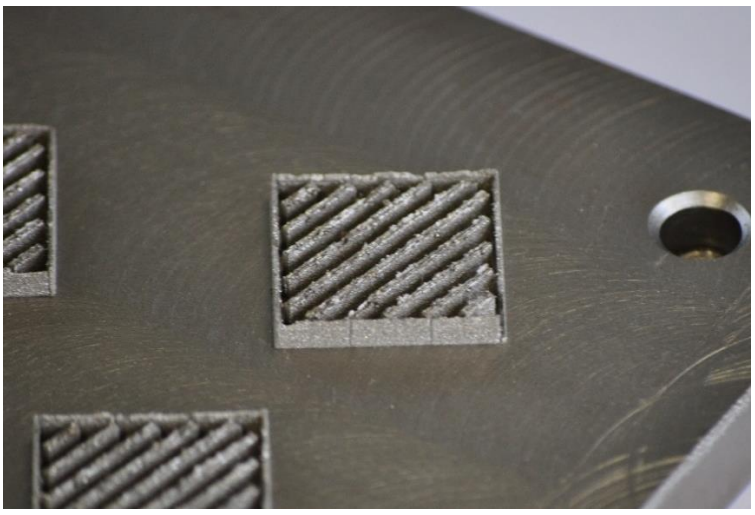

Fig. 3-5 Support structure consisting of internal wall supports and a single contour support

Table 3-2 Support structure parameters

Sample Configuration	Laser Energy Density (J/mm^3)	Support Height (mm)	Contour Support Thickness (mm)	Bulk Wall Support Thickness (mm)	Wall Support Spacing (mm)
Cubic	47.9	2	1	0.85	2
Flat Tensile Samples	47.9	4 (Lowest edge)	1	0.85	4
Vertical Rectangle	70.5	4	1	0.85	4

3.1.4 Build Design and Job Setting

Component layout and appropriate design of the positioning on the build substrate are critical in ensuring a consistent spread of the powder and to minimise the effects of condensation and splatters in the printed parts. An example of part spacing and gas flow influence on sample properties is detailed hereafter. A 62 MPa variance in UTS results was observed by Fitzgerald *et al.* in samples spaced between 10-64 mm with the greatest average strength occurring at 40 mm spacing [152]. A 1.7% decrease in porosity and 7 MPa reduction in standard deviation of the compression test results were observed by Ferrar *et al.* by optimising the gas flow and achieving the removal of the condensate [153]. Normally, the job setting on the build platform depends on the part geometry. The arrangement used for the single layer sample printing will be shown in Fig. 4-1 and discussed further in Chapter 4.

Cubic samples used in the bulk of experiments (Chapter 4-5) follow the build layout as presented in Fig. 3-6. The staggered spacing of 9 mm is used to minimise the overlap during powder spreading in each column. Staggering also ensures for each powder layer that the column of samples is not affected by the adjacent columns, as the adverse effects

of the splatter of the soot is minimised. More importantly, the staggered arrangement allows to distribute the load on the silicone sweeping blade more evenly, thus reducing the chances of the build failures. The array of the samples is also kept as close as possible to the top edge of the plate, in order to conserve on the powder usage for each layer. The overall scheme of the build parameter settings used for printing the cubic samples used for characterisations at different levels are elaborated in each respective chapter.

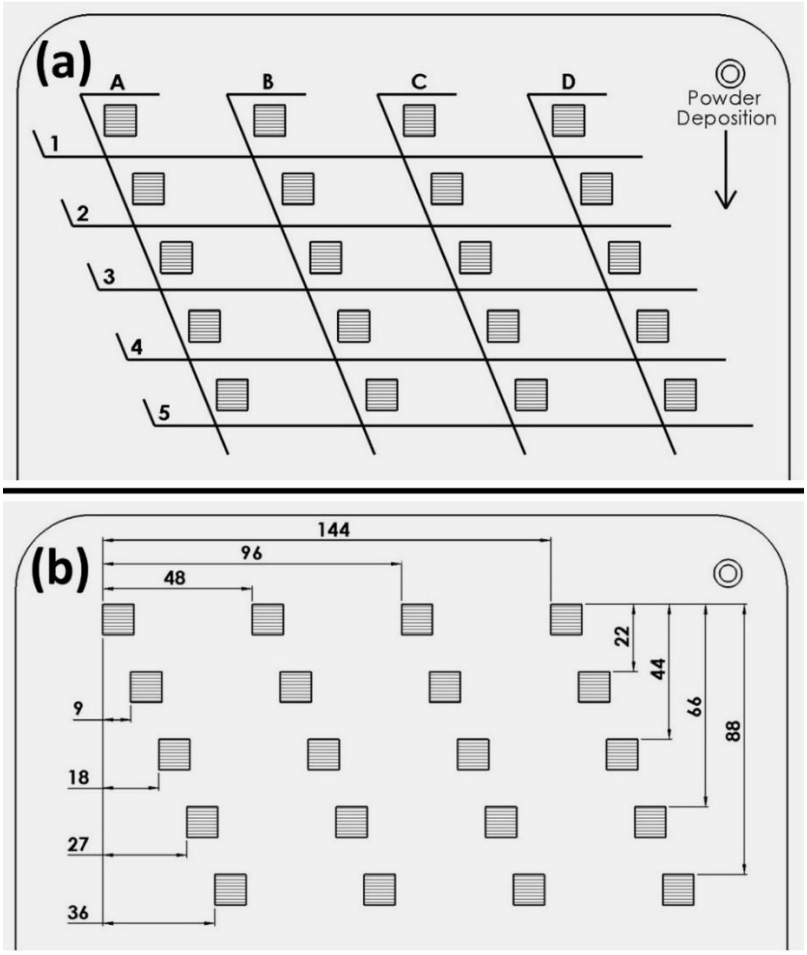

Fig. 3-6 Build layout for cubic samples; (a) Naming convention, (b) Build dimensions (dimensions in mm)

The tensile test samples are placed on the build substrate, along their length as shown in Fig. 3-7, as building vertically would require large quantities of the powder material. This resulted in a narrow spacing between samples of 10.7 mm, as shown, while a 5° angle is incorporated to prevent linear damage to the wiper blade used for powder dispersion. Alternate samples are shifted 27 mm downwards so as to minimise the overlap and the potential influences of splatter. Four identical builds were produced with two being subjected to heat treatment solution annealing conditions as detailed in Section 3.10.

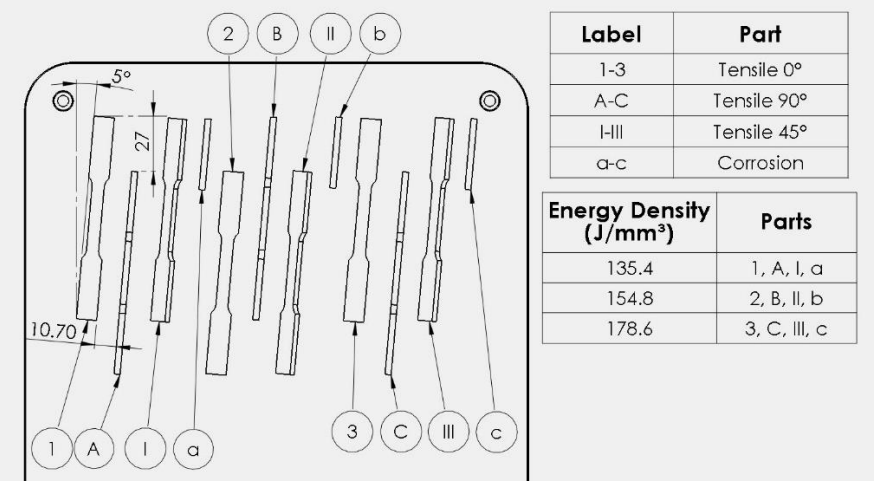

Label	Part
1-3	Tensile 0°
A-C	Tensile 90°
I-III	Tensile 45°
a-c	Corrosion

Energy Density (J/mm³)	Parts
135.4	1, A, I, a
154.8	2, B, II, b
178.6	3, C, III, c

Fig. 3-7 Tensile sample build layout (dimensions in mm)

Laser melting samples for the drill tests as reported in Chapter 7 were built oriented at 34° to the vertical on the build platform, as shown in Fig. 3-8. This is to minimise the part distortion by depositing the powder perpendicular to the scan direction and to minimise the damage to the powder dispersion wiper from straight edges aligned at right angles to the direction of sweep. Similar sample orientation was also used by Gu *et al.* for cubic samples [154]. Samples in adjacent rows are staggered as per Fig. 3-8-(b), to minimise the effect of splatter from adjacent parts and a 1mm offset in the third and fourth row samples was implemented to further minimise the chance of the wiper damage. The build parameter layout for the drill samples is presented in Table 3-3 below with a colour key denoting the sample allocation for each of the specific machinability studies. Samples without colour were produced for further trials unable to be completed due to tooling cost constraints.

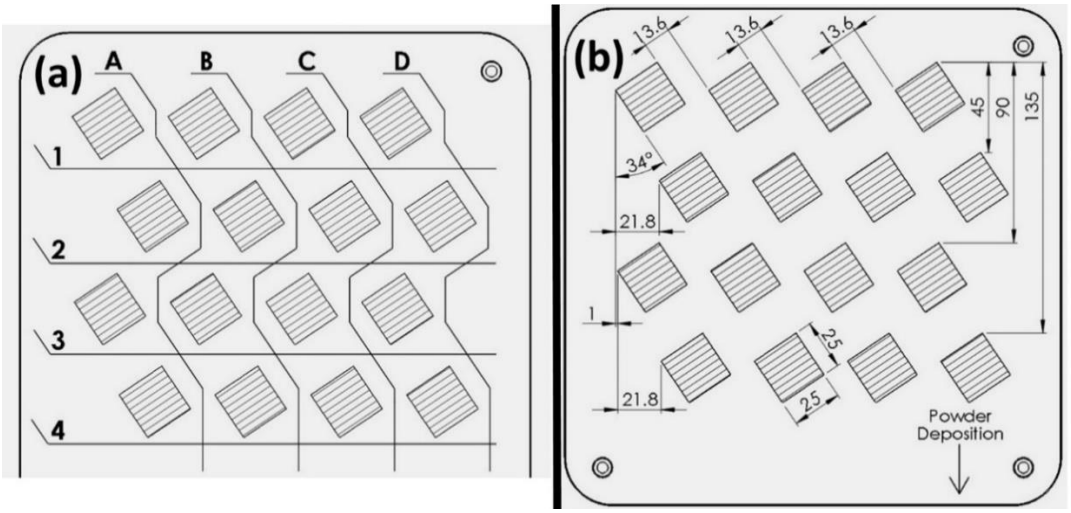

Fig. 3-8 Build layout for drill samples; (a) Naming convention, (b) Build dimensions (dimensions in mm)

Table 3-3 Drill sample build parameter layout

Test Name	Parameter	Set	*Row*	*Column*			
				A	**B**	**C**	**D**
Machinability Studies (Chapter 7)	Laser Energy Density (J/mm^3)	1	**1**	194.4	154.8	135.5	178.6
			2	135.5	178.6	154.8	194.4
		2	**1**	178.6	135.5	194.4	154.8
			2	194.4	154.8	135.5	178.6
			3	154.8	194.4	178.6	135.5
			4	178.6	135.5	194.4	154.8
		3	**1**	194.4	178.6	135.5	194.4
			2	154.8	135.5	178.6	154.8
			3	178.6	154.8	194.4	178.6
			4	135.5	194.4	154.8	135.5
		4	**1**	154.8	135.5	178.6	154.8
			2	194.4	178.6	135.5	194.4
			3	135.5	194.4	154.8	135.5
			4	178.6	154.8	194.4	178.6
		5	**1**	135.5	178.6	154.8	194.4
			2	154.8	194.4	178.6	135.5

Key		
		Comparative assessment of SLM vs Wrought Trials
		The role of the varying LED Trials
		Evaluation of SLM samples: As Built
		Evaluation of SLM samples: Solution Annealed
		Unused samples

3.2 Duplex stainless steel powder material

Metal powder used throughout this research is equivalent to the super duplex stainless steel grade SAF 2507 (UNS S32750) (Fig. 3-9) with the chemical composition as detailed in Table 3-4. The gas atomised powder supplied by Sandvik Osprey Ltd., GB is spherical in morphology and has a powder size distribution of 24.29-50.22 µm with a mean

diameter of 34.0 µm. Tap density of the powder was measured to be 4.3 g/cc and was validated in conjunction with powder size distribution by laser diffractometer analysis as represented in Fig. 3-10.

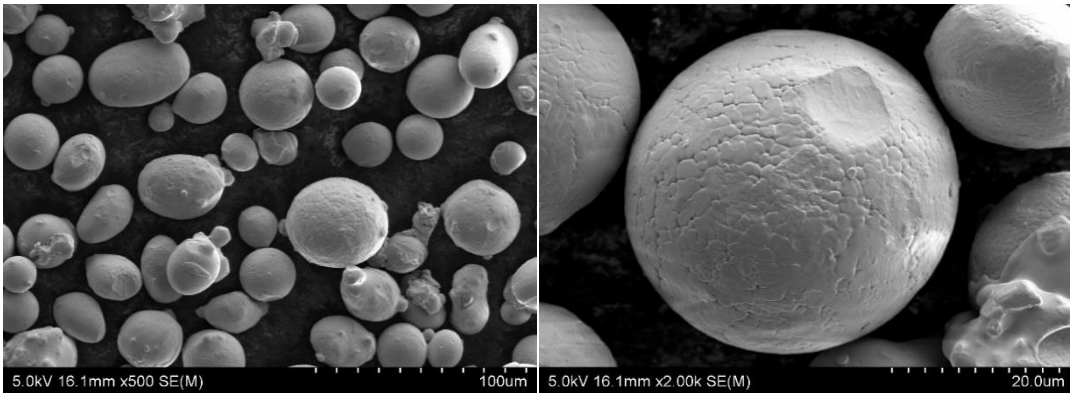

Fig. 3-9 Duplex stainless steel powder morphology (from Davidson and Singamneni [155])

Table 3-4 Chemical composition of SAF 2507 super duplex stainless steel powder

Powder Constituents (wt%)															
Cr	***Ni***	***Mo***	***Mn***	***Si***	***N***	***Co***	***Al***	***C***	***Sn***	***Ti***	***W***	***P***	***S***	***B***	***Fe***
24.6	6.9	3.88	0.9	0.5	0.31	0.04	0.02	0.02	0.01	0.01	0.01	0.009	0.005	0.001	Bal.

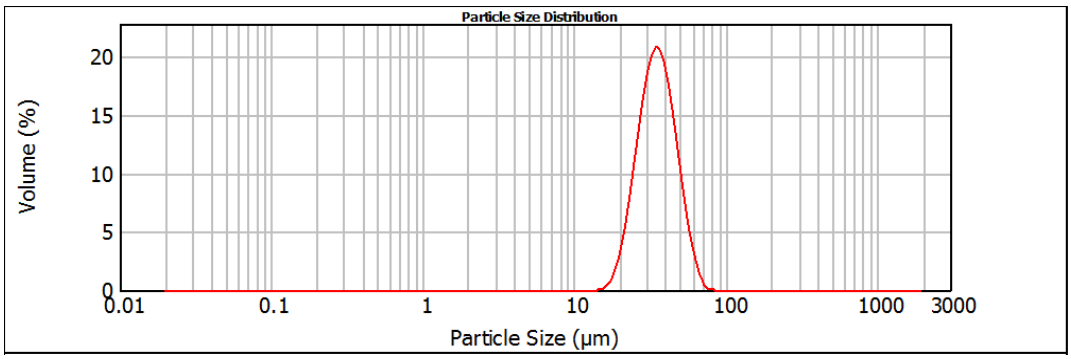

Fig. 3-10 Powder size distribution (from Davidson and Singamneni [155])

3.3 The laser melting system

All selective laser melting experiments are conducted using a Renishaw AM250 laser melting system as shown in Fig. 3-11 (Renishaw PLC, GB), which is available at the 3D Printing Laboratory of the Auckland University of Technology. The AM250 system uses an Ytterbium fibre laser of 400 W maximum power output and 1070 nm wavelength, with a laser spot size of 140 μm. Powder consolidation is conducted atop a mild steel substrate; 250X250 mm in profile and 16 mm in thickness, held at an elevated temperature of 170 °C. Laser melting is performed within an Argon filled processing chamber, ensuring O_2 levels are below 0.5% during processing.



Fig. 3-11 Renishaw AM250 SLM machine (from AUT 3D Printing Lab[156])

3.3.1 Pre-build preparations

Prior to commencing a build job the sample shapes are individually designed on SolidWorks (Dassault Systèmes Co., FR) computer aided design software and saved as .stl files. These files are then imported into Renishaw AutoFab (Marcam Engineering

GmbH, DE) for processing parameter selection, build design and layer slicing and then exported to the actual laser melting system. This process consists of three steps, with the sample saved as three consecutive separate files. The first of which is used in the addition of support structure on the sample and in the definition of processing parameters and is saved as a .vfx file. The second stage concerns the slicing of the sample into individual layers with the predefined processing parameters and saving the data as a .fab file. The final step is to import the separate .fab sample files on to the build platform and arranging as per the plans explained in Section 3.1.4. Once all the specimens of a given build are in place, a final .fab file is generated for the whole build, which will then be transported to the machine hardware in the form of .mtt file. While the .stl file format is the universal method of representing the CAD model as a triangulated object, the .fab and .mtt are typical file formats generated and used on the Autofab software that outputs to the Renishaw system at the time this experimental research was conducted.

3.3.2 Post-build tasks and Sample Removal

One of the post-build tasks is to collect the supporting powder from the build and recycling for further use. A vibrating sieve system, Russell Finex P3 Vibrasonic sieve (Russell Finex Ltd.,UK) was used for this purpose. Once the excess powder is pushed over into the over-flow bins, the base plate is detached from the machine and the samples are removed from the base, by breaking the support structures. The base-plate is mounted on a bench vice, and a ball-peen hammer and an aluminium impact block are used to remove cubic and drill test samples from the substrate.

The cubic samples to be discussed in Chapter 4, and built directly on the substrate are removed using a hacksaw with a HSS blade. Combinations of hacksaw, ball-peen hammer and chisel application are used to remove the tensile test samples (Chapter 5) from the substrate. Once taken off the base plate, the residual support structures of the tensile test pieces are further removed from by a Makino U3 (Makino Milling Machine Co., JP) and a wire electro discharge machining (EDM) system. After removal, samples are contained within Tactix 2pc storage box set (Meridian International Co., CN) and labelled as per their build and location on the substrate as noted in Section 3.1.4 above. The substrates

are then machined until square, followed by a media blasting on the exposed surface to promote laser absorption in the first layer and cleaning with isopropyl alcohol.

3.4 Physical Properties

3.4.1 Dimensional accuracy

Dimensional accuracy tests conducted on the multi-layer samples discussed in Chapter 4 are done prior to removal from the build substrate. Measurements are taken for their length, width, and height, using a Mitutoyo Digital Vernier Caliper (Mitutoyo Co. JP) accurate within ±0.02 mm. Dimensional accuracy results are presented as a percentage of the deviation from the design dimensions.

3.4.2 Density Analysis

Bulk density of samples reported in Chapter 4 and 5 were established by using the Archimedes method, in particular by following the Equations 3.2 and 3.3 reported by Spierings *et al.* for SLM samples [157].

$$\rho_{Sample} = \left(\rho_{fluid} - \rho_{air}\right)\frac{m_{air}}{(m_{air} - m_{fluid})} + \rho_{air} \quad \text{(Eq. 3.2)}$$

$$\%\ Density = \left(\frac{\rho_{Sample}}{\rho_{Material}}\right) \cdot 100 \quad \text{(Eq. 3.3)}$$

Masses of the as-built samples were first measured in air (m_{air}) and then suspended in deionised H_2O on a custom apparatus to establish m_{fluid}. Mass measurements were conducted on a Shimadzu AUW220D mass balance (Shimadzu Co., JP) shown in Fig. 3-12 with a 0.1 mg accuracy, repeating each test four times. Temperatures of both measurements were recorded with a Digitech QM1601 digital thermometer and K-type thermocouple (Jaycar Electronics Pty Ltd, AU) with an accuracy of 0.5% of the reading +1 °C, for their effects on water and air density. The percentage density evaluated in

Equation 3.3 uses the bulk material density ($\rho_{Material}$) of 7.8 g/cm^3 as per the data provided by Sandvik AB, SE [158].

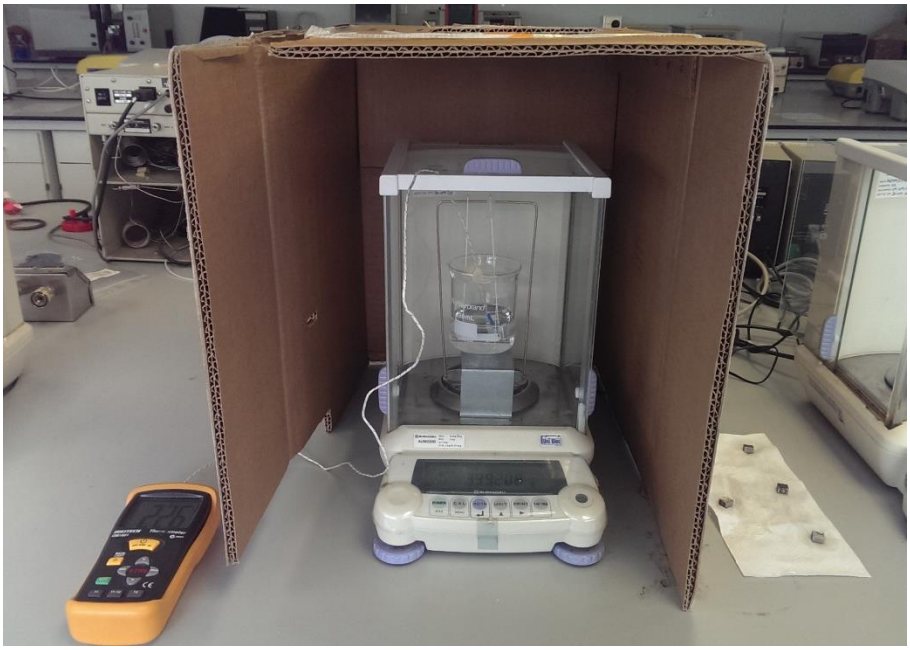

Fig. 3-12 Archimedes density experimental setup

3.5 Metallography

3.5.1 Sample Preparation

Sample preparation started with the slicing of printed specimens for micro-hardness, and microstructural evaluation. Cubic samples used in Chapter 4 and 5 were sliced centrally perpendicular to the laser scan tracts via a Struers Labotom-3 (Struers ApS, DK), under flood cooling conditions as observed in Fig. 3-13-(a). One half of each specimen is used for the metallographic studies, while the other half is kept as a spare sample. Specimens for the metallographic evaluation of the tensile test samples discussed in Chapter 5 were cut, removing 7 mm off one end of each sample in the first set of both as-built and annealed samples and the rolled plate samples. Cutting was done via a Buehler Isomet low speed saw (Illinois Tool Works Inc., US) with a 15HC wafering blade and water cooling.

After slicing, samples were hot mounted with the sliced face down in either PolyFast or ClaroFast resin in a LaboPress-3 press (Struers ApS, DK). PolyFast resin (Fig. 3-13-(b)) was used in the mounting of samples for micro-hardness and porosity evaluation due to the hardness and the black colour. However, ClaroFast resin (Fig. 3-13-(c)) was used in the mounting of samples for metallographic evaluation. This allowed the subsequent thinning for magnetic property analysis (Section 3.8) as it was easy to remove the sample with minimal residue when compressed and the residual material was also easily dissolved in Acetone. The mounted samples were ground on a Metaserv Rotary Grinder (Illinois Tool Works Inc., US) using polishing papers of diminishing grit; 180, 500, 1200, 2400 and polished on felt pads at two stages on a LaboPol-2 (Struers ApS, DK), with both 6 µm and 1 µm diamond pastes followed by a wash in isopropyl alcohol and drying in hot air. The same grinding and polishing stages were repeated for machinability samples which were first sliced via Makino U3 (Makino Milling Machine Co., JP) wire EDM and polished to a 1 µm finish without mounting.

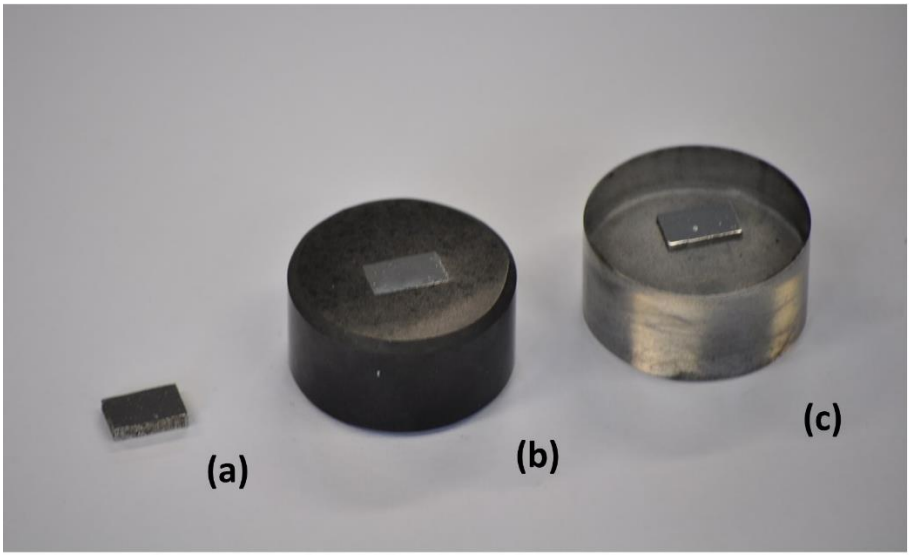

Fig. 3-13 Sample mountings; (a) Cut Sample, (b) PolyFast Resin, (c) ClaroFast Resin

3.5.2 Void fraction / Porosity measurements

Polished and mounted samples to be discussed in Chapter 4 are examined for their void fraction under an Olympus BX51 M (Olympus Co., JP) digital optical microscope shown in Fig. 3-14. Sample cross sectional images are taken at 50X magnification at four locations within the sample. Next, ImageJ imaging software (National Institutes of Health, US) is used to convert each image into a binary black and white image. Thresholding of the image is applied to eliminate any anomalous black spots and the volumes of black pixels relating to the void area in the binary image are measured via the inbuilt "Analyse Particles" function. Similar processes were completed by Gu *et al.* in the porosity analysis of SLM 17-4PH stainless steel, whereby three images were taken at 50X magnification, converted into black and white images, and then analysed for the ratio of the two in a MATLAB program [154].

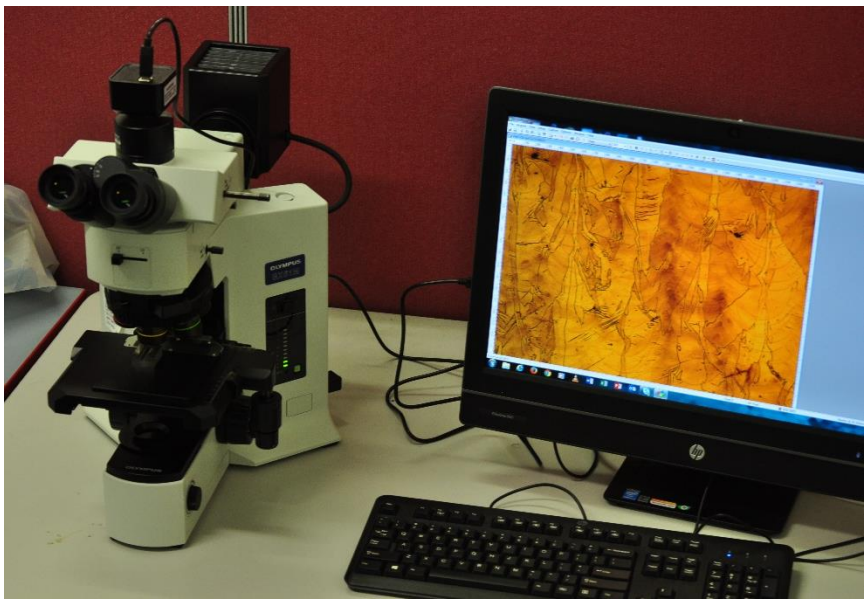

Fig. 3-14 Olympus BX51 M optical microscope

3.5.3 Etching for metallography

Samples cut either across or along the laser scan direction for metallography are etched by chemical or electrochemical methods. Chemical etching is solely conducted on the solution annealed heat treated samples presented in Chapter 4. Chemically etched samples

are hot mounted, ground and polished as per Section 3.5.1. Beraha's reagent is produced as per the composition detailed by Vander Voort; 85 mL H_2O, 15 mL HCl, 1 g $K_2S_2O_5$ [159]. Mounted samples are dipped into a shallow volume of the etchant, in a petri dish for 35-45 s, followed by rinsing with Isopropyl Alcohol and drying in hot air.

Electrochemical etching is used on as built samples reported in Chapter 4, 5, and 7. Grinding and polishing is done with the samples hot mounted in ClaroFast resin (Struers ApS, DK), following the technique in Section 3.5.1. Once the polishing is complete, each sample is broken from its mounting in an industrial bench vice and cleaned in isopropanol alcohol. The electrochemical etching setup shown in Fig. 3-15 is developed, which consists of a Aim-TTi EL302R bench DC power supply (Aim and Thurlby Thandar Instruments Ltd, GB) with banana plug test leads and alligator clips connected at the negative terminal to a AISI 316L stainless steel cathode (blue lead) and to the SLM sample at the positive terminal (yellow lead). Both the cathode and SLM sample are immersed in a 60% HNO_3 : 40% H_2O solution and etched at 10 V for 6 s inside a fume cupboard. The drill samples from the machinability tests are etched at 35 V for 30 s due to their large size and exposed surface area.

Immediately after etching, each sample is cleaned thoroughly in isopropyl alcohol and dried in hot air. The etching reagent is only used for three samples, after which, it is disposed of and then a fresh quantity is mixed again. This is to reduce the risk of contamination and keep the etchant active. The electrolytic etchant and the etching voltage settings are based on the compilation by Michalska and Sozańska, formulated for selectively revealing phases present in duplex stainless steels [160]. Prior to converging on the use of the 60% HNO_3 : 40% H_2O solution, numerous other etchants were trialled at various etching times and voltages. These etchants were; 20% NaOH : 80% H_2O, 10% Oxalic acid ($C_2H_2O_4$) : 90% H_2O and 10N KOH (30%) : 70% H_2O from the base test conditions defined by; Michalska and Sozańska, Tan *et al.* and Zucato *et al.* respectively [160-162]. The 60% HNO_3 : 40% H_2O solution was selected over these other etchants by virtue of its clear exposure of Widmanstätten and grain boundary austenite, in addition to chromium nitride precipitates and fusion zones.

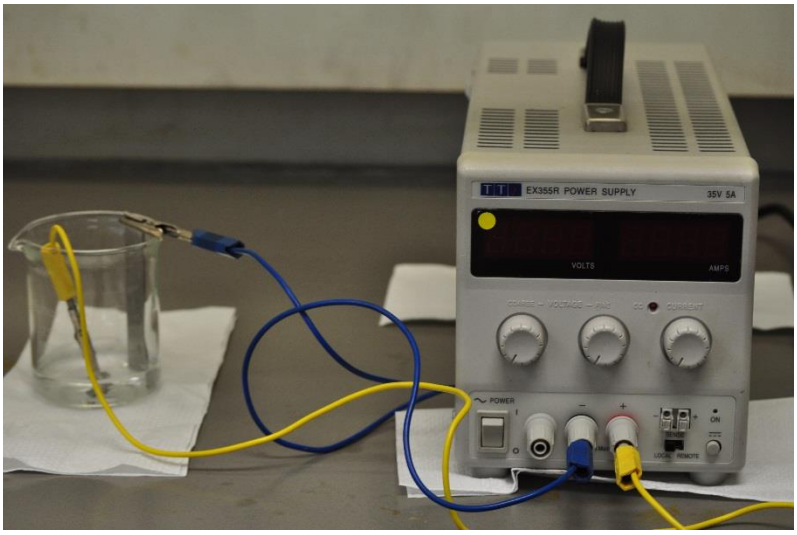

Fig. 3-15 Electrochemical etching setup

The microscopy studies are conducted primarily on the Olympus BX51 M (Olympus Co., JP) digital optical microscope shown in Fig. 3-14. For each etched sample, images are taken at increasing magnifications 50, 100, 200, 500 and 1000X at five locations on the sample, including the centre and the border. An additional set of images is taken of a calibration slide with a scale of 1 mm overall length and 10 μm increments which is used as a reference scale in sizing images and measuring grain sizes on ImageJ imaging software (National Institutes of Health, US) detailed in Section 3.5.4. Additional higher magnification imagery used in Chapter 5 is taken on a Hitachi SU-70 (Hitachi High-Technologies Co., JP) scanning electron microscope shown in Fig. 3-16. Images were taken at decreasing magnification; 40000, 20000, 10000, 6000, 2000, 500X magnification at four locations on each sample.

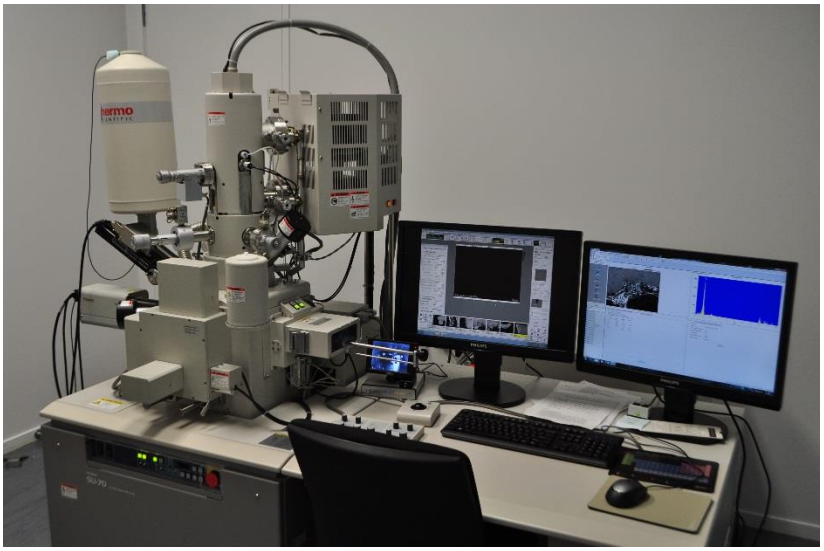

Fig. 3-16 Hitachi SU-70 SEM

3.5.4 Grain Size measurements

Grain size measurements based on the samples used for the microstructural evaluations reported in Chapter 5 were obtained from the photomicrographs generated by optical microscopy. ImageJ imaging software (National Institutes of Health, US) was used to measure the grain width and height. A ratio, determined off the image of the calibration slide at 100X magnification was used as a benchmark, to quantify the grain size of images at equivalent magnifications. The line tool in ImageJ was used to measure the grain width and height at three different locations, establishing the grain height to length ratio. Average grain width to height ratios are presented as part of the results of Chapter 5.

3.5.5 EBSD preparation for SEM

Samples prepared for Electro backscatter diffraction (EBSD) imaging (Chapter 5) were mounted and polished as per Section 3.5.1 and lightly electro etched in a 60% HNO_3 – 40% H_2O solution as per Section 3.5.3. Preliminary attempts were made to establish EBSD patterns by electropolishing samples on a LectroPol-5 (Struers ApS, DK) in Struers A3 solution at an applied voltage and polishing time of 35 V and 25 s, as per Struers recommendations [163]. EBSD imaging of etched samples was conducted at the Research Centre for Surface and Materials Science at the University of Auckland on a

FEI Quanta 200 scanning electron microscope as shown in Fig. 3-17, with a TSL EBSD camera at 500X magnification.

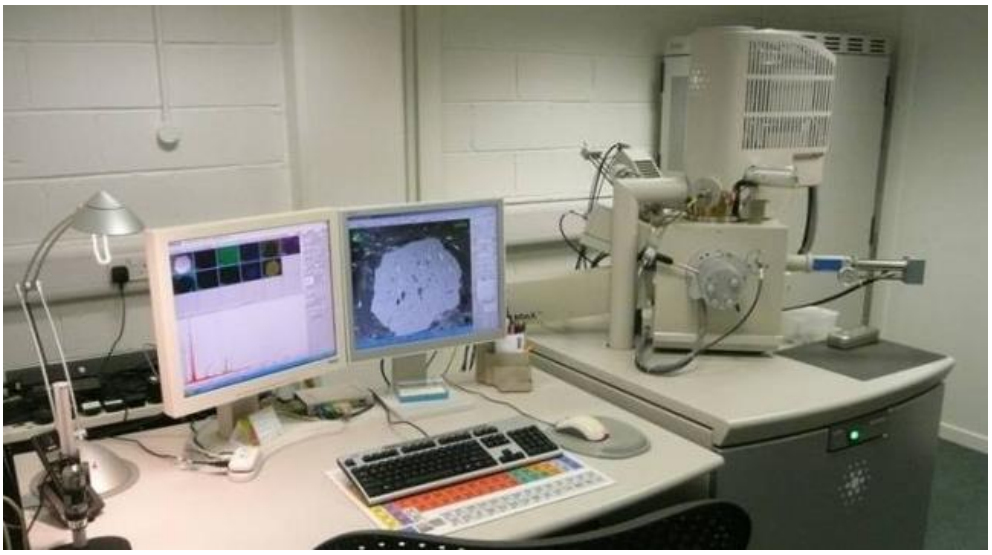

Fig. 3-17 FEI Quanta 200 scanning electron microscope (from the University of Glasgow [164])

3.5.6 XRD preparation for SEM

X-ray diffraction (XRD) analysis of metallography samples discussed in Chapter 5 was conducted on an Xpert Pro Analytical XRD system shown in Fig. 3-18, employing Cu-Kα radiation with the assistance of the overseas collaborator in the department of metallurgical engineering of the Indian Institute of Technology, Chennai, India. Samples for XRD were polished as per Section 3.5.1 above, broken from their mounting and scanned in the 2Θ range of 30-90° with a 0.02° step size, followed by slow scans in the 2Θ range of 38-48° and 0.01°step size. Reference intensity method was used to identify the phases, considering α (011) and γ (111) peaks.



Fig. 3-18 Xpert Pro Panalytical XRD (from James Hutton Institute [165])

3.5.7 Feritscope

The γ-austenite:α-ferrite ratio of SLM samples in Chapter 6 was established by contact probe Feritscope measurements. Feritscope measurements are used throughout literature in the quantification of duplex stainless steel grades. An example of which is Tavares *et al.*'s research on σ-sigma phase precipitation in UNS S31803 duplex stainless steel. After calibration of the Feritscope probe to a duplex stainless steel sample with equilibrium microstructures, actual readings were taken at 10 different locations on each sample produced [166]. The inspiration for this work was the Feritscope tests conducted at Optomec International Ltd., via a Fischer Fischerscope MMS with an EGAB1.3-FE probe (Helmut Fischer GmbH, DE) as presented in Fig. 3-19.

Samples used for the Feritscope tests were sliced perpendicular to the scan tracts. Subsequently, they are surface ground on a KGS-1020WMA2 (Kent Industrial Co., TW) saddle surface grinder along their length and width to a uniform size of 10.2X5.1X3.1

mm. Tests were conducted on the ground 10.2X5.1 mm face of each sample, as two different sets, marked as 10 and 8 points as detailed in Fig. 3-20. An additional control sample is developed from a SAF 2507 rolled plate supplied by Vulcan Steel Ltd., NZ which was used as a reference for equilibrium ferrite:austenite content. All Feritscope measurements of SLM samples are inferred based on the rolled duplex steel specimen reading as the benchmark and considering the ratio of the actual reading and the benchmark reading as the measure of the ferrite content.

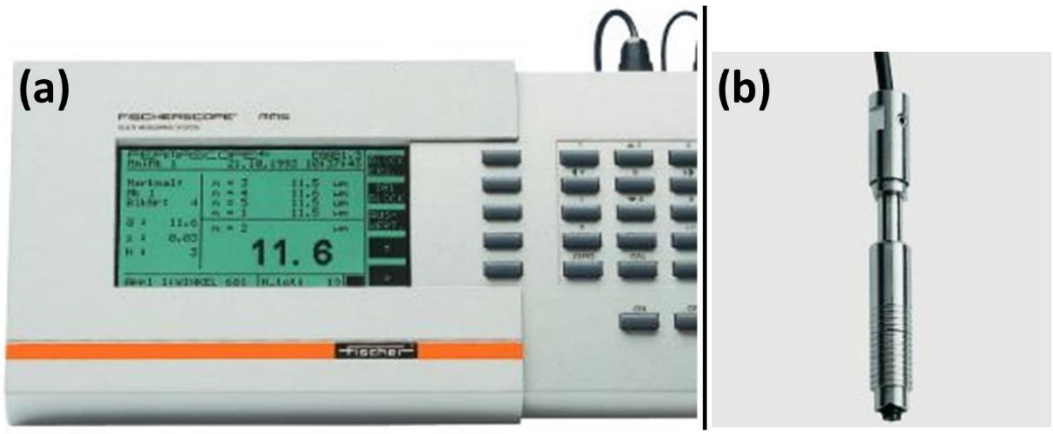

Fig. 3-19 Fischer Fischerscope MMS (a) with an EGAB1.3-FE probe (b) (Adapted from Helmut Fischer [167])

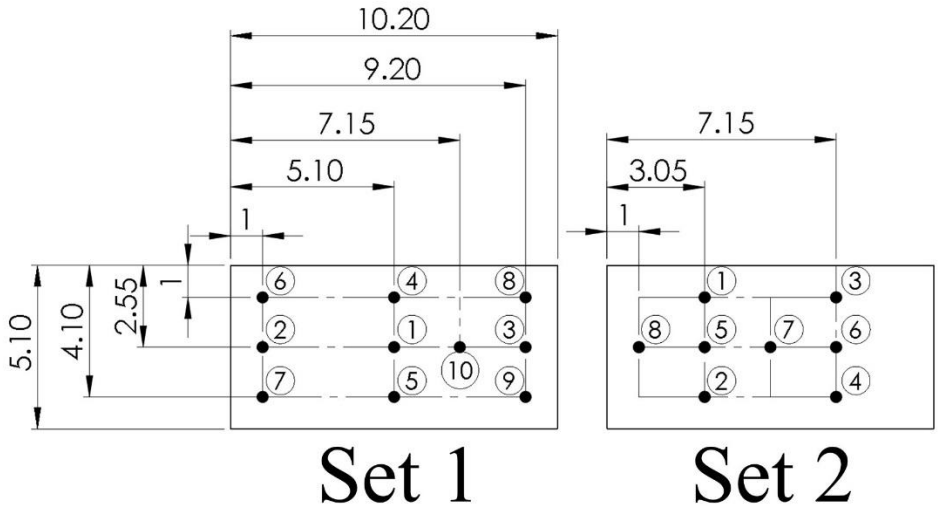

Fig. 3-20 Feritscope testing locations (dimensions in mm)

3.6 Mechanical properties

3.6.1 Hardness Evaluation

Micro and macro hardness tests were conducted on samples with the purpose of establishing microstructural and bulk material variation. A Leco LM800AT system shown in Fig. 3-21 (LECO Co., US) was used to conduct Vickers micro-hardness tests at a load of 200 g and dwell time of 15 s for samples presented in Chapter 4 and 5, for which testing conditions are similar to those reported by Hao *et al.* for a SLM 316L stainless steel-hydroxyapatite composite and by Zou *et al.* for GTAW welded duplex stainless and ferrite steels [168, 169]. Micro-hardness tests were completed over the cross section with each sample hot mounted, ground, and polished as described in Section 3.5.1.



Fig. 3-21 Leco LM800AT Vickers micro-hardness tester

Three separate sets of locations were used for micro-hardness testing on the samples evaluated in Chapter 4, 5 and 7. A lower spread of micro-hardness test-points was used on the preliminary SLM samples (Chapter 4), providing a basic insight into the microstructural variations. To establish this, five micro-hardness tests were completed along the horizontal centreline of the sample as represented in Fig. 3-22. A bigger number

of tests were done on the samples used in the metallographic characterisation (Chapter 5). As observed in Fig. 3-23, testing consists of five rows of six points at intervals of 1 mm. Tests commence 80 µm from both the top and left edges as per the ASTM standard E384, with other test locations as detailed in Table 3-5 [170]. Micro-hardness measurements conducted on the samples drilled for the machinability studies (Chapter 7) included sets of four tests, starting at 20 µm from the hole surface and the other three trials spaced 30 µm apart as per ASTM standard E384 [170]. These sets of four measurements are repeated five times along the length of the hole. Macro hardness tests on the drilling samples in the machinability study (Chapter 7) were evaluated via the Rockwell Hardness C (HRC) method consisting of a 10 kg preload and 150 kg main load using a Lyric HR-150A (Laizhou Lyric Testing Equipment Ltd, CN) hardness tester as shown in Fig. 3-24. Hardness tests were taken on the top surfaces of the drill samples prior to machining at intervals of 4mm at the locations as shown in Fig. 3-25.

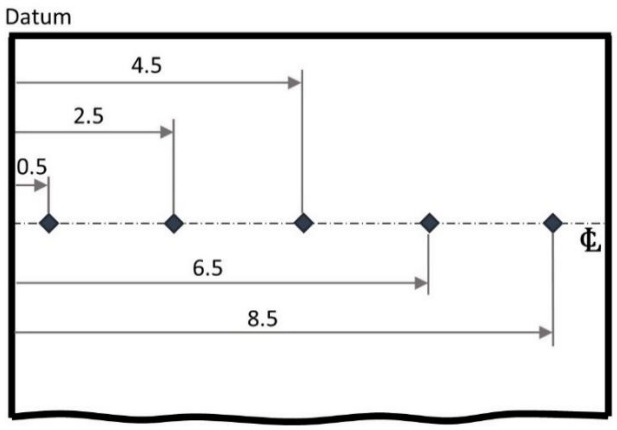

Fig. 3-22 Micro-hardness testing locations on preliminary multi-layer samples (dimensions in mm)

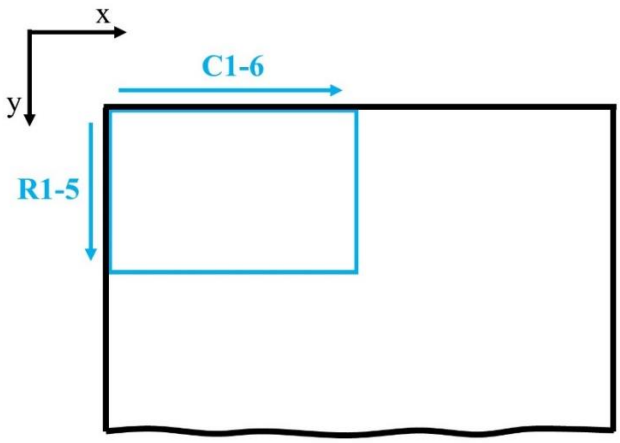

Fig. 3-23 Micro-hardness test area on sample cross-section for metallographic characterisation samples

Table 3-5 Micro-hardness testing locations of metallographic characterisation samples

Coordinates of Test points [mm] *(x,y)*	*C1*	*C2*	*C3*	*C4*	*C5*	*C6*
R1	(0.08, 0.08)	(1.08, 0.08)	(2.08, 0.08)	(3.08, 0.08)	(4.08, 0.08)	(5.08, 0.08)
R2	(0.08, 1.08)	(1.08, 1.08)	(2.08, 1.08)	(3.08, 1.08)	(4.08, 1.08)	(5.08, 1.08)
R3	(0.08, 2.08)	(1.08, 2.08)	(2.08, 2.08)	(3.08, 2.08)	(4.08, 2.08)	(5.08, 2.08)
R4	(0.08, 3.08)	(1.08, 3.08)	(2.08, 3.08)	(3.08, 3.08)	(4.08, 3.08)	(5.08, 3.08)
R5	(0.08, 4.08)	(1.08, 4.08)	(2.08, 4.08)	(3.08, 4.08)	(4.08, 4.08)	(5.08, 4.08)



Fig. 3-24 Lyric HR-150A hardness tester

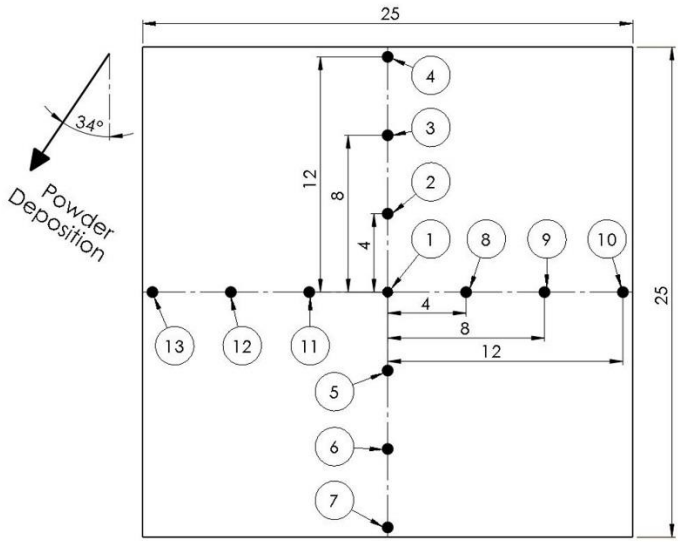

Fig. 3-25 Drill sample hardness test locations (dimensions in mm)

3.6.2 Tensile testing

Mechanical properties were further established by tensile testing the results from which are presented in Chapter 5. Tensile tests were completed on a Tinius Olsen H50KS (Tinius Olsen Material Testing Machine Co., US) as shown in Fig. 3-26, following the ASTM standard E8M for rectangular samples at a crosshead speed of 0.2 mm/min comparable

to the test conducted by Facchini *et al.* [171, 172]. A sub-size sample defined with a gage length, width and thickness of 25, 6 and 3 mm respectively and other dimensions as shown in Fig. 3-27 was used as the base model. The rolled plate of SAF 2507 duplex stainless steel of 3 mm thickness was supplied by Vulcan Steel Ltd., NZ and was cut into samples via a Makino U3 (Makino Milling Machine Co., JP) wire EDM both parallel and perpendicular to the direction of rolling. SLM sample build parameters, orientations, layout and part removal are defined in respective sections above. Similar tests and sample dimensions were used by Luecke *et al.* while studying selective laser melting responses of 17-4 PH stainless steel at three different orientations [173].

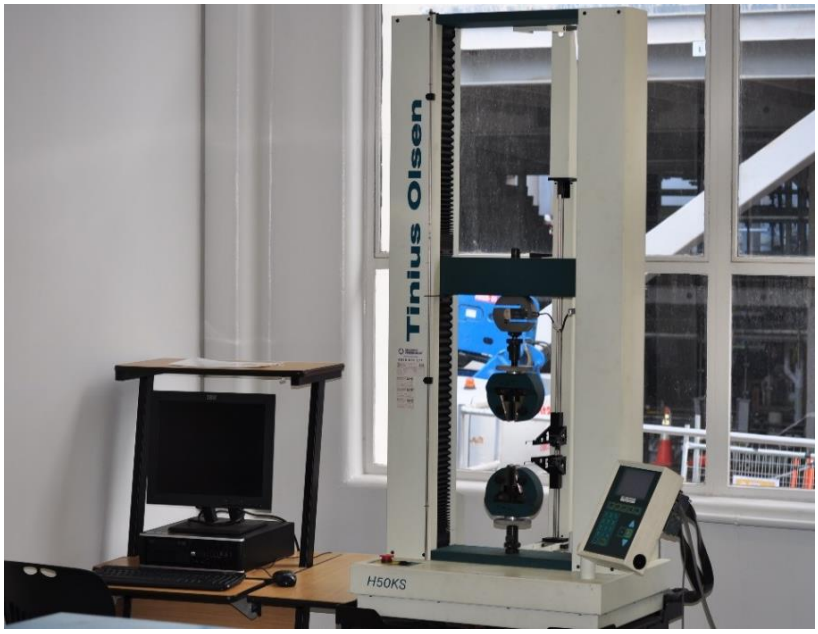

Fig. 3-26 Tinius Olsen H50KS tensile testing machine

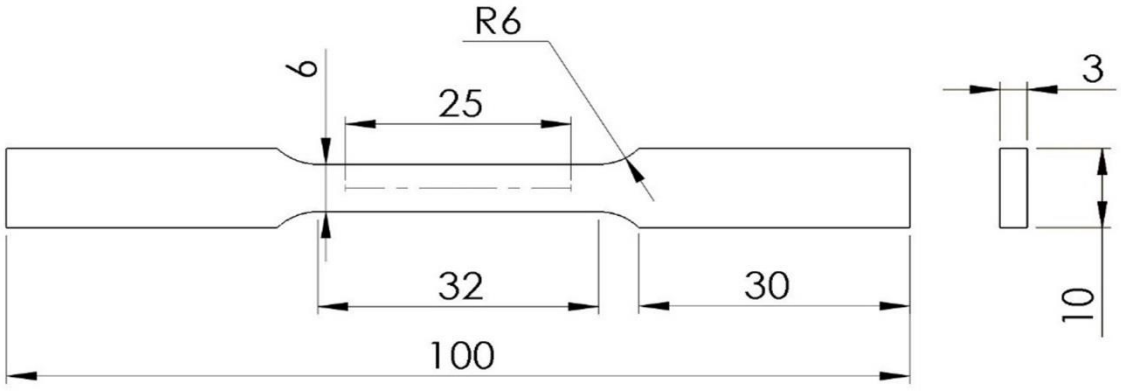

Fig. 3-27 Tensile test sample dimensions (dimensions in mm)

Post tensile-testing analysis included microstructural evaluation, following the procedures outlined in Sections 3.5.1 and 3.5.3. Fracture surfaces were analysed further to tensile testing, by hacksaw cutting a 10 mm section from the long broken piece off each sample. Fracture surface imagery was evaluated based on a Hitachi SU-70 (Hitachi High-Technologies Co., JP) scanning electron microscope with images taken on the whole fracture zone, at 35X magnification and detailed images taken at four different locations with diminishing magnifications; 20000, 10000, 5000, 2000, 1000, 500 X.

3.7 Surface roughness

Surface roughness analysis was conducted on drill test samples (Chapter 7), via the use of a Taylor Hobson Talysurf 50 (AMETEK Inc, US) stylus profilometer shown in Fig. 3-28. Mumtaz *et al.* measured surface roughness values along the side and the top surfaces of thin-walled Inconel 625 samples produced by SLM using a scan length of 12.5 mm [174]. Similarly a stylus profilometer was used by Singh *et al.* to determine the surface roughness of dry-machined SAF 2507 duplex stainless steel under varying cutting parameters [175]. Similar stylus profilometer tests are done and the responses from the rolled and SLM samples were assessed comparatively.

The drilled surfaces of the samples used to ascertain the machinability responses were also measured for the surface roughness values. Once the drill tests are complete, the rectangular samples with the central hole are split into two halves along the length of the drilled hole by wire EDM. The stylus probe is then used to measure the surface roughness at right angles to the scan tracks. These measurements were done at both the entry and exit of the hole on both halves of each sample. Totalling in four locations as per Fig. 3-29 with conditions following that detailed in Table 3-6 below as per ISO 4288-1996 [176].

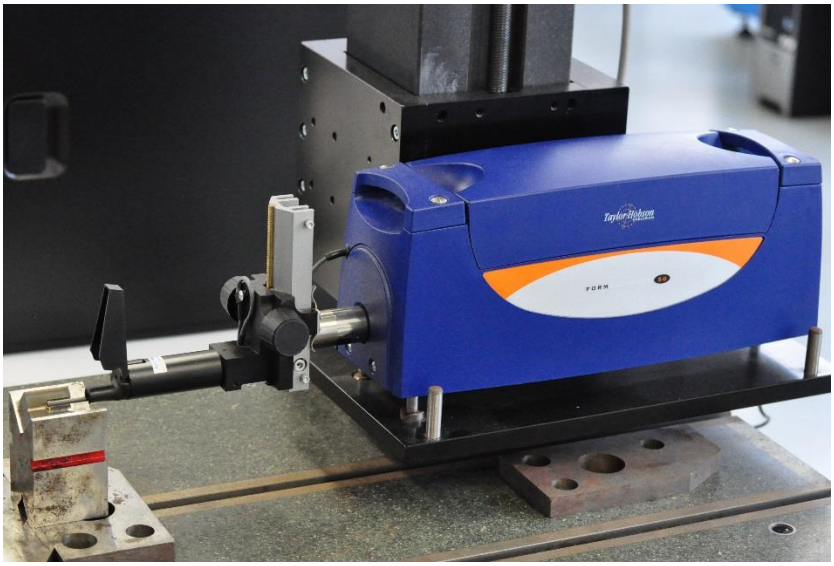

Fig. 3-28 Taylor Hobson Talysurf 50 stylus profilometer

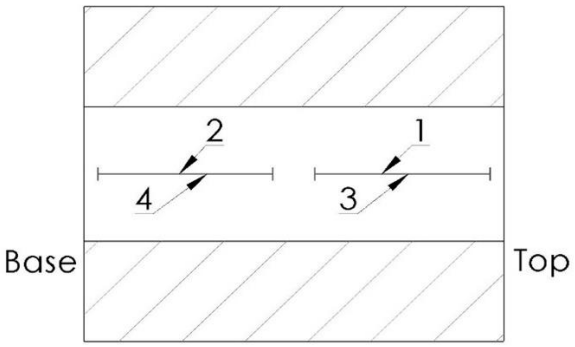

Fig. 3-29 Drill test surface roughness measurement locations

Table 3-6 Surface roughness test parameters

Test Name	Sample Configuration	Sampling Length (*lc*)	Test Length (*ln*)	Shortest cut off length (*ls*)	Stylus Speed
Machinability Studies (Chapter 7)	Drill Samples	2.5mm	12.5mm	0.008mm	0.25mm/s

3.8 Magnetic properties

The other halves of the sliced samples produced for the preliminary multi-layer studies (Chapter 4) are used for the vibrating sample magnetometer (VSM) studies leading to the results discussed in Chapter 6. The cut face of each of the sample was ground and polished to a 1 μm surface roughness, as per Section 3.5.1. A 1 mm thick slice was cut off the polished face of each sample, via a Makino U3 (Makino Milling Machine Co., JP) wire EDM. Further grinding and polishing of the mounted cut face followed, with the mass of the sample regularly measured using a Shimadzu AUW220D mass balance (Shimadzu Co., JP), to ensure the sample meeting the maximum mass requirements of the VSM.

After thinning to the possible extent, the sample is sliced into two halves so that the mass of each sample is below the VSM limit of 100 mg. A Lake Shore 3900 VSM (Lake Shore Cryotronics Inc, US) system shown in Fig. 3-30 was employed to develop the hysteresis loops. The samples are subjected to a demagnetisation loop from 1 T, prior to hysteresis loops, at an applied field between -0.5 and 0.5 T. An additional sample was tested between -1.4 and 1.4 T for anisotropy analysis. Samples were vibrated with the polished faces parallel to the magnetic poles and grain growth direction aligned perpendicular to the direction of vibration of the holder. Results are presented with normalisation by mass, for the tests conducted at the Department of Geology, the University of Otago.



Fig. 3-30 Lake Shore 3900 VSM (from Lake Shore Cryotronics used for magnetic characterisation [177])

3.9 Machinability studies

Machinability responses were studied through drill-tests based on the samples prepared with process parameters as listed in Table 3-1. These tests are done in two different sets. The first one targets the machinability responses of the laser melted samples in comparison with those of a wrought bar stock SAF 2507 duplex stainless steel for similar conditions. The other set is designed to ascertain the role of varying SLM process conditions on the machinability responses. After a careful consideration of the cost and time constraints and the essential extent of the experimental domain, four cutting speeds and two feeds are selected as listed in Table 3-7. While the tests were successful at all the four speeds with the SLM samples, only three levels of speeds could be used for the wrought bar stock samples, due to the repeated failure of drill tools at the highest speed within the limits of the current experimental domain.

All machining trials are done dry, in order to keep the experimental conditions simple and easy to evaluate and ascertain the specific role of selective laser melting on the machinability of duplex stainless steels. Through holes 30 mm in length are drilled in all the samples, except in the tests conducted at the cutting speed 20 m/min. In this case, sufficient data could be generated within a drilling depth of 18 mm, and so, it was left as a blind hole. The process parameter ranges for the drilling trials were initially developed based on the values recommended by the British Stainless Steel Association for drilling duplex stainless steels at Vc = 40 m/min and feed, f = 0.13 mm/rev [178]. Following, some preliminary tests were done with mild steel, SAF 2205 and 2507 duplex stainless steel samples with varying cutting speeds and feeds, and based on the results, the final speed and feed ranges were set as listed in Table 3-7.

Table 3-7 Process parameter settings for the Machinability studies

Test Name	Sample Type	LED (J/mm³)	Cutting Speed (*Vc*) [m/min]	Feed (*f*) [mm/rev]
Wrought vs SLM	SLM	194.4	20, 40, 60, 80	0.025, 0.05
	Wrought SAF 2507	-	20, 40, 60	0.025, 0.05
Varying LED Evaluation	SLM	135.5, 154.8, 178.6, 194.4	60	0.025
SLM: As-Built vs Solution Annealed	As Built	178.6	20, 60, 100, 140	0.025
	Solution Annealed			

3.9.1 Sample preparation and machine tools

A Fanuc Tape drill mate Model T (Fanuc Co., JP) CNC compact machining centre shown in Fig. 3-31 was used for all the drilling experiments. Prior to the actual drilling tests, the supported-end of each SLM sample is machined, in order to achieve a flat reference surface for mounting on the dynamometer fixture. Similarly, the SAF 2507 wrought bar

stock of 30 mm diameter, supplied by Vulcan Steel Ltd., NZ is parted off on a lathe and machined square to 25X25X30 mm samples. All machining during the sample preparation stage is also done on the same Fanuc Tape drill mate Model T as used for the actual drill tests. Side faces of SLM samples are filed prior to testing to achieve a proper fit into the dynamometer jig.

After machining the base, thermocouple holes are drilled in the samples along one of the faces and parallel to the laser scan tracts, at the locations as depicted in Fig. 3-32. Thermocouple holes are 1.5 mm in diameter and drilled under flood cooling conditions. In the case of drill breakage, a supplementary hole is drilled below the hole with the broken drill. Thermocouple holes are blind drilled to a depth, maintaining a 0.8 mm space between the surface of the actual drilled hole and the tip of the thermocouple. As a result, the length of each of the holes drilled to insert the thermocouple became equal to 6.7 mm. The final step in the preparation of the samples is the drilling of a pilot hole which is done under flood cooling conditions with a 3 mm parabolic fluted drill. The pilot hole is drilled whilst the sample is in its jig atop the dynamometer, so as to minimise the drill wobbling.

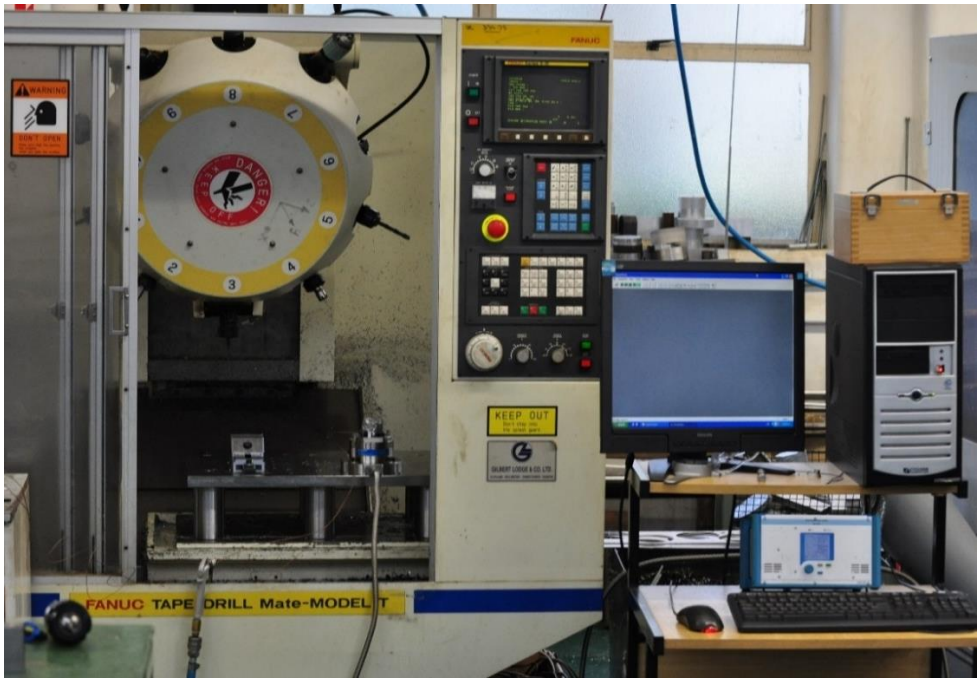

Fig. 3-31 Fanuc Tape Drill and dynamometer setup

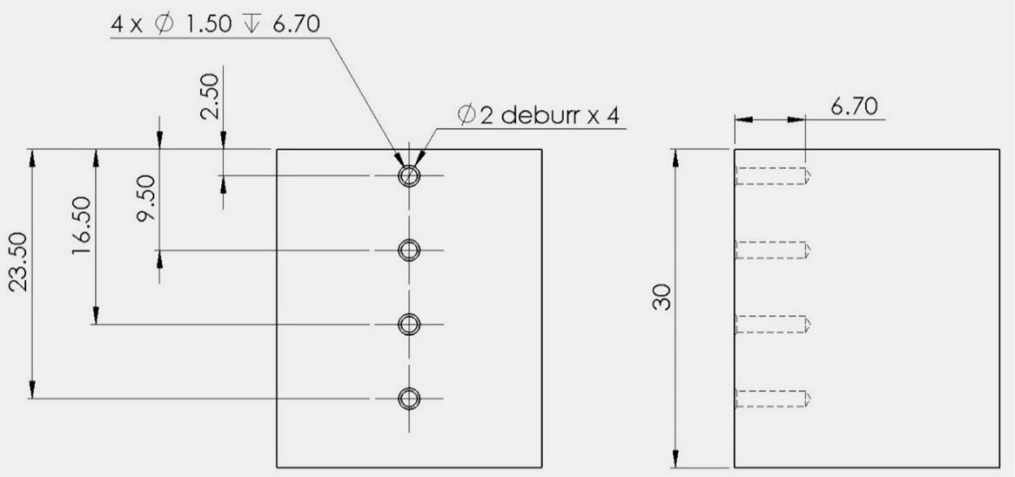

Fig. 3-32 Thermocouple hole locations and depth (dimensions in mm)

3.9.2 Drill tools and inserts

Two different drill tools of 10mm diameter are used in this study; indexable insert head type and solid carbide drills. An Iscar Sumocham DCN 100-050-16A-5D indexable head drill body and the Sumocham ICM 100 IC908 insert with TiAlN PVD coating (ISCAR Ltd, IL) presented in Fig. 3-33-(a) and (b) are used while assessing the SLM samples against the wrought duplex stainless steel samples. The same tools are also used in the evaluation of the machinability of SLM samples processed with varying laser energy densities. For all the machining trials involving comparative assessments between the wrought bar stock and the SLM samples as listed in Table 3-8, the insert type drill bits used repeatedly, as each insert was employed for two or more successive machining trials. This was due to the high costs involved in the tooling (Each insert costing $125NZD). This may have induced some uncertainty in these results, as the responses from all the trials are not from fresh tools with sharp cutting edges. Also, one of the drill bodies failed with one of the elevated speed case and so, a replacement body was procured and used for the remaining trials in this set.

Considering the high costs of the insert-type drill bits and in order to be able to use a fresh tool for each trial, the solid carbide drills were identified to be cheaper and better for the later part of the machining trials. These are the machinability studies comparing the as-built and the annealed SLM samples, using Sandvik CoroDrill 460.1-1000-050A0-XM GC34 with TiAlN PVD coating (Sandvik Coromant AB, SE) as depicted in Fig. 3-33-(c)

and (d). Based on the results of the experiments done to assess the role of the energy density, 178.6 J/mm^3 was identified as the most suitable laser energy density, due to it resulting in the most favourable machinability responses. In view of this, the as-built vs solution annealing machining responses are obtained based on test pieces built at 178.6 J/mm^3 energy density. The experimental plans with the solid carbide drills are listed in Table 3-9, with a fresh tool used for each of the experimental trials. Laser energy density parameter selection for machinability studies are detailed in Section 7.1.

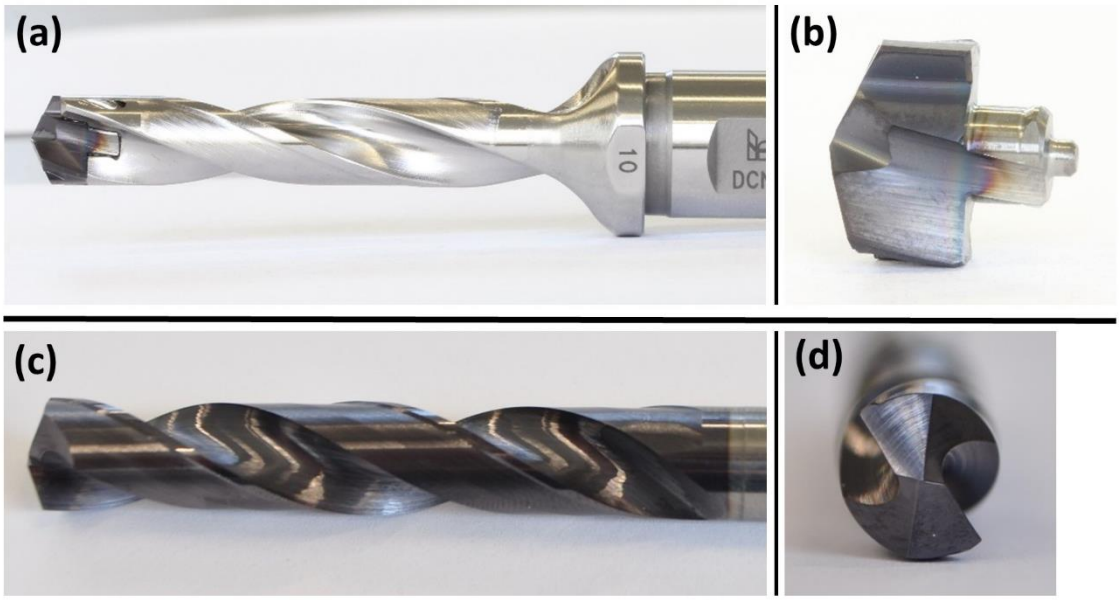

Fig. 3-33 Iscar indexable head drill and insert (a)-(b) and Sandvik solid carbide drill (c)-(d)

Table 3-8 Insert and Drill body allocation SLM vs Wrought SAF 2507 trials and LED evaluation

Test Name	Sample Type	Test Order	Cutting Speed (*Vc*) [m/min]	Feed (*f*) [mm/rev]	Insert	Drill Body
Wrought vs SLM	Wrought SAF 2507	1	60	0.025	1	1
		2	20	0.05		
		3	60	0.05		
		4	20	0.025		
		5	40	0.05	2	2
		6	40	0.025		
	SLM 194.4 J/mm³	1	60	0.025	3	
		2	60	0.05		
		3	20	0.025	4	
		4	20	0.05		
		5	40	0.025		
		6	40	0.05	5	
		7	80	0.025		
		8	80	0.05	6	
Varying LED Evaluation	135.4 J/mm³	3	60	0.025	3	
	154.8 J/mm³	4			4	
	178.6 J/mm³	2			2	
	194.4 J/mm³	1			1	

Table 3-9 Solid carbide drill allocation for SLM as built vs solution anneal trials

Test Name	Sample Type	Test Order	Cutting Speed (*Vc*) [m/min]	Feed (*f*) [mm/rev]	Repetitions
SLM: As–Built vs Solution Annealed	As-Built (194.4 J/mm^3)	1	20	0.025	1
		2	60		
		3	100		
		4	140		
	Solution Annealed (194.4 J/mm^3)	1	20	0.025	1
		2	60		
		3	100		
		4	140		

3.9.3 Dynamometer

The torque and the thrust forces of the drill-tests were measured using a Kistler 9272 4 component dynamometer shown in Fig. 3-34. The load cell unit is connected to a Kistler 5070A charge amplifier (Kistler Instruments AG, CH) shown in Fig. 3-34-(b), via the specified cable. The recordings of torque (Mz), thrust force (Fz) and side forces (Fx & Fy) were taken on a computer using Dynoware software at a sampling rate of 1000 Hz and exported as .csv files for analysis. Samples were held on the dynamometer by a jig, designed and fabricated for the purpose, as shown in Fig. 3-34-(a). A 25.2X25.2 mm opening holds the sample, which is then clamped via two M6 cap screws. Cutting force readings from the dynamometer were validated in two stages, first by adding consecutive masses atop the dynamometer and verifying the Fz component and second by correlating the results with reported data for known cutting conditions. For the latter, the machining parameters were selected from the work by Chen *et al.*, drilling of 304 stainless steel with coated high speed steel (HSS) drills [179]. Using the same material in a 25X25X30 mm block, holes were drilled 15 mm deep with a comparable 10 mm TiN coated HSS drill at two boundary conditions; Vc = 4.9 m/min, f = 0.21 mm/rev and Vc = 3.7m/min, f = 0.12mm/rev. Torque (Mz) reading were within 50 Ncm of the reported results for the same conditions.

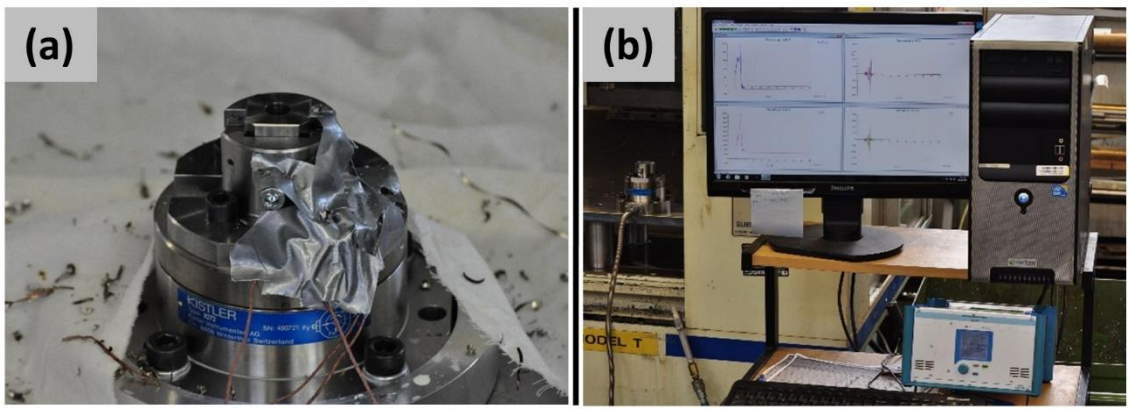

Fig. 3-34 Kistler drill dynamometer setup; (a) Dynamometer, (b) Charge Amplifier

3.9.4 Temperature measurement

Temperature measurements during drilling were undertaken by means of 0.25mm wire glass insulated E-Type thermocouples (OMEGA Engineering Inc, US) embedded into the

block at the four locations noted in Fig. 3-32 above. Thermocouples were affixed to the block with a duct tape. A Measurement Computing USB-2416 (Measurement Computing Co., US) data logger shown in Fig. 3-35 was connected to the thermocouples to record the temperature results on a computer using DAQami software at a sampling rate of 3750 Hz. Result files were exported as .csv files for further analysis.

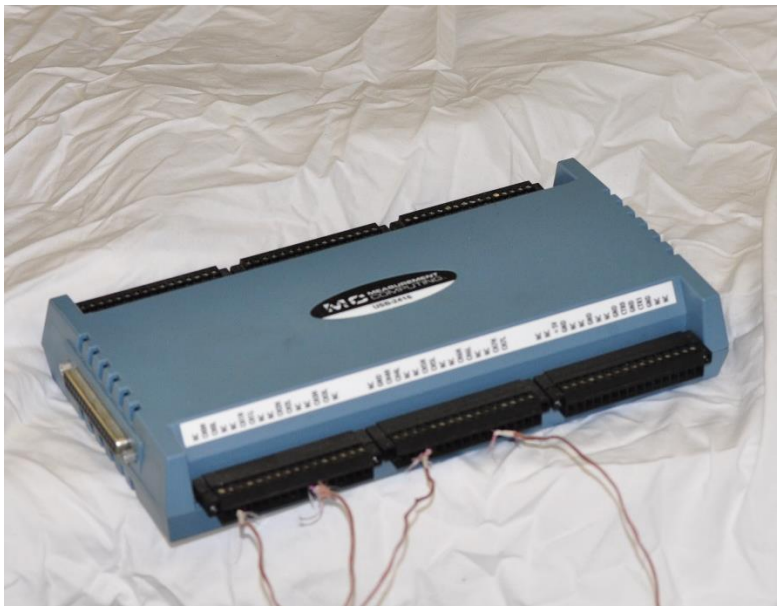

Fig. 3-35 Thermocouple data logger

3.9.5 Insert analysis

Images of the principal cutting edges of the tools were taken after each cutting trial, in order to keep track of the condition of the tool. With the insert-type drills, the insert is removed from the drill body, after each cutting trial. It is then held on a glass slide by putty and images are taken on Olympus SZX9 (Olympus Co., JP) stereo microscope shown in Fig. 3-36 at 6.3, 10, and 20X magnification. Images of the Iscar ICM 100 inserts used in the machining trials leading to the Wrought vs SLM sample responses are taken at the flank face, cutting edge, and the chisel edge. However, images are solely taken at the cutting edge of Sandvik solid carbide drills used in machining experiments conducted to establish the relative responses of SLM as built and solution annealed samples.

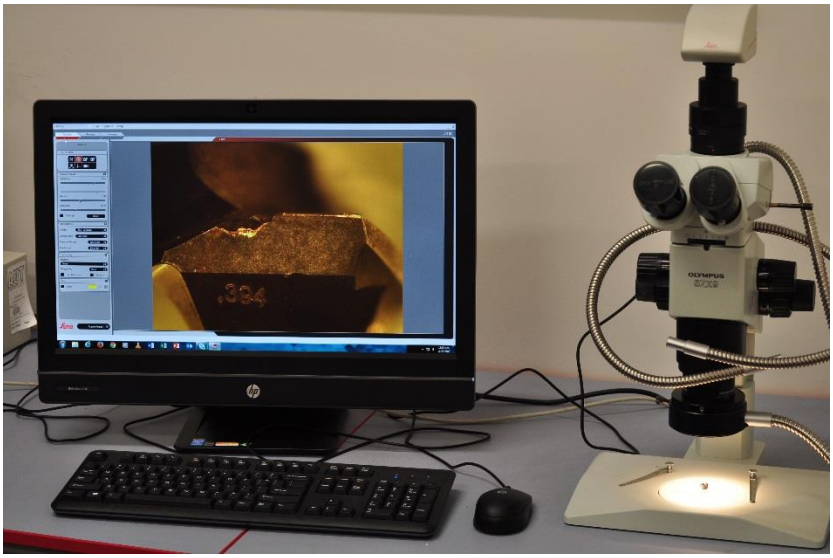

Fig. 3-36 Olympus SZX9 stereo microscope

3.10 Solution Annealing Heat Treatment conditions

Solution annealing heat treatment was applied to restore the equilibrium microstructure within the laser melted duplex stainless steel samples. This was done by Heat Treatments Ltd in a Abar Ipsen HR-50 (Ipsen Inc., US) vacuum furnace (Fig. 3-37), with conditions selected to exceed the critical cooling rate reported by Calliari *et al.*, at 0.8-0.9 °C/s in order to prevent formation of the deleterious precipitates [180]. The SLM samples reported in Chapter 4 were removed from the substrate and subjected to a heat treatment cycle at Heat Treatments Ltd., consisting of heating to 1040 °C for 1 hour prior to continuous cooling at a rate of 1.8 °C/s. This heat treatment cycle was formed from the solution annealing heat treatment at 1050 °C and cooling at 2 °C/s conducted by Sathirachinda *et al.* [181].

Considering the bigger sample size and the larger internal stresses, samples used for both the tensile and drilling tests reported in Chapters 5 and 7 respectively, were solution annealed at a slightly higher temperature and with the samples attached to the build substrate. The long and slender specimens would undergo deformation and warping, if heat treated after removal from the base plate. For large scale SAF 2507 weldments, Bockelmann *et al.* conducted solution annealing heat treatments at 1000, 1050, and 1150

°C with the latter resulting in less α-ferrite after solution annealing [182]. Using this as the basis, the tensile testing and drilling samples were heat treated at 1150 °C for 30 min, prior to a high pressure nitrogen quench. The furnace settings as used by Heat Treatments Ltd, New Zealand for the annealing of the current samples are presented in the temperature vs time graphs presented in Fig. 3-38-(a) and (b), where Fig. 3-38-(b) is an enlargement of a portion of Fig. 3-38-(a). The cooling rate as calculated off the purple trace in Fig. 3-38-(a) and comes out to be around 1.72 °C/s, with a 5 °C/s cooling rate over the first 500 °C as shown in (b).

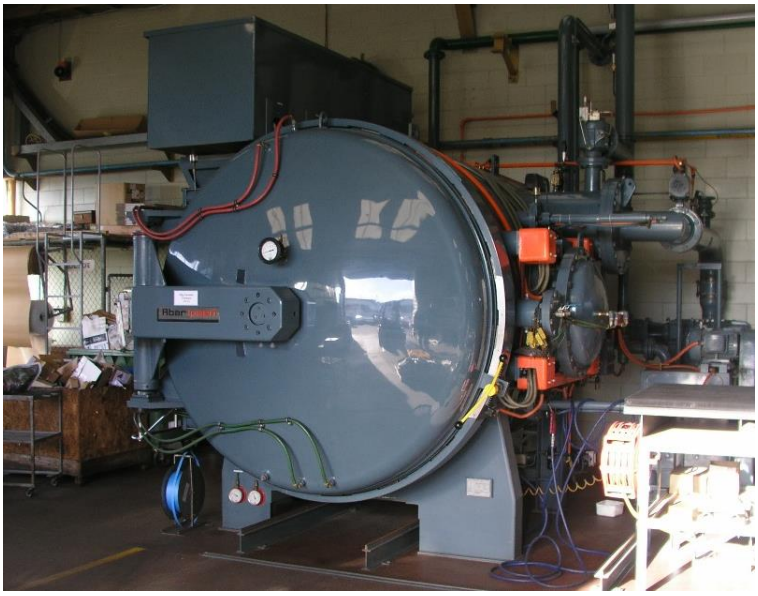

Fig. 3-37 Abar Ipsen HR-50 vacuum furnace

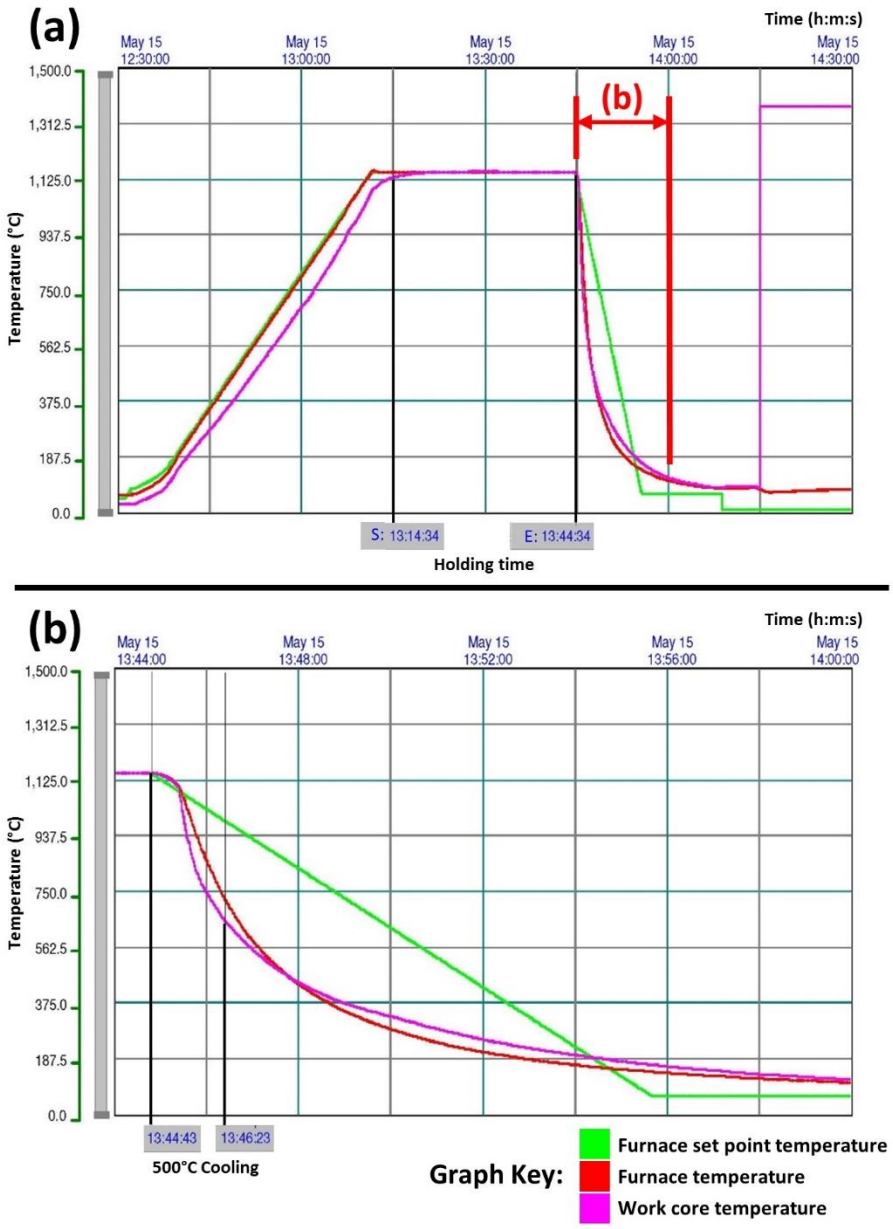

Fig. 3-38 Solution annealing heat treatment cycle - (a), First 500°C cooling - (b)

3.11 Summary of methodology

This chapter elucidated the experimental plans and conditions to be implemented in the two different stages, as per the overall scheme of implementation designed to achieve answers to the research questions raised in Chapter 2. The Renishaw AM250 laser melting system was at the heart of all the powder consolidation trials. Varying laser power and speed settings together with build orientations and scan strategies were identified for

experimental sample printing at different stages. The instrumentation and the methodologies to be used for characterising the printed samples for different responses as necessary are identified and discussed. Considering the widely varying nature of the experimental characterisation methods employed, it became a little difficult to go in depth with all the process conditions used. So, some of the data pertaining to the actual process conditions is deferred to be included within the actual contexts, in the chapters that will follow. The preliminary trials designed to prove that duplex stainless steels for laser melting are the first step towards the implementation of Stage 1 of these experimental plans, and will be the topic for the next chapter.

Chapter 4
Preliminary experiments

4.1 Evaluation of a new material for selective laser melting

Selective laser melting is based on the point-by-point and line-by-line consolidation of metal powders, based on the continuously moving point heat source. The layer-by-layer addition of powder metal and the dynamic thermal fields lend to complex consolidation mechanisms and mechanics. When a new metal system is evaluated for the first time and in the absence of any *a priori* data, the identification of the initial levels of the critical process parameters becomes quite tricky. In most cases, there is only a very narrow working window, if any, that may allow the metal powder to be consolidated to the expected quality levels through laser melting. As was the case with other researchers, this task has been carried in the current work with duplex stainless steels, considering the laser melting of single layer samples first.

4.2 Single layer samples

The process window of any new metal for SLM is generally established by analysing the samples produced with varying process conditions such as laser power and scan speeds, as explained by Attar *et al.* while evaluating commercially pure Ti, considering the influence of varying laser power on the porosity [183]. The initial trials in this study were used to establish the powder consolidation mechanics, and hence, an array of rectangular samples of single layers were consolidated atop a 2 mm thick duplex stainless steel powder base, preventing the interaction of the laser with the substrate. This interaction was further complicated by the machine requiring a return of the powder wiper to the home position after each layer which lead to damage of the fragile sample in initial trials, prior to the application of an emergency stop after consolidation. The sample design, layout, and scan strategy were comparable to Hao *et al.*'s single layer trials on the 316L

stainless steel-hydroxyapatite composite [168] and are shown in Fig. 4-1 with corresponding laser powers. The single layer samples were of 30X15 mm size, laser energy density was varied between 14.1-113 J/mm^3 in 7.1 J/mm^3 increments and scan speed set to 590 mm/s with a linear scan strategy.

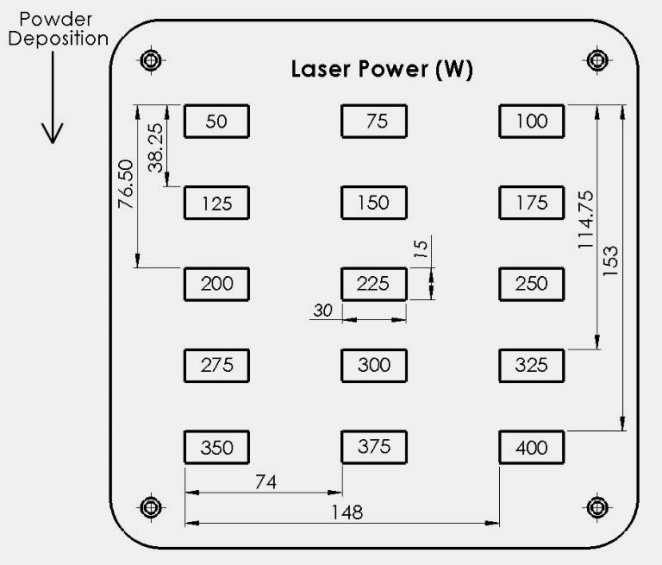

Fig. 4-1 Single layer trials build layout (dimensions in mm)

Considering the above difficulties, only a few single layer samples could be built with some success. As the energy density levels varied, the single layer samples suffered due to balling and other associated problems. Four of the relatively successful samples are presented in Fig. 4-2. Evidently, the relatively successful sintering trials clearly demonstrate sufficient fusion and inter-particle and inter-strand coalescence and possible formation of a solid layer. However, the role of laser power is quite significant and in general, reasonable results were obtained with laser energy density settings above 28.2 J/mm^3.

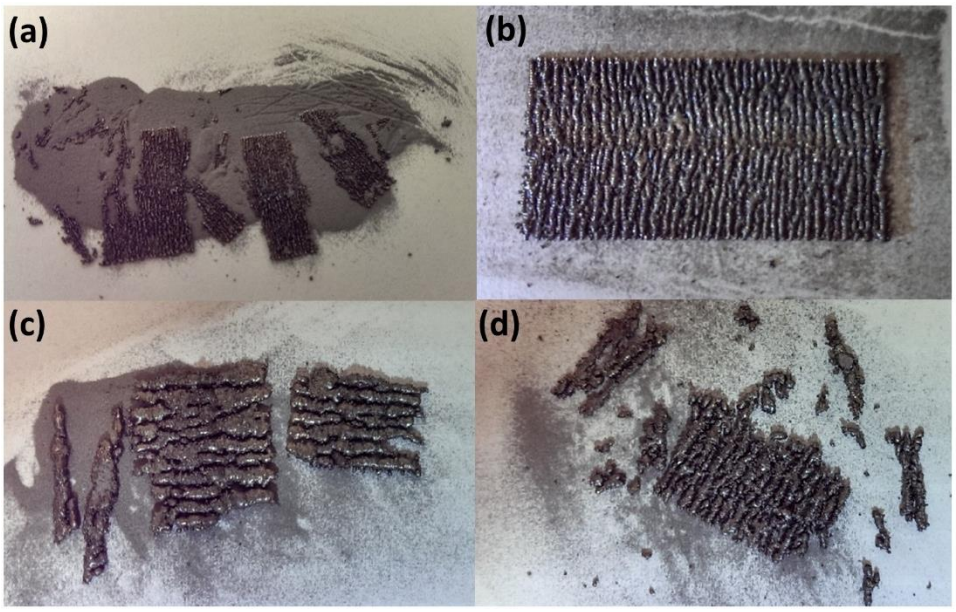

Fig. 4-2 Single layer laser melted duplex samples. (a) 28.2 J/mm^3: (b) 56.5 J/mm^3; (c) 84.7 J/mm^3; (d) 113 J/mm^3 laser energy density samples

Melt track dilation is observed with increasing laser power, as a result of the widening heat affected zone and the reduction of the melt tract viscosity, yielding further consolidation of the surrounding powder particles as was also noted by Yadroitsev *et al.* [184]. Single layer samples without direct contact to a solid substrate show unique melt flow characteristics. The melt tract actually develops perpendicular to the laser scan vector. As noted by Rombouts *et al.* [185] this is the result of overlap between agglomerated particles in adjacent scan tracks. This agglomeration is defined in literature as “balling” and is noted by Kruth *et al.* [186] to be influenced by insufficient wetting of the powder atop the underlying substrate as a result of the surface tension effects of the melt. Surface energy reduction resulting from surface tension effects including Plateau-Raleigh instability was observed by Yadroitsev *et al.* [187] with excessive laser scan speeds. This leads to insufficient time for consolidation with surrounding particles. Similar observations were also noted by Hao *et al.* [168] during the single layer laser melting of a 316L-Hydroxiapatite composite. Considering that the mechanism of consolidation changes altogether with multilayer laser melting, the information generated from these initial trials is only useful to establish the actual range of laser power to work with for the multi-layer laser melting of duplex stainless steels as discussed next.

4.3 Multilayer cubic samples

Based on the data collected from the single layer samples, the most favourable range of the laser energy density could be identified to establish the material's response to multi-layer laser melting as the next step. Samples were built directly atop the substrate with a 10X10 mm profile and a height of 8mm, comparable to the samples produced by Spierings *et al.* in 17-4 PH stainless steel [188]. Samples are produced with the laser energy density varied between 49.4-113 J/mm^3 at increments of 7.1 J/mm^3. As in the case of the single layer trials, a constant scan speed was applied at 590mm/s with laser power varying from 175-400 W. The experimental conditions are listed in Table 4-1 below, with the locations named as per the conventions defined in Section 3.1.4. Also, a linear scan strategy is employed with a scan line spacing of 120 µm and powder layer thickness of 50 µm as explained in Section 3.1.

Table 4-1 Multilayer cubic sample build parameter layout

Parameter	***Row***	***Column***			
		Parameter			
		Laser Power (W)			
		A	**B**	**C**	**D**
Laser Power (W)	**1**	175	300	175	300
	2	200	325	200	325
	3	225	350	225	350
	4	250	375	250	375
	5	275	400	275	400

It may be noted that the two sets of samples shown in Fig. 4-3 are exact replicas and the samples in the second column of each set made with higher laser energy density settings in the range 84.7-113 J/mm^3 showed visible signs of decolouration. This is similar to the top surface decolourisation observed and reported by Louvis *et al.* [189] in the laser melting of aluminium 6061. The cause of the discolouration was attributed to oxidation, as oxygen could not be removed completely from the build chamber. In the current case, the oxygen level in the chamber is reduced to 0.5% and may have caused the colour change.

A similar discolouration to that observed in the 84.7-113 J/mm^3 samples was witnessed in the 50 and 60kHz pulsed wave and continuous wave samples of 316L stainless steel produced by Morgan *et al.* [190]. The uneven top surface observed in Fig. 4-4 was noted to be due to the non-uniform distribution of energy in each of the laser scan tracks by Su and Yang [191]. The overlapping of tracks directly atop each other results in the energy accumulation in each track centreline, ultimately resulting in the over melted topology observed on the top face. The vertical projection clearly visible at the centre of the side face of the specimen shown in Fig. 4-4 is the result of the scan strategy, in which each layer is scanned in two halves, resulting in a double scanning at the centre line and accumulation of excess melted powder.

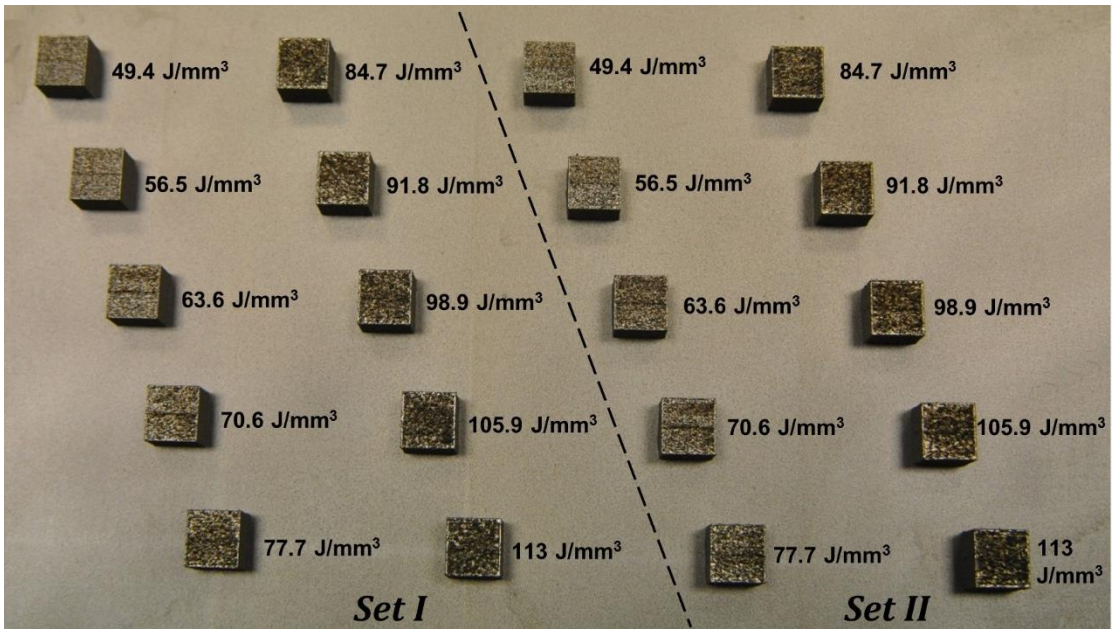

Fig. 4-3 Multi-layer test pieces on the substrate plate and laser energy density settings

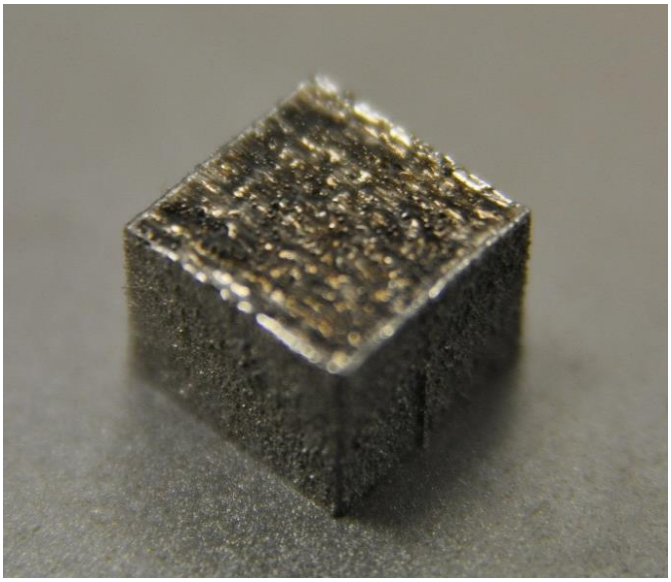

Fig. 4-4 113 J/mm^3 sample showing discolouration of top surface and sintered powder line on LHS wall

4.3.1 Dimensional stability

The application potential of SLM produced items is directly related to the dimensional accuracy possible to be achieved from the near net shape manufacturing process. Fundamentally, the dimensional inaccuracy is attributed to the melt characteristics of the metal and process parameters. Yadroitsev *et al.* [184] deduced that increasing laser power results in an enlargement of the melt volume and reduction in the melt viscosity. These phenomena result in the widening of the laser melt tract, causing dimensional instabilities. Despite SLM being a near net shape process, literature on dimensional accuracy of 3D forms is limited. Ilčík *et al.* [192] produced test parts for evaluating the process capabilities in terms of geometrical accuracies achieved. They also noted an increase in diameters of cylindrical test pieces with increasing laser power across all five possible laser scan speeds.

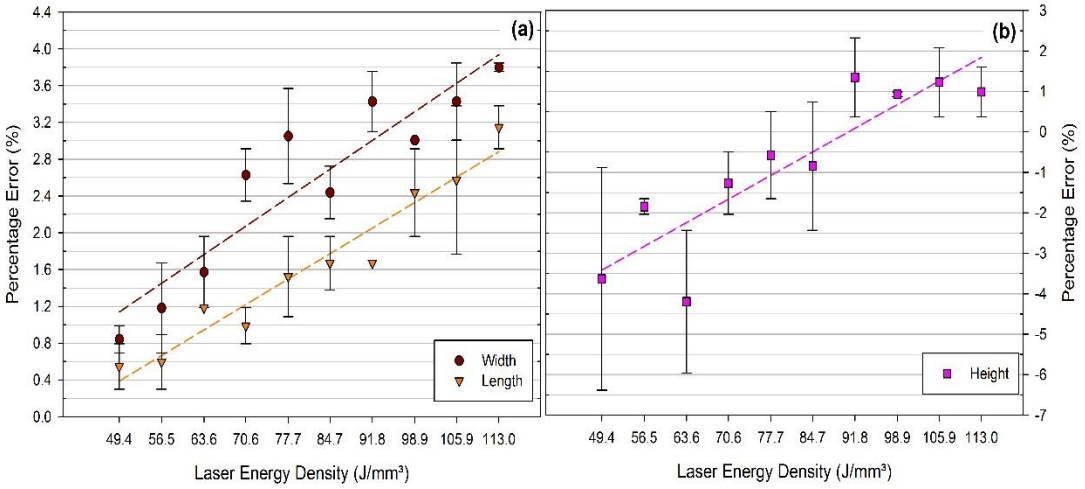

Fig. 4-5 Percentage error in; (a) width and length, (b) height with increasing laser energy density;

The percent dimensional error results plotted against laser power as shown in Fig. 4-5 are similar to those reported by Yadroitsev *et al.* [184] and Ilčík *et al.* [192]. However, the percent dimensional error of the height measurement is the more predominant one. While the percent height error is negative between 49.4 and 84.7 J/mm^3, it is positive, though to a lesser extent, at above 84.7 J/mm^3, which is mainly caused by a concave shaped meniscus observed at the top of these parts. The negative error along the z-direction is understandable, considering increased viscosity of the melt pool, widening of the tracts and layers and consequent loss of the height. Both length (parallel to the scan direction) and width (across the scan direction) increased almost linearly with increasing power. However, the percent error in the length is more pronounced due to the alignment with the laser scan tracts. As the laser scan direction changes at the end of each stroke, a slight dwell period arises, resulting in possible semi-melted powder pickup and elongation of the track length.

4.3.2 Metallographic observations

Considering the severely distorted metallographic structures resulting from the thermal variations of the laser melting process, etching and metallographic imaging of the samples proved to be challenging. After a few trials, the electrolytic etching as already mentioned in the methodology section (Section 3.5.3) was found to be effective and had been applied to evaluate the metallographic responses of all laser melted duplex stainless steel samples.

The photomicrographs obtained of the cross sections of the cubic samples shown in Fig. 4-3 are presented in the same sequence in Fig. 4-6-(a) to (i), corresponding to increasing laser energy densities from 49.4 W to 113 J/mm^3 respectively, in steps of 7.1 J/mm^3.

Thermal distortions caused due to laser melting are clearly evident as the dual phase duplex structure is transformed into a predominantly ferritic (α) microstructure (light areas) with austenite (γ) interspersion as the grey or dark lines and speckles. While laser welding 2205 duplex stainless steels, it was ascertained by Yang *et al.* [14] that high cooling rates result in an average ferrite content of 93%, with austenite forming primarily along grain boundaries and secondarily as Widmanstätten plates and intra-granular dispersions. Photomicrographs of all samples presented in Fig. 4-6, demonstrate austenite precipitation from ferrite either at the grain boundaries or as Widmanstätten needle colonies. Grain boundary austenite is primarily columnar with orientation in the direction of the build (Z height) resulting from the heat loss to the substrate and the freshly deposited powder layer. However, there is very little evidence of intra-granular precipitation of austenite in the multilayer samples developed as part of these preliminary studies.

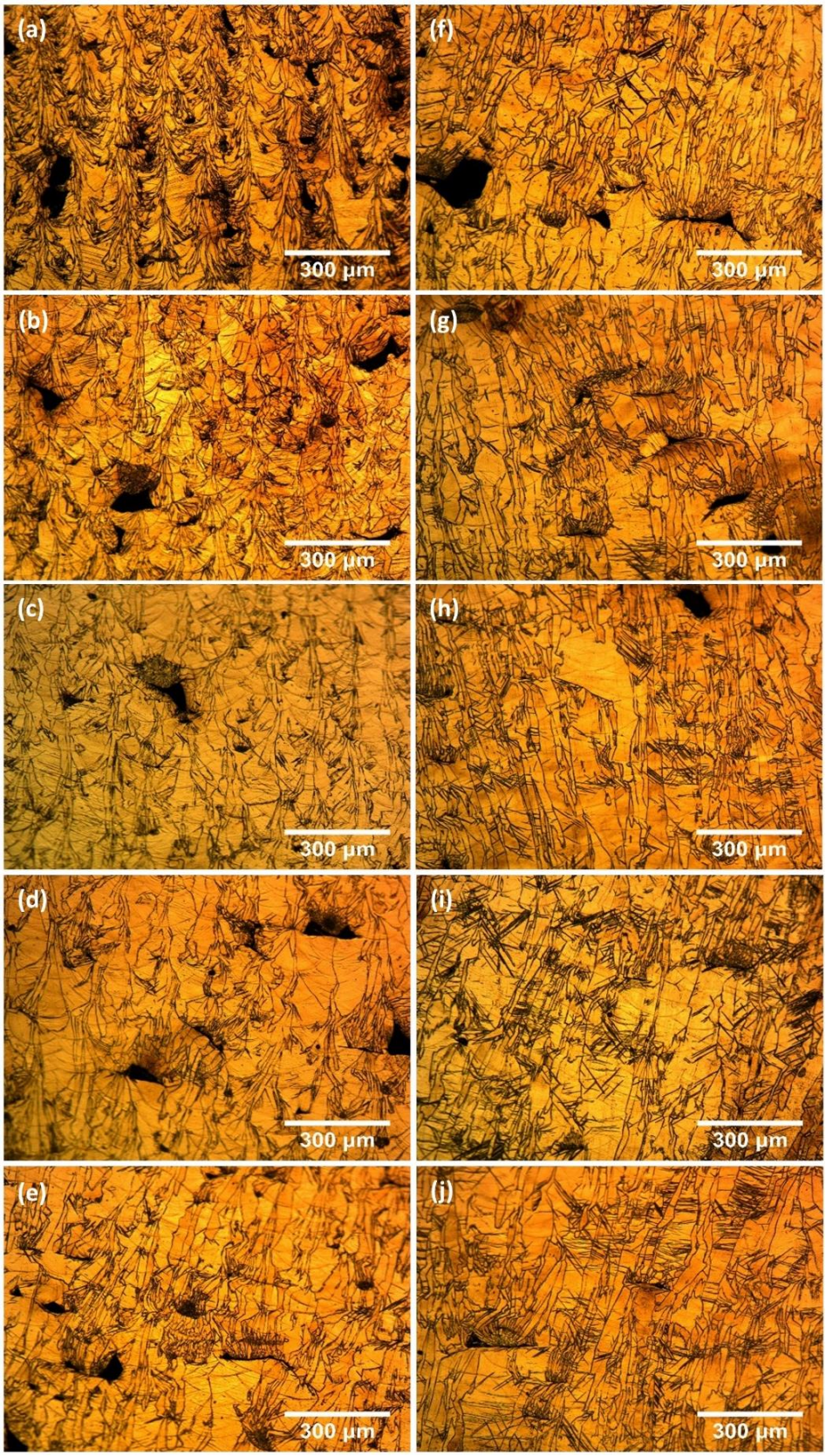

Fig. 4-6 Photomicrographs of cross sections of multi-layer samples in order of build position. (a)-(e), 49.4-77.7 J/mm^3; (f)-(j), 84.7-113 J/mm^3

A closer look at the photomicrographs of Fig. 4-6 reveals that the inter-strand and inter-layer fusion and subsequent homogenisation increases with increasing laser power at the given scan speed. The dark areas are indicative of the formation of internal pores and discontinuities. At lower energy densities, pores are probably formed due to insufficient mixing of consecutive fusion zones resulting from a lack of internal energy. Fig. 4-6-(a) is a clear example, in which, solid growth in vertical columns is achieved to some extent, while inter-strand discontinuities are clearly evident, leaving almost vertically aligned porous holes. This tendency is eliminated at higher energy densities as the porosity is more randomly distributed. Also, the number of cavities decreased at laser energy densities of 105.9 and 113 J/mm^3 respectively, and the shape of the occasional cavity is also reduced to almost a thin line discontinuity.

The random formation of cavities even at relatively higher energy densities is probably due to balling and subsequent localised growth, resulting in an improper filling of the powder metal in successive layers. Liou *et al.* [39] noted that the ferritic structures are further influenced by the low solubility of nitrogen in ferrite at around 0.05%; super-saturation occurs during austenite retardation resulting in the formation of Cr_2N precipitates along grain boundaries. Considering that it is still formative stages in understanding the laser melting responses of duplex stainless steels, evaluation of the possible precipitation of secondary phases is not considered in the current research. However, the formation and growth of the ferrite grains and the austenite precipitation mechanisms and modes are of importance. The precipitation of austenite within the ferrite zones appears to conform to the elongated fusion zones stacked one over the other at relatively lower energy densities such as the ones employed for the cases in the photomicrographs of Fig. 4-6-(a) and (b). However, at higher densities such as the ones used for the photomicrographs in Fig. 4-6-(f) to (j), the fusion zones are more homogenised with more transverse growth of austenite plates across the vertical columnar ferrite grains.

In the case of high power selective laser melting of 316L stainless steel, Niendorf *et al.* [193] noted that higher energy input, larger induced melt pools and low thermal gradients show little variation in both the thermal gradient and the grain growth rate. It is observed

in the current cases that as the power increases, the amount of the grain boundary austenite increases due to reduced cooling rates resulting from the higher energy density. Considering that the major heat transfer mechanism in SLM is conduction and the thermal conductivity of duplex steels being relatively poor, Badrossamay and Childs [194] note the resulting solidified layers to retain the heat and assist in the enlargement of the grains. While similar observations are made from the samples of the current research, it may also be noticed that relatively higher grain boundary austenite growth around pores formed during solidification. This is probably due to a thermal barrier created by the cavity itself, resulting in a poor heat loss and consequent slower cooling rates. Incidentally, the austenite growth is almost in all cases confined to the top surfaces of the cavities which are hot spots, rather than the bottom surfaces, where there is better chance to dissipate and lose heat to the bulk of the layers already formed below. Orientation of this austenite is also predominantly outwards from the pore border with the grain size increasing with distance from the pore.

Dengiz [141] reported around 66 to 85% of ferrite concentration in laser welded samples in different parts of the heat affected zones, while also noting that this volume ratio decreases with increasing heat input. As the heat input is increased, the cooling time increases, resulting in more nitrogen diffusion in ferrite and subsequent growth of austenite predominantly as Widmanstätten plates across the ferrite grains. Similar patterns are observed in all samples evaluated in the current research. A reduction of laser scan speed or an increase in the laser power could lead to prolonged heating at elevated temperatures and consequent slower cooling rates, resulting in greater Widmanstätten austenite formation. Muthupandi *et al.* [195] noted that grain boundary allotriomorphs and Widmanstätten plates are expected to precipitate at high temperatures. While Ohmori *et al.* [15] observed Widmanstätten austenite to form from 700 °C to 1100 °C. At the lower end (800-900 °C), its formation is characterised by decomposition into fragments resulting from the inter-diffusion of alloying elements. As the Widmanstätten plate growth observed in all SLM samples being continuous, it may be inferred that its formation occurs at the upper temperature limits.

4.3.3 Void fraction and density evaluation

Void fraction analysis provides a preliminary insight into the degree of consolidation of samples made form varying process conditions. The percent void fraction values established based on optical photomicrographs are presented against laser power as shown in Fig. 4-7. Overall, it may be observed that the fraction of voids to solid mass decreases as the laser power is increased with an observed minimum of 0.51% at a laser energy density of 113 J/mm^3. These results are in similar lines to the observations made by Gu *et al.* [154] while selective laser melting 17-4 PH stainless steels, showing decreased porosities at higher laser powers. The high experimental variation within each sample results from the sporadic formation of voids within the sample cross section and randomisation of image taking location.

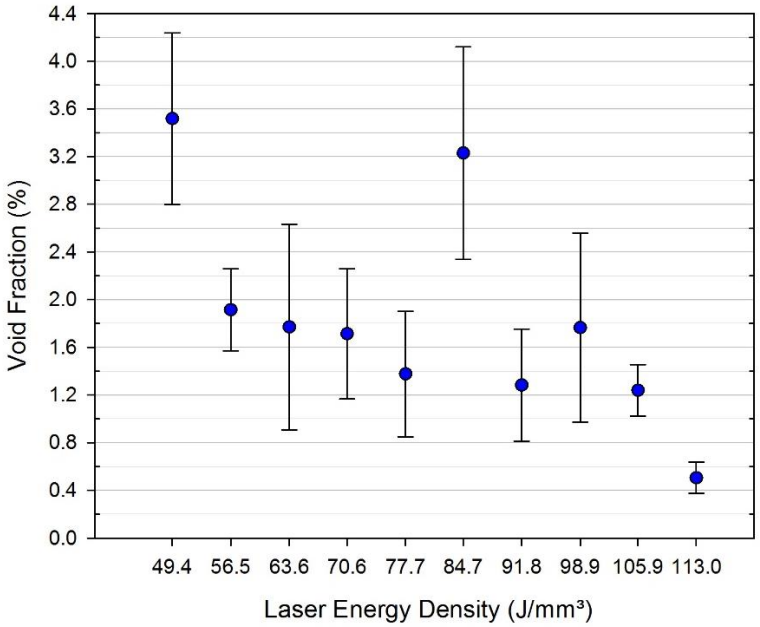

Fig. 4-7 Void fraction vs laser energy density at a fixed scan speed of 590mm/s

Further, the data in Fig. 4-7 also shows a significant irregularity in pore fraction readings of the 49.4 and 84.7 J/mm^3 samples. This is probably due to positioning these samples closest to the direction of sweep of the powder over the build platform and associated problems. Additionally, both the 49.4 and 84.7 J/mm^3 samples and the 63.6 and 98.9 J/mm^3 samples show the greatest deviation from the average, probably due to the flow characteristics of the argon gas in conjunction with the trajectory of the dispelled sparks

from the consolidation of powder particles. Using a similar SLM system, Ferrar *et al.* [153], noted that the argon flow speed was greater along the front of the build chamber and reduced along the back. This is seen to have an adverse effect on part density as there is insufficient argon to remove the condensate vapour which can cause absorption of incident laser radiation or scattering of the laser beam resulting in semi sintered particles on the part surface.

The morphology and sizes of pores formed at varying laser powers are also of interest. It is noted that the pores are aligned in the direction of the build atop each other with irregular morphologies and varying sizes in the 49.4 J/mm^3 sample. Similar observations were also made by Rombouts *et al.* [185] in the laser melting of iron powder. As power is increased it was observed that the pores become more random within the solidified matrix with shape characteristics remnant of the powder particle form as noted in Fig. 4-8. Gu *et al.* [154] noted this irregular pore morphology formation to be a result of insufficient laser power to penetrate the underlying layer and reduction in plasma formation diminishing powder absorptivity. Monroy *et al.* [196] attribute this pore formation to both the powder deposition process and the processing environment. At laser energy densities above 91.8 J/mm^3, small nanoscale pores were observed which occur from gas entrapment during densification [196]. These pores do not affect the density too adversely, as they are smaller in size and less frequent and also have reduced stress levels than irregular shaped pores as Chawla and Deng [197] reported with the sintering of steel powder.

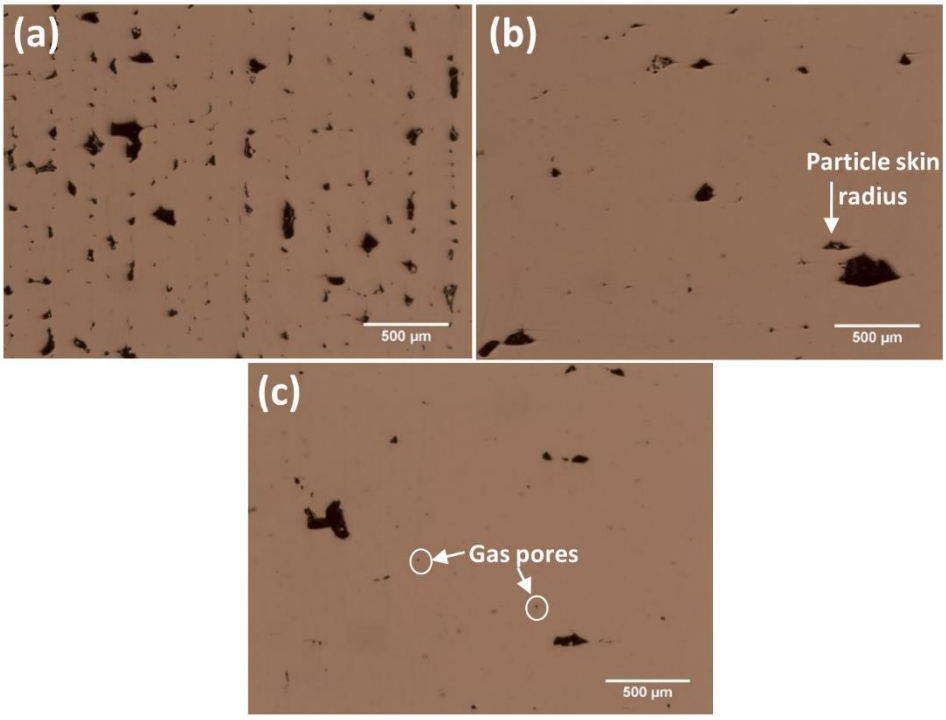

Fig. 4-8 Pore morphology of samples with increasing laser energy density; (a) 49.4 J/mm^3, (b) 77.7 J/mm^3 and (c) 105.9 J/mm^3

The average values of densities obtained with varying power and the spread in each case are presented in Fig. 4-9. Sample density is observed to be contained between a maximum of 90.8% occurring at 70.6 J/mm^3 and minimum of 82.5% occurring at the greatest laser energy density, 113 J/mm^3. A plausible cause of this decrease is the increased formation of gaseous bubbles in the melt pool as detailed by Dai and Gu [198] on the formation and flow movement of gas bubbles within the laser induced melt pool. An increase in the movement of gas bubbles was also reported with increasing laser energy density at 20 kJ/m and above, as caused by the enhanced Marangoni convection flow, resulting in gas entrapment and greater porosity levels. Further, the 113 J/mm^3 sample was located in the further most right of the build and was the last to be consolidated prior to the wiper sweep as detailed in Fig. 4-3. Possible locational effects may have led to the formation of an enlarged pore deep in the sample, not evident in void fraction analysis.

Eliminating a few extreme cases, and comparing the rest of the void fraction and density results, it is interesting to note that while the void fraction appears to be gradually decreasing with increasing power, the density remains ~88.1 %. However, as already noted, void fraction measurements are based on observations from single sections and

should mainly be used to understand variations in pore morphologies, while the bulk density results are truly representative of the process quality. Evidently, certain discrepancies still exist, but the current research clearly established the suitability of duplex stainless steels for processing by SLM ensuring at least 90% dense parts. Based on the significant role of the process parameters observed, further work is necessary evaluating the roles of both laser scan speed and power together with raster orientations in order to fully establish the process capabilities. The most important aspect however is to evaluate the possibility of regaining the equilibrium microstructures by means of a suitable solution annealing treatment, which will be presented in the next section, but the micro-hardness results will be presented before that.

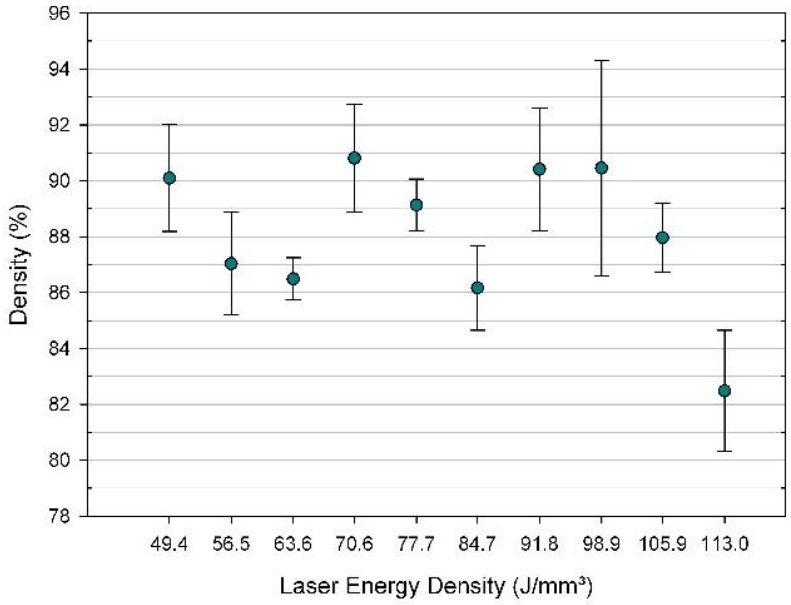

Fig. 4-9 Part density vs laser energy density with the scan speed fixed at 590mm/s

4.3.4 Micro-hardness measurements

The equipment and experimental conditions used for the micro-hardness measurements are presented in Chapter 3, Section 3.6.1, while readings are taken at five locations along the centre-line of the sliced cubic samples. From the test results presented in Fig. 4-10, micro-hardness values may be observed to separate into two LED regions; 49.4-77.7 J/mm^3 and 84.7-113 J/mm^3. At the lower LED range an average micro-hardness of 434.6 HV is observed probably due to the higher ferrite content as evident from micrographs in

Fig. 4-6. Microstructurally, the greater in hardness correlates to the findings presented by Guo *et al.* for 2507 duplex stainless steels, with the understanding that the ferritic phase is on average 0.84 GPa harder than the austenitic phase [199]. Furthermore, higher cooling rates resulting from less consolidation time between adjacent scans tracts likely led to increased thermally distorted small grains, noted by Attar *et al.* to lead to increased hardness [183]. The decrease in micro-hardness values above 84.7 J/mm^3 may be attributed to the increasing austenite contents with increasing laser energy densities as observed from the photomicrographs of Fig. 4-6. However, the micro-hardness values slightly increased at the higher end of the energy density settings, 105.9 and 113 J/mm^3, probably due to the increasing Widmanstätten austenite precipitation in which Nowacki and Łukojć observed to be harder than the ferrite phase [200]. Further, it is possible that precipitate formation could have led to increased hardness values such as chromium nitride precipitation discussed in Section 5.2.6.

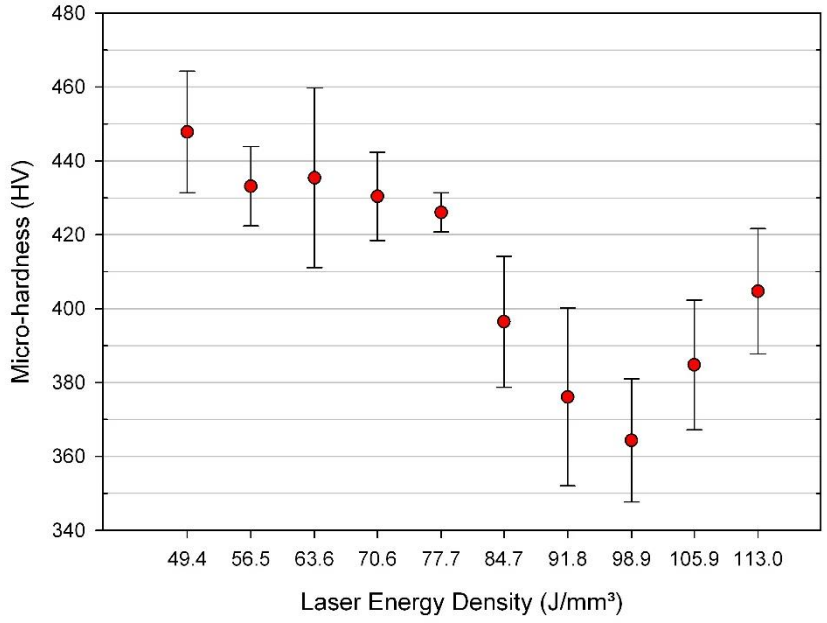

Fig. 4-10 Micro-hardness vs laser energy density with the scan speed fixed at 590mm/s

Comparatively, the average hardness values observed are greater than those reported for the wrought UNS S32750 duplex stainless steel and the GTAW weld root, at 318 and 337 HV respectively [158, 201]. Microstructural observations by Tavares *et al.* ascertained increased hardness values in duplex stainless steels subjected to gas tungsten arc welding (GTAW) as a result of the formation of Cr_2N precipitates [201]. Song *et al.* also observed

an increase in hardness due to the columnar microstructure produced by the SLM process [202]. It is noted that the standard deviation of the results is large for the majority of the samples tested. Song *et al.* also noted similar trends and attributed this to the thermo-mechanical and macroscopic effects including melt pool solidification rates and pore formation characteristics. Further, the surfaces of indentations showed alterations similar to those noted by Song *et al.* and attributed to varying internal stresses caused from the selective laser melting process and the associated thermal loads [202].

4.4 Laser scan speed influence on void fraction

Supplementary to the preliminary multi-layer samples, trials were also conducted at laser scan speeds set above and below the baseline of 590 mm/s at 290, 390 490 and 790 mm/s in order to establish the possible influences on the void fraction densities. Considering a 200 mm/s interval, the lower and upper limits were set at 390 mm/s and 790 mm/s, based on the previously used 590 mm/s as the central value with samples positioned atop the build platform as per Table 4-2. The next build consisting of cubic samples of 10X10X8 mm was done at scan speeds 290 and 490 mm/s, with linear scan strategy and the laser power varied from 175 to 400 W. The results are presented in Fig. 4-11, which show an overall decreasing trend in the void percentage with increasing laser energy density. A strong correlation between the laser scan speed and the percent void fraction is evident in Fig. 4-11, with samples produced at higher scan speeds resulting in greater average void fractions. Teng *et al.* observed similarly increasing percent void fractions with laser scan speed at four laser power settings in the laser melting of a Co-Cr alloy [203].

Table 4-2 Laser scan speed influence on void fraction cubic sample build parameter layout

Parameter	***Row***	***Column***							
		Parameter							
		Scan Speed (mm/s)				*Scan Speed (mm/s)*			
		390		*790*		*290*		*490*	
		A	**B**	**C**	**D**	**A**	**B**	**C**	**D**
Laser Power (W)	**1**	175	300	175	300	175	300	175	300
	2	200	325	200	325	200	325	200	325
	3	225	350	225	350	225	350	225	350
	4	225	375	225	375	225	375	225	375
	5	275	400	275	400	275	400	275	400

The influence of laser scan speed on the percent void fraction is further evident when comparing samples produced at similar laser energy densities, but at different laser scan speeds. Despite similar laser energy densities, the laser scan speed has a controlling influence on the formation of the void fractions, as evident by the decreasing trend in the percent average void fraction levels with decreasing laser scan speed. This is clearly evident from the photographs of the void fractions of Fig. 4-12, based on the samples produced at near identical laser energy densities but varying scan speeds. Evidently, the variation in the percent void fraction with the laser scan speed is quite significant at lower energy densities, below 120 J/mm^3, as the presence of the lack of fusion defects and the un-melted powder particles increased as seen in Fig. 4-12. Teng *et al.*'s made similar findings with the void fraction percent decreasing from 12.5 to 5.5 % when the laser scan speed was reduce from 2087.5 to 1675 mm/s at near comparable laser energy densities, 28.4 and 28.5 J/mm^3 (385 and 310 W) respectively [203]. The morphology of the pores is comparable to the findings in Section 4.3.3 above, with the lack of fusion defects being irregular in shape and randomly distributed in the matrix. Further, the lack of fusion defects as seen in Fig. 4-12-(b) and (c) have distinctive curved borders, signifying insufficiently consolidated melt tracts, as also reported by Gu *et al.* [154].

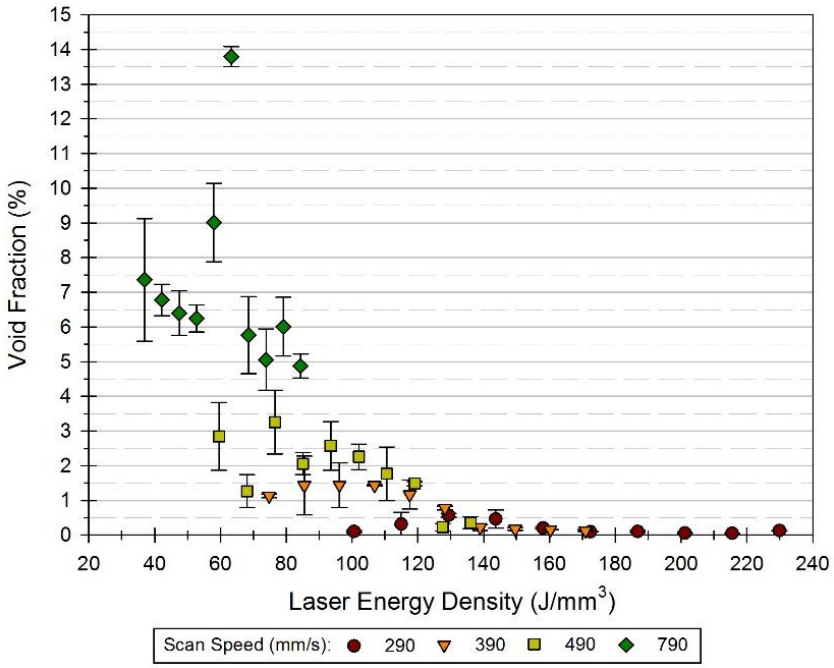

Fig. 4-11 Void fraction for 290, 390, 490 and 790 mm/s

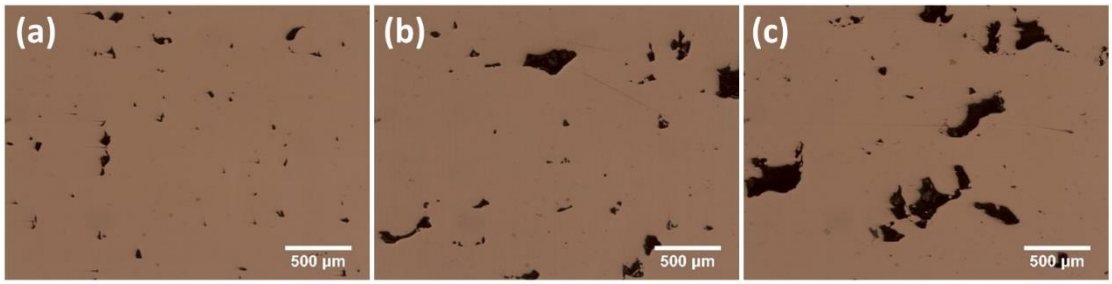

Fig. 4-12 Void fraction variation with scan speed (a) 74.8 J/mm^3 390mm/s, (b) 76.5 J/mm^3 490mm/s and (c) 79.1 J/mm^3 790mm/s

Focusing on the samples produced at 290, 390 and 490 mm/s as presented in Fig. 4-13, a decreasing trend close to a 2nd order polynomial regression curve is evident in the percent void fraction levels. It may be noted that the error bar lines are quite large at lower energy densities, as the error levels are high and also the experimental difficulties are magnified as similarly observed in Fig. 4-7. A close fit with the regression line is observed though, above 125 J/mm^3, whereby void fractions are below 0.75%, and reaching a minimum of 0.053% at 215.5 J/mm^3 and 290 mm/s as observed in the inset in Fig. 4-13-(c). Additionally, above 125 J/mm^3, the standard deviation of the samples is narrowed considerably due to the improved consolidation and the reduction in the lack of fusion defects. Void fractions at laser energy densities above 150 J/mm^3 lie between 0.053 and 0.20 % with an average of 0.12 %, signifying the maximum consolidation of the powder.

Small circular voids in the form of black dots are evident in Fig. 4-13-(c) at these conditions, probably due to entrapped gases, as also observed by Monroy *et al.*, in Section 4.3.3 [196]. Formation of these gas pores is reported by Gong *et al.* to result from evaporation of low melting temperature alloys due to the increased heat input, although alternatively Sun *et al.* have suggested pore formation to result from gas contained within the powder from the atomisation process [132, 204]. Substantial reduction in porosity for each scan speed in Fig. 4-13 is observed in samples produced at the five elevated laser energy densities, corresponding to a laser power range of 300-400 W. The increased laser power results in an enlarged scan tract, encompassing a greater volume of powder particles. Yadroitsev *et al.* determined laser power to contribute the greatest to the single scan line geometry, by improving the bonding to the substrate [205].

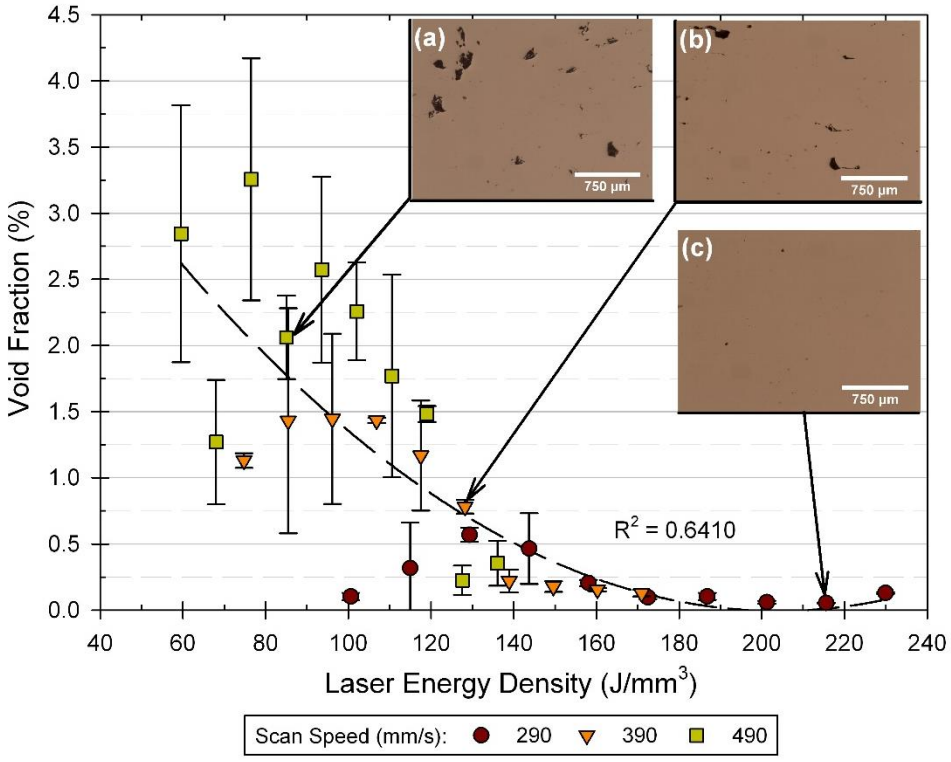

Fig. 4-13 Void fraction of 290-490 mm/s samples with images at; (a) 85 J/mm^3 490mm/s, (b) 128.2 J/mm^3 390mm/s and (c) 215.5 J/mm^3 290mm/s

4.5 Post-process solution annealing

From the results of these preliminary laser melting trials, it is evident that densities above 90% are possible with laser energy densities set at around 91.8 and 98.9 J/mm^3, with the scan speed set at 590 mm/s. It is also obvious that the highly transient thermal variations of the process induce non-equilibrium microstructures. The final step of the process is to try the solution annealing treatment commonly used with welded duplex steels and verify if structural equilibrium can be obtained. For this, Samples for solution annealing treatment were built identical to the preliminary multi-layer samples in profile, however, a 2 mm of support structure was used for easy part removal. As a result, the height was shortened to 8 mm. Laser power settings at 375 and 400 W were used for the samples to be solution annealed, but with the same scan speed and strategy as with the preliminary multi-layer trials. Four repetitions were produced as presented in Table 4-3 however, only one of the four repetitions was studied evaluating the microstructural responses to solution annealing. Solution annealing heat treatment was conducted on the samples after the removal from the substrate, following the procedure as discussed in Section 3.10.

Table 4-3 Post process solution anneal cubic sample build parameter layout

Parameter	***Row***	***Column***			
		Parameter			
		Laser Power (W)			
		A	**B**	**C**	**D**
Laser Power (W)	**1**	375	375	375	375
	2	400	400	400	400

As evident from the photomicrographs of Fig. 4-14 of samples following solution annealing treatment, there is a greater volume of austenite precipitation (light areas) within the ferrite (dark zones) microstructure, mainly as Widmanstätten plates and intra-granular precipitates. Though traces are still evident, grain boundary austenite is significantly reduced and the grain orientation is camouflaged by the Widmanstätten lath growth visibly orientated in the build direction, suggesting growth from the pre-heat treatment Widmanstätten laths. Widmanstätten plate colonies are orientated in the

direction of build with side laths extending outwards and sloping towards the build substrate.

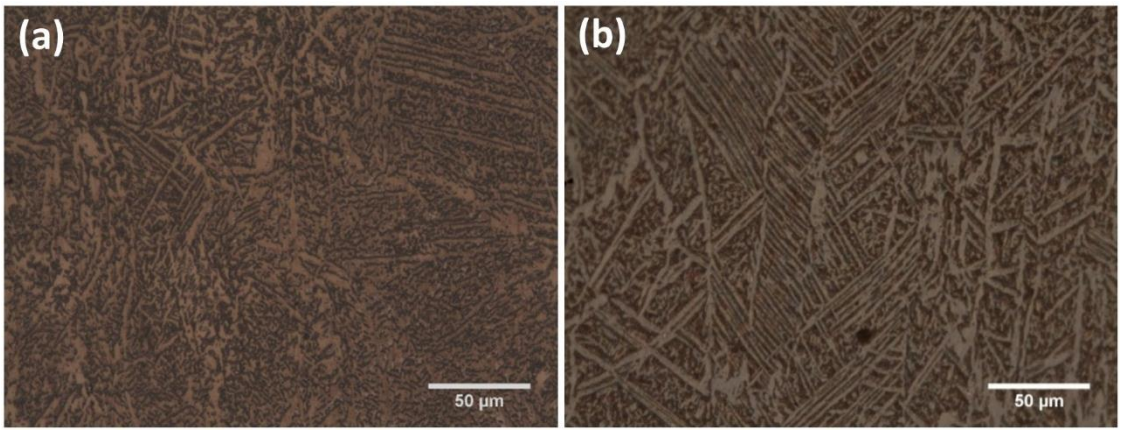

Fig. 4-14 Photomicrographs of solution annealed samples; (a) 105.9 J/mm^3, and (b) 113 J/mm^3

Yang *et al.* [14] noted similar microstructures, based on the post-weld solution annealing of laser welded duplex stainless steel plates. The intragranular austenite formation was found to coarsen with increasing annealing temperature. At a solution annealing temperature of 1040 ˚C, ferrite contents of 59% and 55% were predicted at 1 and 3 min holding times respectively. Comparable results are obtained with the current samples too. Image analyses of both the 105.9 and 113 J/mm^3 samples revealed ferrite percentages of 55.2% and 54.5% respectively. This proves the hypothesis that duplex stainless steels can be processed by selective laser melting with bulk densities reaching above 90% and the dual phase microstructure preserved through a post-process heat treatment. However, process optimisation and characterisation of the mechanical and other attributes require further attention, as will be paid in the subsequent chapters.

4.6 Summary of the preliminary laser melting trials

The physical and microstructural responses of the super duplex stainless steel SAF 2507 to processing by selective laser melting are investigated. Based on the *a priori* data generated from single layer samples, multi-layer cubic samples are developed with

varying laser energy density settings while, keeping the scan speed constant. Dimensional, physical, and metallographic evaluation of the samples led to the general understanding that duplex stainless steels can be processed by selective laser melting, in spite of the severe thermal variations, and the ensuing microstructural variations. A post-process solution annealing process is proved to have reinstated the dual phase microstructures though in varied forms.

Chapter 5
Metallographic and mechanical characterisations

5.1 Roles of process parameters

The preliminary investigations based on the experimental evaluation of the laser melted duplex steel sample allowed to prove the hypothesis that selective laser melting is feasible with these alloy systems. However, the process conditions were kept at relatively simple combinations, as the laser scan speed was maintained the same for most part of the experimental conditions. Now that the material-process combination is identified to be viable, a closer look at the specific roles of the critical process parameters is essential to be undertaken now. Experiments are designed varying the critical process parameters and targeting a deeper understanding of the metallographic changes as well as the characterisation of the mechanical properties. This chapter presents the experiments done to achieve this, the results obtained, and the inferences drawn and it may be noted that the second phase of investigations as presented in the overall research plan begin from here.

5.2 Metallographic evaluation

A deeper investigation into the variations in the microstructural features of laser melted duplex stainless steel powder will be undertaken and reported in this section. In particular, the process-structure relationships will be established through a systematic evaluation of the microstructures of samples laser melted with varying process conditions. Influences of both laser power and scan speed will be considered at different energy density levels in order to establish their influences on the changes in the microstructures.

Based on the porosity results from the second stage multi-layer samples (Section 4.3), the 300-400 W laser power range was identified as the best in terms of achieving better material consolidation. As a result, the samples used for the metallographic studies presented herein were produced at eight different energy density levels, with the laser power varying from 300 to 400 W in 25 W increments. The preliminary laser melting trials also allowed to converge on 112.8 J/mm³ as the best energy density to achieve the lowest void fraction. Considering this as the base energy density, seven other energy density levels were fixed at 91.7, 98.7, 105.8, 119.9, 126.9, 134, and 141 J/mm^3. As the energy density settings vary in this build, the cubic samples of the same dimensions as in the other builds were produced with laser speeds varied as necessary, but using the linear scan strategy. The order of samples is presented in Table 5-1, with sample location and specific naming convention defined in Section 3.1.4.

Table 5-1 Metallographic evaluation cubic sample build parameter layout

Parameter	***Row***	***Column***							
		Parameter							
		Laser Energy Density (J/mm³)					*Laser Energy Density (J/mm³)*		
		91.7	*98.7*	*105.8*	*112.8*		*119.9*	*126.9*	*134*	*141*
		A	**B**	**C**	**D**		**A**	**B**	**C**	**D**
Laser Power (W)	**1**	300	300	300	300		300	300	300	300
	2	325	325	325	325		325	325	325	325
	3	350	350	350	350		350	350	350	350
	4	375	375	375	375		375	375	375	375
	5	400	400	400	400		400	400	400	400

5.2.1 Epitaxial ferrite crystals growth and the precipitation of austenite

Photomicrographs of the polished and etched cross sections of duplex stainless steel samples produced by selective laser melting with varying energy densities are presented in Fig. 5-1. The etchant reacted more with the austenite regions than the ferrite zones, resulting in the dark grain boundary contours and the Widmanstätten laths against the relatively lighter ferrite matrix. Evidently, the microstructure in all the cases is

predominantly ferritic, with a columnar morphology in the direction of the build. Ferritscope tests on selected sample sections showed an average ferrite content of 68.8% and maximum ferrite content of 69.6% in the 98.7 J/mm³ sample at 350W, which is in accordance with the microstructures discussed in the previous chapter.

Austenite precipitated both as the grain boundary contours and the dendritic needle-like Widmanstätten laths. XRD analysis of the sample produced at 300 W and 119.9 J/mm^3 as in Fig. 5-2 showed only ferrite and austenite peaks with the latter weaker than the former, validating the findings of ferrite predominance. The α-ferrite peaks were observed at 2Θ locations of approximately 44.5, 64 and 82°, while ɣ austenite was observed at a 2Θ location of 43.2° as in Fig. 5-2-(b). No intermetallic or nitride phases were evident from the XRD scan, probably due to a low quantity in the sample. The highly elongated and columnar microstructure is evident in the build direction, propagating epitaxially through the fusion zones, as also observed in the literature as due to the continual recrystallisation and heat flow in the Z-direction [206, 207]. The columnar growth in all samples surpasses the fusion zones, resulting in a vertical grain structure elongated across multiple layers. Grain measurements taken randomly from the etched microstructural images yielded an overall mean grain length of 372 μm and width of 35.7 μm. Greatly elongated grains up to around 1200 μm in length and 50 μm width have been observed in the elevated energy density samples at 141 J/mm^3. Grain aspect ratios depicted in Fig. 5-3 show an increase in grain length and a decrease in the width with increasing laser energy density, reaching up to a maximum aspect ratio of 16.2 at 119.9 J/mm³, followed by an increase in average grain width in elevated laser energy density samples. Jia *et al.* noted similar increase in the columnar grain growth due to the increased melt temperature, caused by decreasing melt pool cooling when the scan speed was reduced [206]. Overall, an excess amount of energy is absorbed in the melt pool, increasing the melt pool temperature and enlarging the columnar grains.

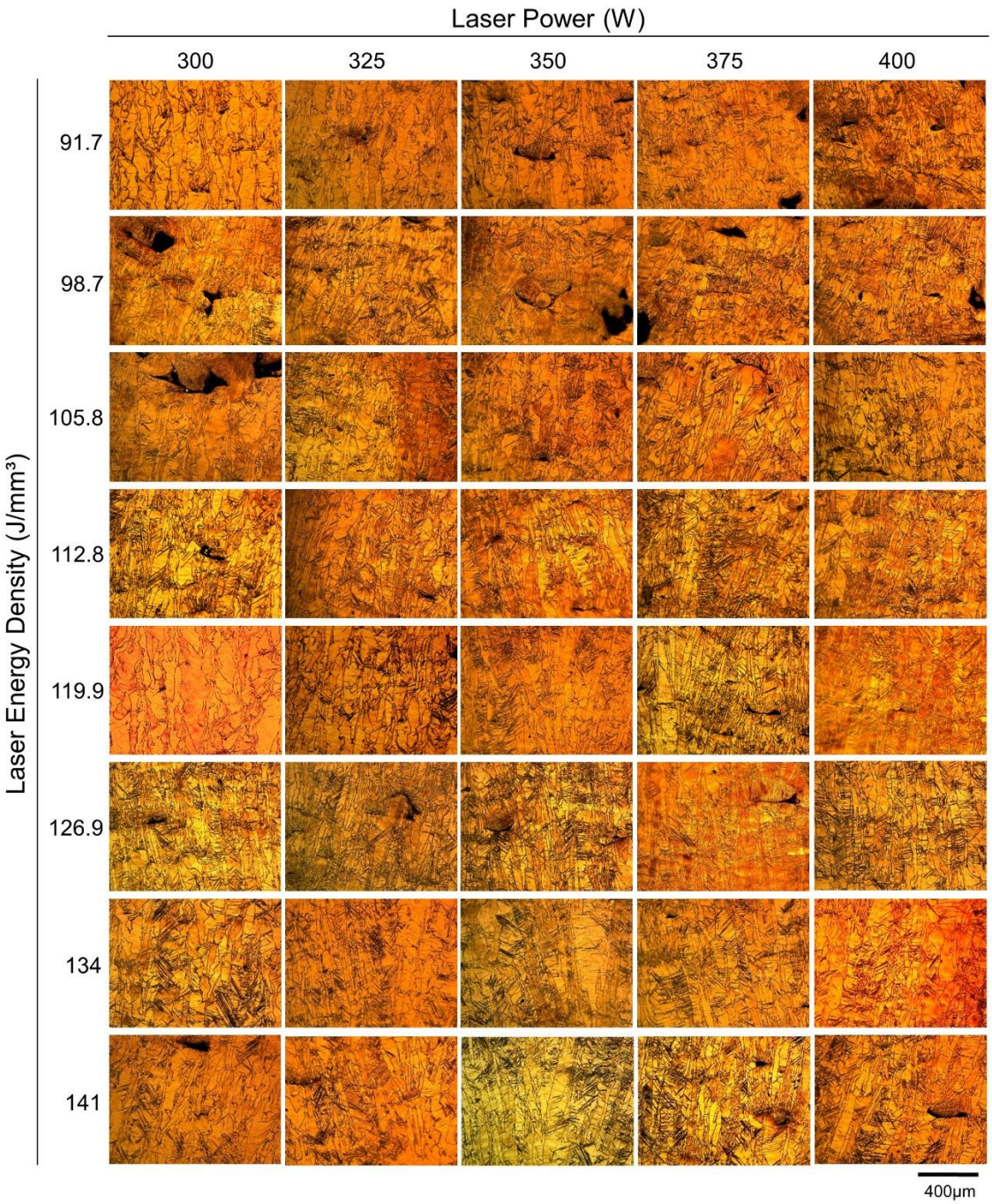

Fig. 5-1 Photomicrographs of the cross sections of laser melted duplex stainless steel samples with varying energy densities

While investigating selective laser melting of Fe-based alloys strengthened by oxide dispersion, Boegelein *et al.*, noted that the elongated columnar grains result in ductile fracture mechanics when loaded in the direction of the grain orientation (Z-direction). Additionally, metallurgical slip was observed at grain boundaries on the fractured surfaces [208]. Anisotropy and randomisation of grain growth were hypothesised by Boegelein *et al.* to be the cause of multi-mechanism fracture modes involving both brittle

and ductile fractures in samples. Similar responses could be attributed to duplex samples developed from the current studies involving selective laser melting, as columnar grains are supported by irregular grain growth due to defect generation. Song *et al.* observed similar ductile fracture mechanisms in Ni20Cr specimens at columnar grain boundaries when specimens are loaded parallel to the direction of the grain growth, though the hardness values were lesser when measured perpendicular to the direction of growth [209]. The length to width grain aspect ratios as shown in Fig. 5-3 may further influence the mechanical responses of the material with the greater length to width ratios of the 119.9 and 126.9 J/mm³ samples probably resulting in greater strength and ductility in specific directions. Niendorf *et al.* noted high aspect ratio grains in 316L stainless steel processed at 1000W leading to a high ductility with an engineering strain in excess of 35% along the direction of the grain orientation [193].

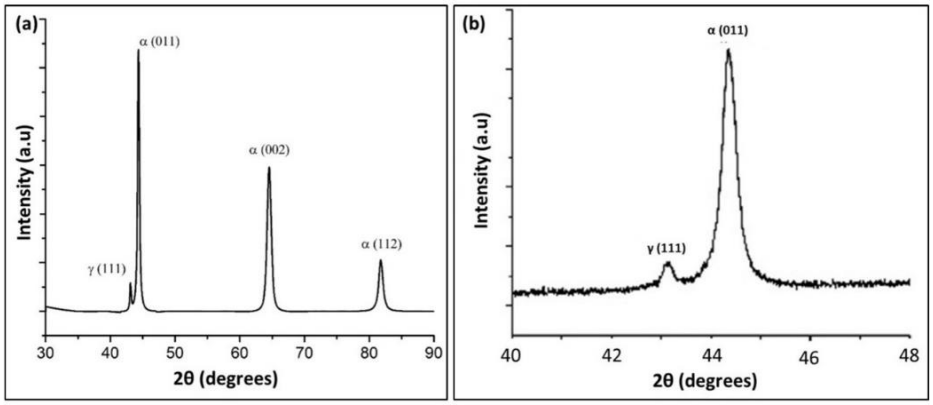

Fig. 5-2 (a) XRD pattern of the sample produced at 300W and 119.9 J/mm^3, (b) XRD pattern obtained from a slow scan in the 2Θ range of 38 to 48°

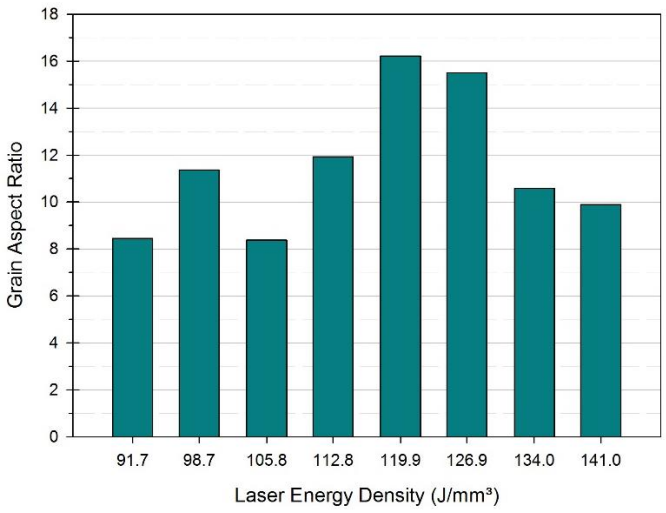

Fig. 5-3 Average grain aspect ratio at corresponding laser energy densities

EBSD orientation maps obtained by indexing ferrite in the microstructure of the 400W and 141 J/mm^3 sample are presented in Fig. 5-4. Evidently, columnar grain growth is seen predominantly in the <001> direction parallel to the direction of build, as was commonly reported with the components made by SLM. While selective laser melting the 316L stainless steel, Niendorf *et al.* observed strongly columnar growth with a <001> predominance, resulting from the thermal gradient (G) and the grain growth rate (R) that are greatly affected by the heat flow in the direction of the build [193]. Zhou *et al.* attribute this growth mechanics to the loosely packed powder layers spreading on active heat sources and yielding the grain growth in the build direction [210]. Re-heating and recrystallisation of the already consolidated substrate prior to laser melting a new layer lead to the highly columnar microstructures in the direction of the build [211]. The relatively less elongated epitaxial grains seen at the top left corner of Fig. 5-4 are also formed from similar conditions, but the sub-surface void probably caused a local break in the continuity of the vertical grains.

Evidently, the grain growth in the laser melting process is directional and greatly influenced by the thermal history along the build direction. These observations are very similar to the microstructures obtained and evaluated by both Song *et al.* and Boegelein *et al.*, indicating a strong anisotropy in the SLM components generated [208, 209]. Thus likely to result in directional mechanical properties, probably leading to a better ductility along the Z-direction and tendencies to undergo brittle fractures in the transverse directions.

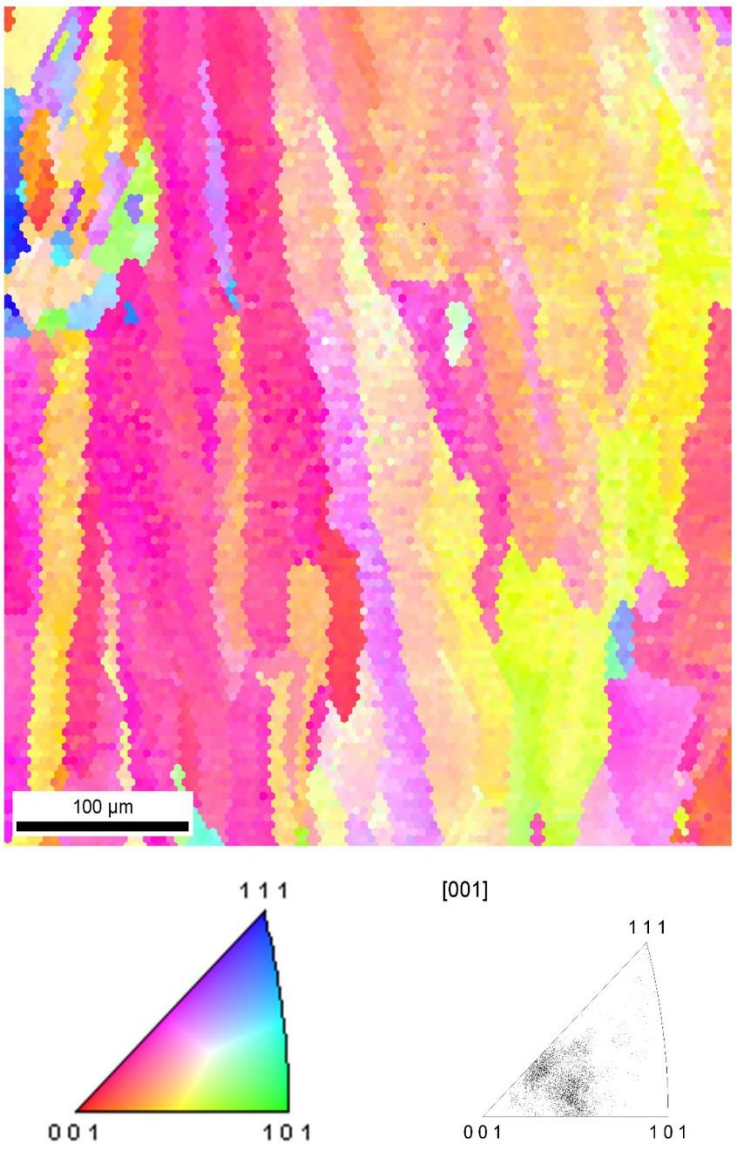

Fig. 5-4 EBSD orientation map and inverse pole figures of the sample produced at 400 W and 141 J/mm^3

5.2.2 Widmanstätten austenite growth

The austenite growth in SLM predominantly follows the Widmanstätten patterns as was clearly evidenced in Chapter 4 as well as from the photomicrographs of Fig. 5-1. Further, Widmanstätten austenite formation may be noted to be greater at laser powers in excess of 325 W for all laser energy densities tested. The Widmanstätten austenite growth is usually associated with higher cooling rates (>10^7 K/s) which are characteristic of SLM, while the grain boundary austenite growth is a function of slow cooling rates [212]. It may be observed from Fig. 5-1 that the number of Widmanstätten austenite colonies also increases with increasing laser energy density. Ohmori *et al.* also observed

Widmanstätten growth to initiate and progress between 973 and 1373 K (700 and 1100 °C) [15]. At higher energy densities and reduced scan speeds, samples are held at relatively elevated temperatures for longer durations, possibly aiding the enhanced formation of the Widmanstätten austenite. Widmanstätten side laths are also observed to propagate downward into the ferrite grains as the side plate colonies from the vertical substructure laths and through the grain boundary austenite.

Formation of Widmanstätten austenite was found to lower the ductility of plasma welded UNS S32760 super duplex stainless steel specimens in an argon shielding environment [213]. Nowacki and Łukojć also observed higher hardness in the secondary austenite precipitated primarily as Widmanstätten laths, over the ferrite grains [200]. This is alleged to be the result of variations in silica contents in the Widmanstätten austenite. Similarly, nickel and chromium content variations in ferrite, primary, and secondary (Widmanstätten lath) austenite were projected as the leading causes of the variability in the corrosion resistance [200]. The Widmanstätten austenite growth observed in most of the specimens produced and investigated currently will probably influence the final mechanical properties in similar lines. However, systematic mechanical testing of standard samples produced to similar conditions should be undertaken to establish the true nature of the process-structure-property relationships.

5.2.3 Location on the build plate

While the microstructure appears to be influenced predominantly by the process conditions, there are also occasional variations observed in samples produced at specific locations on the build plate. An example of this variance is presented in Fig. 5-5 for samples produced at 300 and 325 W and laser energy densities 91.7 and 119.9 J/mm^3 respectively. Widmanstätten lath growth is minimal, and the structure consists primarily of long columnar ferrite grains. The EBSD orientation map for the 300 W and 91.7 J/mm^3 case as presented in Fig. 5-6 shows a greater intensity of grain growth in <101> and <111> directions as against the growth along the <001> direction as obtained at relatively higher laser power settings (Fig. 5-1). Similar observations were also made by Niendorf *et al.* in 316L SLM samples attributing this to the reduced laser energy input into the material [193, 214]. The highly randomised microstructure seen in Fig. 5-6 is likely to

form from a lower laser penetrability, preventing the complete recrystallisation of the solidified grains and the long columnar elongation aspects.

Furthermore, both samples are also placed at the top left hand corner of the build platform and both show a reduction in the fusion pores. This could be due to a greater argon flow along the top corner, resulting in a better removal of the condensate. Ferrar *et al.* also noted that inconsistent argon flow in the build chamber affects the laser melting conditions based on the dual roles of argon; preventing oxide formation on the parts and removing ablation condensate from the laser melting process [153]. It may also be noted that the new Renishaw systems developed solutions addressing these issues and the new laser melting systems are designed to improve the gas flow patterns within the build chamber.

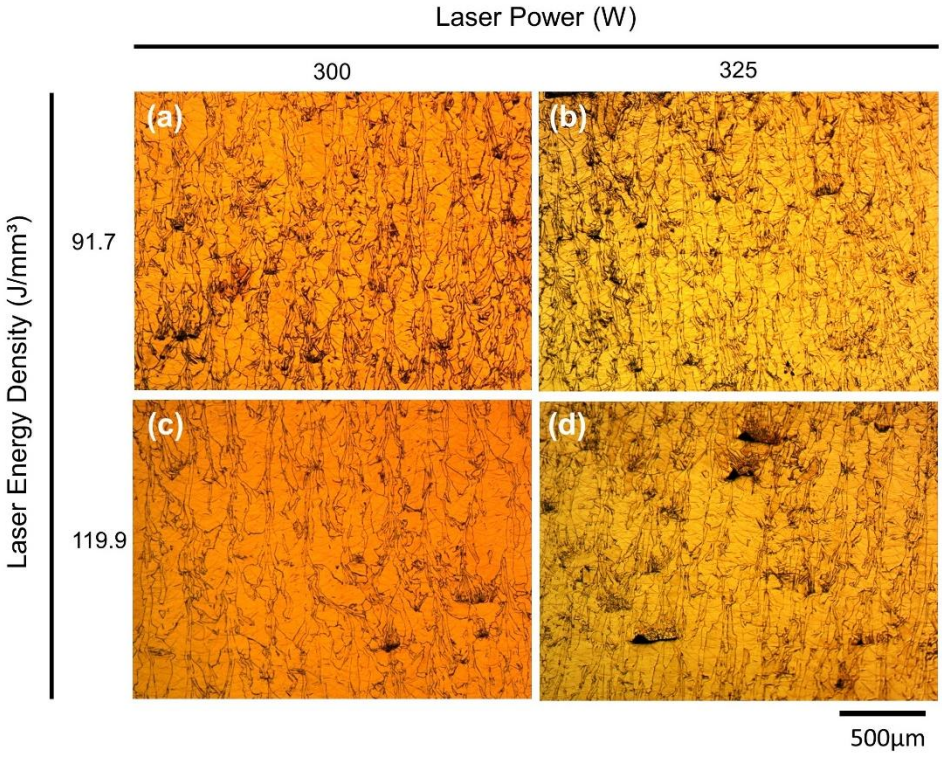

Fig. 5-5 Samples produced with 91.7 and 119.9 J/mm^3 at 300 and 325 W respectively

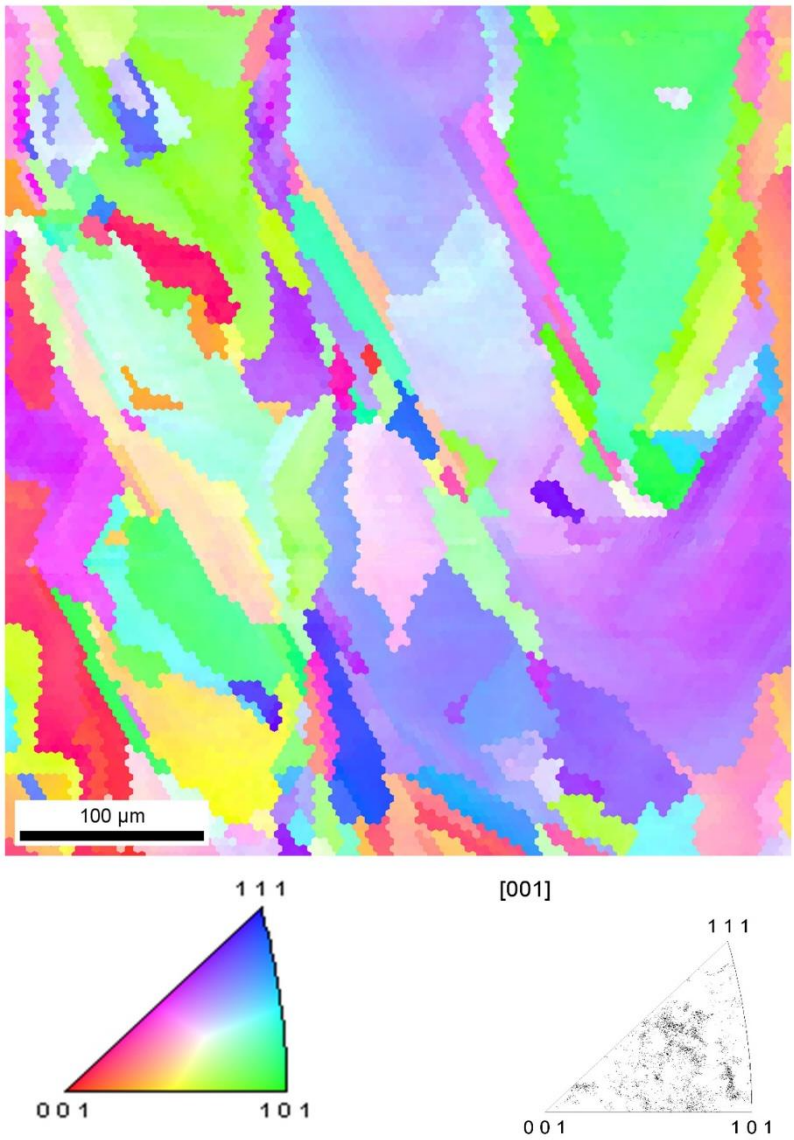

Fig. 5-6 EBSD orientation map and inverse pole figures of the sample produced at 300 W and 91.7 J/mm^3

5.2.4 The role of the scan strategy

A characteristic ferritic grain structure with wide and long columnar grains resulted vertically around the centreline of each specimen, as seen in Fig. 5-7. This enlarged columnar growth is evident in all samples at the central zone, forming a characteristic inverted cone-shaped growth with a 16.5° angle about the central line as a result of the scan strategy employed. The laser scans every section from one end, up to the mid-point and then proceeds from the top to the mid-point. As a result, the central line of each layer gets double laser melted. Widmanstätten austenite growth is reduced in this area due to the increased heat input recrystallising the prior solidified structure, however occasional needle like horizontal laths are observed in the enlarged central grain.

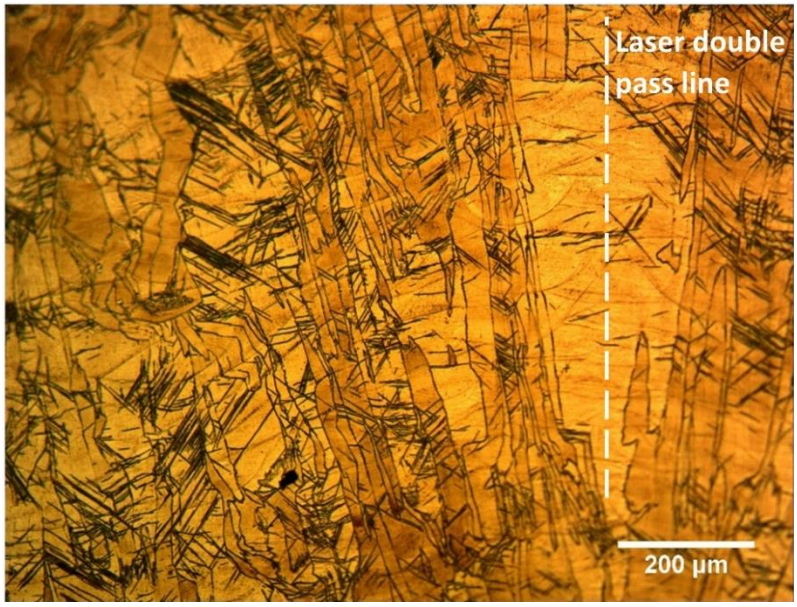

Fig. 5-7 The 350 W sample at 134 J/mm^3 showing widened columnar grain at the double scanned centreline

The contour scan strategy also resulted in large columnar grains around the edges as shown in Fig. 5-8. After the zig-zag laser scanning of the interior of each layer, a final finishing contour scan is done running the laser around the periphery to improve the dimensional quality. This results in a double laser melting at the boundary regions again, leading to the columnar growth of the V- zone at around 7-9° with the vertical as shown in Fig. 5-8-(b). Widmanstätten laths are observed to grow around 250 µm from the edge, though the level of precipitation is reduced in samples at lower laser powers. Recrystallisation occurred due to the contour scan strategy overlapping on the internal

raster scan lines by 40 μm. The large-grain and prominently columnar microstructure around the boundary contour of the samples is indicative of a slower cooling rate relative to the bulk of the material structure. The argon filled powder bed all around the outer surface of each specimen with relatively lesser thermal conductivity provides a local insulation effect [215]. The dark horizontal bands along the edge of the sample represent the layers processed, as was also noted by Kruth *et al.* [216]. The colour change within the region affected by the contour scanning is due probably to over-etching, resulting from the thermal distortion and possible impurity build-up during cooling.

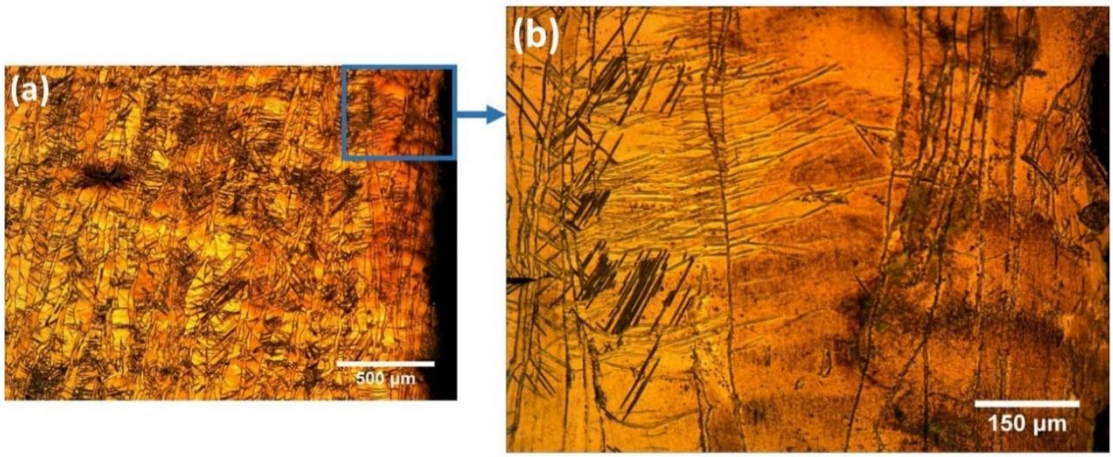

Fig. 5-8 The 400 W sample at 141 J/mm^3 showing columnar grains around the outer contour

In addition, fine Widmanstätten laths are also observed to grow horizontally between the opposite faces of the columnar ferrite grains. Samples produced at 126.9, 134, and 141 J/mm^3 show densely packed Widmanstätten colonies consisting of side laths intersecting one another as shown in Fig. 5-9. Further, the side-lath growth is thicker at the higher energy densities as may be noted from Fig. 5-9 and grow deeper into the ferrite grains. Evidently, Widmanstätten austenite growth is quite directional in nature in the laser melting case, as against the relatively complex growth patterns resulting from the laser welding of duplex stainless steels. Kolenič *et al.* reported very irregular Widmanstätten austenite patterns, predominantly in the horizontal direction when laser welding duplex stainless steels [217]. The repeated heating and cooling cycles during laser scanning, the powder bed with relatively poor thermal conductivity, and the high thermal gradient in the direction of the build are the likely causes resulting in the growth of the Widmanstätten austenite in preferred directions in SLM.

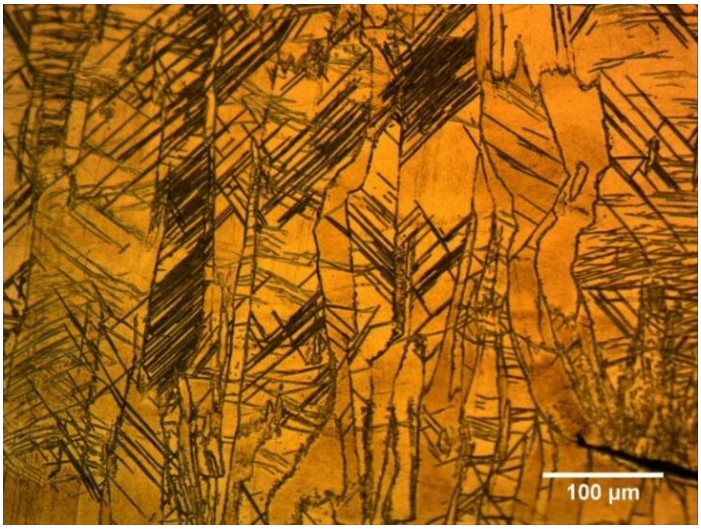

Fig. 5-9 Sample at 141 J/mm^3 and 375 W showing densely packed intersecting Widmanstätten growth

The microstructural variations sensitive to the process conditions will have consequential influences on the mechanical properties. Further, the microstructural variations from the bulk to the centre and then the contour scanning areas might also have significant effects on the fracture mechanics as well as the corrosion characteristics of the laser melted duplex stainless steel materials. The strong columnar grain growth combined with the <001> crystallographic orientation and high ferrite contents are attributes for promoting good magnetic responses as will be explored in Chapter 6.

5.2.5 Fine cellular grain growth

SEM photomicrographs of a couple of samples produced at 300 W and 400 W are presented in Fig. 5-10. Fine cellular grain growth is evident within the ferrite grains from these photomicrographs. At a higher magnification as shown in Fig. 5-11, the ferrite grains are separated by the jagged troughs of the grain boundary austenite, together with the sharply etched recesses of the Widmanstätten austenite. This cellular microstructure was also observed by both Cherry *et al.* and Yasa *et al.* while investigating the selective laser melting of 316L stainless steels, the latter attributing this growth to the rapid solidification of the metal in SLM [130, 218]. A differential cellular growth is also evident in the ferrite regions of Fig. 5-10-(a), as the cellular growth to the right of the grain boundary is equiaxed, while an elongated columnar growth almost at right angles to the grain boundary austenite resulted on the other side. The image in Fig. 5-11 at a higher

magnification also shows similar cellular orientation effects on either side of the grain boundary austenite.

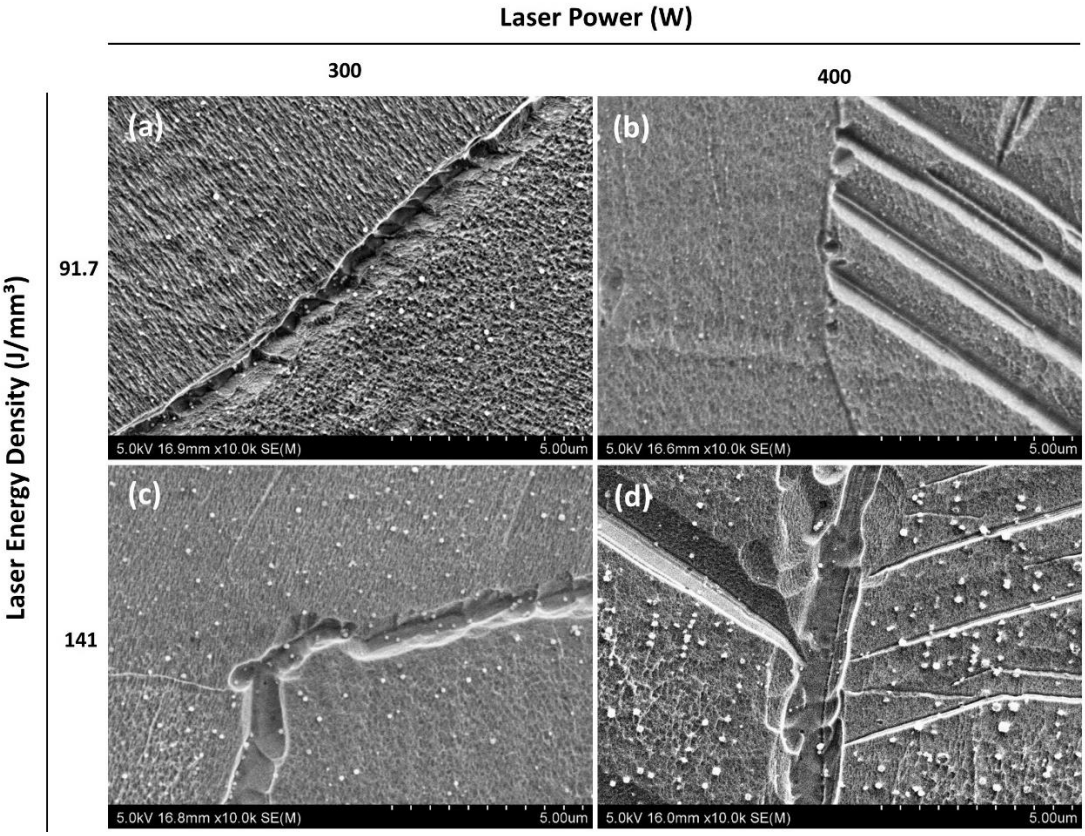

Fig. 5-10 SEM images of 91.7 and 141 J/mm^3 samples at 300 and 400 W

This differential alignment of the cellular growth is most likely representative of the orientation of the crystallographic planes within the adjacent grains. The most possible reason for this variation is the varying direction of motion of the laser in adjacent scan tracks. As the laser follows a zig-zag pattern, moving forward and backward with a side-step at the end of each raster scan line. For example, considering the case in Fig. 5-10-(a), the laser scanning is in opposite directions for the two grains, presumably resulting from two liquid pools. Similar microstructures are also reported by Cherry *et al.* and Kruth *et al.* though no conclusive evaluation was undertaken [130, 219]. Further, it is also evident that the boundaries of the cellular grains are showing predominantly white lines. Electro Dispersive Spectrometry (EDS) results obtained by Kell *et al.* based on the laser welded 316L samples showed increased concentrations of chromium, molybdenum and sulphur along the cell boundaries, indicating a decrease in the iron content due to the increased alloying elements [220].

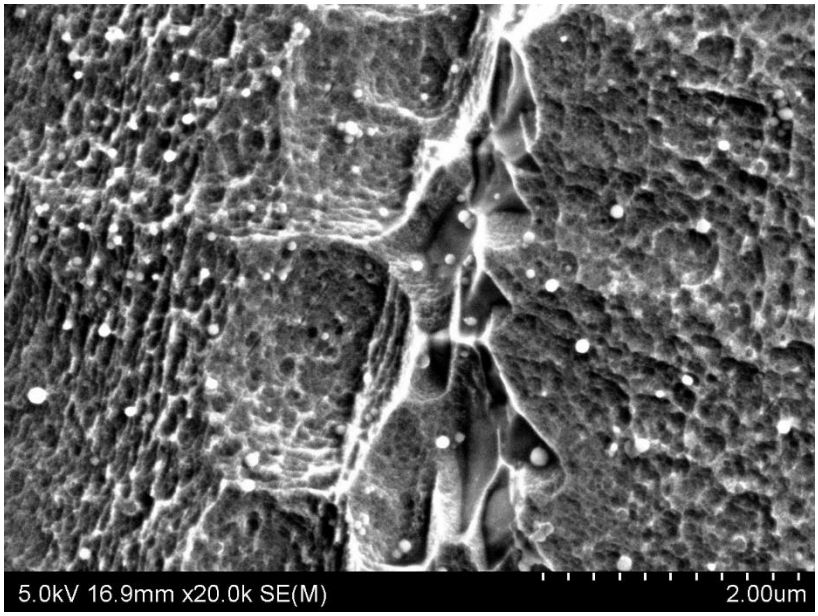

Fig. 5-11 SEM image of 112.8 J/mm^3 sample at 300 W showing cellular grain growth

Anisotropic differences of cellular ferrite grains is perceived as the primary factor in the variance in the microhardness of SLM samples by Ma *et al.* [134]. Considering the Hall and Petch formula for grain boundary strengthening, Song *et al.* predicted superior mechanical properties with finer grain sizes [221]. The fine cellular ferritic growth as evidenced in the photomicrographs of Fig. 5-10 and Fig. 5-11 could also have resulted in anisotropy and higher mechanical strengths.

5.2.6 CrN precipitation

Finely dispersed spherical precipitates in the form of white speckles are also seen in the photomicrographs of Fig. 5-12, predominantly in the ferrite zones. Conde *et al.* reported precipitation of spherical phases identified to be either M_7C_3 or $M_{23}C_6$, during laser surface melting of the 430 ferritic stainless steel [222], while Kwok *et al.* observed exactly similar precipitates in the martensitic stainless steel 440C with an increased carbon content [223]. Further, Knyazeva and Pohl reported that $M_{23}C_6$ carbides are the most commonly observed precipitates in duplex stainless steels, but the precipitate growth was noted to occur along the austenite/ferrite grain boundaries [224]. However, nitride precipitation is more common in welded duplex stainless steels. The rapid cooling rates resulting from the welding process restricts the nitrogen solubility in ferrite leading to the

precipitation as either Cr_2N or CrN [224]. CrN precipitation occurs when the duplex metal is heated to above 1273 K (1000 °C) and cooled rapidly in excess of 20 K/s [17].

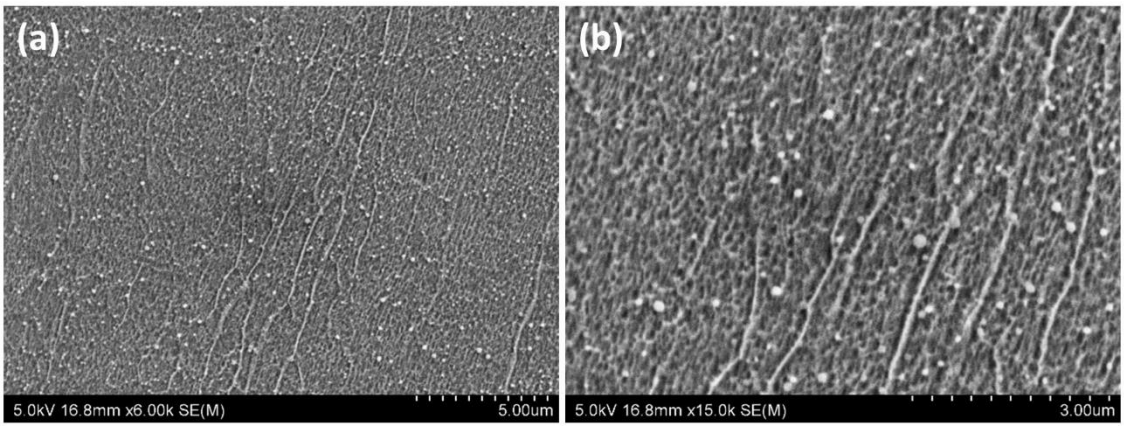

Fig. 5-12 CrN precipitate formation in the 141 J/mm^3 sample at 300 W

Based on this, it is proposed that the white spheres seen in Fig. 5-10 and Fig. 5-11 are most likely the precipitated nitride CrN phase. Pettersson *et al.* also noted that the CrN precipitation is primarily intra-granular inside the ferrite grains, and the higher the cooling rates, the higher are the level and size of the precipitates formed [225]. The precipitated white flaky particles observed in Fig. 5-10 and Fig. 5-11 are in accordance with these inferences from the literature. Morphologically, CrN precipitation is plate-like in appearance with a {001} orientation [226]. While investigating the corrosion resistance of duplex stainless steels, Wischnowski identified traces of spherical CrN precipitates similar in size and appearance to those in Fig. 5-10 [227]. Apart from the spherical precipitates, long, slender, and acicular precipitates also appeared in ferrite grains as shown in Fig. 5-10. Similar precipitates are observed by Sathirachinda *et al.* in the 2507 duplex stainless steel grade subjected to water quenching from 1398 K (1125 °C), although their composition is not clearly stated [228]. These are very similar to the nitrides (CrN) with the characteristic irregular orientation and growth as also observed by both Liao and Pettersson *et al.* [17, 225]. There appears to be an accumulation of these precipitates along specific lines, most likely at the grain boundaries or at the end of the long columnar ferrite grains formed, as indicated in Fig. 5-12.

The process conditions and subsequent thermo-mechanical variations presumably led to the CrN precipitation, which is greatly detrimental to both mechanical and chemical properties of the duplex stainless steel. Knyazava *et al.* reported CrN precipitation leading to a brittle fracture [224], while Zucato *et al.* noted the formation of both carbides and nitrides of chromium decreasing the toughness of duplex stainless steels [162]. Pettersson *et al.* noted duplex samples containing CrN and Cr_2N nitrides had a reduced critical pitting temperature than the as supplied rolled SAF 2507 super duplex stainless steel [225]. Pitting corrosion was observed preferentially in the secondary austenite by Nilsson and Wilson due to the reduced chromium and nitrogen content [38]. It was also theorised by Pettersson *et al.* that the size and the location of the precipitates in the microstructure is of greater importance than a large quantity of small precipitates [225]. Based on these observations, current samples produced at elevated energy density and laser power are theoretically more prone to pitting corrosion due to the increased size and numbers as evidenced in Fig. 5-10-(d).

5.2.7 Fusion zones and lack of fusion defects

The fusion zones as seen in Fig. 5-13 are elongated forms with irregular boundaries and dimple-like recesses formed on the face during the etching process. Nitride precipitation is evident within the cavities, suggesting the probable segregation of nitrides during the cooling process. While analysing the fusion zones of laser melted 316L, Shifeng *et al.* noted a reduction in the non-metallic elements (C, O, and Si) and concluded that they were most likely removed due to the etching process [229]. The fusion zone marked in Fig. 5-13 could have resulted for similar reasons. Overall, the fusion zone is where two solid fronts from adjacent laser scans meet and will have wider metallographic and physical variations compared to the interior.

Based on results of tensile tests, Shifeng *et al.* observed that the shear failure follows the fusion zones which act as areas of weakness [229]. Experimental evaluations involving tensile samples made with varying orientations led to the understanding that the fusion zones with relatively weaker bond strengths allow for easier shear failures compared to the grain boundaries. Laser welded 2205 duplex stainless steel samples were reported to have shown a greater correlation between the size of the fusion zone and the corrosion

resistance compared to the ferrite to austenite ratio [230]. The distinct fusion zones as may be noted in Fig. 5-13 could also act as sources of weakness.

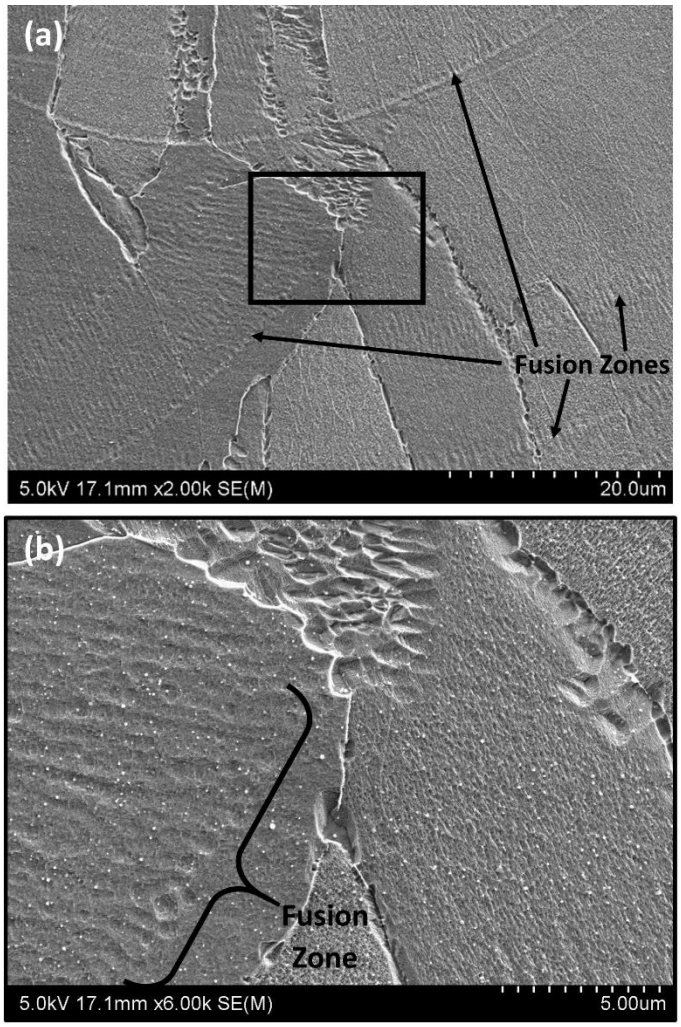

Fig. 5-13 Fusion zones of the 91.7 J/mm^3 sample at 300 W at (a) 2000x and (b) 6000x magnification

Varying levels of porosities resulted in different samples, mainly due to the incomplete fusion of the melt tract, leaving behind defects due to lack of fusion. Gong *et al.* and Gu *et al.* reported that the intensity of fusion defects decreases with increasing laser energy densities [154, 231]. Similar observations may also be made from the photomicrographs presented in Fig. 5-1, as the size of the fusion defects decreased with increasing laser energy density. Possible effects of these defects on the surrounding microstructure are interesting to note, while there is a clear evidence of variation and a certain amount of refinement in the microstructure, around these defects.

Very fine columnar grains less than 10μm are observed to form around the top edges of the thin line defects, mainly in the samples produced at the lower laser energy densities. Fine columnar vertical parallel grains resulted on the top surfaces of the long slender fusion defects as shown in Fig. 5-14-(a) & (c). Thin and slender lack-of-fusion defects connecting triangular cavities as seen in Fig. 5-14-(b) are observed to impart interesting microstructural features. Small equiaxed grains are observed along the top edge of the defect, with grains observed to elongate outwards from the slender defect. The triangular defects are seen to act as heat sinks and direct the columnar grains outwards from the centre of the semi-circular melt.

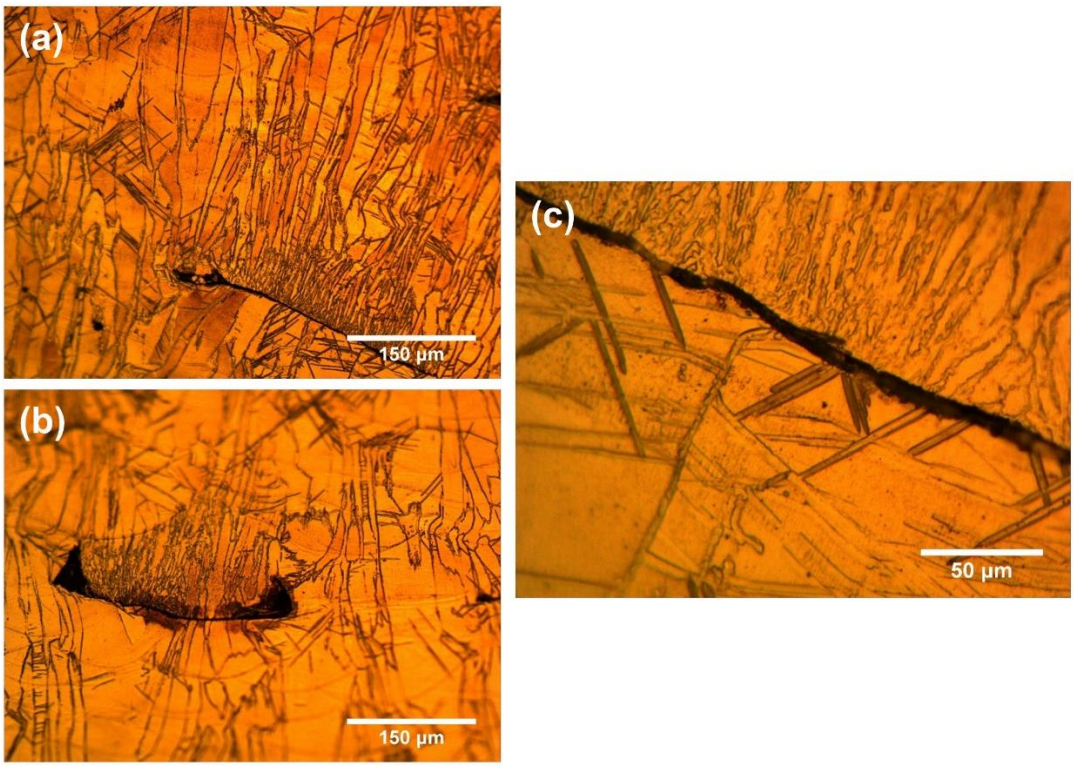

Fig. 5-14 Lack of fusion defects in samples produced at (a) - 105.8 J/mm^3 375 W and (b) - 91.7 J/mm^3 350 W, (c) - higher magnification of (a)

It may be recalled from Fig. 5-4 that the relatively small columnar grain growth above a lack-of-fusion defect imparts a highly randomised crystallographic orientation. This is the consequence of the irregular substrate morphology resulting from the disconnected laser scan tract, and the lack of significant recrystallisation. It may be observed in Fig. 5-15 that closely spaced lack-of-fusion defects allow the columnar grains to be narrowed and squeezed between the defects with a ‘S’ like morphology. Irrespective of this, a high

length to width ratio is still observed suggesting only contraction in the lateral direction. Fig. 5-15 also shows a discontinuity in the columnar microstructure along the bottom edge of the defects. This suggests that the lack of fusion defect is formed during building with the bottom edge solidified prior to the formation of the next layer.

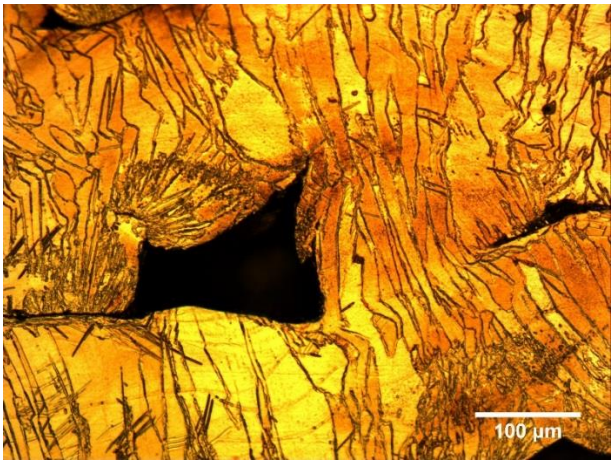

Fig. 5-15 Sample produced at 91.7 J/mm^3 and 400 W showing impinged columnar grain growth between lack of fusion defects

Lack of fusion defects and the consequent porosities observed in all the samples with varying intensities might adversely affect the mechanical properties of laser melted samples [183, 232]. However, the extent and nature of which will depend on the powder composition and the process conditions, while the build direction was also identified to be a critical factor. Chlebus *et al.* noted that building samples in the direction of testing often results in reduced strengths due to the anisotropy associated with the pore formation perpendicular to the direction of testing [233]. This is further accentuated with stress concentration effects at the small tip radii of flat defects formed due to lack-of-fusion. As a result of local collapsing and fracturing, higher porosities were also noted to decrease both hardness and wear resistance of SLM samples [130, 234]. Further, fusion defects were also observed to affect the corrosion resistivity of SLM samples detrimentally, due to preferential pitting attack and higher anodic potentials [234].

5.2.8 Density analysis

Archimedes density results presented in Fig. 5-16 show density values ranging from 88-93% and an overall average of 91.6%. Density variance with laser energy density was minor with the overall minimum and maximum density observed at 105.8 J/mm³ and 126.9 J/mm³ respectively. Samples produced at the elevated laser energy densities 134 and 141 J/mm³ resulted in similarly dense samples at 92.7 and 92.6% respectively. The bulk density variation with laser power at different laser energy density levels is depicted in Fig. 5-17. While the response is quite varied at different levels of the experimental factors, overall, the range of variation in the bulk density is quite high across different energy densities achieved at the lower power setting 300 W. This range decreased with increasing laser power from 17.3% between the 119.9 and 105.8 J/mm³ sample at 300 W, to 4.7% at 400 W between the 141 and 91.7 J/mm³ samples.

Generally, all the curves are closely bunched together at the 400 W laser power, indicating lesser variation in the bulk density probably due to larger melt pools achieved at higher power settings. Laser powers of 350 and 400 W were selected to represent the relationship between scan speed and bulk density as shown in Fig. 5-18. With an average density of 91.4%, measured for the range of energy densities presented.

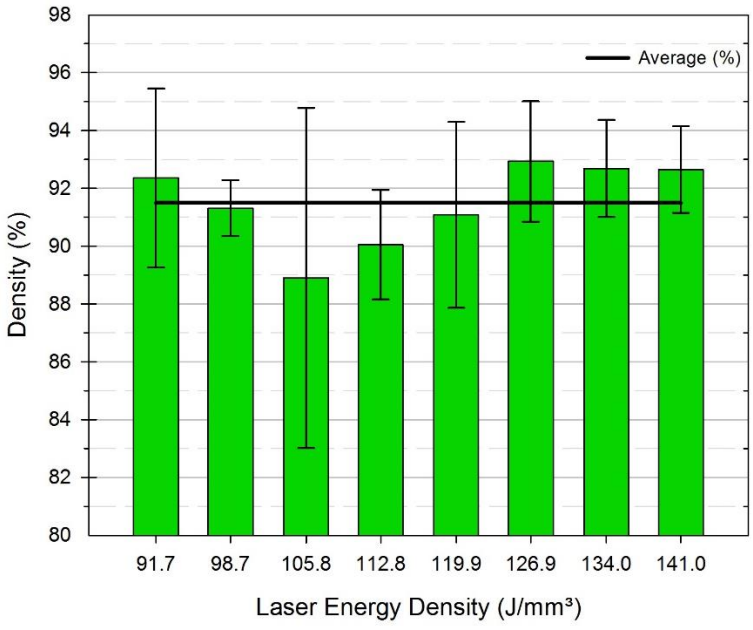

Fig. 5-16 Bulk densities of samples at laser energy densities

The overall variation of the bulk density values ranged from 89% to 93% as depicted by the bar chart in Fig. 5-16. The energy densities employed appear to be effective in achieving an average of 92% density in the samples, though there is an anomalous drop at the 105.8 and 112.8 J/mm^3 energy density levels. Within the limits of the experimental parameters, the higher energy densities from 126.9 to 141 J/mm^3 resulted in the highest bulk densities, probably due to increased melt volumes and wider heat dispersion into the surrounding microstructure leading to better bonding of the melt tracts. The average bulk densities obtained from the current experiments are lower compared to the 99.5 % values reported by Saeidi *et al.* while laser melting SAF 2507 duplex stainless steel. This is probably due to the differences in the raster scan strategies employed; the current experiments are done with unidirectional raster paths in which the melt tracks are laid one over the other, as against the 45° bidirectional scanning employed by Saeidi *et al.* leading to the elimination of the lack of fusion defects [235]. Analysing bulk density with respect to laser scan speed and laser power in Fig. 5-18, concludes with comparable densities with elevated scan speeds. The majority of bulk density measurements are contained within the zone encompassing the 400 W sample trend line (90.1-92.5%), suggesting that the constant processing parameters of hatch spacing and layer thickness are the greater contributor to bulk density values.

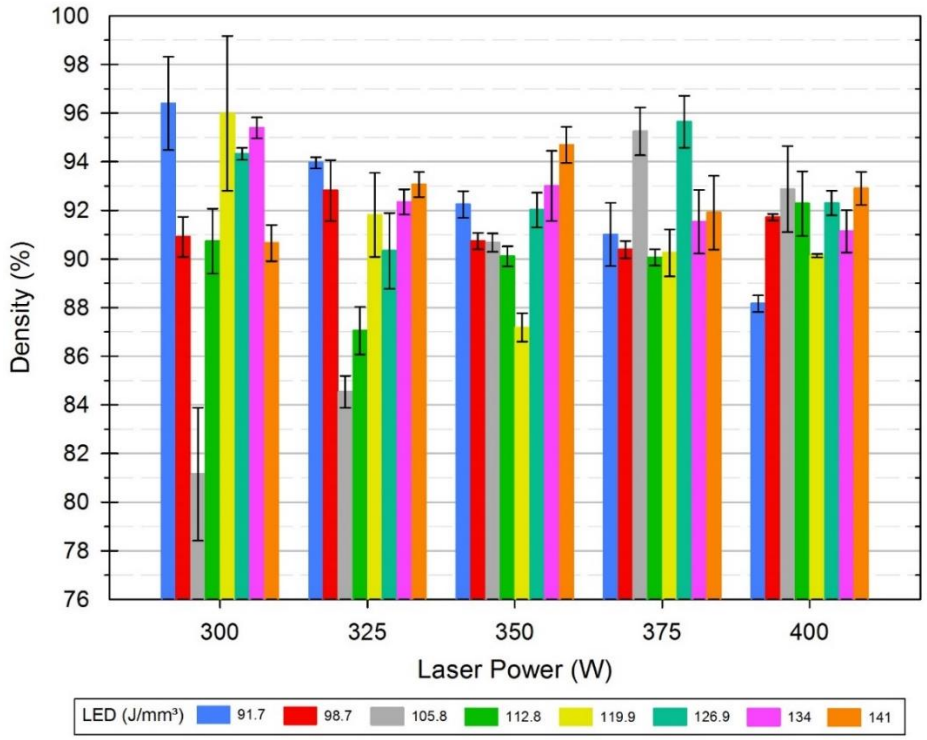

Fig. 5-17 Bulk density variation with laser power and energy density

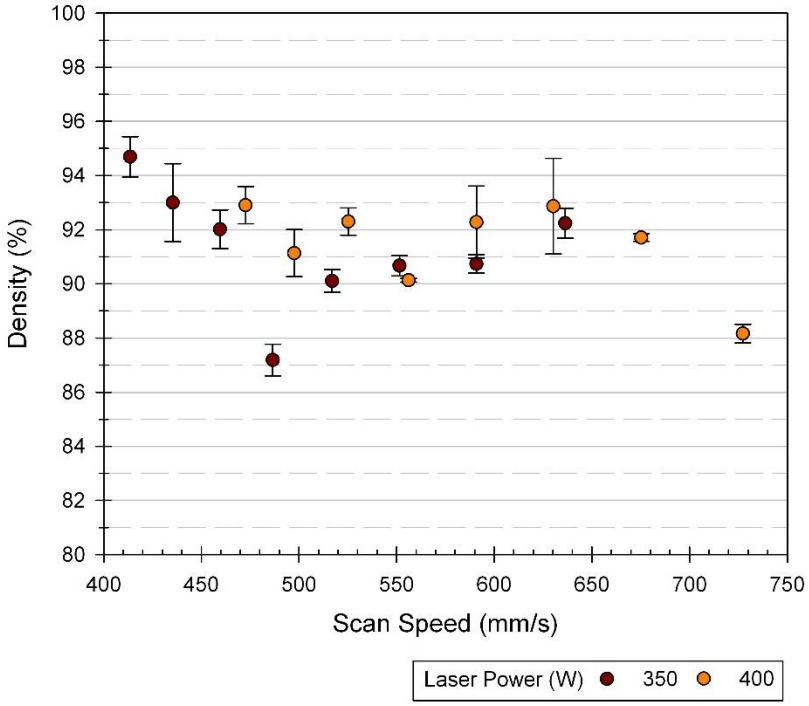

Fig. 5-18 Variation of density with respect to scan speed at 350 and 400 W

5.2.9 Micro-hardness evaluation

The aforementioned microstructural variation along the centre line of the samples resulting from the double laser pass scan strategy is most likely to cause an increase in the hardness over the microstructure at the centre. This is verified by the differences in hardness values at the centre line of the sample and the surrounding microstructure as presented in Fig. 5-19. This difference in hardness is noted to decrease with increasing laser energy density from a maximum difference of 30.8 HV at 91.7 J/mm³ to 0.9 HV at 141 J/mm³. This trend is probably the result of achieving more homogeneous microstructures at higher laser energy densities. The columnar grain growth along the edge of the sample and the associated differences in hardness values compared to the bulk of the sample are also depicted in Fig. 5-19. The micro-hardness values in the bulk of the microstructure are generally larger than those obtained in the columnar contour grains, except for the samples produced at the lower laser energy densities 98.7 and 105.8 J/mm³. However, the overall micro-hardness readings are 89.5-167.7 HV greater than those reported with the wrought SAF 2507 duplex stainless steel by Devendranath Ramkumar

et al. [236]. The average difference in the hardness values exceeded 20 HV with samples produced at elevated laser energy densities 119.9-141 J/mm³.

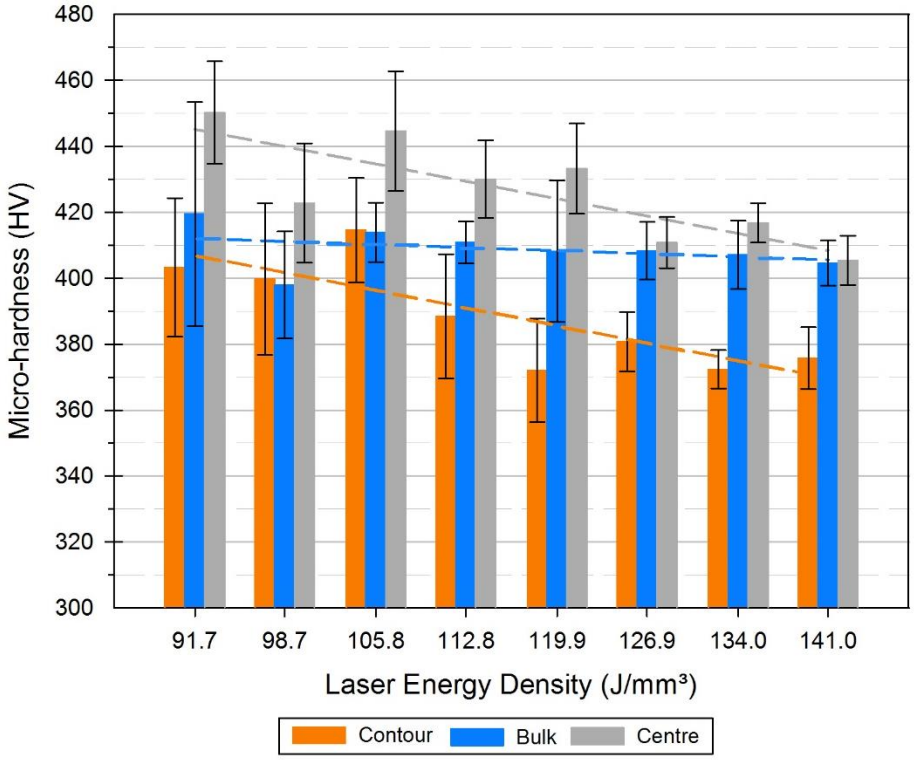

Fig. 5-19 Micro-hardness variation along part contour, bulk and centre with increasing laser energy density

Micro-hardness results presented in Fig. 5-19 provide a greater insight into the microstructural variation of samples produced with different processing conditions. The small cellular grain growth of ferrite and the chromium nitride precipitation result in the superior hardness of the selective laser melted duplex stainless steel. Comparing the microstructures of Fig. 5-1 with the micro-hardness results presented in Fig. 5-19, it may be correlated that the 91.7 J/mm^3 and 119.9 J/mm^3 cases resulted in the lowest amounts of austenite precipitation and gave the highest micro-hardness values. There are some slight variations in the micro-hardness values obtained at the other energy densities, however, the average micro-hardness is at around 408 HV.

The double scan central zones resulted in higher micro-hardness values compared to the bulk of the other areas as depicted in Fig. 5-19, probably due to the formation of larger ferrite grains and the lesser precipitation of the austenite phase. This may be validated

observing the decreasing trend in the micro-hardness values at the centre as depicted in Fig. 5-19; samples at elevated laser energy densities 126.9 and 141 J/mm³ have greater Widmanstätten austenite precipitation throughout the cross-section, including the centre line, resulting in an overall similar micro-hardness values across the sample. The areas close to the contour scan tracks as depicted in Fig. 5-8 result in elongated larger grains due to repeated heating and possible heat treating effects. This could have resulted in an annealing effect leading to a possible elimination of some of the residual thermal stresses and strains. The decrease in the micro-hardness values from the bulk to the border areas as presented in Fig. 5-19 elucidate this with the micro-hardness values at the border being lesser. There is an increasing trend in the effectiveness of the repeated heating as the energy densities are increased.

5.3 Alternative scan strategies

In an attempt to improve the consolidation of the duplex stainless steel powder, cubic samples (10X10X8 mm) are produced at scan speeds 300, 350 and 400 mm/s over a laser power range of 300-400 W in 25W increments. Checkerboard and meander scan strategies as detailed in Section 3.1.2 were used within this SLM processing window, with one repetition of each set. Table 5-2 depicts the order of sample for each of the scan strategies and repetitions, with the location of samples atop the build platform and naming convention defined in Section 3.1.4.

Table 5-2 Scan strategy evaluation sample build parameter layout

Parameter	***Row***	***Column***		
		Parameter		
		Scan Speed (mm/s)		
		350	*400*	*450*
		A	**B**	**C**
Laser Power (W)	**1**	300	300	300
	2	325	325	325
	3	350	350	350
	4	375	375	375
	5	400	400	400

5.3.1 Scan strategy vs density

The Archimedes density results developed based on samples produced with the meander and checkerboard scan strategy are presented in Fig. 5-20, showing the density levels ranging from 88.3 to 93.1 %. A decreasing trend in the density variation within a laser power is observed for all samples from 4.06 % at 300 W to 1.53 % at 400 W. This can possibly be attributed to the enlarged melt pool at the higher laser powers, leading to increased inter-track consolidation, as noted by Wang *et al.* [237]. The higher power might lead to lower the viscosity of the melt metal and allows for the improved flowability into pores, thus reducing the volume of lack of fusion defects [237]. However, elevated laser powers and energy densities can also lead to the formation of gas pores, detrimentally affecting the part density. Gas pores are observed by Gong *et al.* in laser melted Ti-6Al-4V for the samples produced at 74 and 100 J/mm^3 resulting in densities of and 99.1 and 95.5% respectively [238]. A similar study by the same author suggested the gas pore formation to result from vaporisation of low melting point elements of the alloy [204]. The formation of gas pores probably explains the average density of 91.1% observed in the 400 W samples produced by both scan strategies in the current study.

While minor variations are noted from the results of Fig. 5-20 with varying process conditions, the most notable observation is that the checkerboard samples are slightly better in terms of the bulk density overall. This is probably due to the consolidation mechanics of the scan strategy, whereby, the short scan lengths in each checker prolong the dispersion of heat in the layer, as reported by Zhang *et al.* [147]. The meander scan strategy leads to relatively longer raster lines and shorter reheating cycles, and may lead to the larger variation in part densities. Casati *et al.* observed partial re-melting in SLM of 316 L stainless steel, while pore frequency and micro segregation were observed by Mertens *et al.* to increase across two layers between melt pools [150, 239]. Additionally the longer scan vectors in the meander scan strategy prospectively exacerbated this density variance as a 13% reduction in the sample curling was observed by Kruth *et al.* through reducing the scan vector length from 10 to 2 mm [216]. The three densest samples from these results occurred with the checkerboard scan strategy and are presented in Fig. 5-21, along with the laser energy density levels and other process conditions. Standard deviation error bars show that there is a minimal variation in the Archimedes density results, while the overall variation in density is within 0.69% across the three energy densities used.

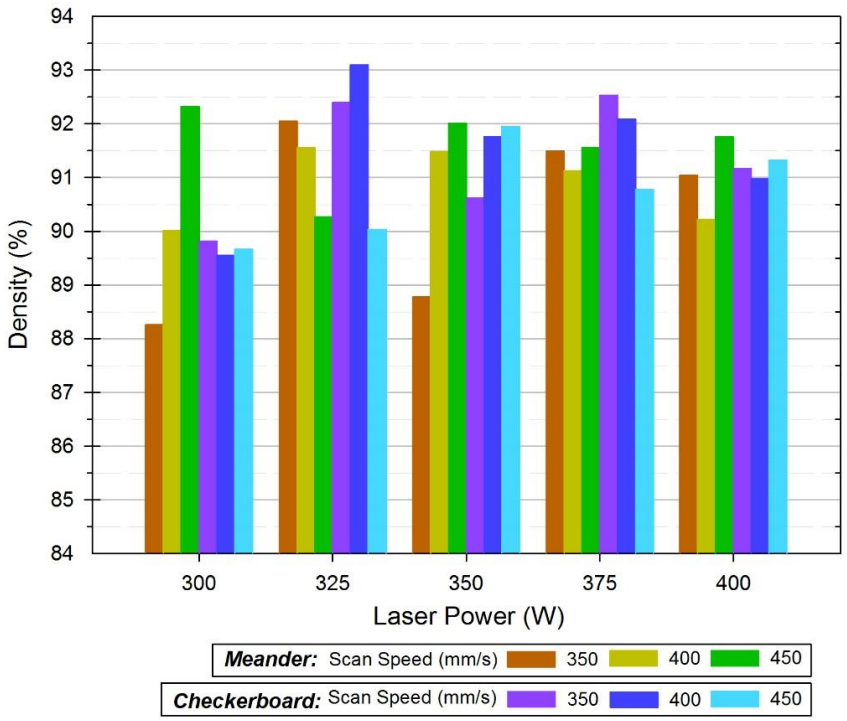

Fig. 5-20 Bulk density of meander and checkerboard samples with varying laser power and speed

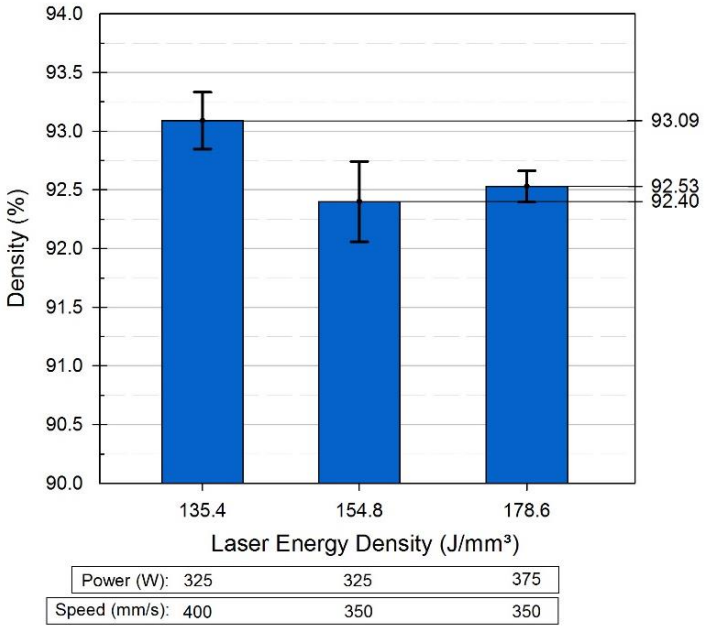

Fig. 5-21 Highest density values and corresponding parameters

5.4 Mechanical characterisation

As observed above, processing parameters of the three densest samples from the scan strategy evaluation were selected for building the tensile test samples. The parameters containing the three energy density levels; 135.5, 154.8, and 178.6 J/mm³, checkerboard scan strategy and laser power and scan speed were listed in Table 3-1. Three different orientations were used for the tensile test samples (0, 45 and 90° to the build platform), with dimensions as detailed in Section 3.6.2. Tensile test samples are placed on the build substrate as shown in Fig. 3-7, oriented for the minimisation of the wiper damage and the powder splatter from the adjacent samples. An extra set of samples was also produced for annealing studies as per the solution annealing conditions in Section 3.10. Reference samples were prepared from rolled SAF 2507 plate in two different orientations. All tests were repeated at least once for establishing the repeatability of the experimental results. A summary of the strongest sample at each condition is presented in Table 5-3 with the comparable wrought duplex stainless steel sample.

Table 5-3 Tensile test result summary

	LED (J/mm^3)	135.4			154.8			178.6		
	Orientation	***0°***	***45°***	***90°***	***0°***	***45°***	***90°***	***0°***	***45°***	***90°***
As Built Samples	UTS (MPa)	833.4	908.1	867.7	801.5	871.1	875.8	775.2	817.8	824.8
	Elongation (%)	15.2	25.2	18.9	17.5	27.3	22.6	16.5	28.9	21.1
Solution Annealed Samples	UTS (MPa)	757.6	661.5	612.9	789.4	768.4	731.1	744	664.7	708.1
	Elongation (%)	38.1	49.5	32.6	44.5	49.6	36.9	38.5	44.2	33.7
Wrought SAF 2507	UTS (MPa)	881.2								
	Elongation (%)	60.7								

5.4.1 Structure-property relationships

Photomicrographs of the as-built and the solution annealed samples used for the tensile tests are presented in Fig. 5-22 in order to establish the structure and property relationships. The distorted microstructure of the laser melted duplex stainless steel is likely to result in the poor tensile strength and the elongation comparted to the equilibrium microstructure of the wrought SAF 2507 duplex stainless steel. As-built microstructures consisting of long columnar ferrite grains with austenite precipitation along the grain boundaries and the intersecting Widmanstätten needles are observed in Fig. 5-22. The grain morphology is retained in the solution annealed samples though, compositionally, the austenite precipitation is increased with finer Widmanstätten needles and inter-granular precipitates. Build orientation also influences the microstructure of the samples in the as-built state and correspondingly after the solution annealing. Samples oriented at 0 and 45° are seen to contain more Widmanstätten austenite than the samples produced at 90°. A possible explanation for this is the larger exposed surface area to laser melting in each slice for the 0 and 45° samples, which results in the heat being retained in the component for longer, promoting further austenite growth. Similar observations are seen in solution annealed samples with the least amount of Widmanstätten austenite in the 90° sample.

The significant volume of ferrite in the as-built samples greatly influences the strength properties of duplex stainless steel as will be established in the following section. Park *et al.* observed a linear decreasing trend in the tensile strength and elongation with increasing ferrite content in 25Cr duplex stainless steel castings [240]. An opposing observation was presented by Asif *et al.*, where the tensile strength was noted to increase with ferrite ratio in friction welded (FSW) duplex stainless steel although [241]. Apart from the phase constituents, the relative grain sizes also influence the material strength. Laser melted duplex stainless steel samples can be expected to be weaker than the wrought duplex stainless steel due to the ferrite-austenite dispersion and the epitaxial grain growth along the build direction, while the finer grain size in wrought duplex stainless steel also contributes to its higher strength. The underlying grain dispersion and internal porosities is likely has a more profound influence on tensile strength than the equilibrium phase ratio as evident by the weaker SLM samples subjected to solution annealing.

As alluded to earlier in this chapter in Section 5.2.1, grain orientation also significantly influences the tensile strength and the elongation responses. In the as-built condition, with the linear scan strategy, grains are predominantly orientated in the <001> direction, perpendicular to the orientation of the tensile test. This strong grain orientation is further observed in the rolled wrought SAF 2507 duplex stainless steel plate shown in Fig. 5-23 probably contributing to higher strength values as a result of the smaller grain sizes. By conducting tensile tests of AA5083 aluminium at three orientations on the rolled plate; 0, 45 and 90°, Najib *et al.* observed that as the orientation angle increased the UTS also increased [242]. Additional observations include the greater rate of work hardening at 45° to the tensile direction. As the checkerboard scan strategy is employed, for each checker, the scan direction rotates by 90° after each layer. This commonly results in the long elongated grains observed in Fig. 5-22 along the sample cross-section and fine elongated grains along checker boundaries and equiaxed within the checker on the samples surface, as observed by Carter *et al.* [243]. Carter *et al.* further reports the equiaxed grains within checkers on the sample surface to result in a strong {001} texture, while the fine elongated boundary grains were random in orientation. In the tensile testing of SLM samples built; horizontal, 45°, and vertically to the build platform, Guan *et al.* noted the highest tensile strength in the horizontal samples due to layer formation parallel to tensile direction and perpendicular to columnar grains [244]. This layer formation and lack of defect formation

within the layers acting as points of weakness are the causes of poor tensile strength in vertically built samples. Alternatively Vrancken *et al.* reported the residual stresses induced during consolidation to be the predominant factors influencing the anisotropic effects [245].

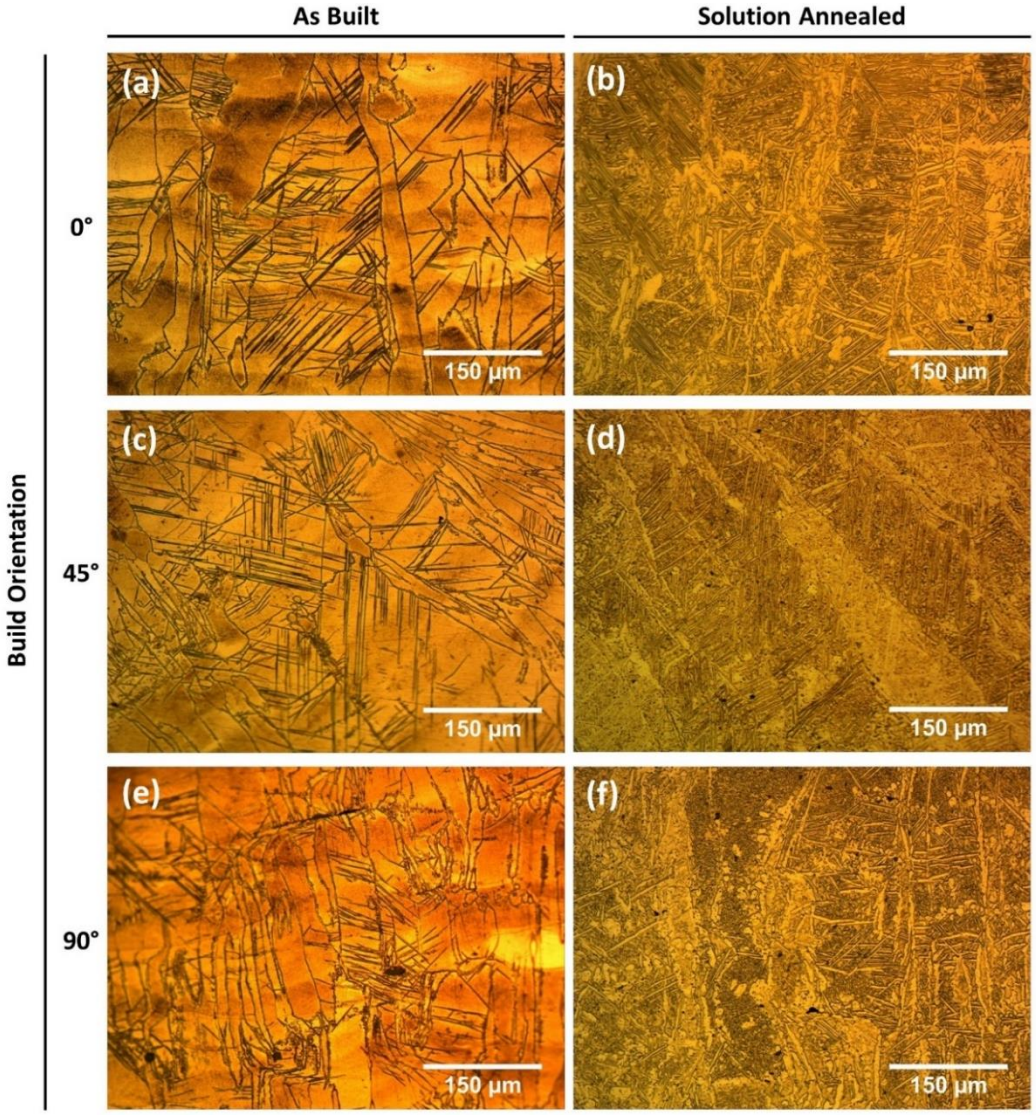

Fig. 5-22 Cross-sectional microstructures of samples produced at 154.8 J/mm^3

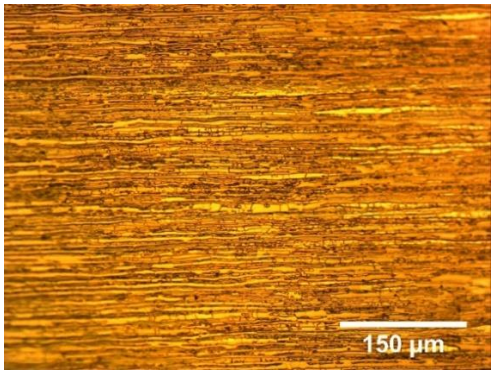

Fig. 5-23 Wrought rolled plate SAF 2507

5.4.2 Tensile tests and results

The ultimate tensile strength values measured based on different samples are presented in Fig. 5-24. It may be observed that the average UTS values of the as-built and solution annealed samples are lower than the normal tensile strength levels of the wrought SAF 2507 samples. The average differences are 39.4 MPa and 165.9 MPa with the as-built and the annealed SLM samples, respectively as compared to the wrought specimens. Despite the fact that the tensile strength values are lower compared to the wrought specimens, the average UTS values of the as-built and the annealed samples at 841.7 and 715.3 MPa respectively, exceed the observations made by Zhang *et al.* in the case of SLM 316L austenitic stainless steel (630.1 MPa) and Boegelein *et al.* with the oxide dispersion strengthened ferritic steels (500 MPa) [208, 246]. Further, the post-printing annealing process employed led to softening of the samples, in all the cases, but to varying degrees.

These results are also in accordance with the observations made by Saeidi, based on laser melted 316L samples. They attributed the greater strength in the as-built SLM samples to the fine cellular sub grains, high dislocation concentration, and the grain pinning [247]. An average UTS variance of 167.5 and 172.1 MPa is observed between the as-built and the annealed samples oriented at 45 and 90° respectively. However, it is interesting to note this variation is only around 39.7 MPa in the case of the samples printed at 0° orientation, despite the microstructural refinements attained. Evidently, the samples produced at the 0° orientation attained tensile strength values below the average. The average reduction in the tensile strength attained with the annealing process is also not very high across the range of the samples. Consequently, the differences in the tensile strength values from the as-built to the annealed samples became quite narrow with the 0° cases. Possibly, the structures are already quite elongated due to the wider dispersion of the heat in 0° build orientation, based on the larger area of laser scanning.

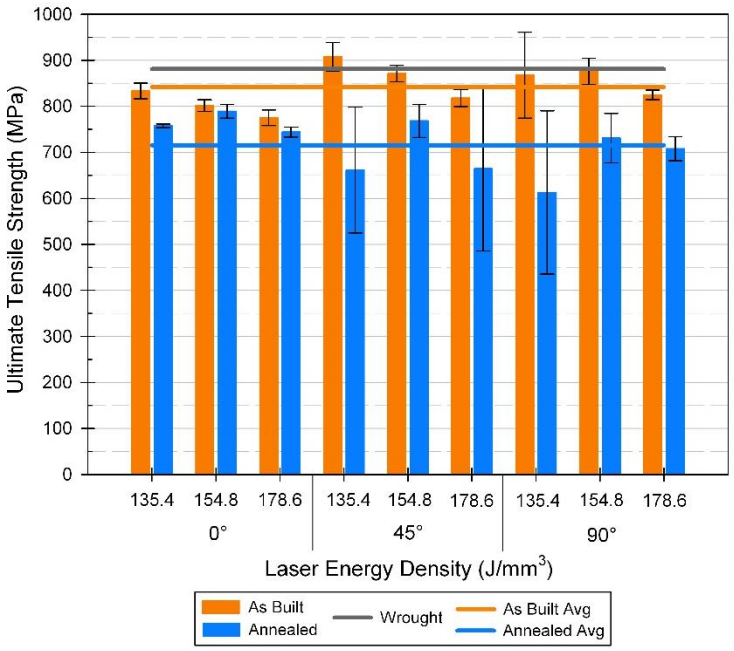

Fig. 5-24 Average tensile strength of SLM and wrought duplex stainless steels

Elongation at break values are similarly lower for the as-built and the annealed samples, compared to the wrought SAF 2507 as shown in Fig. 5-25. The as-built and the annealed SLM samples averaged at one third and two thirds (21% and 41%) of the elongation of the wrought duplex stainless steel. Comparable results were observed by Wang *et al.* in the laser melted 316L austenitic stainless steel with percent elongation values ranging from 15 to 21%. They also observed an increasing trend in the elongation, from 104.2 – 156.3 J/mm^3 to a maximum elongation of 21.1% and a decrease in elongation to 16% at 178.6 J/mm^3 [248]. As expected, the annealing process relieved some of the embrittlement attained during the laser melting process, as all the samples showed higher levels of deformation compared to the as-built samples.

Song *et al.* reported similar findings in vacuum annealed laser melted iron components, and attributed this to the recrystallisation, driven by the residual stress [202]. The effect of recrystallisation and the absolution of residual stress between the as-built and the annealed samples is seen to decrease in intensity with increasing orientation angle, with a difference in the elongation of 23.9, 20.6 and 13.5% at 0, 45, and 90° respectively. Comparing the average values of the elongation and the UTS, the as-built and the annealed samples at 0° orientation reach near comparable UTS results while there is a large difference in the elongation. This suggests that the lack of fusion defects formed

along the width of the gage length have a more profound influence on the elongation at break than the recrystallised microstructure similar to the observations made by Mahmoudi *et al.* in the laser melting of 17-4 PH stainless steel [249].

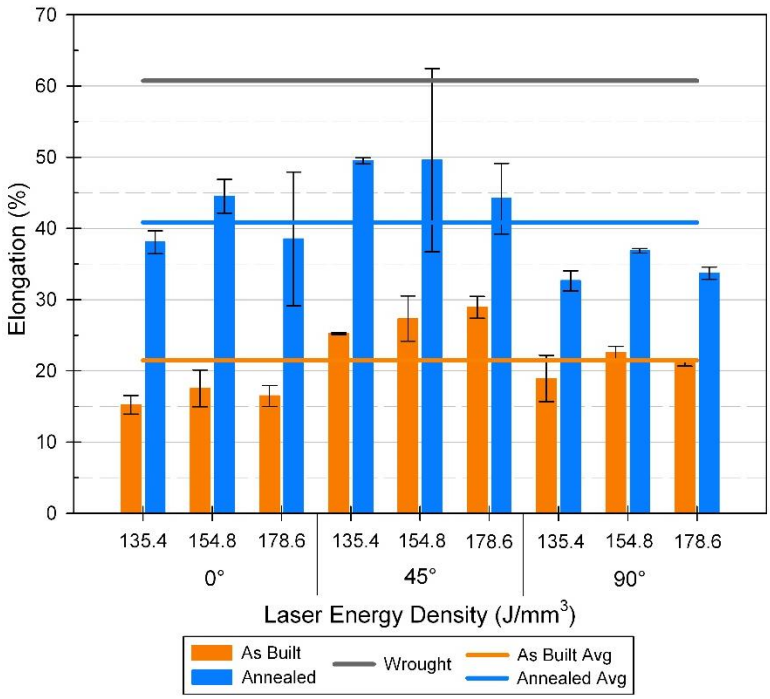

Fig. 5-25 Average elongation of SLM and wrought duplex stainless steel

Once again, considering the UTS and percent elongation graphs presented in Fig. 5-24 and Fig. 5-25 together with the stress-elongation graphs presented in Fig. 5-26, it may be noted that the effects of the build orientation appears to have a more significant role than the laser energy density. Both the UTS and the percent elongation values are very close across the three energy density levels within any specific build orientation. Similar trends are also noted further to the annealing process, with some slight variations. The average UTS and percentage elongation values however, showed definite variation from one build orientation to the other. Overall, the 45° orientation appears to give the best average UTS as well as percent elongation values both in the as-built and the annealed stats.

Overall, the UTS values varied by 132.9 MPa from the average level at 841.7 MPa, in the case of the as-built samples, considering all three laser energy densities and orientations as presented in Fig. 5-24. While, a larger variation at around 176.5 MPa is observed with

the annealed samples. The larger range in annealed samples could be the result of differences in ferrite:austenite ratio in the base microstructure prior to solution annealing as ferrite grain morphology is retained after solution annealing as detailed in Section 5.4.1. Badji *et al.* observed α-ferrite content to increase in a duplex stainless steel weld with solution annealing temperatures above 1050 °C [250]. Similarly, the variation in the percent elongation from the average is 13.68% in the as-built samples and 16.94% in the annealed samples.

In essence, the SLM samples are not as strong or as ductile as the wrought samples, in both the as-built and the annealed states. In many of the experimental cases, and in particular, the 45° and 90° cases, the differences in the ultimate tensile strength values are only marginal, as compared to the wrought samples. However, considering that the micro-structures of the as-built SLM samples are predominantly made of ferrite, a comparison to the ferritic stainless steels would be more meaningful. The ultimate tensile strength values reported by Lakshminarayanan and Balasubramanian in the case of the 409M grade ferritic stainless steels in the wrought state are about 305.7 MPa lesser than the values noted with the current laser melted duplex steels in the as-built state, with the predominant ferritic structures [251]. It exemplifies the fact that the laser melted steels do not behave like the ferritic stainless steels, in spite of the predominant ferritic structures. However, the internal porosity might have played its role in adversely affecting both the tensile strength and the percent elongation responses. Porosity in SLM samples is greatly detrimental to tensile strength, with Ilie *et al.* observing a 140 MPa decrease in UTS with a 3% reduction in density [252].

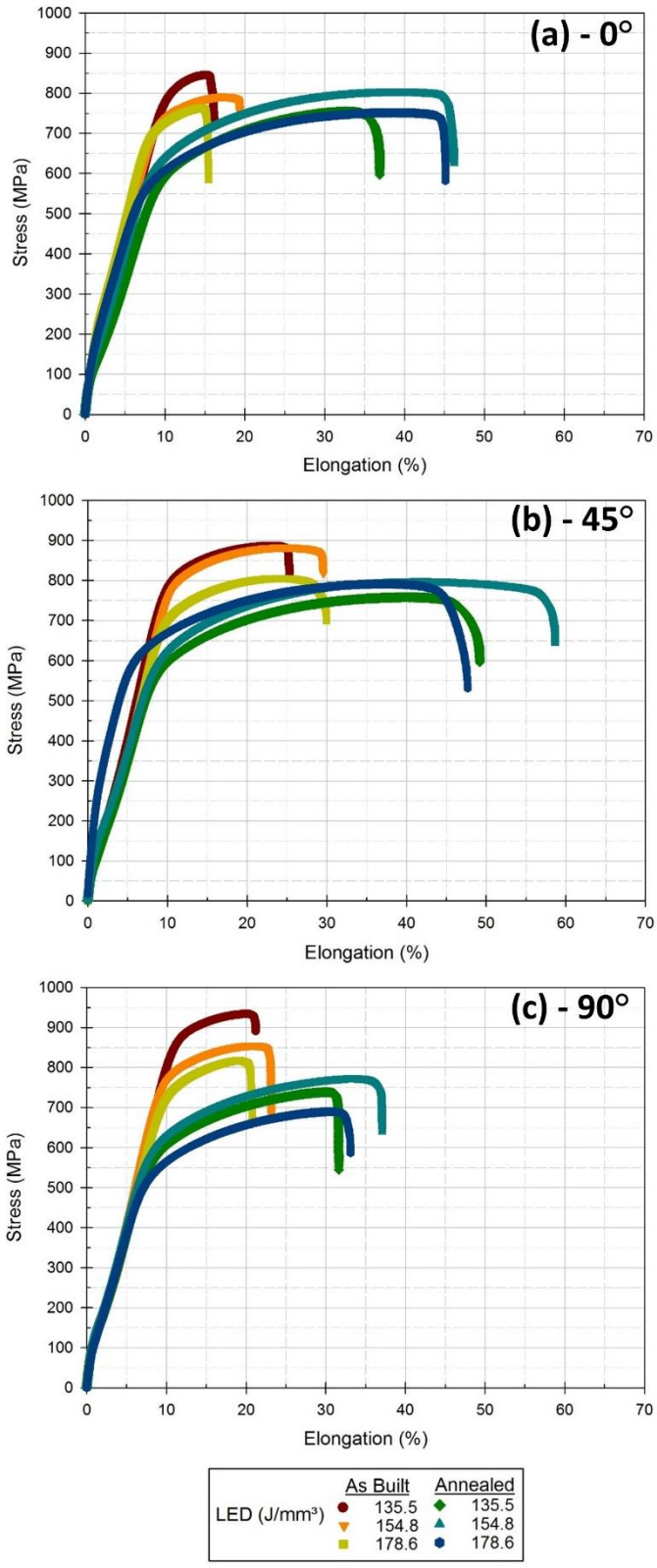

Fig. 5-26 Tensile results for a select As Built and Annealed samples at orientations; (a) - 0°, (b) - 45°, (c) - 90°

5.4.3 Fracture surfaces and modes

The variance in tensile strength and elongation in samples oriented at; 0, 45 and 90° is predominantly due to the modes and the propagation of cracks from the defects. Lack of fusion defects formed in between the supports of the surface closest to the build platform as shown in Fig. 5-27 are probably the main sources of crack initiation and propagation in both 0° and 90° samples. Fracture was observed to be predominantly perpendicular to the direction of testing in 0° samples (Fig. 5-28-(a)), whereas samples oriented at 45° and 90° show crack propagation along the thickness of the sample 45° to the direction of testing (Fig. 5-28-(b) and (c)). Fracture at 45° is seen to be commonly attributed to the shear criterion with the angle corresponding to the plane of maximum shear stress and constitutes ductile or semi-ductile fracture as noted by Kubík *et al.* [253]. Necking is found to be more predominant across the thickness of each sample and the solution annealed samples, in particular, the 45° ones led to a greater reduction in the cross sectional area due to necking.



Fig. 5-27 Underside surface of sample produced at 178.6 J/mm^3 and 0°, showing defects in between supports

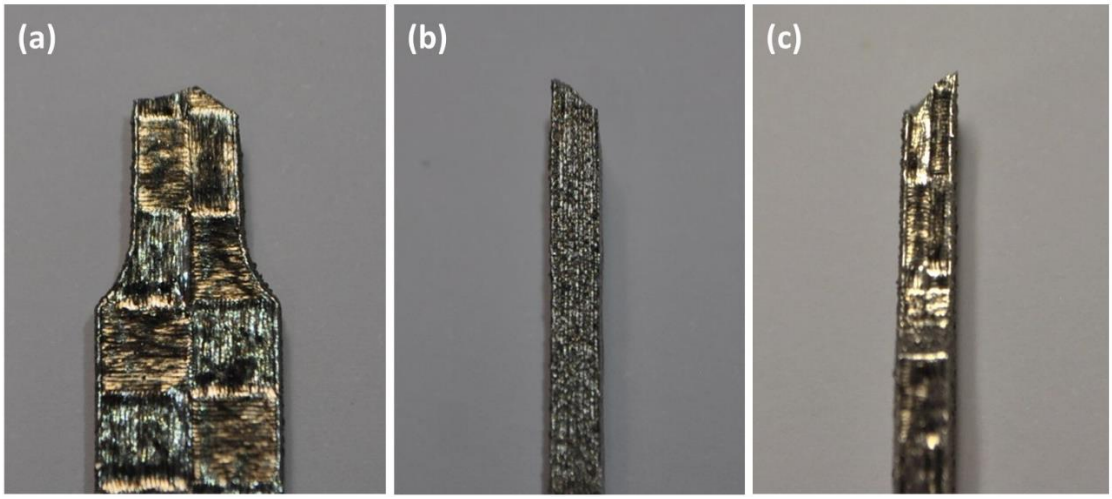

Fig. 5-28 Fracture angle in; (a) 0°, (b) 45° and (c) 90° samples at 178.6 J/mm^3

It was also noted with the 45° samples that the bottom surface experiences a rippling effect further to stretching on the tensile testing equipment as depicted in Fig. 5-29. A ripple distance of 5 mm peak-to-peak is observed, consistent with the checker length in the checkerboard scan strategy. This could be due to the support structures and the gaps in between, causing cyclical variations in the thermal histories along the length of the built specimen. Further, the checkerboard scan strategy leads to double lasing at lines where adjacent checkers meet and might cause a periodic variation in the grain size as was already noted in Section 5.2.4. These effects are not so predominant in the 0° case as the specimen was built horizontally, though the 90° cases showed similar effects but to a light extent. The difference in the thermal histories and the ensuing variations in the microstructures might lead to differential work-hardening results in different zones. In tensile testing 17-4 PH stainless steel parts fabricated by SLM, LeBrun *et al.* observed the transformation of retained austenite into martensite which contributed to increased work hardening [254]. Örnek *et al.* further theorised the formation of strain induced martensite in SAF 2205 duplex stainless steel, resulting from strain hardening [255].

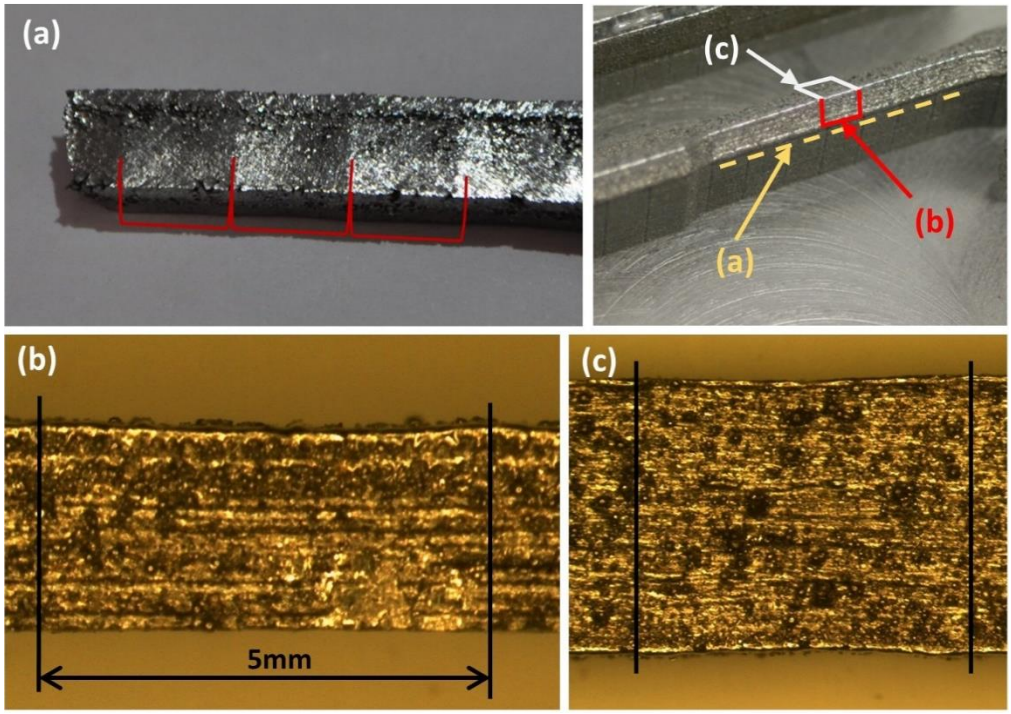

Fig. 5-29 Rippling in 45° sample at 154.8 J/mm^3. (a) Ripples along underside, (b) Ripple on thickness, (c) Ripple on width, and respective location image

The actual fractured surfaces of both the as-built and the annealed samples for one particular case are presented in Fig. 5-30. Overall, the as-built samples (Fig. 5-30-(a), (c), and (e)) show evidences of cleavage fractures consistent with the brittle fracture modes. Cleavage facets are observed along the centreline of Fig. 5-30 (e) and at two short locations in Fig. 5-30-(a). Fracture is seen to occur along the build orientation in as-built samples at 45 and 90° as distinctly evident in Fig. 5-30-(c) whereby the shear is 45° along the top of the figure. Areas of ductility are evident in the 0° and 90° as-built samples at along the upper face as evident in Fig. 5-30-(a) and (e) as regions of necking and at the centre of the 0° sample as a cone-shaped fracture. Necking and evidence of ductility are not visible in the 45° sample however, probably due to the periodic regions of ductility noted above, and might have fractured at an inter-checker boundary. This mixed fracture mode was also observed in plasma welded SAF 2507 samples by Migiakis *et al.* where poor ductility was noted in the heat affected zone of the weld due to nitride precipitation [213].

However, solution annealed samples show ductile trans-granular fracture with sufficient necking along the gage width as evident in Fig. 5-30-(b), (d) and (f). The solution

annealing treatment results in a change in the microstructure and possible recrystallisation of the austenite phase growing within the ferrite matrix. This is expected to enhance the ductile nature of the specimens, which is clearly evident looking at the necking and other features of the photographs presented in Fig. 5-30-(b), (d), and (f). It may also be observed that cracks are initiated and evidently dispersed in the central regions of the fractured surfaces, but there was insufficient energy to allow them to grow and propagate the fracture across the surface.

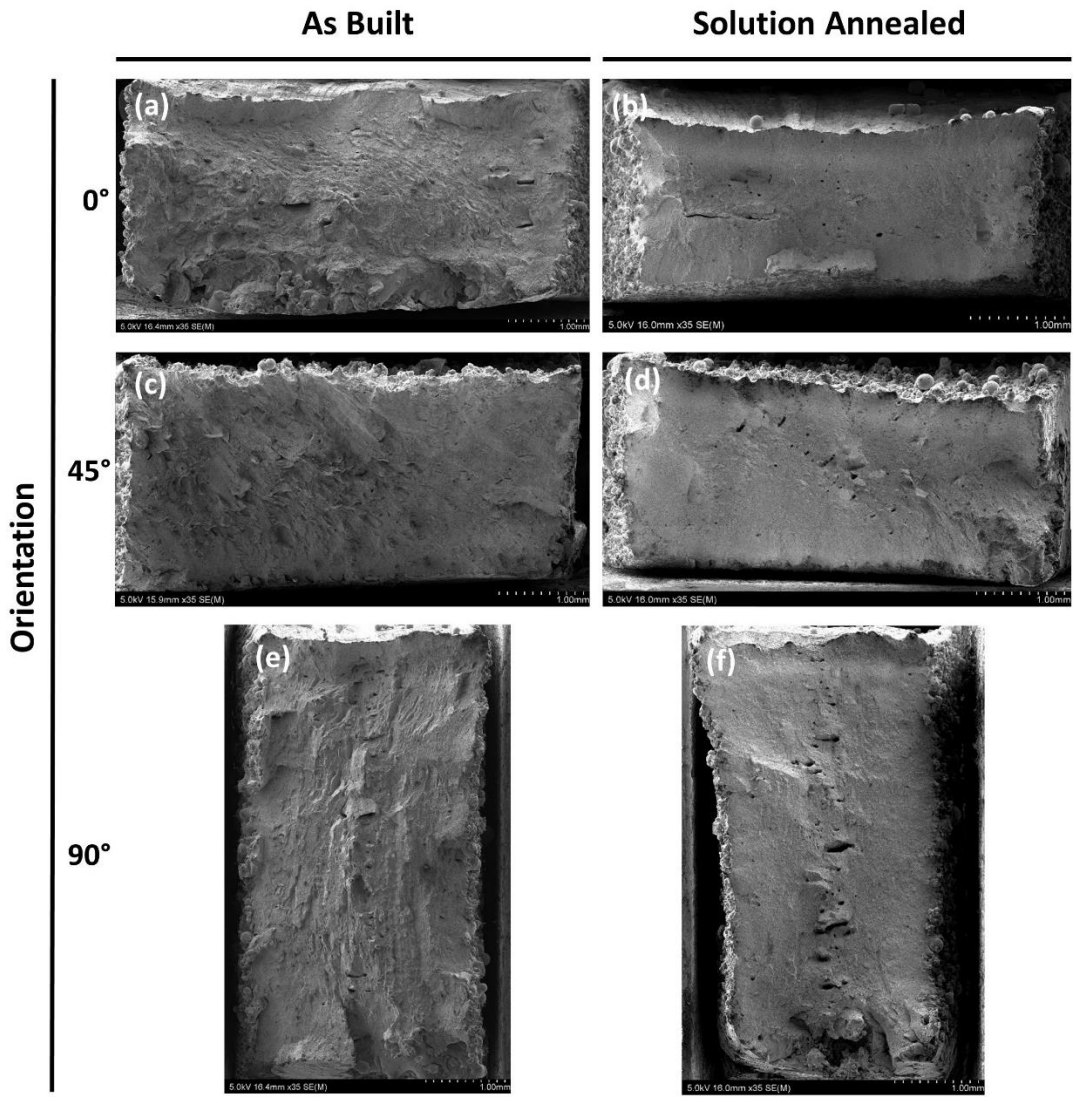

Fig. 5-30 Fracture surfaces of samples produced at 154.8 J/mm^3

SEM images of the fractured surfaces of both the as-built and the annealed samples printed at 0°, 45°, and 90° using different energy levels are presented in Fig. 5-31 to 5-33. Distinctive micro sized dimple fracture features are evident in all these images.

Sufiiarov *et al.* noted these to constitute ductile transgranular fractures and suggested as comparable in size to columnar dendritic cells [256]. Clear differences are also evident between the as-built and the annealed cases. The dimples are enlarged in the case of the annealed samples. While the average size of the dimple structure with the as-built samples range in diameter from 0.3 to 1.2 μm, it is around 0.8-4.5 μm in the case of the solution annealed samples. The enlargement of dimples is observed by Manfredi *et al.* in the SLM aluminium alloys solution annealed and aged, with the greater aging temperature of 160 °C resulting in the largest dimple size [257]. Enlargement of dimples is likely to result from recrystallisation effects resulting from a more equilibrium formation of austenite and ferrite.

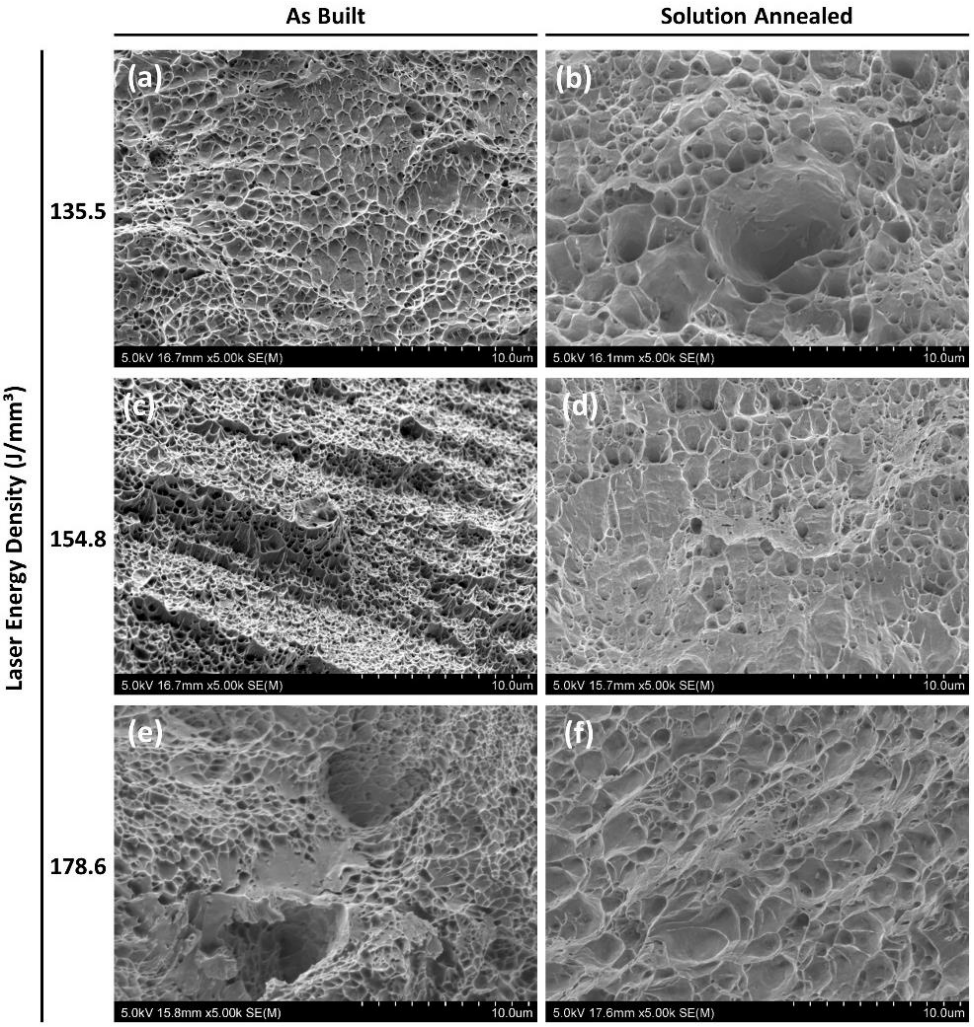

Fig. 5-31 Fracture surface of 0° samples at 5000x magnification

The dimple morphologies are also showing variation from one build orientation to the other. As may be observed in Fig. 5-32, the 45° as-built samples show evidence of smaller and more equiaxed dimples than the larger and more elongated dimples in 0° and the 90° samples. As detailed by Janssen *et al.*, uniaxial loading results in equiaxed dimple morphology whereby, tensile tearing produces more elongated dimples [258]. It may be noted that the fracture directions are different in different samples, as already noted. Further, the direction of the growth of the cellular structures is also different from one build orientation to the other. It is understood that the variations in the dimple sizes from one build orientation to the other, as noted in Fig. 5-31 to 5-33 are the results of the combined effects of these two aspects; the direction of growth of the cells and the direction of fracture and the consequent direction at which the fractured cells are looked at.

The more shiny and relatively macro defects observed in some of the photomicrographs of Fig. 5-31 to 5-33 are probably indicative of the presence of lack of fusion defects. For example, Fig. 5-31-(b),(e), Fig. 5-32-(a),(c),(f) and Fig. 5-33-(a),(f) clearly show the presence of these larger dimples with shiny surfaces at the trough. These are lack of fusion defects, remaining as they are further to the fracture and failure of the reaming material structure around them. They might have also acted as sources of stress concentrations. Simonelli *et al.* observed similar defect morphologies and surface conditions in laser melted titanium alloy Ti-6Al-4V [259].

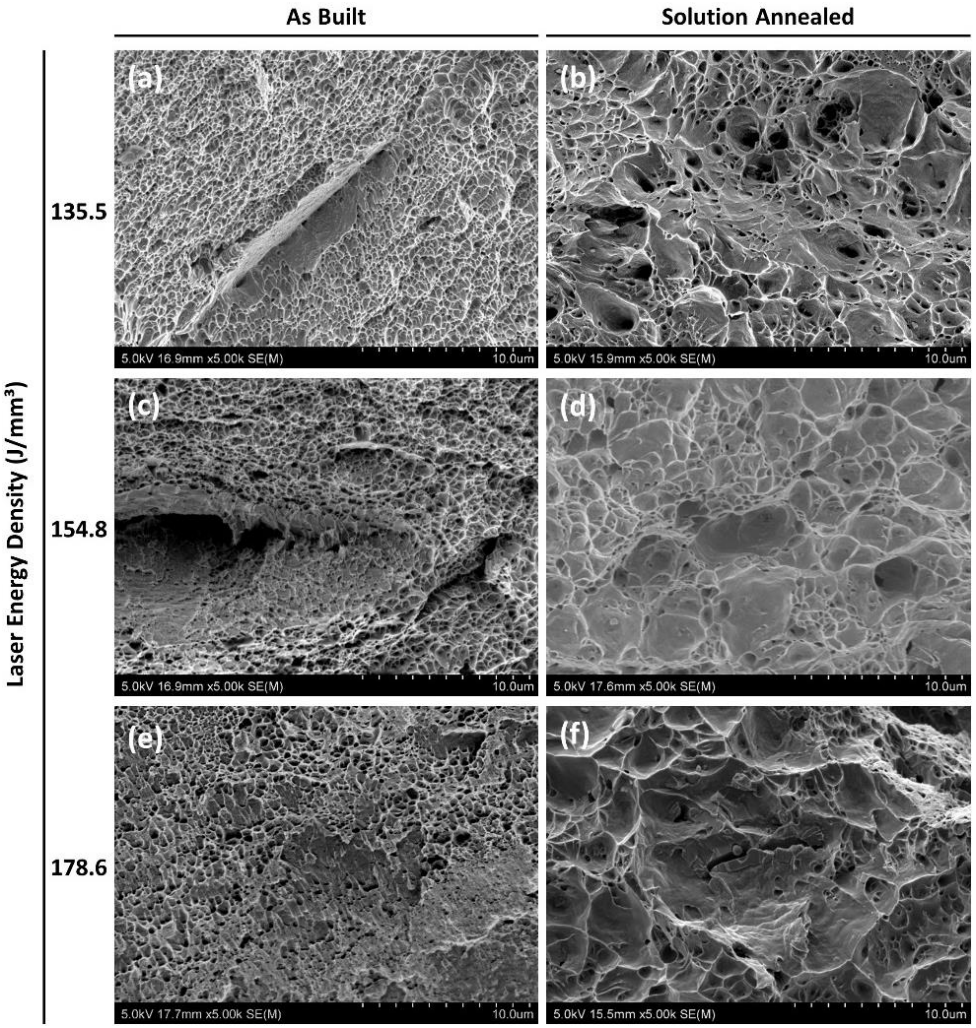

Fig. 5-32 Fracture surface of 45° samples at 5000x magnification

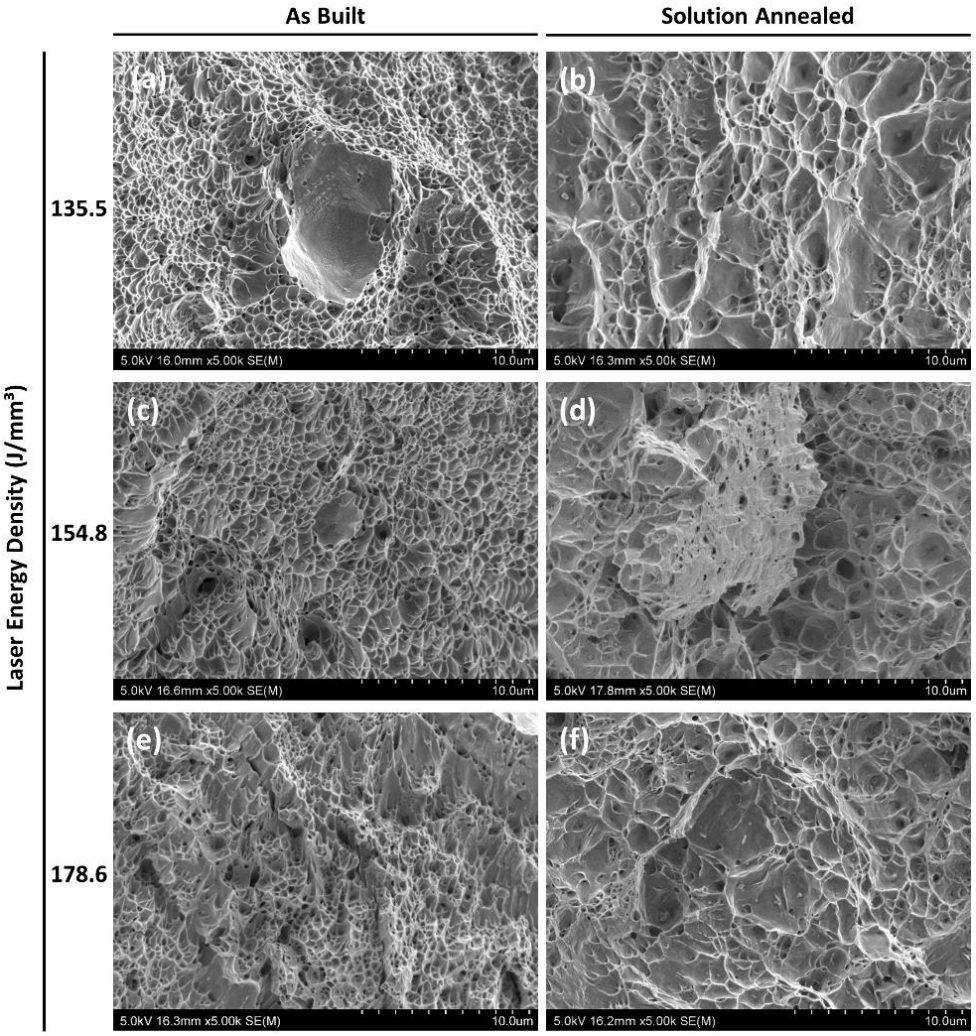

Fig. 5-33 Fracture surface of 90° samples at 5000x magnification

Upon a closer look, a micro crack may be observed at the centre of an enlarged dimple in the photomicrograph presented as Fig. 5-32-(f). The higher magnification image of the same as in Fig. 5-34 shows the crack propagation to separate around a spherical CrN precipitate which was not dissolved after the solution annealing. Further, the crack propagates as a smooth cleavage facet as is common with a brittle fracture. Hilders *et al.* exemplified similar micro-cracking in the ferrite phase in duplex stainless steels due to the 475 °C embrittlement though prolonged ageing. Hydrogen embrittlement in austenitic 316L stainless steel was observed by Herms *et al.* to impart a comparable crack in length and morphology in an similar dimple fracture surface [260]. In the present case, micro-cracks like these are most likely formed due to the rapid cooling during laser melting, and the associated residual thermal stresses.

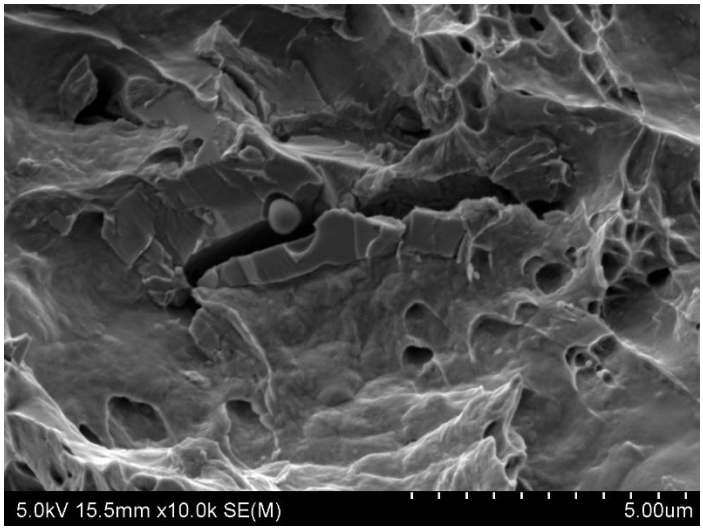

Fig. 5-34 High magnification of Fig. 5-32(f) showing micro-cracking on fracture surface

It is very interesting to note nano-scale spherical precipitates settling within the fracture dimples of samples produced in the as-built condition as evident in Fig. 5-35. Precipitate formation was noted by Brooks and Choudhury to influence the dimple size by void coalescence [261]. The size and morphology of the precipitates is comparable to the CrN precipitates as explained in Section 5.2.6. Kynazeva *et al.* reported CrN precipitation leading to brittle cleavage fracture, while Zucato *et al.* reported a reduction in the toughness with the chromium nitride precipitation [162, 224]. The CrN precipitates probably will have a role to play in the higher strength of SLM duplex stainless steel in the as built state over the solution annealed counterparts. Precipitates in the SLM samples were reported to increase the tensile strength, as Palousek *et al.* and Song *et al.* both noted oxide formation in laser melted iron powder to restrict the dislocation movement and increasing the part strength [262, 263]. Saeidi *et al.* also reported CrN precipitation to strengthen the laser melted duplex stainless steel samples [235].

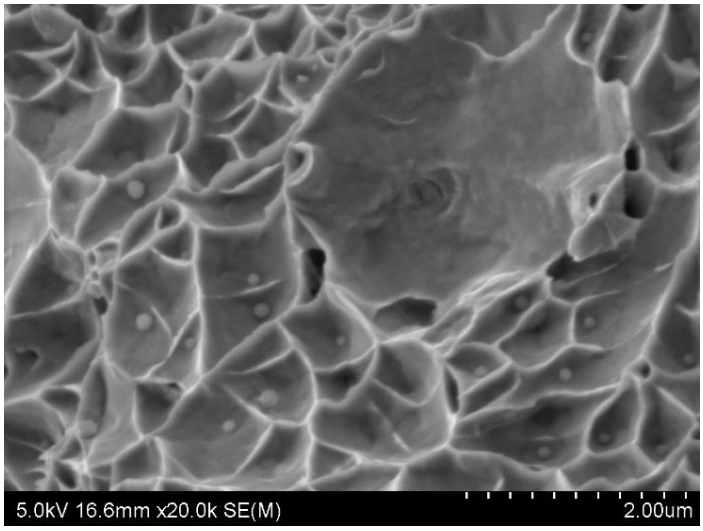

Fig. 5-35 High magnification of Fig. 5-33-(c) showing CrN precipitation on fracture surface

5.5 Summary of Metallographic and Mechanical characterisation

Duplex stainless steel powders are processed through selective laser melting and the metallographic evaluation of samples produced revealed significant changes in the microstructures as well as strong interactions with varying laser power and scan speed settings. The duplex structures are transformed into predominant ferrite grains elongated in the build direction, while the austenite precipitated either at the grain boundaries or as Widmanstätten laths growing across the ferrite grains. The crystal structures and orientations are affected around the cavities, while considerable CrN precipitation is also evidenced. Alternative scan strategies involving checkerboard patterns improved the part densities. Tensile strength levels of the laser melted duplex stainless steel samples are close to those of the wrought samples at all build orientations, but the ductility values reduced considerably after laser melting. Solution annealing heat treatment shows significant improvement in the percent elongation, but at the cost of some of the tensile strength. Micro dimples dominate the fractured surfaces, with CrN precipitation within the dimples, which enlarged after solution annealing heat treatment.

Chapter 6
Magnetic characteristics of selective laser melted duplex stainless steels

6.1 Magnetic Characterisation

Ferromagnetism refers to the nature of metals containing iron, cobalt, nickel, and rare-earth elements to exhibit magnetic responses when exposed to a magnetic field. Such materials are characterised by their magnetic memory, known as hysteresis, as noted by Nave, consisting of a relationship between the materials magnetic flux density (B) and the force of magnetisation (H) [264]. Saturation magnetism (Ms) refers to the condition of achieving alignment of all magnetic domains, with no further variation in the magnetic flux from increasing the magnetic field force. While magnetic saturation level is an important attribute, yet another property, coercivity (Hc), is also significant, which is the measure of the magnetic field (H) required to make the magnetic flux to reach zero. Hard ferromagnetic materials are characterised by their low initial permeability and high coercivities as noted by Fofanov and Riedner in excess of 3.76 mT, with both properties being desirable features for permanent magnets in motors, loud speakers and disk media as noted by O'Handley. Soft ferromagnetic materials exhibit higher permeability and magnetic saturation levels together with coercivities below 0.50 mT, and find uses in transformers and magnetic heads [265, 266].

As is established in the previous chapter, duplex stainless steel processed by SLM is very sensitive to process conditions. Considering the drastic thermal variations in SLM leading to the severe microstructural alterations, significant changes are likely in the ferromagnetic responses of the alloy. Gregorutti *et al.* reported duplex stainless steel to show characteristics of a weak soft ferromagnetic material in both the as-cast and the solution annealing states [57]. Although the ferromagnetism dominates the duplex microstructure through ferrite, austenite is reported by Sathirachinda *et al.* to present paramagnetic behaviour [267]. A significant quantity of research has focused on altering the magnetic properties through aging heat treatments. For example, Mészáros and Szabó,

observed the ferrite decomposition resulting in the decease of the magnetic saturation levels in the SAF 2507 grade duplex stainless steel [268]. Lai and Wong patented the technique of achieving the magnetic property variation with temperature, where magnetic saturation could be decreased with appropriate temperature conditioned, that resulted in the transformation of ferrite into deleterious precipitates and phases [269].

Process-structure relations and the resulting variations are reported in the literature to profoundly affect the magnetic properties. Increasing the σ-sigma phase content by means of elevated aging time and temperature was correlated to decreasing saturation magnetism in duplex stainless steels by Tavares *et al.* [166]. The magnetic properties of 304-austenitic stainless steel were observed to be drastically influenced by the martensitic content. Ferromagnetic α' Martensite induced by cold rolling of the 304 stainless steel was seen to increase with deformation as reported by Mumtaz *et al.*, leading to increasing magnetic saturation, whilst coercivity (Hc) decreased due to grain enlargement [270].

The process-structure relationships are more prominent in SLM, but the consequent variations in magnetic properties attained very little attention by far. Fe-30%Ni and Fe-80%Ni powders were synthesised by Zhang *et al.* via SLM with varying process conditions and the evaluation of the magnetic responses established 5.7 times higher saturation and the lowest coercivity levels, with the higher Fe-powder mixture [271, 272]. Duplex stainless steels in particular are very sensitive to process conditions and considering the drastic thermal variations in SLM, will undergo severe microstructural alterations, as already identified. These aspects may lead to significant changes in the magnetic responses. There is hardly any evidence of such data being reported so far, and this chapter allows an insight into the microstructure-magnetic response relationships in duplex stainless steels processed by SLM. The multi-layer samples developed as part of the initial trials reported in Chapter 4 are used for these studies.

6.2 Ferrite to Austenite Ratios

Samples for magnetic characterisation are developed by slicing the cubic samples analysed in the preliminary experiments (Section 4.2). Accordingly, samples are prepared based on the cubic samples produced at laser powers from 175-400 W in 25 W increments at a constant scan speed of 590 mm/s, corresponding to a laser energy density range of 49.4-113 J/mm^3 with a 7.1 J/mm^3 increment. While printing, these samples are located atop the build platform as per Table 4-1 following the conventions discussed in Section 3.1.4. Sample preparation is detailed in Section 3.8 while an additional slice of SAF 2507 rolled plate is used as a reference. A single sample at each energy density was tested for its magnetic saturation and coercivity due to time and cost limitations.

Table 6-1 Magnetic characterisation sample build parameter layout

Parameter	***Row***	***Column***	
		Parameter	
		Laser Power (W)	
		A	**B**
Laser Power (W)	**1**	175	300
	2	200	325
	3	225	350
	4	250	375
	5	275	400

As discussed previously in Chapter 4, the thermo-mechanical characteristics of the SLM process distorts the equilibrium equal ferrite and austenite structure and results in a predominantly ferritic microstructure. It is important that the balanced duplex structure is maintained, in order to fulfil the mechanical strength and the chemical resistance characteristics expected of duplex stainless steels. Further, the unbalanced, predominantly ferritic structure might give rise to the soft magnetic characteristics to the laser melted duplex stainless steel. The microstructural variations emanating from laser melting of duplex steels are discussed more elaborately in both Chapters 4 and 5. One of the photomicrographs is reproduced here in Fig. 6-1 for an immediate visualisation of the changes caused by SLM, in view of the possible effects on the magnetic responses. Once

again, the white areas are the ferrite matrix, the dark lines depict the austenite growth along grain boundaries and as Widmanstätten needles. The dark void at the top right corner is a lack of fusion defect within the sample.

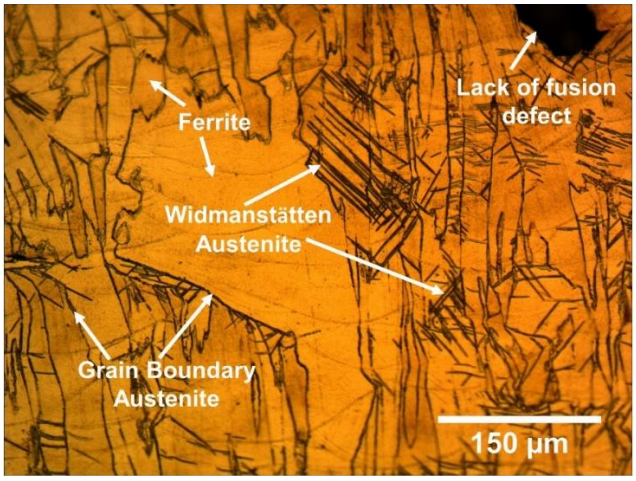

Fig. 6-1 Photomicrograph of a SLM sample built at 98.9 J/mm³

Ferrite contents are accurately determined with each sample, based on Feritscope measurements, evaluating the variances in the magnetic induction as discussed in Section 3.5.7. Fig. 6-2 presents the average values and standard deviations of the Feritscope results for each of the SLM samples. In general, the ferrite content is observed to decrease with increasing LED and reaches a minimum of 67.11% at 84.7 J/mm³, followed by a slight increase from 91.8-113 J/mm³. The maximum ferrite content of 73.2% observed at 49.4 J/mm³ is comparable to the average ferrite content of 75-78% reported by Saeidi *et al.* in the laser melting of the same powder as used in this study [235]. It is evident that SLM processed duplex stainless steels contain an average of 70% ferrite which is characteristic of the rapid cooling rates impairing the austenite growth.

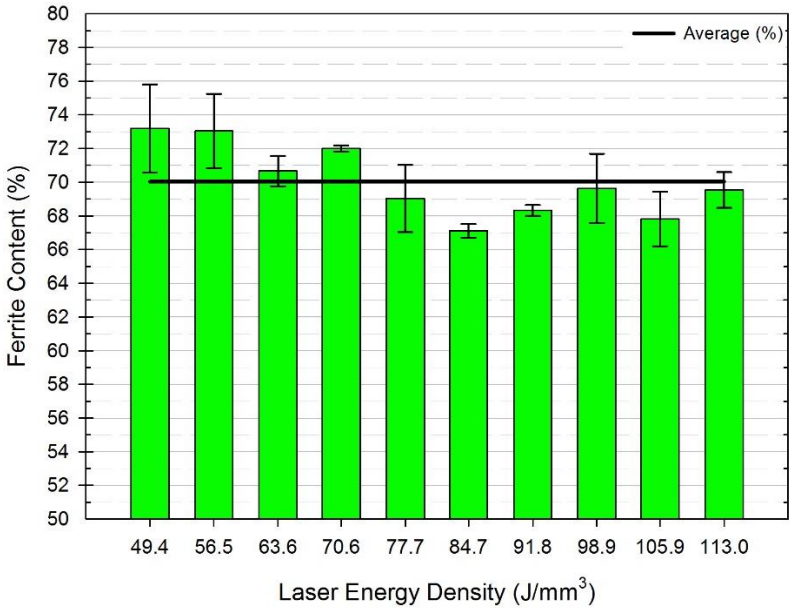

Fig. 6-2 Ferrite content vs LED

6.3 Magnetic Hysteresis Loops

Hysteresis loops obtained via vibrating sample magnetometer tests as explained in Section 3.8 are used to establish the Saturation Magnetism (Ms), Coercivity (Hc), and Remnant Magnetism (Mr) of the current samples. A comparative evaluation of the SLM samples, the wrought SAF 2507 duplex stainless steel, and other sources of information from the literature is presented next.

6.3.1 Saturation Magnetism

Results presented in Fig. 6-3 show a slight variation in the saturation magnetism (Ms) values obtained over the range of energy densities employed with a slight decrease in Ms with increasing LED. This can be related to the ferrite content in the microstructure which noted by Mészáros to be a linear relationship [273]. Comparing the results in Fig. 6-2 and Fig. 6-3, similarities between Feritscope findings and the saturation magnetism results may be noted, though a comparable relationship is not evident, probably due to the complex process mechanics and the presence of porosity. However, it is interesting to

note that there is a dramatic difference in the average Ms value of SLM samples, compared to the wrought duplex stainless steel. SLM samples saturated on average at 110.9 Am²/kg which is over twice as large as the value with the wrought sample at 45.1 Am²/kg. This correlates to an average increase of 20% ferrite in the SLM microstructure, constituting an average rise of 3.29 Am²/kg in saturation magnetism for 1% rise in the ferrite content, beyond the normal 50%. As eluded prior, the predominantly ferritic microstructure of SLM samples is the main contributor to the increased saturation magnetism.

Magnetic saturation levels of duplex stainless steels processed by different means are presented in Table 6-2. Evidently, laser melting gives rise to greater Ms values than normally obtained in any wrought duplex stainless steels. Comparable results are noted with wrought UNS S39205, oil quenched from 1300 °C [274]. As noted by Tavares *et al.*, both the oil and water quenched UNS S32905 duplex stainless steels saturate at a greater potential than the SLM samples. Water quenching was reported to lead to a saturation of 133 Am²/kg which is the equivalent of the saturation levels with 100% ferrite [274]. As the SLM process is highly anisotropic with grain growth in the direction of the build, grain orientation has been reported to have a <001> crystallographic texture in comparable stainless steels by Niendorf *et al.* [193]. This texture is desired in the production of Fe-Si soft magnetic steel where it is known as the Goss texture which facilitates changes in magnetic moment and minimises hysteresis losses. Probably the combined effect of increased ferrite content and potentially <001> crystallographic orientation led to the high magnetic saturation levels noted with the SLM samples.

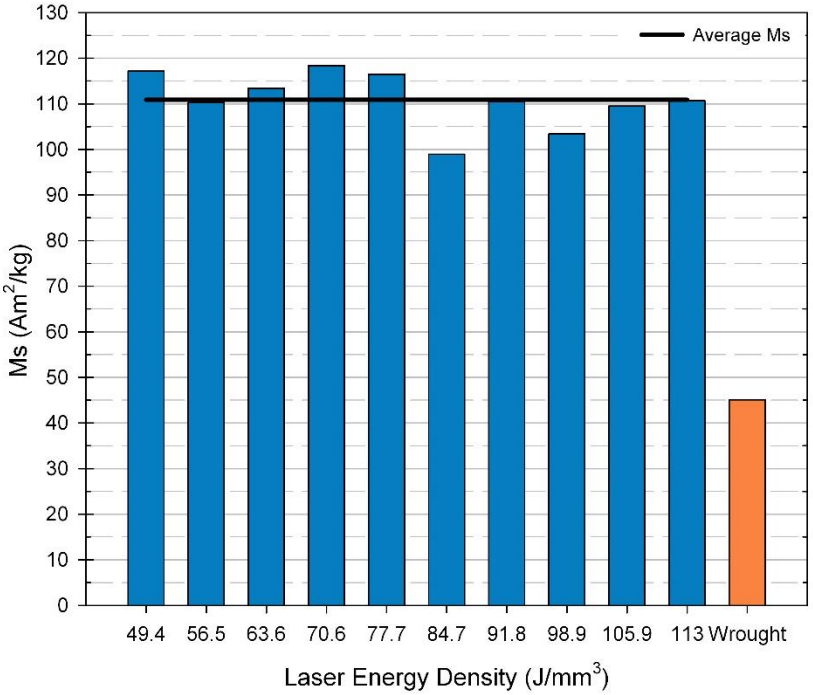

Fig. 6-3 Saturation Magnetism results SLM samples produced at varying Laser Energy Densities

Table 6-2 Magnetic saturation values of comparable duplex stainless steels

Material	Condition	Ms (Am^2/kg)	Researcher
SAF 2507 (UNS S32750)	SLM (Avg)	110.9	This study
SAF 2507 (UNS S32750)	Wrought	45.1	This study
UNS S31803	Wrought	56.6	Tavares *et al.* [166]
	Cold Rolled	57.8	
7MoPLUS (UNS S32950)	Sol Treatment	60	Lo *et al.* [275]
UNS S39205	Furnace Cooled	16.1	Tavares *et al.* [274]
	Air Cooled	84.6	
	Oil Quenched	113.7	
	Water Quenched	133.0	

6.3.2 Coercivity

The variation of coercivity (Hc) with laser energy density is depicted in Fig. 6-4. Compared to the variation in Ms, coercivity is seen to increase with LED from 56.5-98.9 J/mm^3, culminating with the highest value at 2.58 mT, prior to decreasing to 2.13 mT at 113 J/mm^3. However, as there is only a single sample tested at each energy density trends

cannot be defined. Comparatively, wrought SAF 2507 duplex stainless steel has a coercivity of 0.92 mT just over half of the average coercivity 1.81 mT of SLM samples. Similarly low coercivities of 0.73 and 0.75 mT were reported by Fofanov and Riedner for SAF 2205 and SAF 2304 in the wrought condition [265]. A similar relationship between Ms and Hc was observed by Mumtaz *et al.* in the cold rolling of 304 austenitic stainless steel, whereby increasing the rolling percent increased the ferromagnetic martensite (α') content in the microstructure and corresponding Ms, while the coercivity decreased [270].

Based on the magnetic property definitions in Section 6.1, duplex stainless steels processed by SLM and comparable wrought duplex stainless steel grades presented in Table 6-3 are predominantly soft ferromagnetic materials. Duplex grades UNS S39205 and S31803 evaluated by Tavares et al. have coercive forces between 14.77-26.46 mT, over eight times the values obtained for SLM duplex stainless steel. SLM processing of duplex stainless steel results in a stronger soft ferromagnetic material than the wrought alternatives. This variance in coercivity is directly related to the grain size. Evidence of this is shown by Zhang *et al.* in the SLM of Fe-30%Ni powder in which coercivity reached a minimum of ~0.094 mT at laser power and speed settings optimised for part density and large grain size [271]. A linear relationship between coercivity and the inverse of grain size was established by Landgraf *et al.* for U260 electrical steel [276]. The variations in the coercivity values depicted in Fig. 6-4 are probably due to the differential grain sizes noticed comparing the SLM and wrought samples.

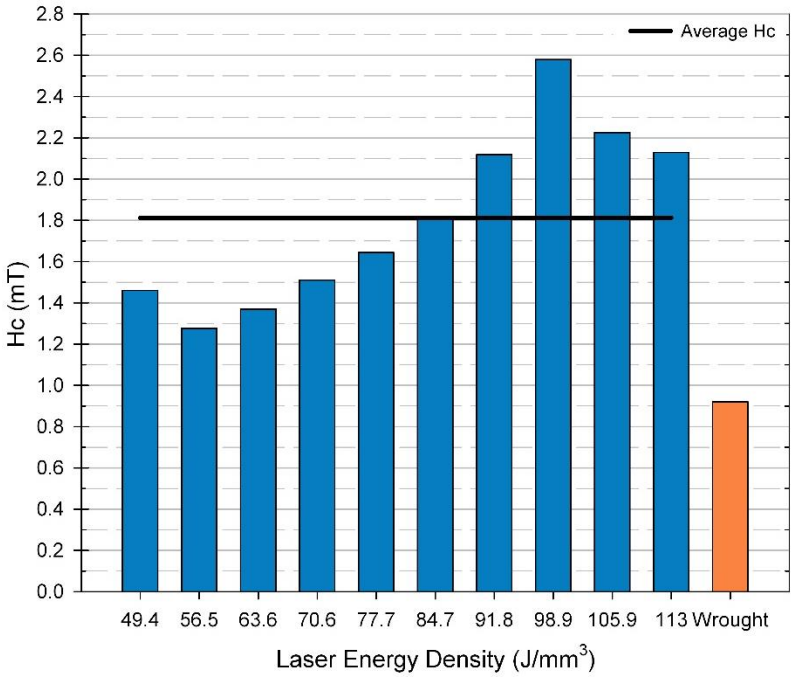

Fig. 6-4 Coercivity results with SLM samples produced at varying Laser Energy Densities

Table 6-3 Coercivity values of comparable duplex stainless steels

Material	Condition	Hc (mT)	Researcher
SAF 2507 (UNS S32750)	SLM (Avg)	1.81	This study
SAF 2507 (UNS S32750)	Wrought	0.92	This study
UNS S31803	Sol Treatment	26.46	Tavares *et al.* [277]
UNS S39205	Furnace Cooled	15.37	Tavares *et al.* [274]
	Air Cooled	15.17	
	Oil Quenched	15.07	
	Water Quenched	14.77	

6.3.3 Anisotropic Features

The selective laser melting process results in the highly anisotropic structures as reported by Neindorf *et al.*, as well as observed from the current results, presented earlier. The grain growth is aligned along the build direction and results in the narrow and elongated grains, with strong crystallographic textures, primarily in the [001] plane [193]. It is important to establish how this anisotropy affects the magnetic responses. The SLM sample produced at LED 91.8 J/mm³ is considered for this purpose.

As shown in the photomicrograph of Fig. 6-5, the magnetic hysteresis results are obtained both perpendicular (a) and parallel (b) to the direction of alignment of the grains. The hysteresis results show that the sample vibrated perpendicular to the grain growth direction has a typical soft magnetic hysteresis curve with a high rate of magnetism, saturating at 120.43 Am²/kg and coercivity 2.23 mT. Comparatively, results in the other direction indicate a similar saturation value (104.98 Am²/kg), but with lesser permeability (M/H) and almost double the coercivity, at 5.49 mT. As the saturation magnetism is primarily affected by the ferromagnetic constituents in the microstructure, the effect of sample orientation on this is relatively low. On the other hand, the coercivity increases with grains orientated along the direction of vibration due to a restriction in the magnetic domain movement, suggesting the formation of the hard axis of magnetisation.

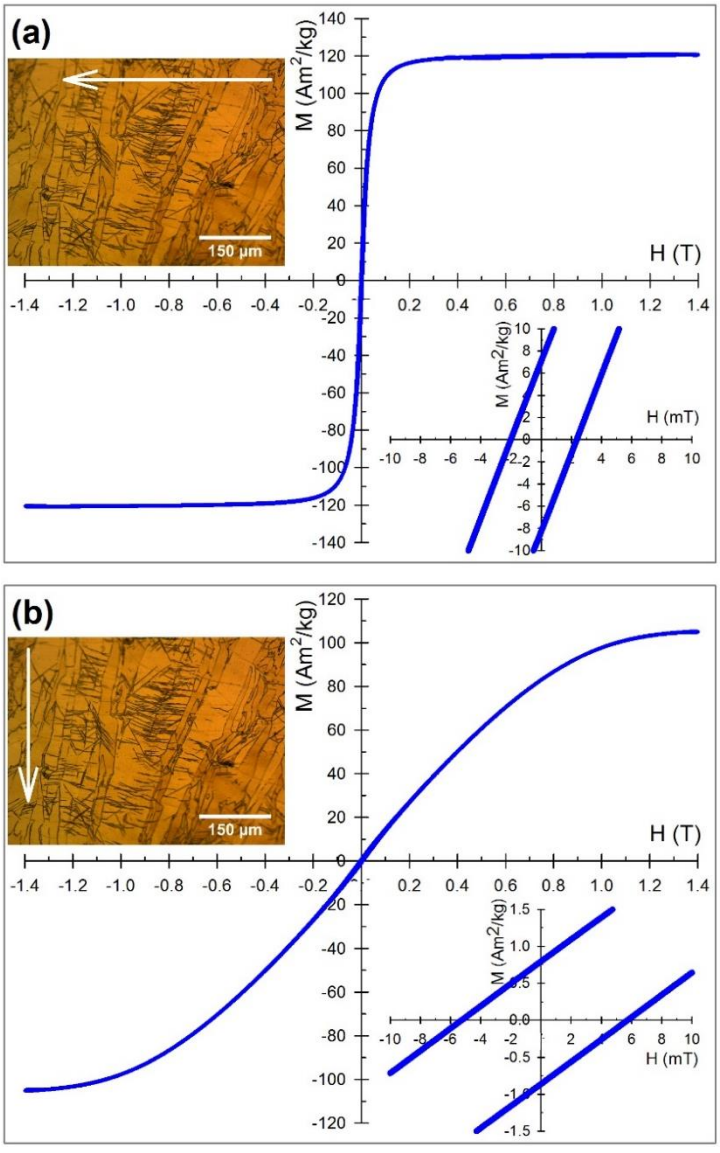

Fig. 6-5 Hysteresis loops for the 91.8 J/mm³ sample with grains; perpendicular (a) and parallel (b) to the direction of vibration. Inset: microstructure orientation. Detail of graph intersection and coercivity.

6.4 Summary of the magnetic responses

Selective laser melted duplex stainless steel samples are evaluated for the magnetic responses. Feritscope readings further ascertained the dominance of the ferrite phase over the austenite phase in the laser melted duplex stainless steel samples. The magnetic responses are also conclusive of the predominantly ferritic microstructure in the laser melted samples. Generally, the magnetic saturation levels are much higher compared to the wrought duplex steels, while the coercivity levels are lower than duplex stainless steel reported in literature. Anisotropic hysteresis results are noted due to the microstructural anisotropy.

Chapter 7
Machining and machinability of laser melted duplex stainless steels

7.1 Non-equilibrium structures and the anomalies

Establishing the principal responses of duplex stainless steels to processing by selective laser melting is the overall objective of this research. The preliminary metallographic structures reported in Chapter 4 and the more advanced micro-structural and mechanical response evaluations elaborated in Chapter 5 proved the material-process combination to be viable. However, the material, process, and structural relationships are complex and lead to the understanding that certain structural abnormalities might arise. The predominant ferritic structure in the duplex steel is an example. Based on the structure and property relationships, these non-equilibrium structures might lead to specific anomalous attributes. The predominant ferritic structures converting the duplex into a soft magnetic material as evaluated in Chapter 6 is an interesting after-effect. Considering the difficult-to-machine nature of duplex stainless steels in the wrought form, it is also interesting to assess how the structural variations induced by laser melting would influence the machinability responses. This chapter is dedicated to the discussion of the experimental evaluations undertaken while machining laser melted duplex stainless steels with varying process conditions and the results obtained.

First, a comparative study is undertaken, evaluating the machinability of the laser melted duplex stainless steel samples against that of the wrought SAF 2507 super duplex stainless steel. The structure vs machinability responses are identified, with varying speeds and feeds as discussed in the later sections of this chapter. Laser energy density is the most significant parameter in the selective laser melting process. Consequently, a set of SLM samples produced with different laser energy densities are compared to wrought duplex stainless steel for their influence on machinability characteristics and the microstructural variations with a specific speed and feed combination. The second-stage tests allowed to converge on 178.6 J/mm^3 as the most promising energy density to achieve the best

machinability. Further studies involving the experimental evaluation of the relative machinability responses of the as-built and the solution-annealed SLM samples are conducted with the energy density fixed at this level, but with varying cutting speeds and feeds.

7.2 Mechanism of machining and metallographic responses

Machinability studies were undertaken through drill tests based 25X25X30 mm samples. The samples size was decided considering the costs involved and also in view of allowing sufficient time to record the machining responses. The machining conditions are summarised in Table 7-1 and discussed at greater length in Section 3.9. As presented in Section 3.9.2, an Iscar Sumocham indexable head drill body and corresponding Sumocham IC908 insert are used in the comparative experiments of SLM and wrought duplex stainless steel and in the evaluation of the machinability of SLM samples processed with varying laser energy densities. The larger machinability study on SLM samples in the as-built and solution annealed state were conducted using solid carbide Sandvik CoroDrill, one for each test.

Table 7-1 Machinability condition window

Test Name	Sample Type	LED (J/mm³)	Cutting Speed (*Vc*) [m/min]	Feed (*f*) [mm/rev]
Wrought vs SLM	SLM	194.4	20, 40, 60, 80	0.025, 0.05
	Wrought SAF 2507	-	20, 40, 60	0.025, 0.05
Varying LED Evaluation	SLM	135.5, 154.8, 178.6, 194.4	60	0.025
SLM: As-Built vs Solution Annealed	SLM – As-Built	178.6	20, 60, 100, 140	0.025
	SLM - Solution Annealed			

Laser energy densities levels used for machinability samples followed those applied to tensile testing samples (Chapter 5); 135.5, 154.8, and 178.6 J/mm³. An additional LED of 194.4 J/mm³ was selected virtue of its improved consolidation in cubic trials produced in Section 4.4, with additional corresponding parameters presented in Table 7-2. A linear scan strategy is employed, with samples placed atop the substrate as per Section 3.1.4. Comparably sized samples are machined from SAF 2507 wrought bar stock and machined at identical conditions to SLM samples produced at 194.4 J/mm^3, forming the initial comparative machinability assessment. With the selection of 194.4 J/mm^3 for this assessment by virtue of its greater disparity from the wrought material.

Table 7-2 SLM processing parameters

LED (J/mm^3)	Laser Power (W)	Laser Scan Speed (mm/s)	Scan Line Spacing (µm)	Powder Layer Thickness (µm)
135.4	325	400	120	50
154.8	325	350		
178.6	375	350		
194.4	350	300		

The order of samples and sample location and specific naming convention is defined in Section 3.1.4.

7.2.1 Wrought vs SLM samples

As already elaborated, microstructural differences are clearly evident between the wrought and the laser melted duplex stainless steel samples, indicative of varying machinability responses across all drilling conditions used. Photomicrographs of drilled samples are presented in Fig. 7-1 and 7-2, and significant microstructural differences are clearly evident. The wrought duplex stainless steel structure shows an almost equal ratio of α-ferrite (darker phase) and γ-austenite (lighter phase) in long slender grains 20-25 µm in width with an irregular morphology. Comparatively, large columnar α-ferrite (lighter phase) grains intertwined by γ-austenite (darker phase) as grain boundary precipitate and Widmanstätten needles are the characteristic features of the SLM structures. Distinctive to the wrought material is the grain elongation from plastic deformation along the length

of the drilled hole as seen in the photomicrographs pertaining to the wrought samples in Fig. 7-1 and 7-2, and to a greater detail in Fig. 7-3.

The relative contents of different phases as well as the structural differences will influence the machining process, which is the drilling of the vertical holes through the specimens in these cases. A quick comparison of both Fig. 7-1 and 7-2 clearly shows significant differences in the microstructures as well as the macro deformations in the wrought and laser melted samples. The sectioned edge of the surface of the hole in all the wrought cases shows a wavy pattern along the length of the hole. Periodic depressions and associated microstructural changes are noted. The nature of formation of these variations, leading to characteristics structural kinks generated at regular intervals as the hole is drilled probably indicate the effects of cold working in the case of the wrought samples. Contrastingly, the corresponding section edges are quite straight and smooth and with no evidence of any structural variations as may be seen in all the photomicrographs of the SLM samples (Fig. 7-1 and 7-2-(b), (d), (f), and (g)).

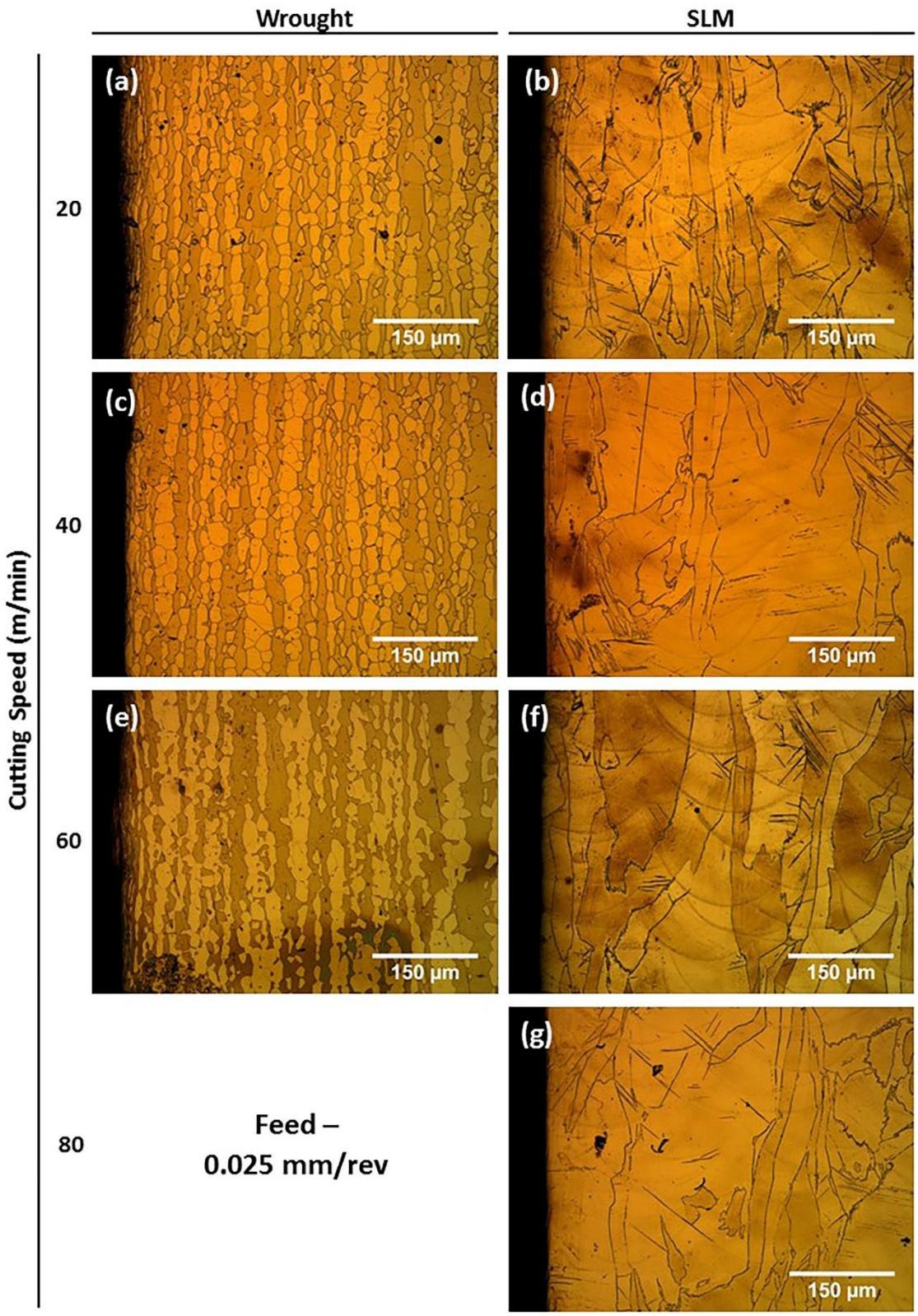

Fig. 7-1 Microstructural images of wrought and SLM samples at a feed of 0.025 mm/rev

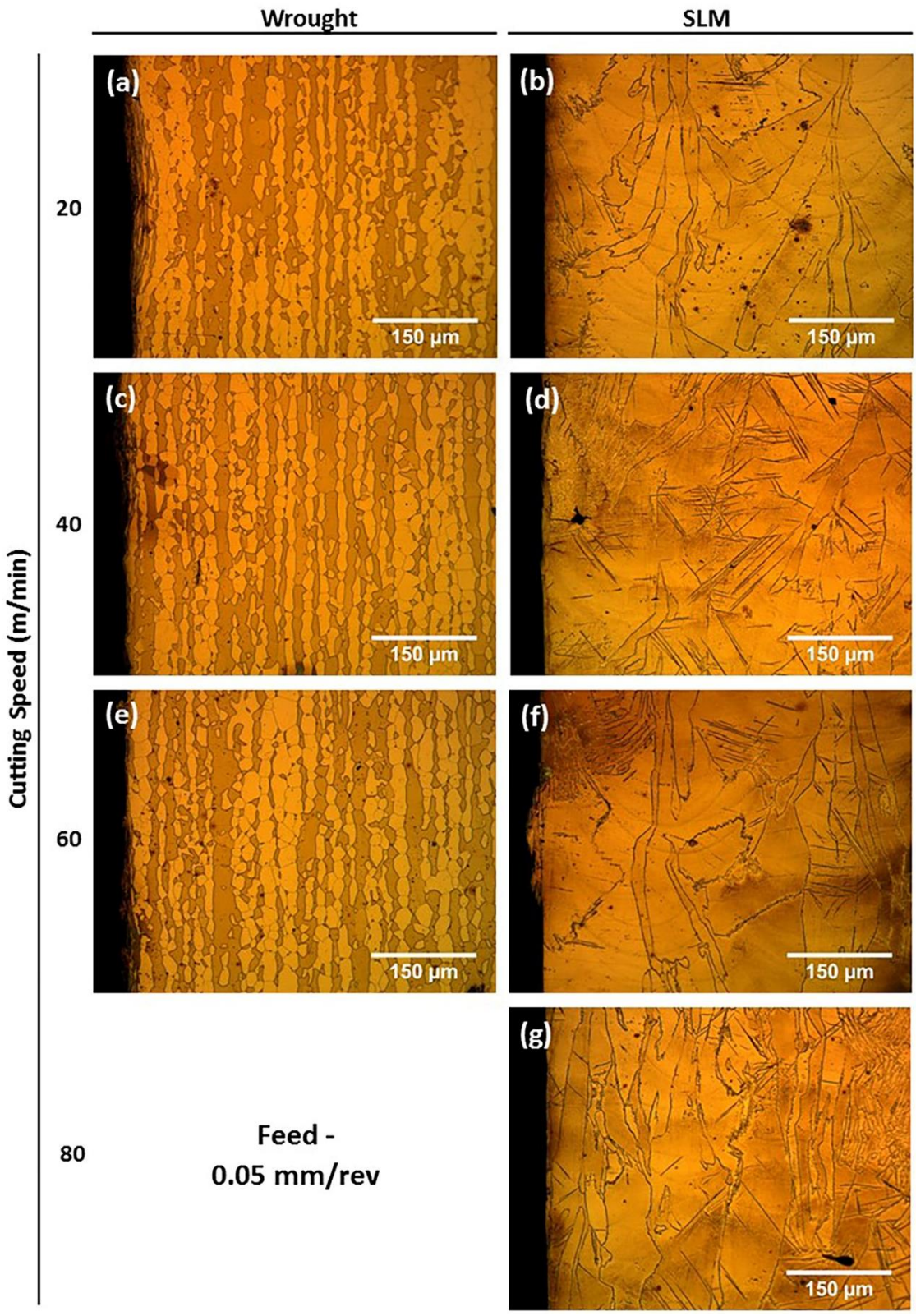

Fig. 7-2 Microstructural images of wrought and SLM samples at a feed of 0.05 mm/rev

A closer look at the characteristic structural kinks formed in the case of the wrought samples as presented in Fig. 7-3 will allow further insight into the mechanism of its formation. The cyclic grain compression process led to arching of the ferrite grains with

the austenite trapped in between, leading to almost closely interspersed and highly stretched alternate ferrite and austenite grains, as evident in Fig. 7-3-(b). Grain deformation is seen to occur at depths as great as 30 µm in which the austenite grains are compressed to <1 µm closest to the hole surface. Austenite also seems to retain its morphology, further to the severe plastic deformation. Similar observations were also made by Nomani *et al.* based on the observations from experiments involving quick-stop drilling operations. These were reported to be regions of work hardening, resulting from large deformations [278].

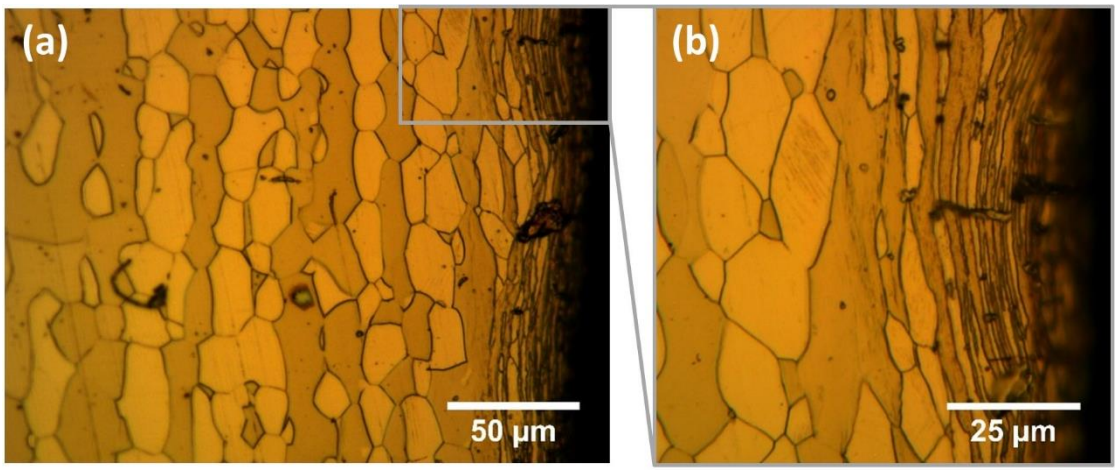

Fig. 7-3 Grain elongation and deformation kinks in wrought duplex stainless steel machined at 20 m/min and 0.025 mm/rev

For a closer comparison, photomicrographs of one wrought and one SLM Laser melted samples are presented at the same magnification in Fig. 7-4-(a) and (b) respectively. There is also some evidence of the work hardening and grain deformation in the SLM sample shown in Fig. 7-4-(b). However, this is rarely observed and considering the severe distortion at the edge of the surface, is probably due to a failure of the cutting edge and subsequent severe local deformation. As a result of the predominantly ferritic microstructure there is less visible compression of austenite, and the dark irregular lines stretching could be cavities generated due to the catastrophic failure of the drill cutting edge.

The microstructural differences between the two duplex stainless steel forms are the deciding factors for the rate of plastic deformation. In addition to the non-equilibrium

ferrite to austenite ratio, CrN precipitates as already reported in Chapter 5 also play a role in the laser melted duplex stainless steel. Knyazeva and Pohl report CrN precipitates in duplex stainless steel making it brittle and hard and probably leading to an improved machinability [224]. In the duplex structure, the austenite phase is in a metastable condition. Work hardening effects or heating will first affect austenite to change over to the other forms. The reduced austenite content in the laser melted samples perhaps results in a lower tendency to work harden and the consequent lack of severely deformed structural kinks. Micro hardness results are obtained and discussed next in order to quantitatively ascertain these structural variations.

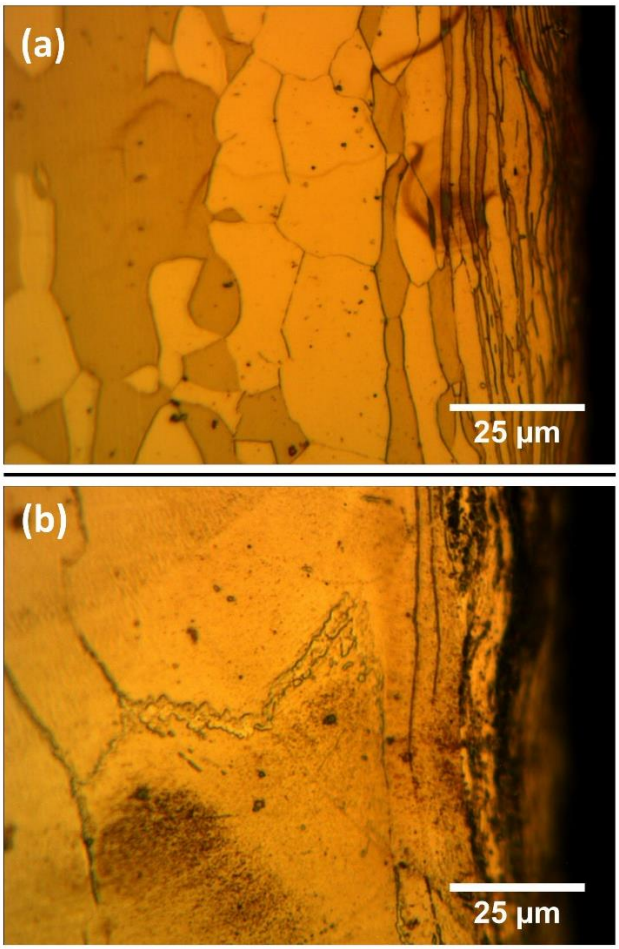

Fig. 7-4 Plastic deformation of austenite grains in wrought (a) and SLM (b) samples machined at 20m/min and 0.05 mm/rev

Micro-hardness results presented in Fig. 7-5 show the variation in the hardness from the hole surface to the bulk material, across the sectioned surface of the drilled specimens. A decreasing trend in hardness with increasing distance from the edge of the hole is evident

for all conditions. The micro-hardness values from the wrought duplex stainless steel samples varied, exponentially decreasing with the distance from the surface edge of the hole as seen clearly in both Fig. 7-5-(a) and (b). Micro-hardness results are closely related to the extent of grain compression. At both feeds used, the lower cutting speeds at 20 m/min and 40 m/min resulted in higher hardness values. Further, the samples drilled at the greater feed of 0.05 mm/rev are on average harder by about 111.3 HV than the lower feed cases, at a distance of 25 µm. The overall maximum hardness is at around 702.6 HV, attained with 40 m/min cutting speed and 0.05 mm/rev feed.

The SLM samples presented in Fig. 7-5-(c) and (d) indicate relatively minor variations in the micro-hardness values across the cross-sectional surface of the drilled hole. While the curves remained almost flat and horizontal in most cases, there is also a drastic variation in the ranges of micro-hardness values obtained from the wrought to the SLM samples. For most cases, the average difference in the micro-hardness values is at around 100- 150 HV between the wrought and SLM samples, for given process parameter combinations. Further, the overall variation in the hardness is at around 186.5 HV between different SLM samples and 392.2 HV with the wrought samples.

A closer look at these results is essential now attempting to correlate the micro-structure and hardness responses. For example, Fig. 7-5-(a) indicates that micro-hardness values increased first, attained a maximum and then decreased with the cutting speed increasing from 20 to 60 m/min at all the points where readings are taken. Looking at the corresponding photomicrographs given in Fig. 7-1-(a), (c), and (e), it is evident that the severity of grain compression is higher at both 20 m/min and 40 m/min, which is not supportive of the micro-hardness variation. However, it may be noted that in the cases where there is a clear formation of the compression kinks, the tool is suddenly released after crossing a grain compression zone, perhaps due to build up forces and consequent increase in the temperature values. When this happens, the strain hardening effects are relatively lesser, immediately after crossing each of the grain compression regions. The variation in the micro-hardness values as presented in Fig. 7-5-(a) and (b) will then be location specific. These discrepancies are relatively minor as the overall variation in the results is less in the case of the SLM samples, as seen in Fig. 7-5-(c) and (d), which is also indicative from the photomicrographs of Fig. 7-1 and 7-2.

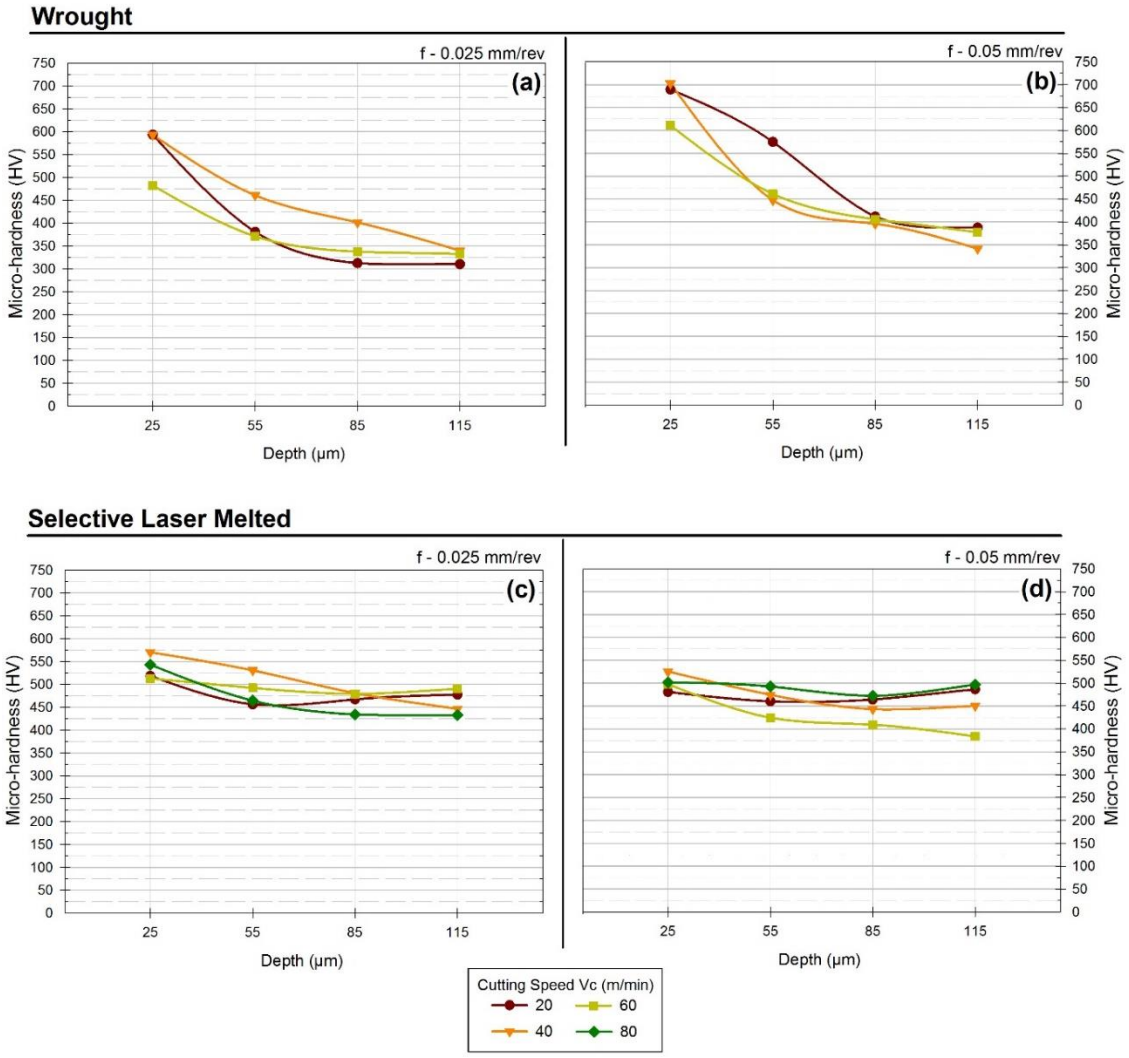

Fig. 7-5 Micro-hardness results from wrought (a)-(b) and SLM (c)-(d) samples

Images of chips presented in Fig. 7-6 and 7-7 show variances in the chip breaking nature, between the wrought and the laser melted duplex stainless steel specimens. Chips produced while machining the laser melted samples are predominantly discontinuous, suggestive of the nature of a brittle material. The straw colour is indicative of temperatures between 370-390 °C, as reported by the British Stainless Steel Association [279]. Hard and brittle materials were noted by König *et al.* to form discontinuous chips, as the high compressive stresses lead to the propagation of the cracks releasing the energy contained [280]. Contrastingly, the chips produced while drilling the wrought specimens are relatively long and thick with a dark brown and blue colour, indicative of average temperatures at around 600 °C [279].

At both the feeds employed, the tendency to form continuous chips is slightly decreased with increasing speed, as evident in both Fig. 7-6-(e) and 7-7-(e). Long ribbon chips were observed due to the ductile nature of duplex stainless steels, at 20 and 40 m/min at both feeds, while drilling wrought duplex stainless steel samples (Fig. 7-6-7.7-(a) and (c)). The long and continuous chips indicate possible lack of removal of heat generated and subsequent heating of the tool and work domains. This will be verified based on the temperature results discussed later. Çiçek *et al.* and Lin *et al.* noted excessive tool wear to result in the transition into long ribbon chips in the drilling of austenitic 304 stainless steel, from the tightly helical chips, evident at the bottom of Fig. 7-7-(a) and (c) [281, 282]. Increasing cutting speeds and feeds are seen to decrease the lengths of chips in the SLM samples, with the latter having a greater effect over the former. These are characteristics of a hard material, as was also noted by Dolinšek *et al.* while machining hard steels, that increasing cutting speeds could lead to lead to increased chip segmentation [283].

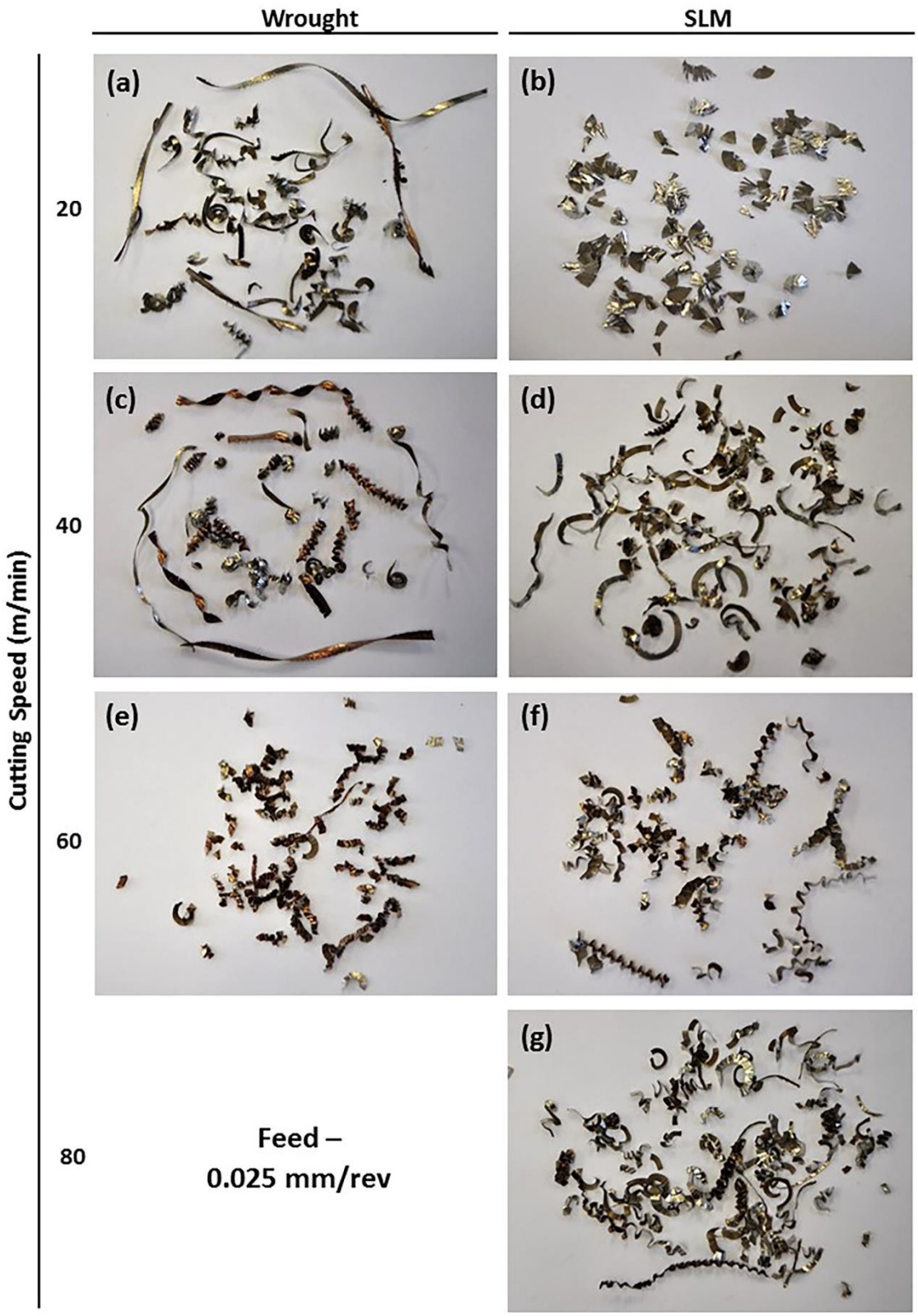

Fig. 7-6 Chip images of Wrought and SLM samples at a feed of 0.025 mm/rev

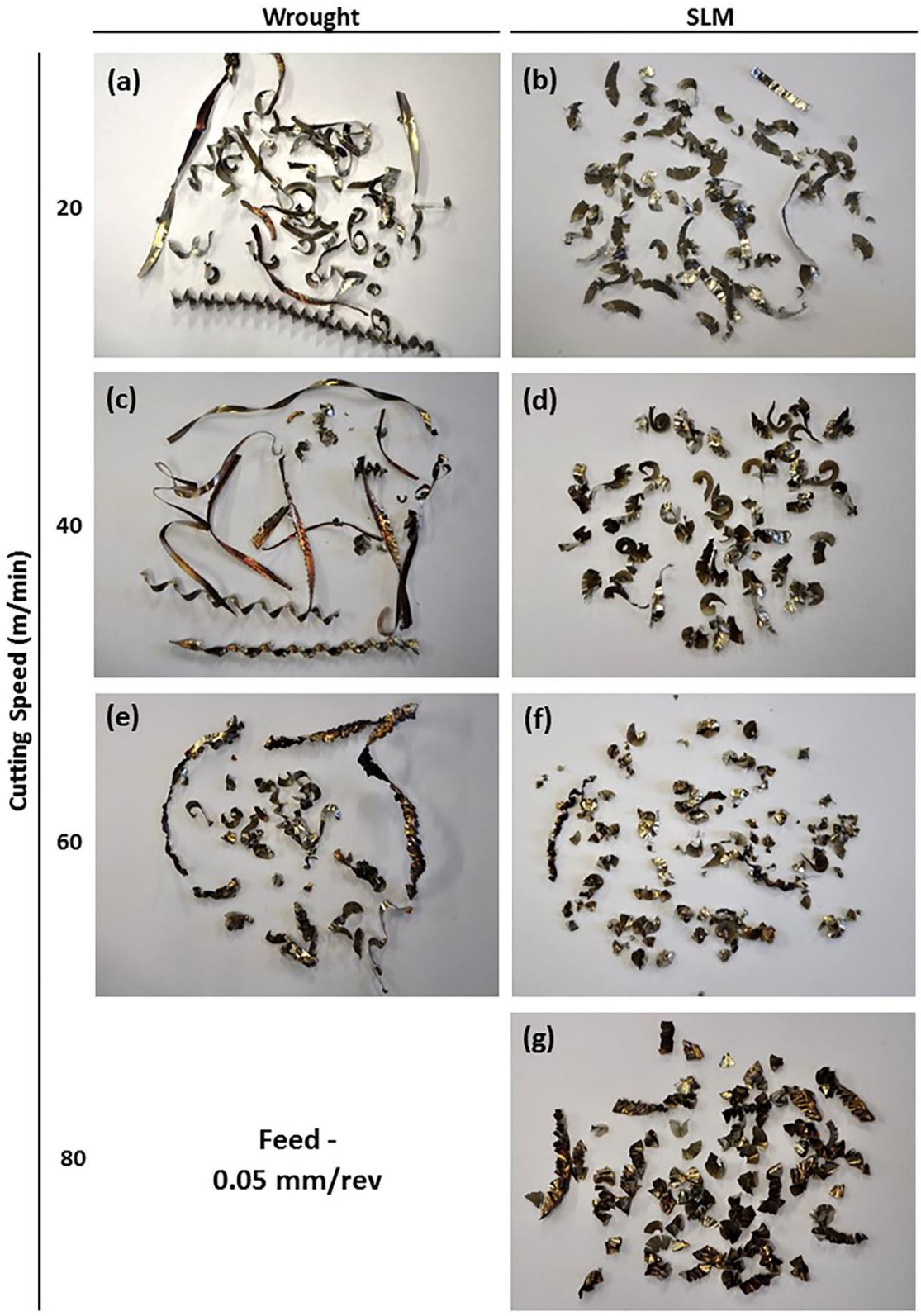

Fig. 7-7 Chip images of Wrought and SLM samples at a feed of 0.05 mm/rev

7.2.2 The role of the varying laser energy density

Photomicrographs of samples produced with varying energy densities and drilled at 60 m/min and 0.025 mm/rev are presented in Fig. 7-8. Overall the SLM samples have comparable microstructures with larger columnar ferrite grains enclosed by grain boundary austenite and intersecting Widmanstätten austenite needles. A greater volume of Widmanstätten austenite is observed in the sample produced at 178.6 J/mm^3 (Fig. 7-8 (c)) however, there is no discernible difference in the plastic grain deformation along the edge of the drilled hole. A greater volume of porosity is observed in the samples produced at 135.5 and 154.8 J/mm^3 probably due to lack of fusion. This might lead to intermittent cutting to a minor extent and possibly damage the cutting edges of the drill tools. As machinability is significantly influenced by the thermal conductivity, increasing porosity decreases the machinability as reported by Agapiou *et al.* in a machinability study on 304L austenitic stainless steel [284]. Dorofeev *et al.* reported a significant increase in tool life in the machining of a ferritic alloy produced by powder metallurgy by reducing the porosity from 2.5 % to 0.5% [285].

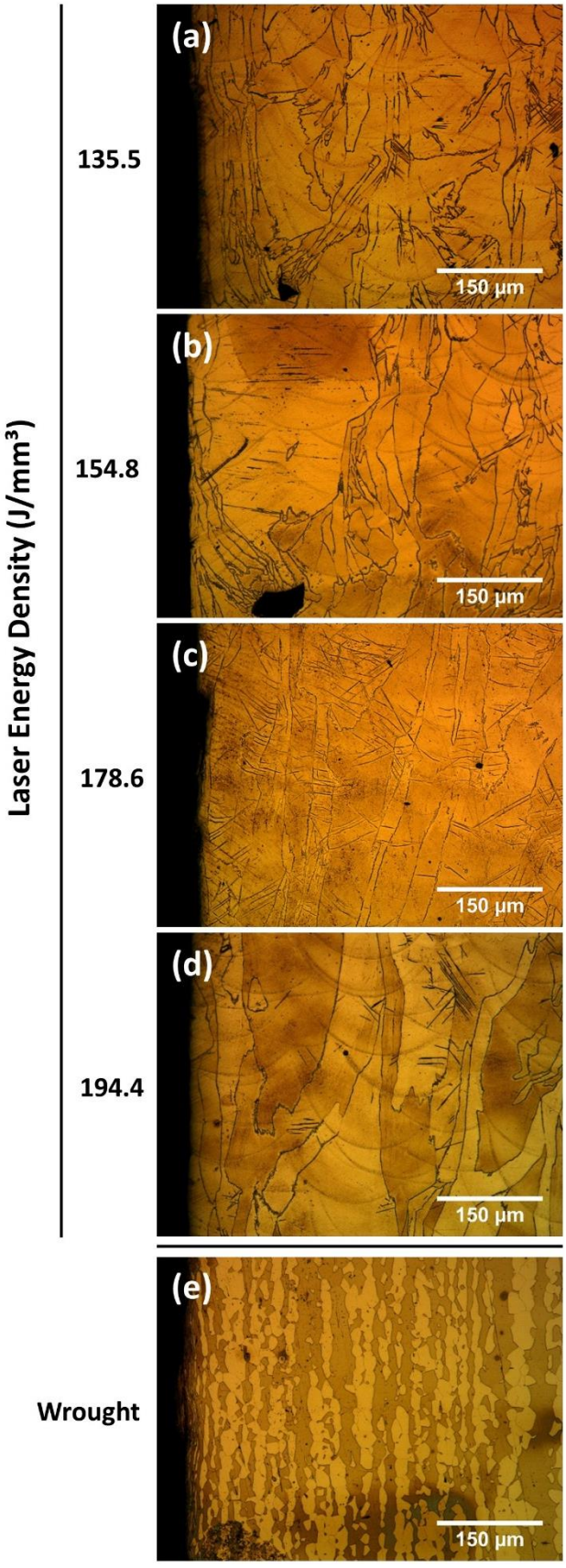

Fig. 7-8 Microstructural images of SLM samples at four LED's and wrought duplex stainless steel at Vc – 60 m/min, f – 0.025 mm/rev

The bulk hardness values measured based on these samples are presented in Fig. 7-9. A clear difference between the SLM and the wrought samples is immediately evident from the results of Fig. 7-9. Laser melted samples are on average 15.1 HRC harder than the wrought duplex stainless steel sample. The highly distorted microstructure with the fine cellular sub grains and the hard CrN precipitates probably led to the higher hardness in the SLM samples. The highly ordered columnar grains of the laser melted samples also likely to result in higher hardness as was observed by Song *et al.* in the laser melting of iron powder [202]. Residual thermal stresses also might cause a rise in the hardness, as Pavel and Srivastava observed tensile residual stresses in laser melted Ti-6Al-4V to result in a 10 HRC increase in the hardness of the top surface in comparison to the side surface [286]. Within the SLM samples, there is a slight variation in the bulk hardness with varying energy density, as depicted in Fig. 7-9. However, the overall deviation from the mean is relatively less, and also considering the variability in the experimental values as indicated by the error bars, these minor variations could be due to the locations at which the indentations were actually done.

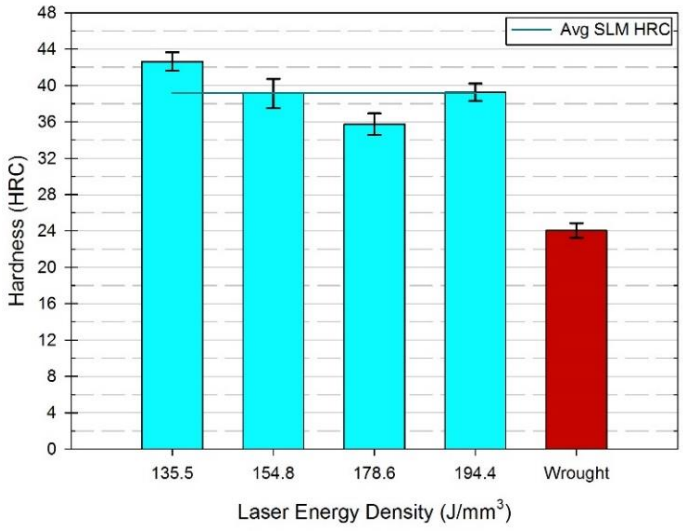

Fig. 7-9 Bulk hardness of SLM samples with varying LED and wrought SAF 2507

7.2.3 As-built vs solution annealing

Photomicrographs of the cross sections of holes drilled at different speeds with the as-built and the solution annealed samples are presented in Fig. 7-10. It may be noted that the etching process resulted in a colour reversal for the ferrite and the austenite phases from the as-built to the solution annealed samples. The left column of Fig. 7-10, with the as-built samples, the white areas are ferrite and dark areas are austenite, which is the other way round for all the samples in the right column, pertaining to the solution annealed cases. It may be observed that there is a variation in the microstructure around the machining edge of the as-built samples with increasing cutting speed. As the cutting speed increases the microstructure becomes more equiaxed with nano-scale austenite precipitation in the ferrite matrix forming to a depth of 230-300 µm at 140 m/min. Similar microstructures are observed in the stir zone of friction stir welds as highlighted by Esmailzadeh *et al.*, with the increase in the welding speed resulting in a decrease in the grain size [287].

The solution annealing process actually rendered a wider precipitation of the austenite phase and an intricate dispersion and intertwining of the two phases, as against the distinct granular appearance in the wrought duplex samples. Some structural variation is also induced around the edges of the sectioned hole based on the machining process and the associated conditions. While the sample machined at 20 m/min (Fig. 7-10-(b) seems to be structurally undisturbed due to the machining, the other samples from 60 m/min onwards appear to have gone through recrystallisation, to varying depths. Both ferrite and austenite assumed uniformly dispersed fine cellular grain structures around the machined edges. Fang *et al.* notes in the hot deformation of duplex stainless steel that ferrite grains are softer than austenite at elevated temperatures leading to greater deformation in ferrite as exemplified by the ferrite rich as-built samples [288]. On the other hand, the more balanced austeo-ferritic structures of the annealed samples resulted in a more uniform less distorted machined surface and sub-surface micro structures.

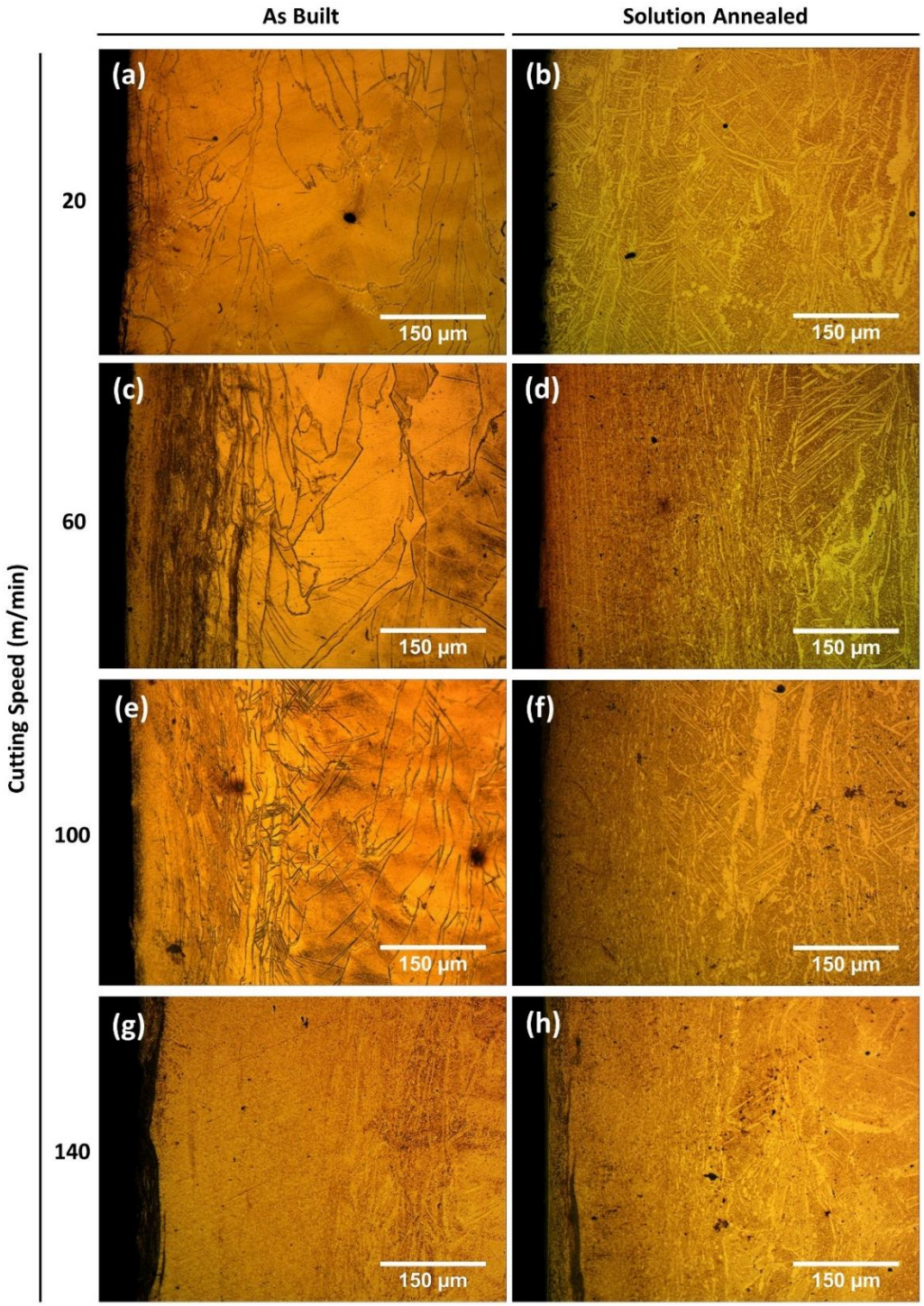

Fig. 7-10 Microstructural images of SLM samples in the as-built and solution annealed condition

The higher magnification images of both the as-built and the solution annealed samples machined at 100 m/min (Fig. 7-10-(e) and (f)) are presented in Fig. 7-11, showing the micro duplex microstructures. The as-built sample (Fig. 7-11-(a)) shows the formation of the inter-granular austenite up to a distance of ~20 µm from the surface of the drilled hole. Progressing from the band of inter-granular austenite there is a zone, which is weakly etched, and showing nano-scale black precipitates in a ferritic microstructure devoid of

grain boundaries and Widmanstätten austenite needles. This microstructure is most likely the result of dynamic recrystallisation during drilling. Similar microstructures were observed in the friction stir welding of duplex stainless steel. Increasing the welding speed was noted by Saeid *et al.* to lead to a reduction in the grain size to as small as 1µm [289]. Further, Sato *et al.* also reported a greater ferrite content in the fusion zones in the friction stir welding of SAF 2507, as due to the greater stability of ferrite over austenite at higher temperatures [290]. The mechanism of deformation was reported by Jorge *et al.* to initially begin with plastic deformation in the ferrite followed by deformation in austenite which increased microstructure hardness until peak stress. After exceeding peak stress, austenite dispersed in fine precipitates throughout the sample until fracture [291]. A similar recrystallised zone up to a width of around 25 µm can be seen to form along the edge of the hole machined in the solution annealed SLM sample as depicted in Fig. 7-11-(b). Intragranular austenite <1 µm with an elliptic morphology in the direction of drilling is visible close to the hole wall, increasing in size with greater morphological irregularity further from the hole is evident in Fig. 7-11-(c).

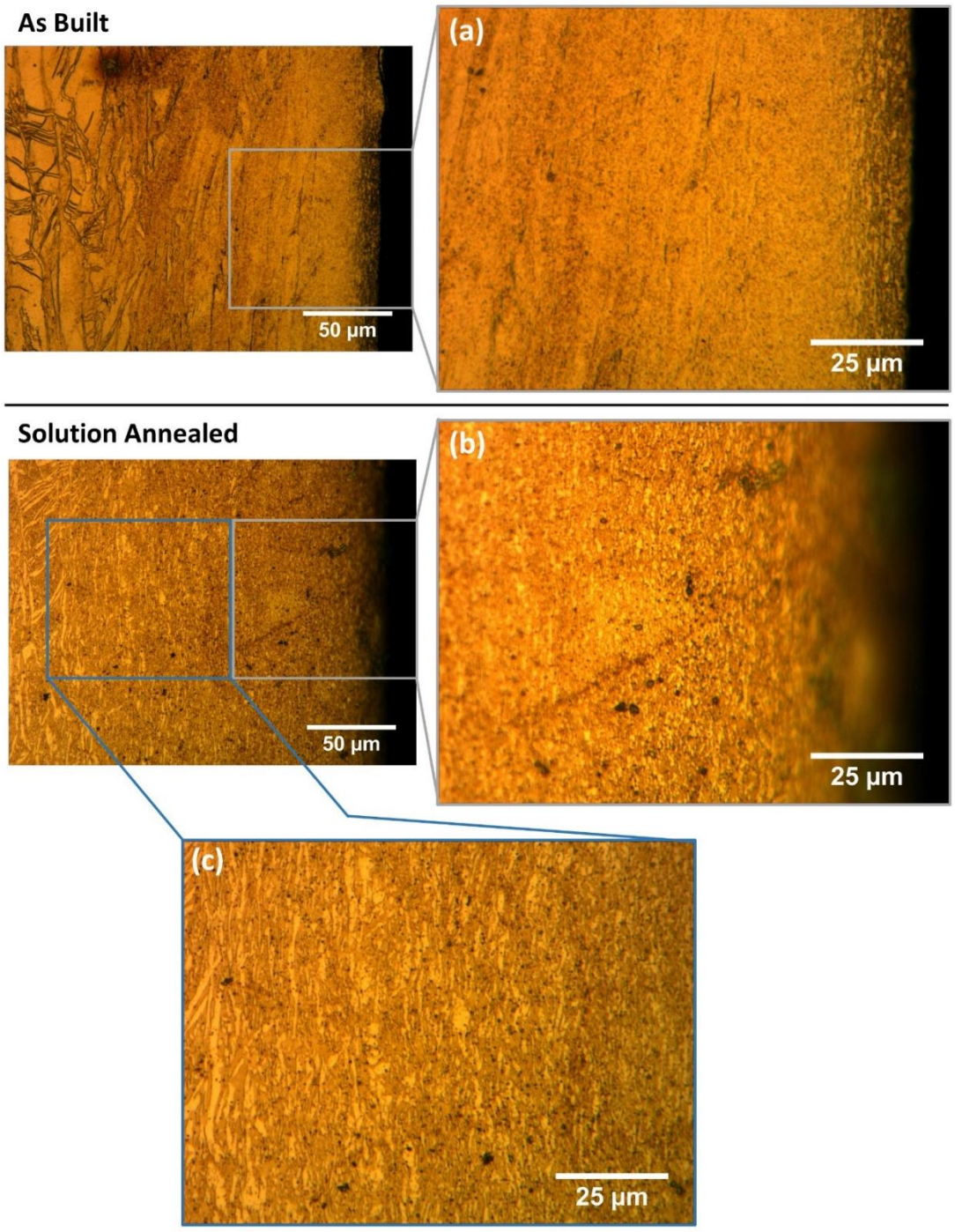

Fig. 7-11 Micro duplex grain structure in as-built and solution annealed samples at 100 m/min

SEM images of samples drilled at 100 m/min at still higher magnification presented in Fig. 7-12 show spherical CrN precipitates formed in the critical zones of the as-built samples. The ragged edges in Fig. 7-12-(b) are mostly the austenite that is broken up under the high plastic deformation near the machined surface. In the images of the solution annealed samples (Fig. 7-12-(c) and (d)), austenite is visible as lighter grey sub

grains with a jagged morphology. It is interesting to note in Fig. 7-12-(d) the precipitation of CrN as it was not dissolved during solution annealing.

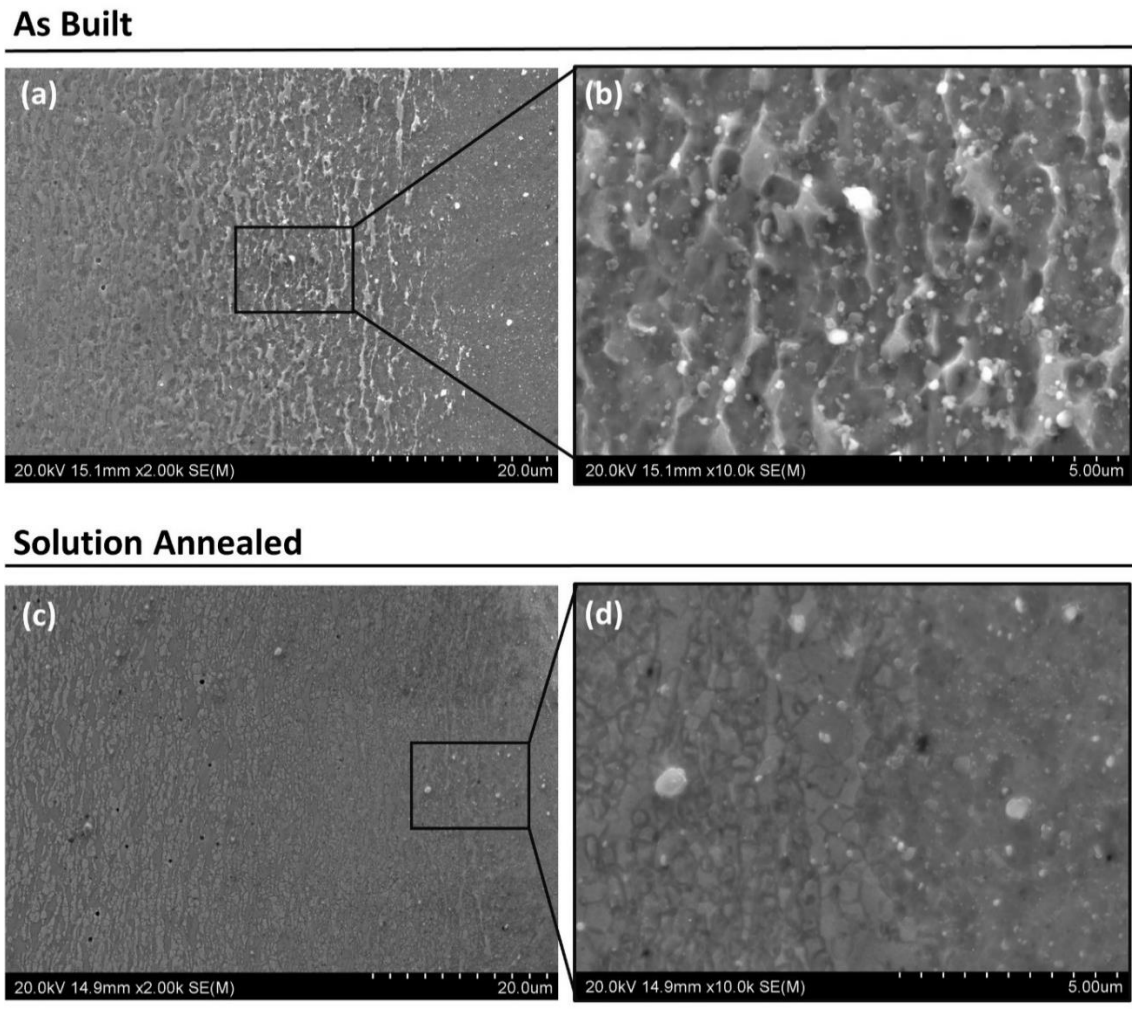

Fig. 7-12 High magnification images of as-built and solution annealed samples drilled at 100 m/min

Another interesting feature observed in the SLM samples drilled at elevated cutting speeds is the formation of the curved whisker-like needles propagating from the deformation zones, as evident in Fig. 7-13. This microstructure is most probably the result of the material flow during the drilling process, whereby the Widmanstätten austenite needles are pulled from the deformation zone developed during the machining process. Similar features were observed and reported with the friction stir welding of the 1008 steel, behind the rotating tool by Liu and Nelson with the needles reported to be spaced at the same distance as the tool feed [292].

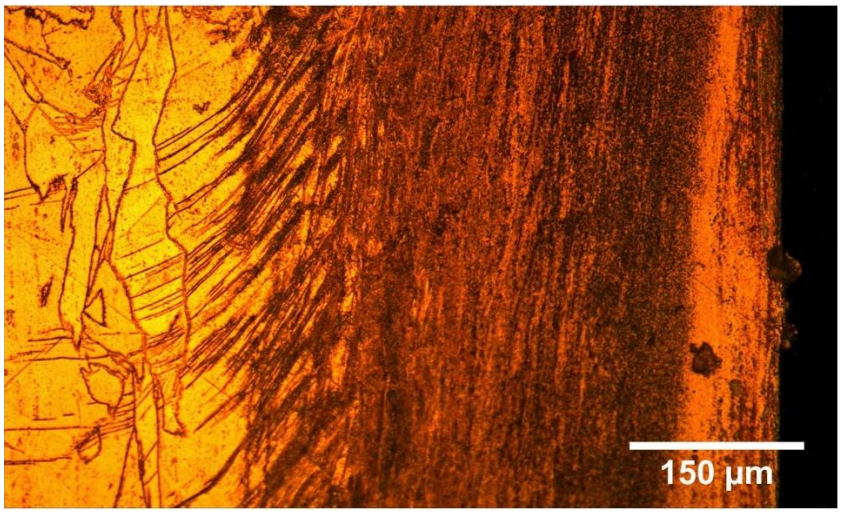

Fig. 7-13 Austenite whiskers formed in the drilling of the as-built sample at 60 m/min

Photographs of the sectioned faces of the drilled holes with varying conditions are presented in Fig. 7-14. It may be noted that both the as-built SLM samples machined at 100 m/min and 140 m/min attained the characteristic thin white layers along the length of the edges of the sectioned hole further to etching. This is mostly indicative of a distinct phase transformation occurring due to plastic deformation and thermal variations. The blue discoloured hole surface is probably due to friction developed during drilling with poor chip and heat removal at the elevated cutting speeds. The wider deformation zones occurring at a depth of 16.5 mm in the 140 m/min sample of Fig. 7-14-(b) probably correspond to the deformation zones which result from a significant temperature spike due to the accumulation and clogging of chips. The hole surfaces of both samples are seen to progress from smooth cutting to the rough friction zone affected areas and then revert back to the smooth cutting 5-7 mm prior to exiting the hole.

Solution annealed samples show similar discoloration of the hole surface to the as-built samples with distinctive blue regions in the 140 m/min sample. Etched surface discolouration is less evident due to the etchant reacting with the refined microstructure and camouflaging the colour change. The solution annealed sample machined at 100 m/min (Fig. 7-14-(c)) shows the formation of a chattered rough surface similar to the as-built one at the same cutting speed and location. Furthermore, the samples machined at 140 m/min at both conditions show improved surface finish compared to the ones machined at 100 m/min. The discolouration of the machined surface results from the

formation of the oxide layer due to the diffusion of chromium into the heated surface and its affinity to oxygen, as reported by Łabanowski and Głowacka [293].

An example of this was presented by Aumpiem and Prateepasen, whereby gas tungsten arc welded SAF 2507 duplex stainless steel welds had been tested for their pitting corrosion resistance with highly discoloured brown-blue welds made in an oxygen environment >445ppm failing the Norsok M601 corrosion standard [294]. In the case of the drilled samples, the intensity of oxidisation is represented by the colour change of the surface and corresponding temperature at the specific location. An approximation of the temperature-colour relationship is detailed by the British Stainless Steel Association for 304 austenitic stainless steel [279]. The dark straw discoloration observed in all samples of Fig. 7-14 approximately corresponds to 370 °C, whilst in Fig. 7-14-(a), (b) and (c) the brown zones correspond to a temperature of 390 °C with purple bands and dark blue zones corresponding to 450 and 600 °C respectively, which will be verified later when discussing the results of temperature measurements.

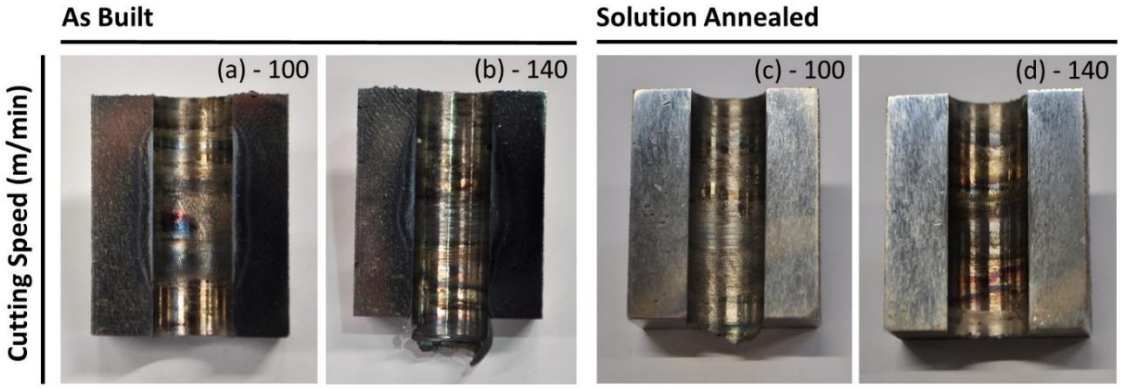

Fig. 7-14 As-Built and Solution Annealed SLM samples drilled at 100 and 140 m/min, showing discoloured plastic deformation

Micro-hardness measurements are made across the width of the sectioned surfaces of the drilled specimens and the results are compiled as the graphs presented in Fig. 7-15-(a) and (b) for the as-built and the solution annealed cases, respectively. It may be noted that in almost all the cases, the micro-hardness values at different locations from the edge of the drilled hole increased with increasing cutting speed. This is also the case with the solution annealed samples, though the spread is a little lesser in this case. There is a lack of literature on the machinability of duplex stainless steels, but similar observations were

made by Li *et al.* in the friction stir welding process. The stir zone was found to impart a harder microstructure, due to grain refinement, dynamic recrystallisation, and the dislocation movement of the grain boundaries [295]. The maximum difference in hardness with cutting speed is noted in samples machined in the as-built condition with a 164.8 HV difference observed at a distance of 25 µm between the 140 and 20 m/min cutting speed. An exponentially decreasing trend in hardness values is apparent, in the solution annealed samples, though to a minor extent.

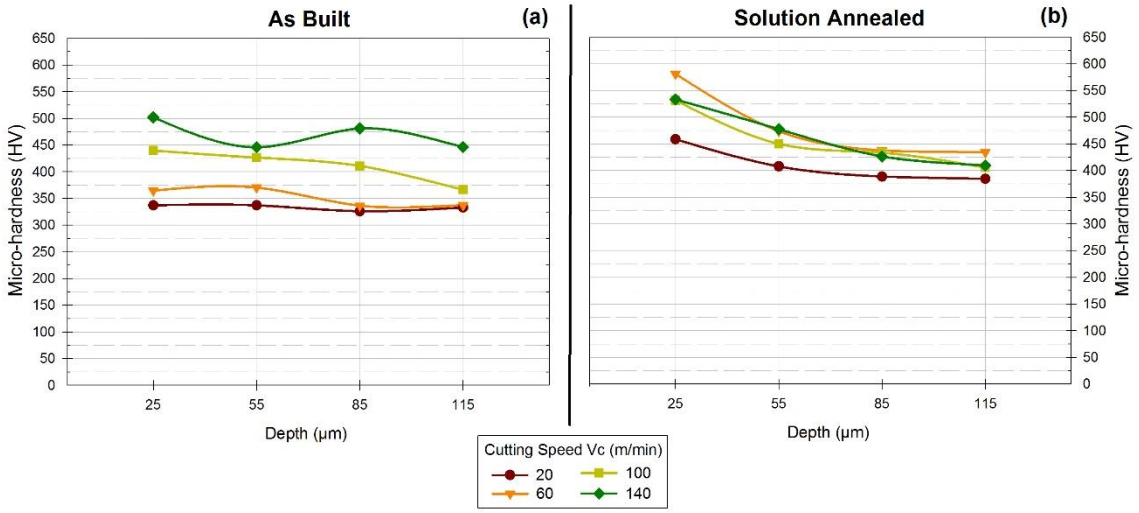

Fig. 7-15 Micro-hardness readings for SLM samples in the (a) as-built and (b) solution annealed condition

7.3 Mechanics of machining

The influences of the material and process variations on the cutting forces and temperatures generated are of importance now. The drill thrust force and torque measurements made from the experiments involving a Kistler 9272 four-component dynamometer (Section 3.9.3) will be presented and discussed in this section. Considering the practical limitations, the thermal fields of the chip and the tool domains could not be addressed, but indicative results are achieved through temperature measurements at specific locations along the length of the drilled hole and within the body of each specimen, using a USB-2416 data logger as detailed in Section 3.9.4.

7.3.1 Comparative assessment of SLM and Wrought duplex steels

The torque and thrust forces measured through machining trials drilling the laser melted and the wrought SAF 2507 samples are presented in Fig. 7-16 and Fig. 7-17 respectively. Considering the torque results presented in Fig. 7-16, the wrought samples showed a reduction in the torque with increasing cutting speeds, reaching a minimum at around 45 m/min and then a slight increase. This has been similar at both feeds, while also, the higher feed resulted in higher torque values, as expected. The SLM samples responded differently. There is a slight increase in the torque as the speed is increased from 20 to 40 m/min, a peak at around 45 m/min and a slight drooping towards the end with the higher feed case, at 0.05 m/min. The torque variation at the lower feed case remained more or less constant. In the case of the wrought samples, it might be predominantly due to a softening of the austeo-ferritic structures with gradually increasing temperatures that resulted in the reduction in the cutting torque as the speed is increased noted by Trent and Wright [296]. However, the laser melted samples, with the predominantly ferritic structures, appear to have undergone a slight work hardening, if any, at the lower speeds, or otherwise remained unaffected with increase in the cutting speed. The abnormal ferritic structures are sensitive, and given a rise in temperature, as the cutting speed increases, there may be phase transition towards the crystallisation of secondary austenite and a gradual increase in the resistance to shear deformation.

The higher feed resulted in higher torque, while also the work hardening effects are almost negligible as the curve for the lower feed case remained almost flat. The increase in torque with feed is natural, as the cross-sectional area of the chip increases, requiring a greater torque to remove the material [297]. Austenite is seen as the predominant phase in the work hardening behaviour. Dolinšek notes this as due to the inherent properties, including low thermal conductivity and the greater number of sliding planes resulting in the greater tendency to deform, increasing the strength with deformation [79]. While machining wrought duplex stainless steels, ferrite was reported by Nomani *et al.* to collect in bands in the stagnation zones with the development of micro cracks due to the high deformation. On the other hand, the austenite grains deform and grow similar to the patterns in Fig. 7-3-(b) flowing into the chip or the work piece domains [298]. This will lead to substantial work hardening effects from the austenite phase. Therefore, the contribution of ferrite is

relatively negligible towards the work hardening aspects, compared to the austenite phase.

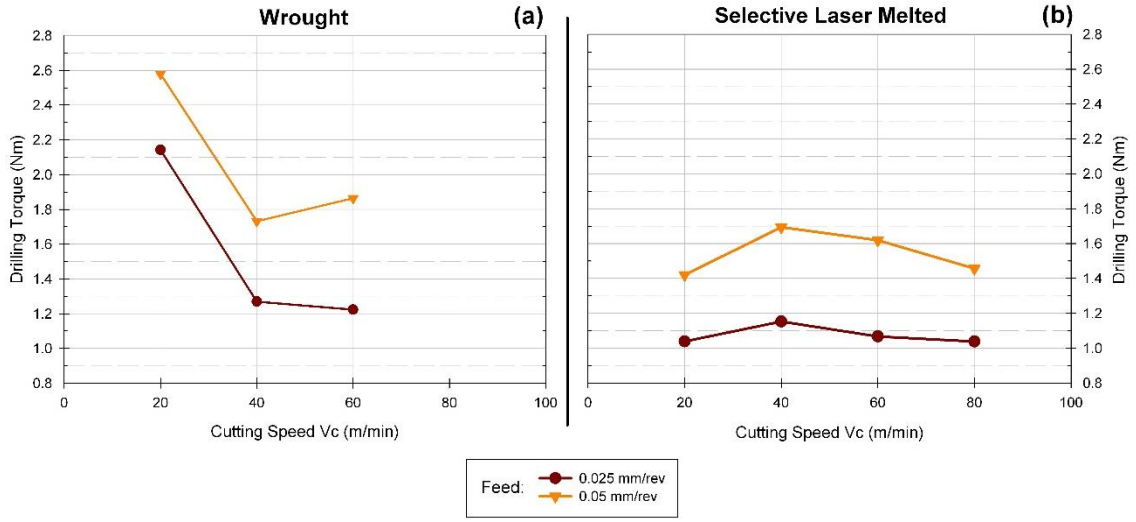

Fig. 7-16 Drilling torque variation while machining (a) wrought and (b) SLM samples

The thrust forces plotted as shown in Fig. 7-17 show similar trends but with a more significant variation in each case. The wrought samples resulted in a drastically reducing thrust force, a minimum at around 42-44 m/min, and then a steep rise subsequently with increasing speed in an almost parabolic form. The SLM samples resulted in a substantial rise in the thrust force, as the cutting speed is increased, achieving the peak values at 40 m/min, and 60 m/min with the lower feed and the higher feed cases respectively. Once again, the thermal softening and the possible precipitation of secondary austenite are at play behind these variations. With thermal softening of austenite likely resulting from the activation of new slip systems in austenite from plastic deformation as noted by Mateo *et al.* [299]. However, considering the nature of generation of the thrust force from the indentation of the drill bit through the bulk of the material for most part of the cutting edges, the variations are more prominent than that observed with the torque. This is likely the result of wear on the cutting edge from the initial contact with the harder SLM microstructure which leads to excessively high thrust forces, observed similarly by Nomani *et al.* in the drilling of SAF 2507 duplex stainless steel. They also reported initial contact with the work piece to contribute to a ~225 N increase in thrust force over the steady state [90]. Further issues including drill centring with the pilot hole may have impacted thrust force readings.

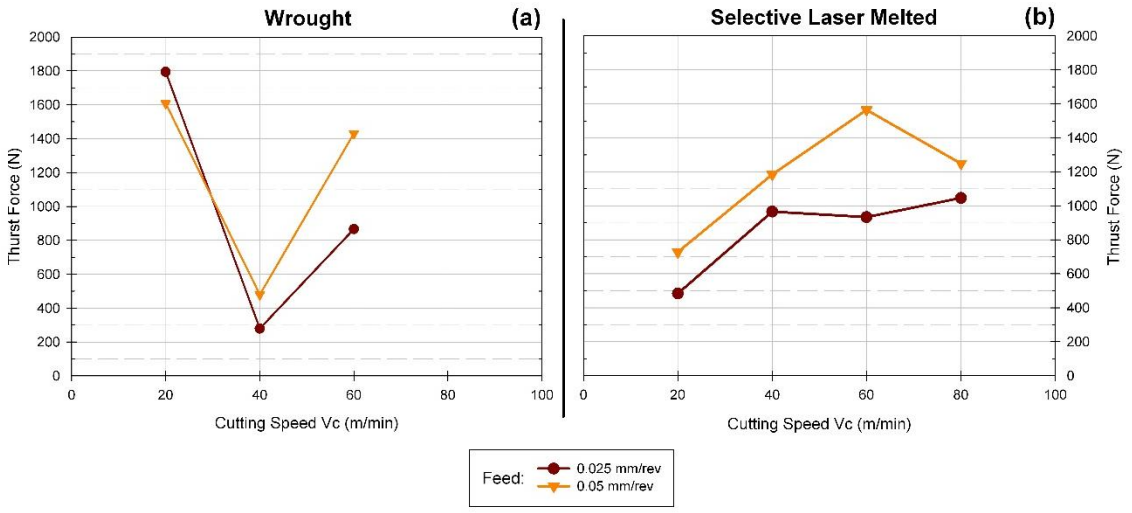

Fig. 7-17 Thrust force variation while machining (a) wrought and (b) SLM samples

For identical process conditions, the SLM samples generally resulted in slightly lower drilling torques compared to the wrought counterparts. The thrust forces are either equal or slightly higher with the SLM samples at different combinations of the other parameters. The chip formation mechanics based on the shear deformation of the work material is greatly improved, as lower main cutting forces and consequently torques are generated while drilling the SLM samples, compared to the wrought form. This is indicative of lower chip compression, lesser chip reduction coefficients and wider shear deformation zones as explained in the classical metal cutting texts by Bhattacharya and Trent and Wright [296, 300]. The shear strength of the duplex stainless steel might have reduced slightly, considering the predominantly ferritic structures resulting from the laser melting process. The fine cellular growth of the ferrite (Fig. 5-10) and the precipitation of the CrN particles along the grain boundaries probably led to shear deformation mechanisms similar to the ones caused by the MnS segregation in the free cutting steels observed by Sidjanin and Kovac [301].

The thrust forces, though higher in the case of the SLM samples, the differences are only minor over the wrought counterparts with similar process conditions. The higher hardness of the ferritic structures noted in Fig. 7-9 is the likely cause for this as described by Shaw and Bhattacharyya [300, 302]. Evidently, the shear deformation mechanics is improved with the micro-structures resulting from SLM, while the indentation resistance is slightly higher. However, the indentation aspect is typical of the drilling process, and with the other machining processes where the mechanism of machining is predominantly by shear

deformation of the bulk material, it may be inferred that selective laser melting actually improves the machinability of duplex stainless steels. High cutting speeds lead to more severe heating and temperature conditions and most likely result in the thermal softening of the work piece material [297]. This could lead to a reduction in the thrust force as evident in the sample drilled at 80 m/min and 0.05 mm/rev in Fig. 7-17-(b). Watson reported thrust force to be a function of the shear flow stress, which in turn decreases with increasing temperature [303].

The time-dependent variation in the temperature at four different locations along the length of the hole as the drilling process progresses is shown in Fig. 7-18 for both the wrought and the SLM samples and at the lower feed and all the cutting speeds considered. First, a quick scan of the temperature profiles comparing the wrought and the SLM samples shows marked differences between the two. The overall temperature values measured, the peaks and general profiles are always much higher at all the points in the case of the wrought specimens, as compared to the SLM samples. Though these values represent the temperature conducted from the principal deformation zones to specific points in the bulk of the test pieces, the temperature values and profiles are generally indicative of the thermal fields generated during machining of the wrought and the SLM samples. The work done during the shear deformation of the work material to form the chip, and the secondary deformation at the chip-tool interface are the primary causes of elevated temperatures in metal cutting as explained in Shaw, Bhattacharyya, and Boothroyd and Knight [300, 302, 304]. Evidently, the shear deformation of the wrought duplex steel is more severe compared to the SLM samples, as is also indicated by the higher torque values noted. This is probably due to the work hardening of the metastable austenite in the wrought state and possible martensitic transformation as reported by O'Sullivan and Cotterell [305]. A frozen chip sample might give a better insight into this, but could not be undertaken due to the lack of experimental facilities, but similar observations were noted elsewhere by Dolinšek [79].

With the wrought samples, the temperature profiles at each point increased in a linear or a parabolic manner, attained a peak, drooped to varying degrees and remained stable to the end, as the drilling process progresses along the length of the hole machined. The heat generated from machining has to flow from the primary and the secondary deformation

zones to the points of temperature measurement and the gradual rise is expected due to the nature of heat conduction. The subsequent dip in the temperature profile in each case is the result of the drill bit leaving the specific point of measurement. Similar trends are noted between the wrought and the SLM samples, though temperature profiles in the SLM cases are not as dramatic as in the wrought ones. Evidently, the deformation work done in the SLM cases is significantly lower and so the overall heat generated is lower and hence the relatively milder temperature variations at all the points of measurement. Considering the thermal conditions are the most critical in determining the tool life, it may further be ascertained that the laser melting process actually improved the machinability of duplex stainless steels in the as-built state.

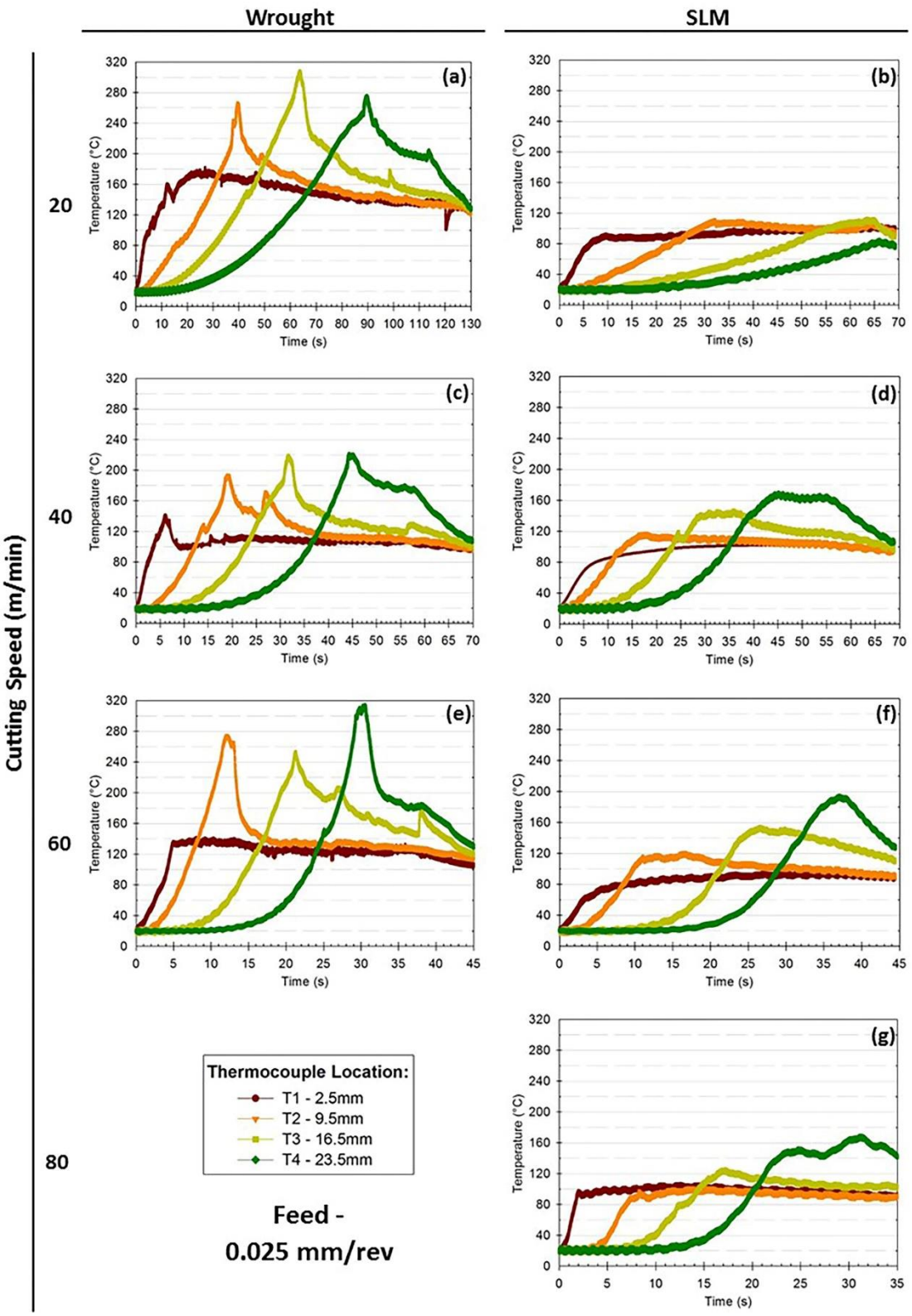

Fig. 7-18 Temperature traces of wrought and SLM samples at a feed of 0.025mm/rev

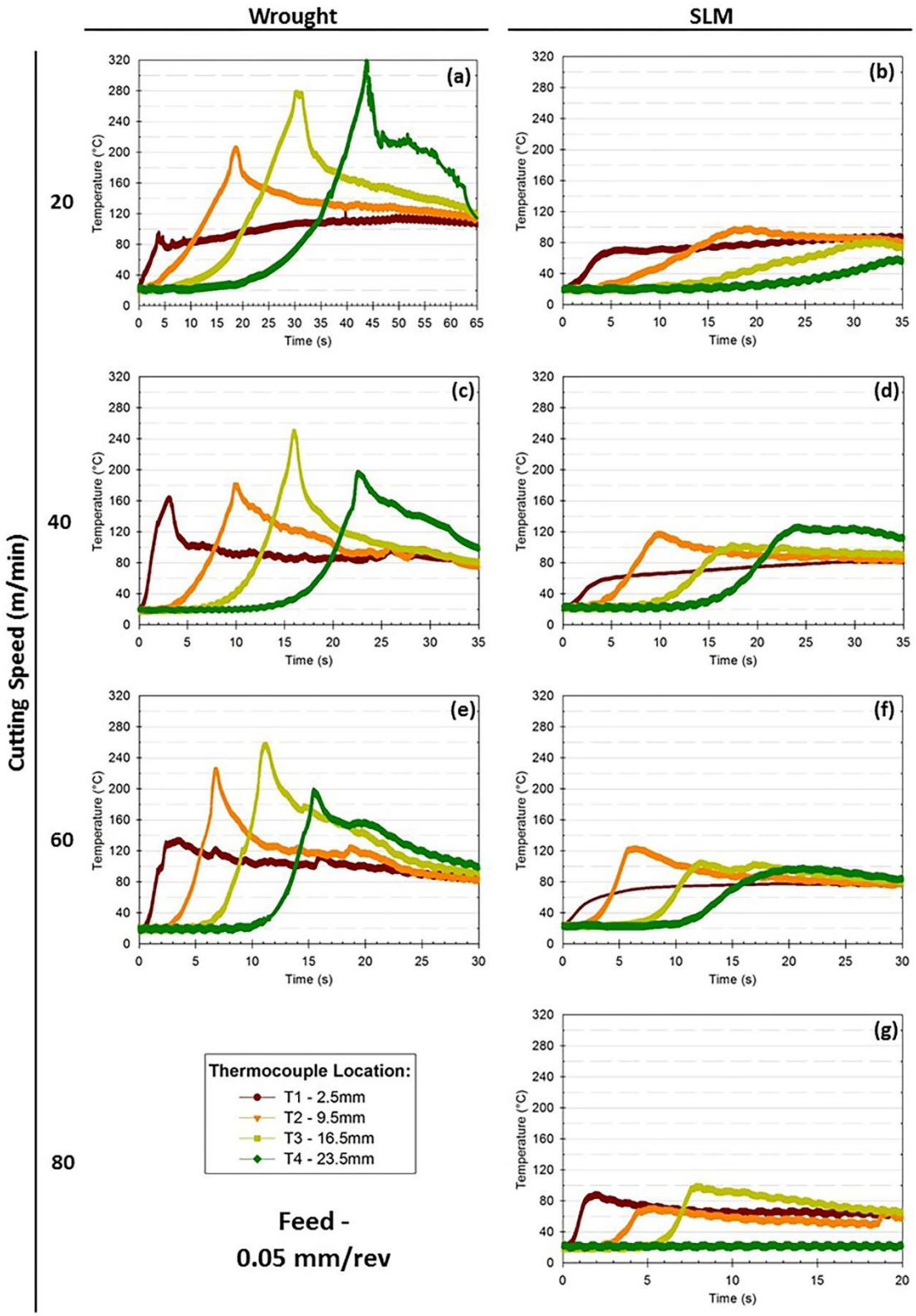

Fig. 7-19 Temperature traces of wrought and SLM samples at a feed of 0.05mm/rev

The temperature profiles plotted in Fig. 7-19 for the corresponding cases at the higher feed 0.05 mm/rev show very similar trends as already discussed. The laser melted duplex steel samples in the as-built state resulted in much lower temperature values at corresponding measurement locations compared to the wrought samples. It is clear that the shear deformation responses are improved due to the laser melting process. The ferritic structures together with the intermetallic precipitates probably led to a relatively harder structure and machining responses similar to those exhibited by hard and brittle material systems such as brass and cast iron.

7.3.2 Varying laser energy density

A comparative assessment of the drilling torque and thrust force values based on the SLM samples printed at four laser energy density levels are depicted in Fig. 7-20. The overall influence of varying the laser energy density has a marginal influence only on the drilling torque as the maximum deviation from the highest to the lowest torque achieved is around 0.2 Nm. The thrust force on the other hand showed a variation of around 200 N from the highest to the lowest values attained. The average torque across the different energy densities is lower with the laser melted samples compared to that of the wrought case. Though this is not a significant difference quantitatively, it eliminates the general impression that laser melting leads to substantially complex internal structures that are likely to deteriorate the machinability of the printed parts in the as-built state, at least in the case of duplex stainless steels. The average thrust force is slightly higher though, around 80 N with the SLM samples, compared to the wrought sample, as evident from Fig. 7-20-(b).

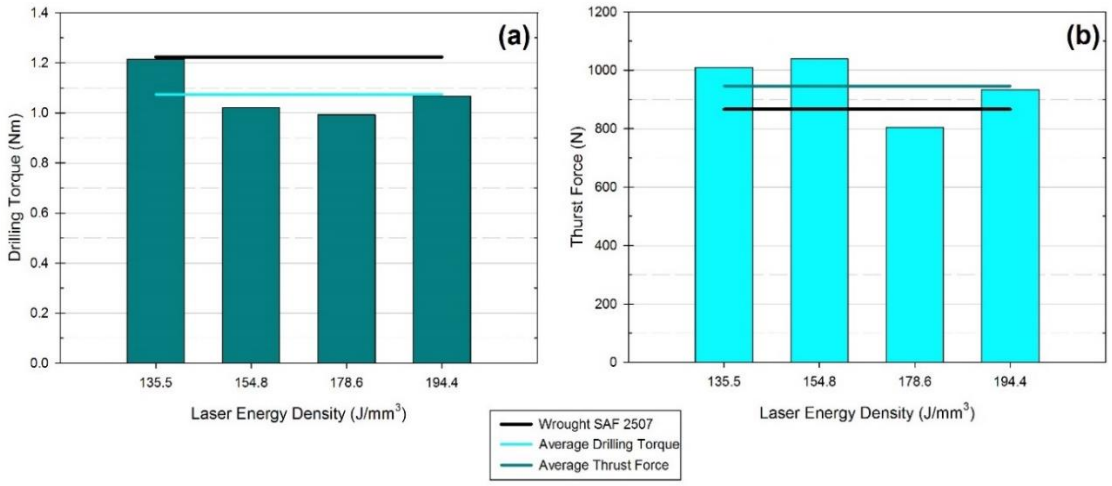

Fig. 7-20 Drilling torque - (a) and thrust force - (b) for SLM samples of varying LED produced at; Vc – 60 m/min, f- 0.025 mm/rev

The influences of varying energy density levels used to print the samples on the temperature profiles at specific locations while drilling at a speed of 60 m/min and feed of 0.025 mm/rev are shown in Fig. 7-21. Significant differences in the maximum temperatures and the profiles may be noted between the SLM and the wrought samples. A maximum temperature of 315.1 °C is recorded with the drilling of the wrought SAF 2507, 119.9 °C higher than the equivalent highest in the SLM sample produced at 194.4 J/mm^3. Within the SLM samples also, there is variation in the temperature profiles with the energy density employed. Overall, the SLM sample produced at the energy density 178.6 J/mm^3 gave the lowest temperature values with the least variation of the profiles with time.

Further evident in the samples produced at these LED's is the truncation of peak temperature measurements suggesting a prolonged heat retention in the block at a lower temperature. The accumulation in heat with drilling depth is evident from all temperature traces as portrayed by the majority of greater temperature measurements in traces at T3 and T4 corresponding to a drill depth of 16.5 and 23.5 mm respectively. Similarly Sato *et al.* observed temperature accumulation near the end of a through hole drill on the bottom surface which resulted in greater tool wear than an equivalent blind hole [306]. Furthermore, the trace at T1 (2.5 mm deep) is seen to stabilise after 10 s of drilling with less prominent peaks than the other traces. Sharp temperature spikes are observed in

traces T2-4 in the sample at 154.8 J/mm^3 and the wrought sample which differs from the more gradual transition in samples at 135.5 and 194.4 J/mm^3. The lowest temperatures recorded occurred at 178.6 J/mm^3 for which the trace T1 is the highest recorded temperature suggesting probably a low BUE formation and the dissipation of heat into the chips as the drilling progresses.

Comparing the results of Fig. 7-20 and 7-21, there is a clear correlation of the trends between the torque and the thrust force values to the temperature profiles. The SLM sample produced at 178.6 J/mm^3 by far gave the least torque and thrust force values, while also scoring the best in terms of the peak values and profiles of the temperature measurements made. Going back further, the bulk hardness of the specimen printed at the same energy density as depicted in Fig. 7-9 is also at the lowest level compared to the other cases. The photomicrograph presented in Fig. 7-8 also indicates the structure to be mostly constituted of ferrite, with occasional austenite in the form of thin needles or plates. All these factors come together to further ascertain that the machinability improves with the laser melting of duplex stainless steels in the as-built state and the energy density setting at 178.6 J/mm^3 is the optimum level of processing overall.

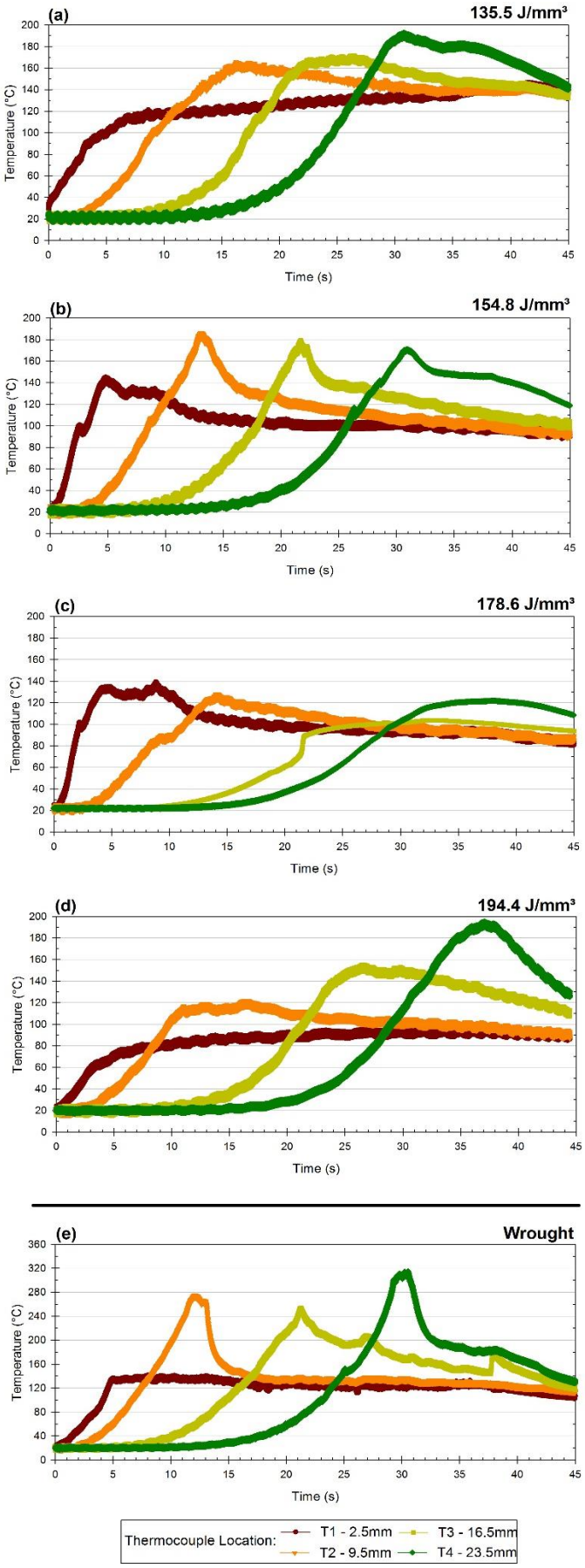

Fig. 7-21 Drilling temperature traces for SLM samples at varying LED and Wrought SAF 2507

7.3.3 The solution annealing effects on the machinability

The torque and thrust force variations with the cutting speed, comparing the as-built and the solution annealed states are presented in Fig. 7-22, with the feed fixed at 0.025 mm/rev in all the cases and select repeated samples evident as error bars. Overall, the as-built and the solution annealed samples follow similar trends in both drilling torque and thrust force results. Both drilling torque and thrust forces are slightly higher in the case of the as-built samples though, indicating the solution annealing to be softening the structures. The drilling torque in solution annealed state, as seen in Fig. 7-22-(a) increases with the cutting speed to a maximum at 60 m/min followed by an exponential decrease, which is similar to the trend already discussed based on the results presented in Fig. 7-17. Maximum torque values at 4.87 and 3.96 Nm may be noted for the as-built and the solution annealed samples respectively, at a cutting speed of 60 m/min. Similar observations were made by Sushinder *et al.* in the drilling of Ti-6Al-4V, attributing the responses to the work hardening and thermal softening mechanisms [307].

A linear incremental increasing trend in the thrust force is observed with increasing cutting speed as depicted in Fig. 7-22-(b). The differences in the thrust forces between the as-built and the solution annealed states also increased with increasing cutting speeds, reaching to almost 300 N at 140 m/min. The SLM samples showed a continuous rise in the thrust force, while the solution annealed samples appear to stabilise at around 700 N with increasing cutting speed. It may be pertinent to point out here that the torque and thrust force results presented in Fig. 7-22 are different from those reported earlier in Fig. 7-16 and 7-17 for similar cutting conditions, mostly due to a change in the geometry of the drill tools used. The average maximum temperature graph in Fig. 7-23 shows a strong relationship with the drilling torque results between 20-60 m/min with both the as-built and the solution annealed samples having comparable maxima at 798.1 and 796.7 °C respectively. A decrease in the maximum temperature occurs at 100 m/min for samples at both conditions with a greater temperature decrease in the as-built sample. At 140 m/min maximum temperature trends diverge as the solution annealed sample continues a decreasing trend similar to the equivalent drilling torque results. The as-built samples however led to an increased temperature to 780.2 °C, but was noted to be the result of the accumulation of the chips and the associated clogging.

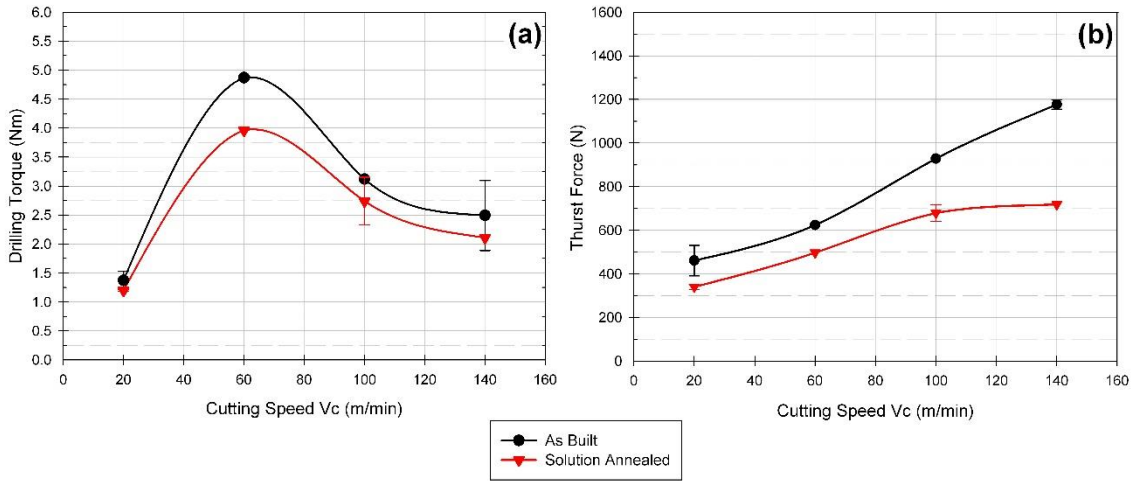

Fig. 7-22 Drilling torque - (a) and thrust force - (b) for SLM samples in the as-built and solution annealed conditions (feed 0.025 mm/rev)

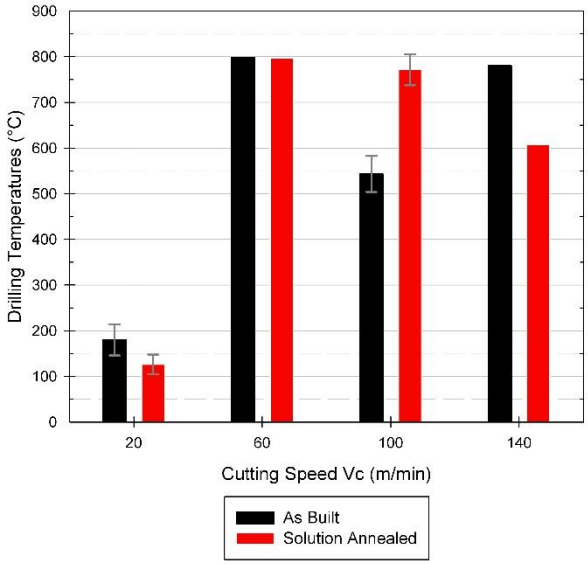

Fig. 7-23 Average maximum temperatures in drilling as-built and solution annealed SLM duplex stainless steel

Temperature traces at specific points along the lengths of the drilled hole are presented in Fig. 7-24 in order to have a closer look at the mechanics of machining comparing the as-built and solution annealed SLM samples. Evidently, the T2 and T3 curves corresponding to the locations at 9.5 and 16.5 mm respectively along the length of the drilled holes show a more dominant variation in the temperature with time in most cases. Each location, where temperatures are measured showed a peak at around 5-10 seconds into cutting and then attained stable conditions. This is indicative of the steady states reached within the first few seconds of cutting at any given point, as observed by Rosa *et al.* [308].

The temperature profile curves from these experiments show more complex variations and intricate and intertwining trends from one set of conditions to the other. Considering the peak temperatures as the basis, it may be noted that the as-built samples scored the highest when machined at 60 m/min and 140 m/min, at the second (T2) and the third (T3) locations respectively. With lower speeds, curves T1 and T2 are the dominant ones, as there is sufficient time to build up to the possible temperature levels. However, at higher speeds, curves T3 and T4 play the lead roles as they have longer times to pick-up the heat conducted from the critical deformation zones. This is the case with all the as-built samples in Fig. 7-24. The solution annealed samples however showed a marked significance of the T2 curve in all the cases. Most other curves remained almost insignificant at all speeds other than the 60 m/min. The sharpness with which temperature at a given location can rise depends predominantly on the thermal conductivity, apart from the amount of heat generated. The drilling torque and the thrust forces influence the rate of generation of heat. Considering that the variation in both torque and thrust forces are very similar between the as-built and the solution annealed samples as depicted in Fig. 7-22, it may be deduced that the differences in the temperature profiles between the two cases might be due to variations in the thermal conductivities. The structural changes achieved through solution annealing appear to have reduced the thermal conductivity from the as-built state. Satyanarayana *et al.* notes austenitic stainless steels to have lower thermal conductivities than the ferritic counterparts at elevated temperatures [309]. This is further validated by the data sheets for ferritic 409 and SAF 2507 duplex stainless steels across a wide range of temperatures [158, 310].

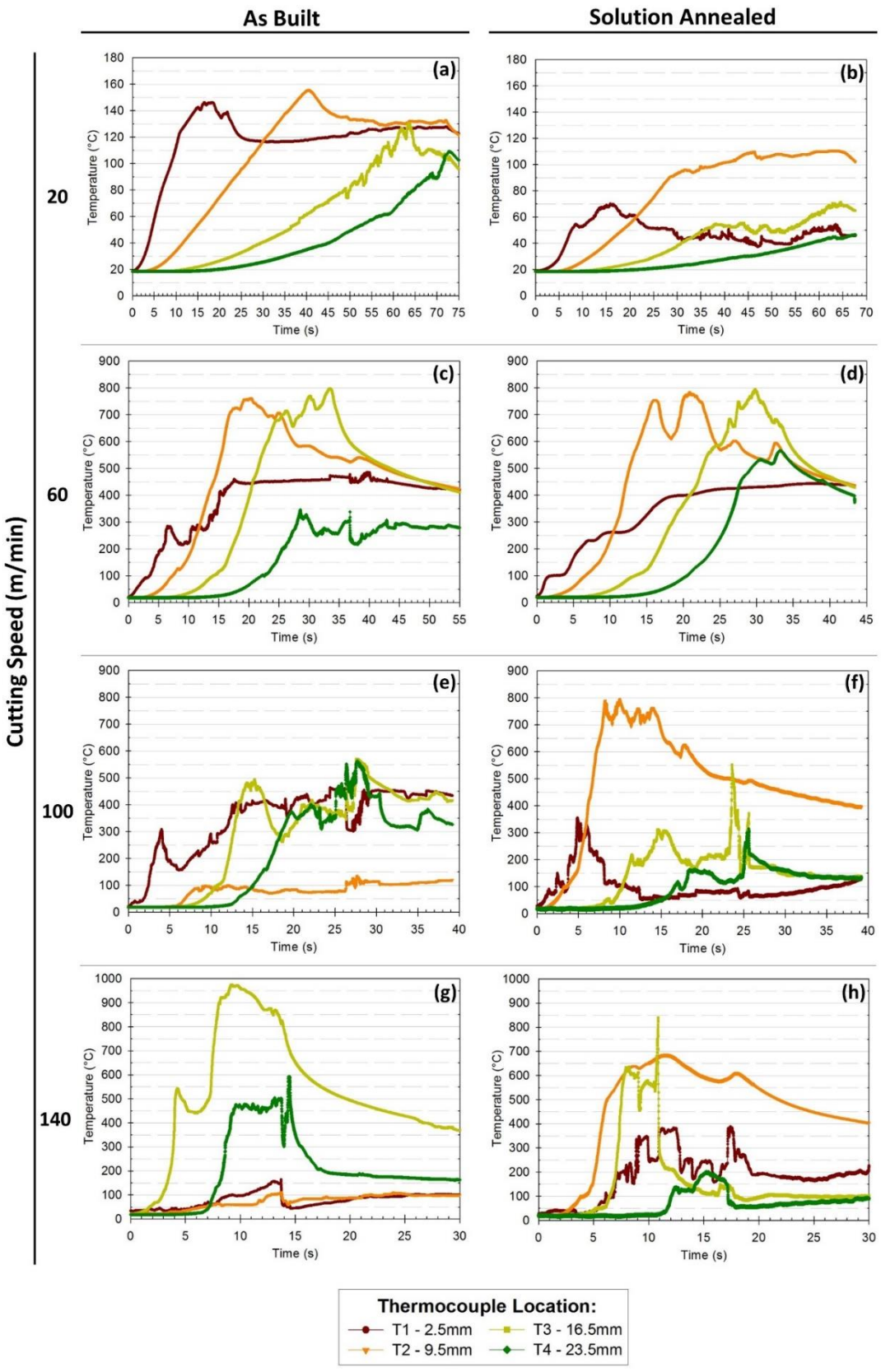

Fig. 7-24 Drilling temperature traces for SLM samples in the as-built and the solution annealed conditions

7.4 Surface roughness responses

The Taylor Hobson Talysurf recordings of the surface roughness values of drilled surfaces of wrought and SLM samples machined with varying process parameters are presented in Fig. 7-25. Microstructural and machinability variations between SLM and wrought duplex stainless steel as detailed prior, evidently will affect the surface roughness results too. Surface roughness of wrought duplex stainless steel is on average greater than the laser melted samples with a maximum surface roughness of 3.78 µm at a cutting speed of 40 m/min and feed of 0.025 mm/rev. Two separate trends in surface roughness with cutting speed are seen in Fig. 7-25-(a). An inverted parabolic trend is evident in samples machined at a feed of 0.025 mm/rev opposing that observed in the maximum temperature and the thrust force trends detailed above in the case of the wrought samples. Comparably a decreasing linear trend from a surface roughness maxima of 3.59 µm at 20 m/min to a minima of 1.69 µm at 60 m/min is visible for the same samples machined at 0.05 mm/rev.

Sinusoidal trends are visible in the surface roughness variations in the laser melted samples with increasing cutting speed as shown in Fig. 7-25-(b). Surface roughness results of samples machined at both feeds are comparable at 20 and 80 m/min. However, at the cutting speed of 40 m/min, a local maximum in the surface roughness is observed for the sample machined at 0.025 mm/rev while this occurred at 60 m/min with the 0.05 mm/rev feed. surface roughness measurements are seen to be at their lowest (1.22 and 1.29 µm) at a cutting speed of 80 m/min. Based on experimental results involving the dry machining of cast duplex stainless steels, Selvaraj and Chandramohan noted surface roughness to reduce with cutting speed and reach a minimum at 100 m/min at three different feeds, possibly due to a reduction in the BUE formation [311]. In the current cases, the overall variation in the surface roughness is generally small, averaging to a maximum deviation of around 1.5-2 µm. Within this narrow range, different trends are noted with different material and process conditions, which might be due to the variations in machining conditions and possible formation or absence of a BUE or even issues around the type and disposal of chips formed.

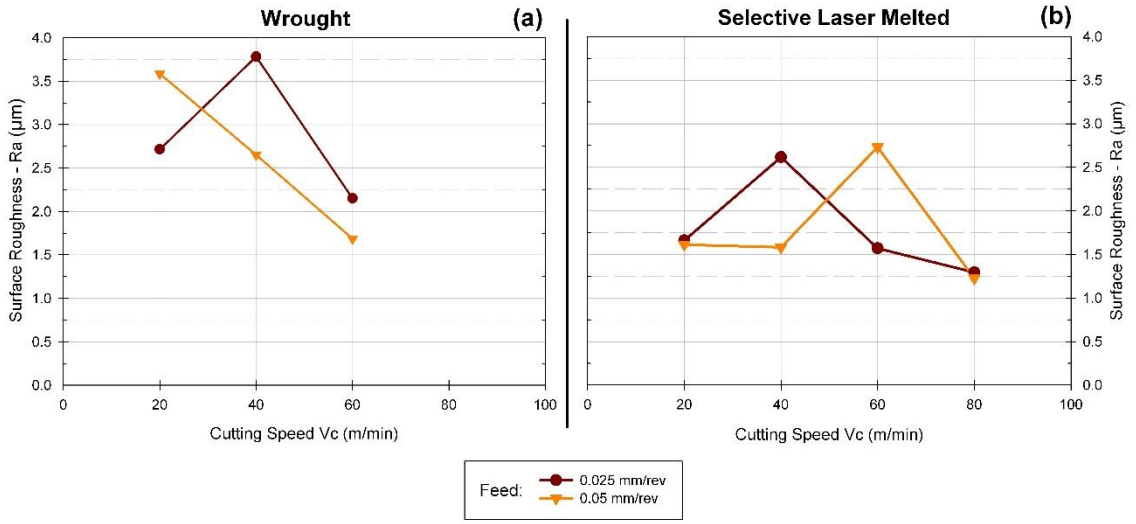

Fig. 7-25 Surface Roughness of (a) wrought and (b) SLM samples

A comparison of the surface roughness values obtained with SLM samples at varying energy densities and the wrought case are presented in Fig. 7-26. Similar to the improvements in the other aspects of machinability reported above, the average surface roughness of the SLM samples is slightly lower than the wrought case as shown in Fig. 7-26 at identical drilling conditions. An increasing trend in surface roughness is seen in samples produced at the lower LED's with a maximum at 154.8 J/mm^3 with a significantly large standard deviation of 0.52 µm. Samples produced at the upper LED's of 178.6 and 194.4 J/mm^3 show comparable average surface roughness results of 1.45 and 1.57 µm with a trend following that observed in drill torque and thrust force results. Despite the higher than average drilling torque and thrust force results, the lowest surface roughness 1.18 µm is attained at 135.5 J/mm^3. The increase in hardness and brittleness in laser melted Ti-6Al-4V led to a lower surface roughness as reported by Polishetty *et al.*, induced by a reduction in the plastic flow during machining [312].

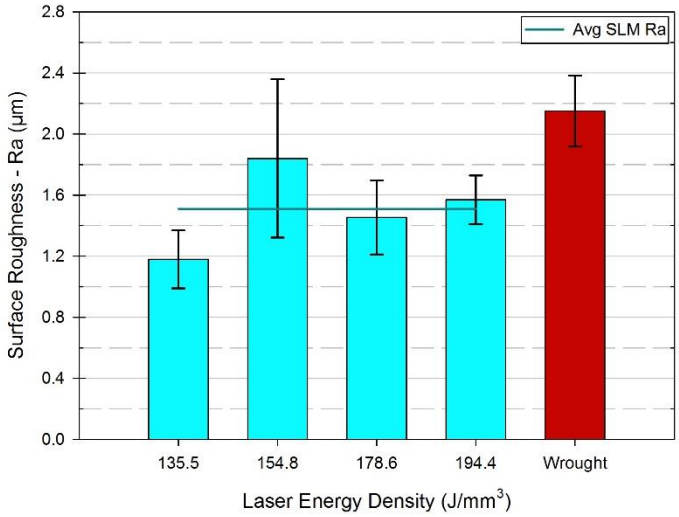

Fig. 7-26 Average surface roughness for SLM samples at varying LED and Wrought SAF 2507

Surface roughness measurements based on the as-built and the solution annealed SLM samples drilled at varying process conditions are presented in Fig. 7-27. An overall decreasing trend in the surface roughness may be observed with increasing cutting speed. The surface roughness values of samples in the as-built condition decrease from an overall maximum of 4.47 µm at 20 m/min to 1.97 µm at 140 m/min with comparable surface roughness values at 60 and 100 m/min. Conversely, the surface roughness of the solution annealed sample increases from 20 to 60 m/min prior to a rapid decrease in the roughness at elevated cutting speeds, culminating in an overall minimum of 1.06 µm at 140 m/min. Other than the minor variations, the surface roughness generally decreased with increasing speed, which was also observed by Sultan *et al.* in the drilling of 316L austenitic stainless steel presumably due to the lower tendency to form BUE [313].

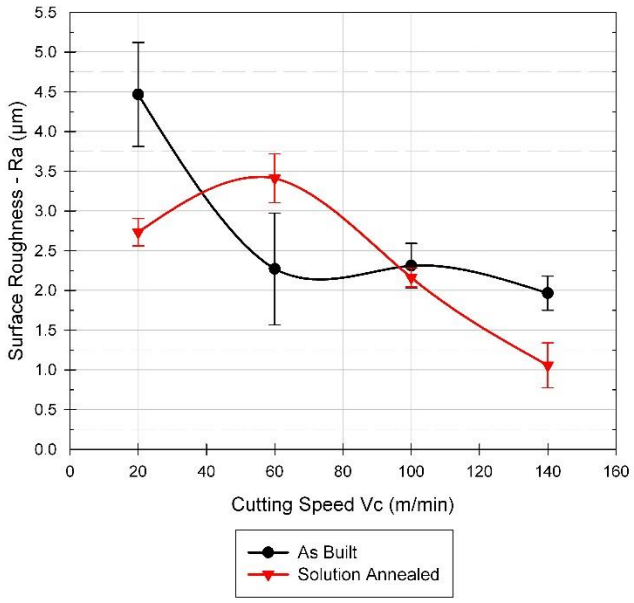

Fig. 7-27 Surface roughness for SLM samples in the as-built and solution annealed condition

7.5 Chipping and breakage of cutting edges

Considering the high costs involved in printing the samples necessary, a full length tool wear analysis could not be undertaken. However, the condition of the cutting edges has been monitored, in order to better understand the variations in specific responses. Surface roughness results can be validated through the observations made on the cutting edge condition and the possible edge chipping and breakage phenomena, if any. Images are taken at the cutting edge and the flank face of each insert used and are presented in Fig. 7-28 below. Edge chipping is noted to propagate predominantly from the interface where the T land, the tool face, and the cutting edge meet. Further, the edge chipping and breaking is seen to start 1.5 mm from the chisel edge, consistent with the pilot hole diameter of 3 mm. However, it is difficult to establish exactly when this could have initiated, as the drill moves down forming the through hole. The chipping phenomena is comparable for all samples produced at the different laser energy densities, and also the wrought duplex stainless steel samples, with the damage spreading for about 2mm from the start point, in a triangular fracture area.

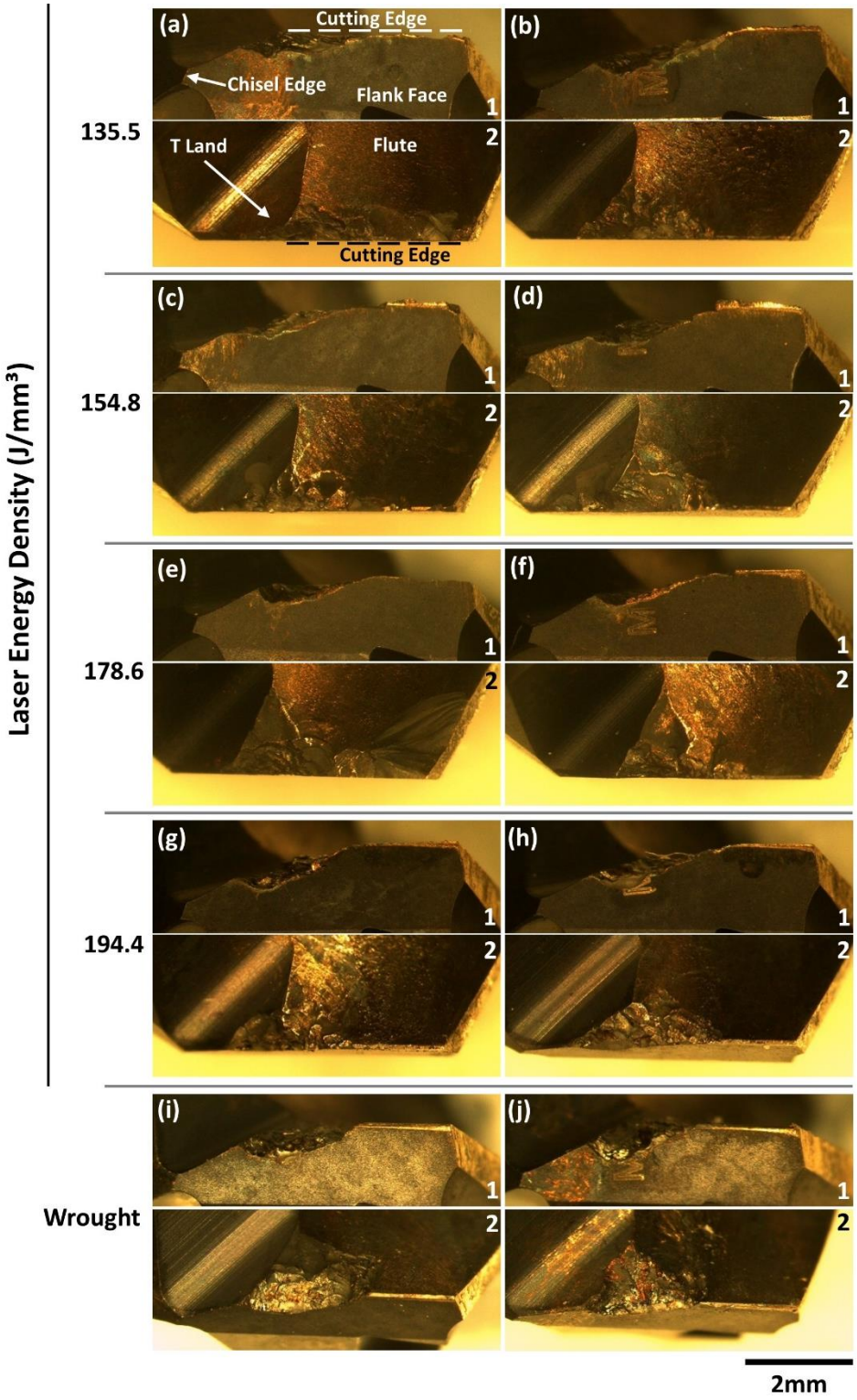

Fig. 7-28 Drill insert damage in the SLM samples at varying LED and Wrought SAF 2507

The drill damage with the as-built and the solution annealed samples is compared through the photographs of the cutting edges presented in Fig. 7-29 and 7-30. In all these cases, each cutting trial is undertaken with a fresh drill bit, and so, the results are relatively representing the machining conditions close to the reality. Drill tool edge chipping and

cracking progressed with the cutting speed for both as-built and solution annealed samples as presented in Fig. 7-29 and 7-30 respectively. The damage to the drill tool is seen to be significantly greater in the machining of the as-built samples for all cutting speeds, which correlates to the increased thrust force results observed in Fig. 7-22-(b). Greater possibilities for the BUE formation in the as-built samples is most likely the cause of the increased tool damage. Chipping on the outer edge of the flute is additionally observed in the 100 m/min (Fig. 7-30-(e) and (f)) sample which is commonly attributed to excessive cutting speed as explained by Drozda and Wick [314]. It may be noted from Fig. 7-29 and 7-30-(e) and (f), that at 140 m/min, the tool edge damage is quite severe in the as-built state, compared to the solution annealed sample cases. This is probably due to the conversion of the microstructures into the austeno-ferritic configurations together with the typical plate-like precipitation of austenite in the solution annealed state. The CrN precipitates still remaining in the structure also could have contributed favourably. This appears to have promoted better machinability in the solution annealed samples of laser melted duplex stainless steel.

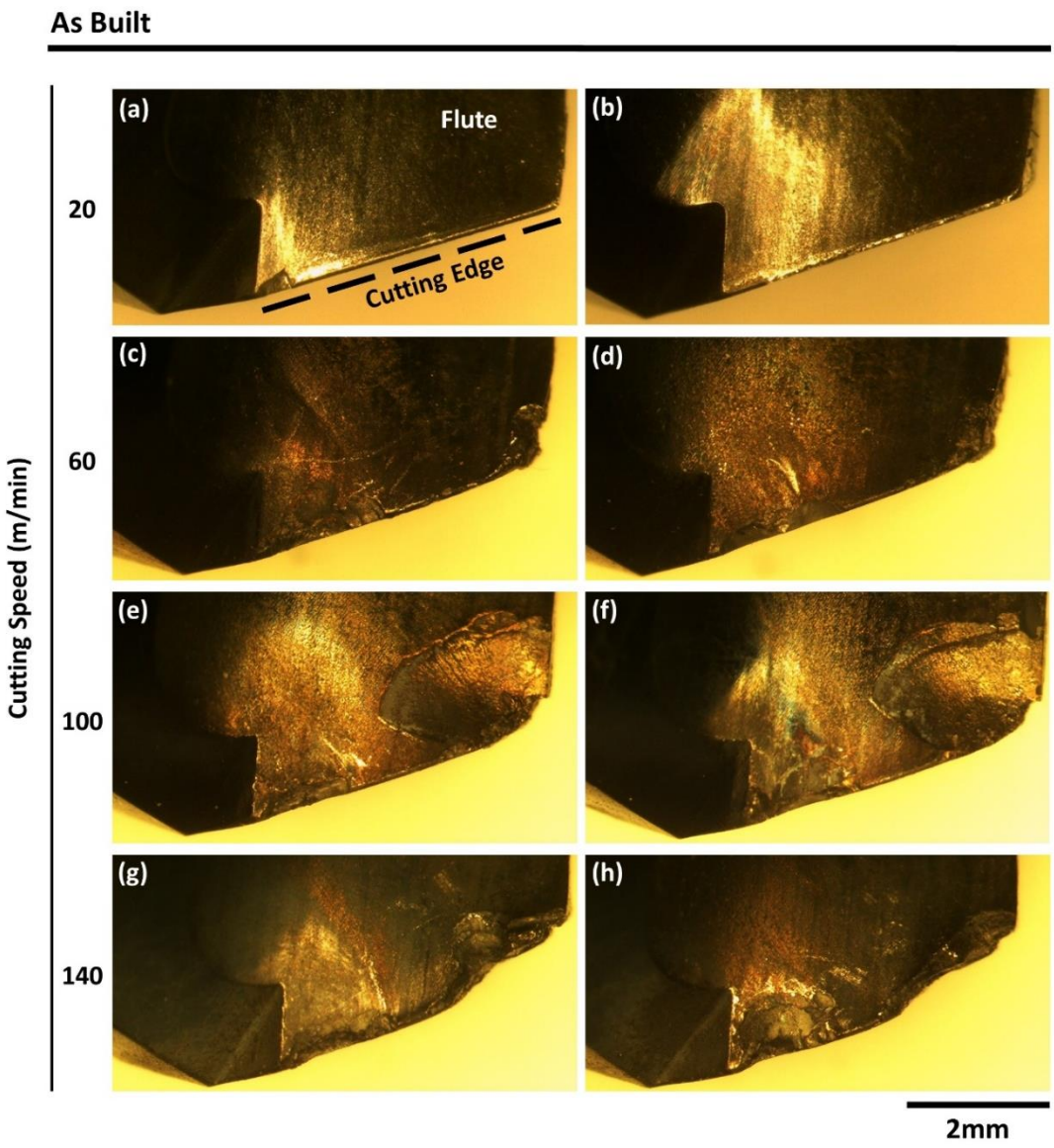

Fig. 7-29 Drill damage in the as-built SLM sample

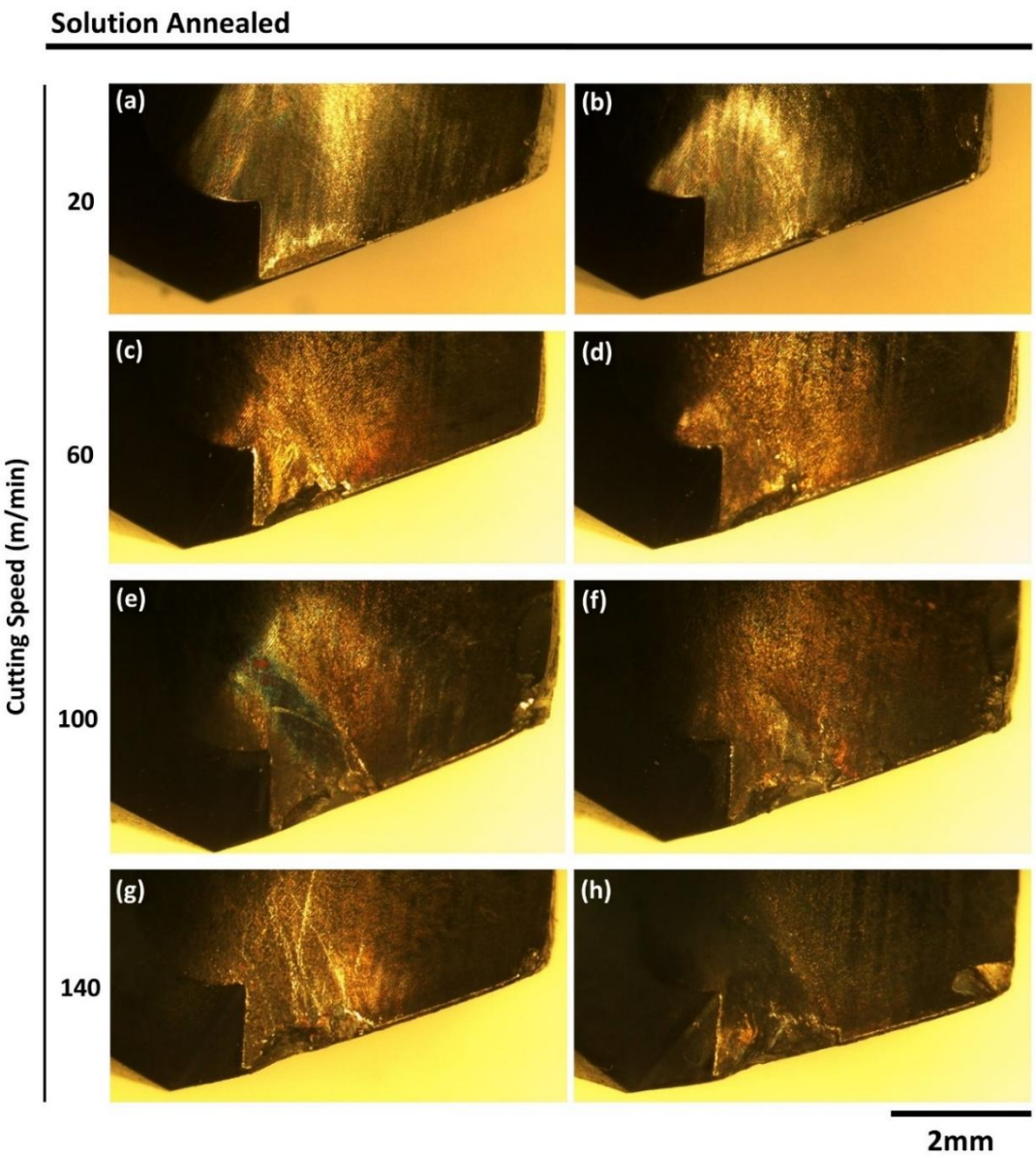

Fig. 7-30 Solution annealed SLM sample drill wear

7.6 Summary of the machinability studies

Experimental work is done to establish the machinability responses of the duplex stainless steel specimens both in the as-built and the solution-annealed states and also compared against wrought duplex cases. Drilling trials are done with varying speed and feed combinations, while microstructures of the drilled specimens, cutting forces, temperatures at specific locations in the work domains, and the surface roughness of the holes drilled are the critical responses. Microstructures of the cross-sectional faces of the

drilled holes showed clear differences amongst the different cases studied. The wrought samples showed the formation of periodic kinks along the length of the hole, probably indicating the effects of work hardening. The SLM samples in the as-built state apparently showed no visible traces of changes in the structures along the length of the holes. The solution annealed samples showed a more uniform dispersion of the austenite and ferrite phases.

The drilling torque values are lower with the as-built SLM samples compared to the wrought duplex case. The thrust forces are slightly higher with the as-built SLM samples compared to the wrought cases. Solution annealing, while preserving the torque and the thrust force variation trends compared to the as-built cases, resulted in relatively lower values overall. The temperature values at the specific locations and the profiles are much lower and milder respectively in the case of the SLM samples in the as-built state, compared to the wrought duplex stainless steel. Similar comparisons of temperature values and profiles with the as-built samples against the solution annealed ones lead to mixed results that will also be varying with the cutting speed. The surface roughness values overall decreased with increasing cutting speed and the SLM samples both in the as-built and the solution annealed states resulted in lower surface roughness as compared to the wrought samples. In general, it is observed that the machinability of duplex stainless steels improves after laser melting, compared to the wrought state.

Chapter 8
Conclusions

8.1 Objectives and Achievements

The dual phase duplex steels with equal ratios of ferrite and austenite contents are realised to possess far superior characteristics compared to the austenitic and the ferritic grades. The wide ranging application potentials are also well documented. The carefully balanced metallographic structures are identified to be sensitive to thermo-mechanical interactions during the secondary processing stages. Significant developments occurring in additive processing technologies, in particular in the case of metals systems are noted. The lack of published research on the possible roles additive processing can play in shaping duplex steels into complex forms led to the current research with an overarching goal to evaluate duplex for processing through the powder based additive manufacturing methods. In particular, the focus has been to search for answers to the key question, as to how a selected grade of duplex stainless steel powder will respond to processing by selective laser melting with varying process parameter combinations.

Experimental research has been designed and conducted searching for the answers to the main research question and the subsequent process evaluation and enhancement aspects. The overall scheme of the experimental research is undertaken in two successive stages. The first stage is dedicated to the proof of concept, that the entire cycle of processing duplex steels by laser melting and then heat-treating the printed objects to restore the phase balance is viable. Once the powders are proved to respond reasonably to processing by laser melting, the second stage of experimental investigation is to ascertain the process-structure-property relationships, together with the establishment of specific attributes achieved, if any.

Experimental work done during the first stage, using the preliminary process parameter settings verified the hypothesis that duplex steels can be processed by selective laser

melting with the structural distortions rectified using a suitable post-process heat treatment cycle. Evidently, the process conditions under the action of the point-by-point heat transfer into the powder bed, through a rapidly scanning laser heat source resulted in thermally distorted microstructures. The micro-structures are predominantly ferritic, with nano-scale sub-cells and the formation of CrN precipitates. Equilibrium equal ferrite to austenite structures are mostly regained through the post-process solution annealing treatment. However, the mechanism of this restoration is in accordance with the structures resulting from SLM, as the austenite is noted to precipitate in the form of Widmanstätten needles, along the grain boundaries and within the intra-granular regions.

The second stage experiments began with a deeper analysis of the process-structure relationships, followed by the establishment of the mechanical property responses and the structure property relationships. The duplex structures are transformed into predominant ferrite grains elongated in the build direction, while the austenite precipitated either at the grain boundaries or as Widmanstätten laths growing across the ferrite grains. The crystal structures and orientations are affected around the cavities, while considerable CrN precipitation is also evidenced. Changes in process parameters led to improved consolidation and variances in the microstructural ratios of austenite and ferrite. Improved processing conditions and scan strategies led to higher density and ultimate tensile strength values. While the strength values in the as-built state are close to the wrought case, the ductility is relatively lower due to the structure-property dependencies. The structural balance achieved through the solution annealing process improved the ductility to some extent, while the tensile strength fell short of the wrought case.

Two significant aspects are considered to be important in view of the nature of the structural variations achieved through selective laser melting of duplex steel powders. The possible role of the resulting ferritic structures on the magnetic responses is the first. It is established that the resulting material exhibits strong soft magnetic characteristics, in comparison with similar steels. The other aspect of interest is to establish the possible role of the resulting micro-structures on the machinability of the printed samples. It is established that the ferritic structures along with the plate-like austenite segregation allow for a better machinability in the as-built state, compared to the wrought counterparts, by means of lower drilling torques, temperatures and surface roughness. The chip

morphologies indicate the brittle nature of the material and the formation of discontinuous chips, possibly due to the CrN precipitates. Solution annealing of the laser melted samples further improved the machinability over the as-built samples. The edge chipping and cracking observations made on the drill tools used for the machinability experiments indicate the least damage attained with the solution annealed laser melted samples, compared to the as-built and the wrought duplex cases.

Overall, the hypothesis that selective laser melting can be applied to duplex stainless steel powders without the extensive loss of the structural and property responses is proved. The other objectives set to answer the principal and the secondary research questions are achieved. Structure-dependent magnetic responses, and improved machinability further to laser melting are the by-products of the typical attributes of the material-process combination. The general and more qualitative conclusions are listed in the next section, followed by the more specific and quantitative conclusions drawn based on the experimental results obtained at different stages.

8.2 General Conclusions

Stage I: Initial laser melting trials

Preliminary Experiments

- Single layer trials proved the ability of duplex stainless steel to be processed by selective laser melting with increasing laser power leading to enlarging of the melt tracts in the direction perpendicular to the laser scan lines.
- Dimensional errors increased with increasing laser energy density. The error in the sample height varied from a negative to a positive error due to a height loss from the melt pool viscosity and the widening of the melt tracts.

- Microstructures resulting from laser melting are predominantly ferritic, with austenite precipitating along the columnar grain boundaries in the direction of the build and as intersecting Widmanstätten needles.
- Inter-tract and inter-layer fusion increased with increasing laser energy density, resulting in a reduction of the lack of fusion porosity to a minimum and a decrease in the pore size
- Density measurements by Archimedes principle concluded in a maximum density of 90.8% at 70.6 J/mm^3.
- Micro-hardness varys in two stages as a result of microstructural differences including increased austenite growth, although, micro-hardness measurements are greater than those of laser welded SAF 2507.
- The post-process solution annealing treatment led to an enhanced austenite precipitation, primarily as intra-granular plates and the Widmanstätten laths, following the as-built growth direction.

Stage II: Further laser melting trials

Metallographic inferences

- Columnar grain growth surpassing fusion zones with Length:Width ratios as high as 16.2:1, resulted from laser melted samples produced under processing conditions, conducive of better consolidation.
- EBSD orientation maps show the grain growth to be predominantly along the <001> direction which also increased further with increasing laser energy density.
- Widmanstätten austenite precipitation increased at laser power levels above 325 W, with the number of sites increasing in frequency at elevated laser energy densities.
- Microstructural variances are noted in samples produced at the top left most portion of the build platform with reduced Widmanstätten austenite precipitation and improved consolidation, indicating the influences of the gas flow patterns inside the build chamber.

- The linear scan strategy employed led to an enlarged ferrite grain in the centre of the cross section from the double laser pass heating and grains devoid of Widmanstätten austenite along the periphery due to differential cooling rates.
- Fine cellular sub-grain growth is evident within the ferrite grains and with the orientation of the cells dependant on the fusion zone interfaces.
- Spherical CrN precipitation is observed intra-granularly collating along specific lines.
- Thin slender lack of fusion defects promoted fine columnar grain growth propagating from the top surface of the defect, with closely spaced defects leading to impingement and elongation of grains.
- Density measurements were near consistent over the laser energy densities employed and the average value is at 91.6%.
- Checkerboard scan strategy improved the density to a maximum of 93.09%, on average, better than the results obtained with the meander scan strategy at all laser powers.

Mechanical properties

- The ultimate tensile strength of the laser melted samples is comparable to that of the wrought material, though significantly more brittle and less ductile.
- The solution annealing process restored the percent elongation but reduced the tensile strength.
- Samples oriented at 45° showed improved tensile strength and elongation in the as-built state.
- A rippling effect was observed along the underside of samples produced at 45° with a peak-to-peak distance conforming to the checkerboard scan sizes.
- Fracture surfaces show brittle fracture features of the as-built samples and ductile trans-granular fractures and ductility in the solution annealed samples.
- Micro dimple fractured surfaces are observed in both the as-built and the solution annealed states, with the enlargement of the dimples evident in the heat treated samples.
- Further, CrN precipitation is observed within the dimples in the as-built state.

Magnetic responses

- Laser melted microstructures contained on average 70% ferrite across all the laser energy density settings used.
- Strong soft magnetic characteristics are evident from the SLM samples in the as-built state with a significant increase in the magnetic saturation over the wrought samples and low coercivities.
- The magnetic responses are recorded to be significantly anisotropic, based on the grain orientations and elongations resulting from laser melting.

Machinability studies

- Lower drilling torques and drilling temperatures are observed in the drilling of laser melted duplex stainless compared to the wrought material.
- Discontinuous chips are formed while machining the laser melted samples, leading to better heat dissipation.
- Thrust forces in drilling SLM samples increased with cutting speed and feed
- Solution annealing of the laser melted microstructure led to machinability improvements with lower thrust forces, drilling torques and tool damages at all cutting conditions.
- Drilling torque and thrust force values followed identical trends in the solution annealed and laser melted SLM samples with drilling torque increasing to a maximum and reducing subsequently with increasing speed.
- Grain deformation up to 30 µm induced via work hardening is evident in wrought duplex stainless steel and to a lesser degree in the SLM samples due, to the ferrite dominated microstructure.
- Grain deformation influences the micro-hardness results of the wrought material with a 392.2 HV difference in the hardness between the grains closest to the hole surface and the bulk material for all cutting conditions.

- Chips produced from machining laser melted samples are discontinuous and brittle, decreasing in size with increasing cutting speed and feed, as against the longer and thicker chips resulting from the wrought material.
- Microstructures of samples produced at differing LED are similar, with the 178.6 J/mm^3 sample showing higher Widmanstätten austenite precipitation
- Laser melted samples are on average 15.1 HRC harder than the wrought material, contributing to the brittle chip formation and higher thrust force results.
- Surface roughness is comparatively lower in SLM samples compared to the wrought material.
- Surface roughness further improved in both the as-built and the solution annealed SLM samples with increasing cutting speeds.
- Dynamic recrystallisation and formation of a micro duplex microstructure is visible in samples machined in the as-built and the solution annealed states, with the zone sizes increasing in width with the cutting speed. This led to micro-hardness results increasing with cutting speed.

8.3 Quantitative Conclusions

The following are the more specific and quantitative conclusions that can be drawn based on the experimental results gathered from the current research:

Stage I: Initial laser melting trials

Preliminary Experiments

- The percentage dimensional error increases linearly with increasing laser energy density, averaging at around 2-3%.
- Bulk density values vary with the laser energy density with an overall average density exceeding 88% based on the results of the preliminary stage experiments.

- Micro-hardness values decrease with laser energy density from a maximum of 447.8 HV to a minima of 364.4 HV at 98.9 J/mm^3 before increasing at the upper energy densities.
- Void fraction is significantly reduced with increasing laser energy, reaching a minimum of 0.053% at 215.5 J/mm^3

Stage II: Further laser melting trials

Metallographic evaluation

- A ferrite dominated microstructure is evident for all processing conditions, with the average ferrite content at around 68.8%
- Grain orientation is predominantly in the <001> direction with an average grain L:W aspect ratio of 11.5:1.
- Samples produced at the top left of the build platform show less Widmanstätten austenite growth, porosity and greater crystallographic irregularity.
- The average bulk density obtained in the laser melted samples is at around 91.6%.
- The checkerboard laser scan strategy led to improved densification with the selected parameters corresponding to density values of; 92.4, 92.53 and 93.09 %

Mechanical properties

- Micro-hardness values exceeded that of the wrought material with an average hardness of around 408.4 HV.
- Ultimate tensile strength results are on average 841.7 MPa for the as-built condition and 715.3 MPa for the solution annealed condition.
- Solution annealing improved the elongation of laser melted samples from 21% in the as-built state to 41%.
- Fracture surfaces are represented by micro dimples 0.3-1.2 µm in diameter in the as-built state and increasing up to 0.8-4.5 µm after the solution annealing treatment.

Magnetic responses

- Feritscope readings indicate an average ferrite content of 70% in SLM samples, much higher than the wrought samples.
- The average saturation magnetism (Ms) of SLM processed duplex stainless steel is 110.85 Am^2/kg, more than double the saturation level possible with the equivalent wrought material.
- SLM samples exhibit strong soft magnetic characteristics with an average coercivity (Hc) of 1.81 mT,

Machinability studies

- Minor variations in the drilling torque and a sizeable variation in the thrust force at around 200 N are evident al the laser energy density is varied, with similar cutting conditions.
- Wrought samples exhibit deformation of ferrite and austenite grains characteristic of work hardening behaviour to a depth of 30 µm, which is rarely visible in the SLM samples.
- Grain deformation in the wrought samples leads to a 392.2 HV maximum increase in the hardness due to machining
- An average bulk hardness of 39.1 HRC is noted over all the four laser energy densities, around 15.1 HRC greater than the hardness of the wrought samples.
- Surface roughness values improved in the laser melted samples, varying between 1.22 to 2.73 µm, as against the 1.68-3.78 µm range observed in the wrought samples.
- Surface roughness decreased with increasing cutting speed in SLM samples produced in the as-built and solution annealing state to a minima of 1.06 µm at 140 m/min in the solution annealed state.

8.4 Future Scope

Based on the experimental results generated from the current research, duplex stainless steels are established to be clear candidates for processing by selective laser melting. A significant insight into the process-structure-property relationships could also be developed. The results indicate a promising future for duplex steels to be processed into relatively complex forms based on the direct digital manufacturing concepts. This will open up opportunities to redesign certain components, utilising the better design freedom additive manufacturing offers. While commercial benefits are obvious of the material and process combination, further work is needed before actually realising the same.

First, a thorough investigation of the roles of different process parameters both individually and in combinations need to be undertaken, in order to optimise the process conditions for different application requirements. Statistical design of experiments and response surface methodologies must be used as is the case with any new material development process undertaken by the commercial laser melting system manufacturers, before releasing the material file. Corrosion resistant is a significant attribute of duplex stainless steels. Both time and equipment limitations did not allow to evaluate the possible influences of the laser processing on the corrosion behaviour of the printed samples as part of the current research. It is important that these aspects are evaluated and understood thoroughly in the future.

References

1. IMOA, *Practical Guidelines for the Fabrication of Duplex Stainless Steel*. 2 ed. 2009, London, UK: International Molybdenum Assosciation (IMOA).
2. BSSA. *The Discovery of Stainless Steel*. About Stainless Steel 2015 [cited 2015 23 January]; Available from: http://www.bssa.org.uk/about_stainless_steel.php?id=31.
3. Gunn, R.N., *Duplex Stainless Steels: Microstructure, Properties and Applications* 1ed. 1997, Cambridge: Woodhead Publishing.
4. Liljas, M. *80 years with duplex steels, a historic review and prospects for the future*. in *6th European Stainless Steel Conference*. 2008. Helsinki.
5. Alvarez-Armas, I., *Duplex Stainless Steels - Brief History and Some Recent Alloys* Recent Patents on Mechanical Engineering, 2008. **1**(1): p. 51-57.
6. Charles, J., *Past present and future of the Duplex stainless steels* in *Duplex Conference*. 2007: Grado, Italy. p. 18-20.
7. Charles, J., *Duplex Stainless steels, A review after DSS '07 held in Grado* Steel Research International 2008. **79**(6): p. 455-465.
8. BSSA. *Calculation of pitting resistance equivalent numbers (PREN)*. Pitting Corrosion & PRE Numbers 2017 [cited 2017 29 September]; Available from: http://www.bssa.org.uk/topics.php?article=111.
9. Sandvik, *Sandvik SAF 3207 HD -Tube and Pipe, Seamless: Datasheet*. 2017, Sandvik AB: Sweden.
10. Pohl, M., O. Storz, and T. Glogowski, *Effect of intermetallic precipitations on the properties of duplex stainless steel.* Materials Characterization, 2007. **58**(1): p. 65-71.
11. Hoffmeister, H. and R. Mundt, *Untersuchungen zum Einfluß des Kohlenstoffs und des Stickstoffs auf die δ-γ-Umwandlung ferritisch-austenitischer Chrom-Nickel-Stähle.* Archiv für das Eisenhüttenwesen, 1981. **52**(4): p. 159-164.
12. Leone, G.L. and H.W. Kerr, *The ferrite to austenite transformation in stainless steels.* Welding Journal 1982. **61**(1): p. 13S-21S.
13. Ogawa, T. and T. Koseki, *Effect of composition profiles on metallurgy and corrosion behavior of duplex stainless steel weld metals.* Weld Journal, 1989. **68**(5): p. 181S - 191S.
14. Yang, Y., Z. Wang, H. Tan, J. Hong, Y. Jiang, L. Jiang, and J. Li, *Effect of a brief post-weld heat treatment on the microstructure evolution and pitting corrosion of laser beam welded UNS S31803 duplex stainless steel.* Corrosion Science, 2012. **65**: p. 472-480.
15. Ohmori, Y., K. Nakai, H. Ohtsubo, and Y. Isshiki, *Mechanisim of Widmanstätten austenite formation in a δ/γ duplex phase stainless steel* ISIJ International, 1995. **35**(8): p. 969-975.
16. Ramirez, A.J., S.D. Brandi, and J.C. Lippold, *Secondary austenite and chromium nitride precipitation in simulated heat affected zone of duplex stainless steels.* Science and Technology of Welding and Joining, 2004. **9**(4): p. 301-313.
17. Liao, J., *Nitride precipitation in weld HAZs of a duplex stainless steel.* ISIJ International, 2001. **41**(5): p. 460-467.
18. Sieurin, H. and R. Sandström, *Sigma phase precipitation in duplex stainless steel 2205.* Materials Science and Engineering: A, 2007. **444**(1-2): p. 271-276.
19. Murr, L.E., E. Martinez, X. Pan, C. Meng, J. Yang, S. Li, F. Yang, Q. Xu, J. Hernandez, W. Zhu, S.M. Gaytan, F. Medina, and R.B. Wicker, *Microstructures and properties of solid and reticulated mesh components of pure iron fabricated by electron beam melting.* Journal of Materials Research and Technology, 2013. **2**(4): p. 376-385.
20. Ramirez, A.J., J.C. Lippold, and S.D. Brandi, *The relationship between Chromium Nitride and Secondary Austenite precipitation in duplex stainless steel.* Metallurgical and Materials Transactions A, 2003. **34**(8): p. 1575-1597.
21. Chen, T.H. and J.R. Yang, *Effects of solution treatment and continuous cooling on σ-phase precipitation in a 2205 duplex stainless steel.* Materials Science and Engineering: A, 2001. **311**(1-2): p. 28-41.

22. Davison, R.M. and J.D. Redmond, *A guide to using duplex stainless steels.* Materials and Design, 1991. **12**(4): p. 187-192.
23. Nilsson, J.O., *Super duplex stainless steels.* Materials Science and Technology, 1992. **8**(8): p. 685-700.
24. Floreen, S. and H.W. Hayden, *The influence of austenite and ferrite on the mechanical properties of two-phase stainless steels having microduplex structure.* ASM Transactions Quarterly, 1968. **61**(3): p. 489-499.
25. Gadelrab, K.R., G. Li, M. Chiesa, and T. Souier, *Local characterization of austenite and ferrite phases in duplex stainless steel using MFM and nanoindentation.* Journal of Materials Research, 2012. **27**(12): p. 1573-1579.
26. Moverare, J.J. and M. Odén, *Influence of elastic and plastic anisotropy on the flow behaviour in a duplex stainless steel.* Metallurgical and Materials Transactions A, 2002. **33A**(1): p. 57-71.
27. Stolarz, J. and J. Foct, *Specific feature of two phase alloys response to cyclic deformation.* Materials Science and Engineering: A, 2001. **319-321**: p. 501-505.
28. Balbi, M., M. Avalos, A. El Bartali, and I. Alvarez-Armas, *Microcrack growth and fatigue behavior of a duplex stainless steel.* International Journal of Fatigue, 2009. **31**(11-12): p. 2006-2013.
29. Mateo, A., L. Llanes, N. Akdut, and M. Anglada, *High cycle fatigue behaviour of a standard duplex stainless steel plate and bar* Materials Science and Engineering: A, 2001. **319-321**: p. 516-520.
30. Vogt, J.B., K. Massol, and J. Foct, *Role of the microstructure on fatigue properties of 475°C aged duplex stainless steel.* International Journal of Fatigue, 2002. **24**(6): p. 627-633.
31. Devillers-Guerville, L., J. Besson, and A. Pineau, *Notch fracture toughness of a cast duplex stainless steel: modelling of experimental scatter and size effect.* Nuclear Engineering and Design, 1997. **168**(1-3): p. 211-225.
32. Topolska, S. and J. Labanowski, *Impact-toughness investigations of duplex stainless steels.* Materiali in tehnologije, 2015. **49**(4): p. 481-486.
33. Smuk, O., *Microstructure and Properties of Modern P/M Super Duplex Stainless Steels* in *Department of Materials Science and Engineering, Division of Ceramics*. 2004, Royal Institute of Technology: Stockholm, Sweden. p. 52.
34. Guo, Y., J. Hu, J. Li, L. Jiang, T. Liu, and Y. Wu, *Effect of Annealing Temperature on the Mechanical and Corrosion Behavior of a Newly Developed Novel Lean Duplex Stainless Steel.* Materials, 2014. **7**(9): p. 6604-6619.
35. Charles, J., *Corrosion resistance properties*, in *Duplex Stainless Steels*, I. Alvarez-Armas and S. Degallaix-Moreuil, Editors. 2009, ISTE Ltd: Great Britain. p. 47-114.
36. Merello, R., F.J. Botana, J. Botella, and M. Marcos, *Determination of the weaker phase in the pitting corrosion of non-standard low-Ni high-Mn-N duplex stainless steels.* Materials and Corrosion, 2004. **55**(2): p. 95-101.
37. Magnabosco, R., *Kinetics of sigma phase formation in a duplex stainless steel.* Materials Research, 2009. **12**(3): p. 321-327.
38. Nilsson, J.O. and A. Wilson, *Influence of isothermal phase transformations on toughness and pitting corrosion of super duplex stainless steel SAF 2507.* Materials Science and Technology, 1993. **9**(7): p. 545-554.
39. Liou, H.-Y., R.-I. Hsieh, and W.-T. Tsai, *Microstructure and pitting corrosion in simulated heat-affected zones of duplex stainless steels.* Materials Chemistry and Physics 2002. **74**(1): p. 33-42.
40. Pardal, J.M., S.S.M. Tavares, M.P.C. Fonseca, J.A. Souza, L.M. Vieira, and H.F.G. Abreu, *Deleterious phases precipitation on superduplex stainless steel UNS S32750: Characterisation by light optical and scanning electron microscopy.* Materials Research, 2010. **13**(3): p. 401-407.
41. Baldo, S., *Innovative steels for structural and corrosion resistance applications* in *Department of Chemical Engineering Processes*. 2010, Università degli Studi di Padova: Padova, Italy. p. 153.

42. Liljas, M. and F. Sjöholm, *Applications*, in *Duplex Stainless Steels*, I. Alvarez-Armas and S. Degallaix-Moreuil, Editors. 2009, ISTE Ltd: Great Britain. p. 403-423.
43. Bendall, K.C., *Duplex stainless steel in the pulp and paper industry*. Anti-Corrosion Methods and Matters, 1997. **44**(3): p. 170-174.
44. Tigerstrand, C., *Enhanced structural efficiency with duplex stainless steel in pressure vessels.* Advance - Outokumpu White Paper, 2016. **April**(1): p. 1-14.
45. Chai, G., U. Kikisäkk, J. Tokaruk, and J. Eidhagen, *Hyper duplex stainless steel for deep subsea applications.* Stainless Steel World, 2009(March): p. 27-33.
46. Sandvik. *Whats next in umbilicals?* Applications 2017 21 April [cited 2017 22 April]; Available from: http://smt.sandvik.com/en/applications/oil-and-gas-upstream/subsea-infrastructure/umbilicals/.
47. Zahurul Islam, S.M. and B. Young. *Use of stainless steel as structural members in bridge construction and fiber reinforced polymer strengthening*. in *Joint Conference on Advances in Bridge Engineering-III*. 2015. Dhaka, Bangladesh: IABSE-JSCE.
48. Medina, E., J.M. Medina, A. Cobo, and D.M. Bastidas, *Evaluation of mechanical and structural behavior of austenitic and duplex stainless steel reinforcements.* Construction and Building Materials, 2015. **78**: p. 1-7.
49. Outokumpu, *Sometimes long lasting materials are the only choice.* n.d., Outokumpu: Australia. p. 1-11.
50. Halling, E., *Stainless steels within desalination for reliable water supply.* International Journal of Nuclear Desalination, 2010. **4**(2): p. 142-148.
51. Olsson, J. and M. Snis, *Duplex — A new generation of stainless steels for desalination plants.* Desalination, 2007. **205**(1-3): p. 104-113.
52. McManus, L. *Stainless solution keeps fresh water flowing*. Choose Stainless 2016 [cited 2017 22 April]; Available from: http://choosestainless.outokumpu.com/stainless-solution-keeps-fresh-water-flowing/.
53. Chater, J., *Storage and transportation tanks: two growing applications for stainless steel* Stainless Steel World, 2014(January/February): p. 1-4.
54. Partington, E., *Stainless steel in the food and beverage industry*, in *Materials and Applications Series*. 2006, Euro Inox: Brussels.
55. Mazinanian, N., G. Herting, I.O. Wallinder, and Y. Hedberg, *Metal Release and Corrosion Resistance of Different Stainless Steel Grades in Simulated Food Contact.* Corrosion, 2016. **72**(6): p. 775-790.
56. Cigada, A., G. De Santis, A.M. Gatti, A. Roos, and D. Zaffe, *In vivo behaviour of a high performance duplex stainless steel.* Journal of Applied Biomaterials 1993. **4**(1): p. 39-46.
57. Gregorutti, R.W., J.E. Grau, F. Sives, and C.I. Elsnerc, *Mechanical, electrochemical and magnetic behaviour of duplex stainless steel for biomedical applications.* Materials Science and Technology, 2015. **31**(15): p. 1818-1824.
58. Platt, J.A., A. Guzman, A. Zuccari, D.W. Thornburg, B.F. Rhodes, Y. Oshida, and B.K. Moore, *Corrosion behaviour of 2205 duplex stainless steel.* American journal of orthodontics and dentofacial orthopedics, 1997. **112**(1): p. 69-79.
59. Filho, A.I., R.V. da Silva, and R.V. Bertolo, *A new stainless steel wire for orthodontic purposes.* Dental Press Journal of Orthodontics, 2011. **16**(4): p. 55-59.
60. Wen, S., C.D. Lundin, and G. Batten, *Metallurgical evaluation of cast duplex stainless steels and their weldments* in *U.S. Department of Energy - Award Number - DE-FC36-00 ID13975*, C.D. Lundin, Editor. 2001, Materials Joining Group - The University of Tennessee: Knoxville, TN. p. 231.
61. Kim, Y.-J., *Phase transformations in cast duplex stainless steels* in *Materials Science and Engineering*. 2004, Iowa State University: Ames, Iowa. p. 144.
62. Pineau, A. and J. Besson, *Thermal embrittlement of cast duplex stainless steels: Observations and modeling*, in *Duplex Stainless Steels*, I. Alvarez-Armas and S. Degallaix-Moreuil, Editors. 2009, ISTE Ltd: Great Britain. p. 161-208.
63. Herrera, C., D. Ponge, and D. Raabe, *Characterisation of the microstructure, crystallographic texture and segregation of an as-cast duplex stainless steel slab.* Steel Research International 2008. **79**(6): p. 482-488.

64. Glownia, J., B. Kalandyk, and K. Hübner, *Delta ferrite predictions for cast duplex stainless steel with high nitrogen content.* Materials Characterization, 2001. **47**(2): p. 147-155.
65. Martins, M. and L.R.N. Forti, *Effect of aging on impact properties of ASTM A890 Grade 1C super duplex stainless steel.* Materials Characterization, 2008. **59**(2): p. 162-166.
66. Martins, M. and L.C. Casteletti, *Microstructural characteristics and corrosion behavior of a super duplex stainless steel casting.* Materials Characterization, 2009. **60**(2): p. 150-155.
67. Johnson, E., Y.-J. Kim, L. Scott Chumbley, and B. Gleeson, *Initial phase transformation diagram determination for the CD3MN cast duplex stainless steel.* Scripta Materialia, 2004. **50**(10): p. 1351-1354.
68. Haušild, P., C. Berdin, P. Bompard, and N. Verdière, *Ductile fracture of duplex stainless steel with casting defects* International Journal of Pressure Vessels and Piping, 2001. **78**(9): p. 607-616.
69. Gutierrez, I. and A. Iza-Mendia, *Process: Hot Workability*, in *Duplex Stainless Steels*, I. Alvarez-Armas and S. Degallaix-Moreuil, Editors. 2009, ISTE Ltd: Great Britain. p. 1-46.
70. Mao, P., K. Yang, and G. Su, *Hot deformation behavior of an as-cast duplex stainless steel.* Journal of Materials Science and Technology, 2003. **19**(4): p. 379-381.
71. Subramanian, K.M. and P. Chandramohan, *Crack Formation during Hot Rolling of Nitrogen Alloyed Duplex Stainless Steels.* Materials and Manufacturing Processes, 2012. **27**(9): p. 996-1000.
72. Feng, Z.-h., J.-y. Li, and Y.-d. Wang, *Mechanism of hot-rolling crack formation in lean duplex stainless steel 2101*. International Journal of Minerals, Metallurgy, and Materials, 2016. **23**(4): p. 425-433.
73. Reis, G.S., A.M. Jorge Jr, and O. Balancin, *Influence of the microstructure of duplex stainless steels on their failure characteristics during hot deformation.* Materials Research, 2000. **3**(2): p. 31-35.
74. Reick, W., M. Pohl, and A.F. Padilha, *Recrystallization-transformation combined reactions during annealing of a cold rolled ferritic-austenitic duplex stainless steel* ISIJ International, 1998. **38**(6): p. 567-571.
75. Pramanik, S., S. Bera, and S.K. Ghosh, *Influence of Cold Rolling on Microstructural Evolution in 2205 Duplex Stainless Steel.* Steel Research International, 2014. **85**(5): p. 776-783.
76. Hättestrand, M., P. Larsson, G. Chai, J.-O. Nilsson, and J. Odqvist, *Study of decomposition of ferrite in a duplex stainless steel cold worked and aged at 450–500°C.* Materials Science and Engineering: A, 2009. **499**(1-2): p. 489-492.
77. Baldo, S. and I. Mészáros, *Effect of cold rolling on microstructure and magnetic properties in a metastable lean duplex stainless steel.* Journal of Materials Science, 2010. **45**(19): p. 5339-5346.
78. Paro, J., H. Hänninen, and V. Kauppinen, *Tool wear and machinability of HIPed P/M and conventional cast duplex stainless steels.* Wear, 2001. **249**(3): p. 279-284.
79. Dolinšek, S., *Work-hardening in the drilling of austenitic stainless steels.* Journal of Materials Processing Technology, 2003. **133**(1): p. 63-70.
80. Nomani, J., A. Pramanik, T. Hilditch, and G. Littlefair, *Investigation on the Behavior of Austenite and Ferrite Phases at Stagnation Region in the Turning of Duplex Stainless Steel Alloys.* Metallurgical and Materials Transactions A, 2016. **47**(6): p. 3165-3177.
81. Krolczyk, G.M. and S. Legutko, *Experimental Analysis by Measurement of Surface Roughness Variations in Turning Process of Duplex Stainless Steel.* Metrology and Measurement Systems, 2014. **21**(4): p. 759-770.
82. Koyee, R.D., U. Heisel, S. Schmauder, and R. Eisseler, *Experimental Investigation and Multiobjective Optimization of Turning Duplex Stainless Steels.* International Journal of Manufacturing Engineering, 2014. **2014**: p. 1-13.
83. Krolczyk, G.M., P. Nieslony, and S. Legutko, *Determination of tool life and research wear during duplex stainless steel turning.* Archives of Civil and Mechanical Engineering, 2015. **15**(2): p. 347-354.

84. Hariharan, V., *The Development of Qualification Standards for Cast Super Duplex Stainless Steel (2507 Wrought Equivalent)*, in *Department of Materials Science and Engineering*. 2005, University of Tennessee: Knoxville, TN.
85. Renaudot, N., E. Chauveau, and M. Mantel, *1.4669, a new lean duplex stainless steel with improved toughness and machinability.* La Metallurgia Italiana, 2012(9): p. 29-35.
86. Jeon, S.-H., S.-T. Kim, I.-S. Lee, and Y.-S. Park, *Effects of sulfur addition on pitting corrosion and machinability behavior of super duplex stainless steel containing rare earth metals: Part 2.* Corrosion Science, 2010. **52**(10): p. 3537-3547.
87. Bordinassi, E.C., C.O.C. Almeida Filho, S. Delijaicov, G.F. Batalha, and M.S. Filho. *Study of the surface integrity in a super duplex stainless steel after turning*. in *4º Congresso Brasileiro de Engenharia de Fabricação*. 2007. Estância de São Pedro, Brazil.
88. Krolczyk, G., P. Nieslony, and S. Legutko, *Microhardness and Surface Integrity in Turning Process of Duplex Stainless Steel (DSS) for Different Cutting Conditions.* Journal of Materials Engineering and Performance, 2013. **23**(3): p. 859-866.
89. Jiang, L., J. Paro, H. Hänninen, V. Kauppinen, and R. Oraskari, *Comparison of grindability of HIPped austenitic 316L, duplex 2205 and super duplex 2507 DSS and as-cast 304 stainless steels using alumina wheels.* Journal of Materials Processing Technology, 1996. **62**(1-3): p. 1-9.
90. Nomani, J., A. Pramanik, T. Hilditch, and G. Littlefair, *Machinability study of first generation duplex (2205), second generation duplex (2507) and austenite stainless steel during drilling process.* Wear, 2013. **304**(1-2): p. 20-28.
91. R, S. and D. Chaira, *Development of nano-structured duplex and ferritic stainless steels by pulverisette planetary milling followed by pressureless sintering.* Materials Characterization, 2015. **99**: p. 220-229.
92. Martín, F., C. García, Y. Blanco, and M.L. Rodriguez-Mendez, *Influence of sinter-cooling rate on the mechanical properties of powder metallurgy austenitic, ferritic, and duplex stainless steels sintered in vacuum.* Materials Science and Engineering: A, 2015. **642**: p. 360-365.
93. Gupta, S., R. Shashanka, and D. Chaira, *Synthesis of nano-structured duplex and ferritic stainless steel powders by planetary milling: An experimental and simulation study.* IOP Conference Series: Materials Science and Engineering, 2015. **75**: p. 012033.
94. Martín, F., C. García, and Y. Blanco, *Effect of chemical composition and sintering conditions on the mechanical properties of sintered duplex stainless steels.* Materials Science and Engineering: A, 2011. **528**(29-30): p. 8500-8511.
95. Mariappan, R., S. Kumaran, and T.S. Rao, *Effect of sintering atmosphere on structure and properties of austeno-ferritic stainless steels.* Materials Science and Engineering: A, 2009. **517**(1-2): p. 328-333.
96. Mariappan, R., P. Kishore Kumar, S. Jayavelu, G. Dharmalingam, M. Arun Prasad, and A. Stalin, *Wear properties of P/M duplex stainless steel developed from 316L and 430L powders* International Journal of ChemTech Research, 2015. **8**(10): p. 109-115.
97. García, C., F. Martin, Y. Blanco, M.P. de Tiedra, and M.L. Aparicio, *Influence of Sintering under Nitrogen Atmosphere on Microstructures of Powder Metallurgy Duplex Stainless Steels.* Metallurgical and Materials Transactions A, 2009. **40**(2): p. 292-301.
98. García, C., F. Martín, Y. Blanco, M.P. de Tiedra, and M.L. Aparicio, *Corrosion behaviour of duplex stainless steels sintered in nitrogen.* Corrosion Science, 2009. **51**(1): p. 76-86.
99. Dobrzański, L.A., Z. Brytan, M. Actis Grande, and M. Rosso, *Properties of duplex stainless steels made by powder metallurgy* Archives of Materials Science and Engineering, 2007. **28**(4): p. 217-223.
100. Coccia, G., N. Lecis, G. Albricci, and R. Dovera, *Sintering of prealloyed duplex stainless steels powders at atmospheric pressure.* La Revue De Métallurgie, 2002. **99**(12): p. 1027-1032.
101. Bautista, A., F. Velasco, M. Campos, M.E. Rabanal, and J.M. Torralba, *Oxidation behaviour at 900°C of Austenitic, Ferritic and Duplex Stainless Steels manufactured by Powder Metallurgy.* Oxidation of Metals, 2003. **59**(3): p. 373-393.

102. Utrilla, M.V., A. Ureña, E. Otero, and C.J. Múnez. *Corrosion behvaviour of sintered duplex stainless steels*. in *EUROCORR 2004*. 2004. Nice, France: European Federation of Corrosion.
103. Gibson, I., D. Rosen, and B. Stucker, *Directed Energy Deposition Processes*, in *Additive Manufacturing Technologies* 2015, Springer: New York, USA. p. 245-268.
104. Jeantette, F.P., D.M. Keicher, J.A. Romero, and L.P. Schanwald, *Method and system for producing complex-shape objects*, U.S. Patent, Editor. 2000, Sandia Corporation: USA. p. 19.
105. Mudge, R.P. and N.R. Wald, *Laser engineered net shaping advances additve manufacturing and repair.* Welding Journal, 2007. **86**(1): p. 44-48.
106. BeAM, *MOBILE Machine*. 2016, BeAM S.A.S: Strasbourg Cedex, France. p. 1-2.
107. Gill, D., *Laser Engineered Net Shaping - Manufacturing Technologies*, S.N. Laboratories, Editor. 2006, Sandia Corporation. p. 1-2.
108. Palmer, T.A., *Additive manufacturing for corrosion and shipbuilding*, in *2017 National Shipbuilding Research Program All Panel Meeting*. 2017, National Shipbuilding Research Program: Charleston, NC.
109. Ziętala, M., T. Durejko, M. Polański, I. Kunce, T. Płociński, W. Zieliński, M. Łazińska, W. Stępniowski, T. Czujko, K.J. Kurzydłowski, and Z. Bojar, *The microstructure, mechanical properties and corrosion resistance of 316L stainless steel fabricated using laser engineered net shaping.* Materials Science and Engineering: A, 2016. **677**: p. 1-10.
110. Ruan, J., T.E. Sparks, J. Fan, S. J.K., A. Panackal, and F. Liou. *A review of layer based manufacturing processes for metals* in *17th Solid Freeform Fabrication Symposium* 2006. Austin, TX
111. Shin, K.-H., H. Natu, D. Dutta, and J. Mazumder, *A method for the design and fabrication of heterogeneous objects.* Materials & Design, 2003. **24**(5): p. 339-353.
112. Larson, R., *Method and device for producing three-dimensional bodies*, U.S. Patent, Editor. 1998, Arcam Limited: USA. p. 11.
113. Terrazas, C.A., S.M. Gaytan, J. Mireles, P. Frigola, D. Espalin, and R.B. Wicker. *EBM fabrication and characterization of high purity niobium for superconductor applications*. in *25th Solid Freeform Fabrication Symposium*. 2014. Austin, TX.
114. Zhong, Y., L.-E. Rännar, L. Liu, A. Koptyug, S. Wikman, J. Olsen, D. Cui, and Z. Shen, *Additive manufacturing of 316L stainless steel by electron beam melting for nuclear fusion applications.* Journal of Nuclear Materials, 2017. **486**: p. 234-245.
115. Gibson, I., D. Rosen, and B. Stucker, *Powder Bed Fusion Processes*, in *Additive Manufacturing Technologies* 2015, Springer: New York, USA. p. 107-146.
116. Arcam-AB. *EBM-Built Materials - way beyond average*. 2017 [cited 2017 3 April]; Available from: http://www.arcam.com/technology/electron-beam-melting/materials/.
117. Biamino, S., A. Penna, U. Ackelid, S. Sabbadini, O. Tassa, P. Fino, M. Pavese, P. Gennaro, and C. Badini, *Electron beam melting of Ti–48Al–2Cr–2Nb alloy: Microstructure and mechanical properties investigation.* Intermetallics, 2011. **19**(6): p. 776-781.
118. Murr, L.E., *Metallurgy of additive manufacturing: Examples from electron beam melting.* Additive Manufacturing, 2015. **5**: p. 40-53.
119. Cormier, D., O. Harrysson, and H. West, *Characterization of H13 steel produced by electron beam melting.* Rapid Prototyping Journal, 2004. **10**(1): p. 35-41.
120. Mahale, T., D. Cormier, O. Harrysson, and K. Ervin. *Advances in electron beam melting of aluminium alloys* in *17th Solid Freeform Fabrication Symposium* 2007. Austin, TX.
121. Qi, H.B., Y.N. Yan, F. Lin, W. He, and R.J. Zhang, *Direct metal part forming of 316L stainless steel powder by electron beam selective melting.* Proceedings of the Institution of Mechanical Engineers, Part B: Journal of Engineering Manufacture, 2006. **220**(11): p. 1845-1853.
122. Larsson, M., U. Lindhe, and O. Harrysson. *Rapid manufacturing with Electron Beam Melting (EBM) - A manufacturing revolution?* in *14th Solid Freeform Fabrication Symposium*. 2003. Austin TX.

123. Arcam-AB. *EBM Hardware*. Electron Beam Melting 2015 10 August 2015 [cited 2017 April 3]; Available from: http://www.arcam.com/technology/electron-beam-melting/hardware/.
124. Hiemenz, J., *Electron Beam Melting.* Advanced Materials & Processes, 2007. **165**(3): p. 45-46.
125. Deckard, C.R., *Method and apparatus for producing parts by selective sintering*. 1989, Board of Regents, The University of Texas System, Austin, TX: United States. p. 1-12.
126. Shellabear, M. and O. Nyrhila. *DMLS - Development history and state of the art*. in *Laser Assisted Netshape Engineering 4*. 2004. Erlangen, Germany.
127. Yap, C.Y., C.K. Chua, Z.L. Dong, Z.H. Liu, D.Q. Zhang, L.E. Loh, and S.L. Sing, *Review of selective laser melting: Materials and applications.* Applied Physics Reviews, 2015. **2**(4): p. 041101.
128. Li, X.P., C.W. Kang, H. Huang, L.C. Zhang, and T.B. Sercombe, *Selective laser melting of an Al86Ni6Y4.5Co2La1.5 metallic glass: Processing, microstructure evolution and mechanical properties.* Materials Science and Engineering: A, 2014. **606**: p. 370-379.
129. Jaćimović, J., F. Bonda, G. Hermann, F. Greuter, J. Genta, M. Calvo, T. Tomse, and R.A. Simon, *Net shape 3D printed NdFeB permanent magnet* 2016: eprint arXiv:1611.05332. p. 1-9.
130. Cherry, J.A., H.M. Davies, S. Mehmood, N.P. Lavery, S.G.R. Brown, and J. Sienz, *Investigation into the effect of process parameters on microstructural and physical properties of 316L stainless steel parts by selective laser melting.* The International Journal of Advanced Manufacturing Technology, 2014. **76**(5-8): p. 869-879.
131. Zhao, X., Q. Wei, B. Song, Y. Liu, X. Luo, S. Wen, and Y. Shi, *Fabrication and Characterization of AISI 420 Stainless Steel Using Selective Laser Melting.* Materials and Manufacturing Processes, 2015. **30**(11): p. 1283-1289.
132. Sun, Z., X. Tan, S.B. Tor, and W.Y. Yeong, *Selective laser melting of stainless steel 316L with low porosity and high build rates.* Materials & Design, 2016. **104**: p. 197-204.
133. Carlton, H.D., A. Haboub, G.F. Gallegos, D.Y. Parkinson, and A.A. MacDowell, *Damage evolution and failure mechanisms in additively manufactured stainless steel.* Materials Science and Engineering: A, 2016. **651**: p. 406-414.
134. Ma, M., Z. Wang, M. Gao, and X. Zeng, *Layer thickness dependence of performance in high-power selective laser melting of 1Cr18Ni9Ti stainless steel.* Journal of Materials Processing Technology, 2015. **215**: p. 142-150.
135. Rafi, H.K., D. Pal, N. Patil, T.L. Starr, and B.E. Stucker, *Microstructure and Mechanical Behavior of 17-4 Precipitation Hardenable Steel Processed by Selective Laser Melting.* Journal of Materials Engineering and Performance, 2014. **23**(12): p. 4421-4428.
136. Saeidi, K., X. Gao, F. Lofaj, L. Kvetková, and Z.J. Shen, *Transformation of austenite to duplex austenite-ferrite assembly in annealed stainless steel 316L consolidated by laser melting.* Journal of Alloys and Compounds, 2015. **633**: p. 463-469.
137. Kempen, K., L. Thijs, E. Yasa, M. Badrossamay, W. Verheecke, and J.-P. Kruth. *Process optimisation and microstructural analysis for selective laser melting of AlSi10Mg*. in *22nd Solid Freeform Fabrication Symposium*. 2011. Austin, TX.
138. EOS-GmbH, *Dental Crowns*. 2015, EOS GmbH.
139. El-Batahgy, A.-M., A.-F. Khourshid, and T. Sharef, *Effect of Laser Beam Welding Parameters on Microstructure and Properties of Duplex Stainless Steel.* Materials Sciences and Applications, 2011. **02**(10): p. 1443-1451.
140. Dobránszky, J., Z. Lőrinc, F. Gyímesi, A. Szigethy, and E. Bitay. *Laser welding of lean duplex stainless steels and their dissimilar joints* in *8th European Stainless Steel and Duplex Stainless Steel Conference*. 2015. Graz, Austria.
141. Dengiz, E.E., *Fiber Laser Welding of SAF 2507 Duplex Stainless Steel*, in *Department of Engineering Sciences and Mathematics*. 2011, Luleå University of Technology: Luleå, Sweden. p. 48.
142. Pekkarinen, J. and V. Kujanpää, *The effects of laser welding parameters on the microstructure of ferritic and duplex stainless steels welds.* Physics Procedia, 2010. **5**: p. 517-523.

143. Liu, H., B. Liu, D. Li, H. Sun, F. Sun, and X. Jin, *Microstructural characterisation of welded joint in duplex stainless steel by laser continuous heat treatment.* Journal of Iron and Steel Research International, 2014. **21**(7): p. 710-714.
144. Amigó, V., V. Bonache, L. Teruel, and A. Vicente, *Mechanical properties of duplex stainless steel laser joints.* Welding International, 2006. **20**(5): p. 361-366.
145. Liu, H., X. Lu, and X. Jin, *Phase transformation and mechanical properties in laser continuous heat treatment welds.* Materials & Design, 2011. **32**(4): p. 2269-2276.
146. Schwarz, L., T. Vrtochová, and K. Ulrich, *Laser Beam Welding of Superduplex Stainless Steel with Post-Heat Treatment.* Materials Science and Technology, 2010. **10**: p. 20-26.
147. Zhang, W., Y. Shi, B. Liu, L. Xu, and W. Jiang, *Consecutive sub-sector scan mode with adjustable scan lengths for selective laser melting technology.* The International Journal of Advanced Manufacturing Technology, 2009. **41**(7-8): p. 706-713.
148. Lu, Y., S. Wu, Y. Gan, T. Huang, C. Yang, L. Junjie, and J. Lin, *Study on the microstructure, mechanical property and residual stress of SLM Inconel-718 alloy manufactured by differing island scanning strategy.* Optics & Laser Technology, 2015. **75**: p. 197-206.
149. Zhou, X., X. Liu, D. Zhang, Z. Shen, and W. Liu, *Balling phenomena in selective laser melted tungsten.* Journal of Materials Processing Technology, 2015. **222**: p. 33-42.
150. Casati, R., J. Lemke, and M. Vedani, *Microstructure and Fracture Behavior of 316L Austenitic Stainless Steel Produced by Selective Laser Melting.* Journal of Materials Science & Technology, 2016. **32**(8): p. 738-744.
151. Hussein, A., C. Yan, R. Everson, and L. Hao. *Preliminary investigation on cellular support structures using SLM process* in *5th International Conference on Advanced Research in Virtual and Rapid Prototyping*. 2011. Leiria, Portugal.
152. Fitzgerald, E. and W. Everhart. *The effect of location on the structure and mechanical properties of selective laser melted 316L stainless steel*. in *27th Solid Freeform Fabrication Symposium*. 2016. Austin, TX.
153. Ferrar, B., L. Mullen, E. Jones, R. Stamp, and C.J. Sutcliffe, *Gas flow effects on selective laser melting (SLM) manufacturing performance.* Journal of Materials Processing Technology, 2012. **212**(2): p. 355-364.
154. Gu, H., H. Gong, D. Pal, K. Rafi, T. Starr, and B. Stucker. *Influences of energy density on porosity and microstructure of selective laser melted 17-4PH stainless steel*. in *24th Solid Freeform Fabrication Symposium*. 2013. Austin, TX.
155. Davidson, K. and S. Singamneni, *Selective Laser Melting of Duplex Stainless Steel Powders: An Investigation.* Materials and Manufacturing Processes, 2015. **31**(12): p. 1543-1555.
156. 3D-Printing-Lab. *Renishaw SLM (selective laser melting)*. Services 2014 [cited 2017 5 April].
157. Spierings, A.B., M. Schneider, and R. Eggenberger, *Comparison of density measurement techniques for additive manufactured metallic parts.* Rapid Prototyping Journal, 2011. **17**(5): p. 380-386.
158. Sandvik, *Sandvik SAF 2507 - Tube and Pipe, Seamless: Datasheet*. 2017, Sandvik AB: Sweden.
159. Vander Voort, G.F., *Color Metallography*. Microscopy Today, 2005. **13**(6): p. 22-27.
160. Michalska, J. and M. Sozańska. *Selective etching of phases and structural components in duplex stainless steel*. in *Sixth International conference on Difusion in Materials*. 2004. Kraków, Poland.
161. Tan, H., Z. Wang, Y. Jiang, Y. Yang, B. Deng, H. Song, and J. Li, *Influence of welding thermal cycles on microstructure and pitting corrosion resistance of 2304 duplex stainless steels.* Corrosion Science, 2012. **55**: p. 368-377.
162. Zucato, I., M.C. Moreira, I.F. Machado, and S.M. Giampietri Lebrão, *Microstructural characterisation and the effect of phase transformations on toughness of the UNS S31803 duplex stainless steel aged treated at 850 °C.* Materials Research, 2002. **5**(3): p. 385-389.
163. Struers, *Preparation of ferrous metals for Electron Backscatter Diffraction (EBSD) analysis*. 2010, Struers ApS: Denmark. p. 1-12.

164. University-of-Glasgow. *FEI Quanta 200F Environmental SEM with EDAX Microanalysis*. 2017 [cited 2017 23 April]; Available from: http://www.gla.ac.uk/schools/ges/researchandimpact/researchfacilities/isaac/instrumentation/feiquanta200fenvironmentalsemwithedaxmicroanalysis/.
165. James-Hutton-Institute. *X-ray diffraction*. Equipment 2014 4 November [cited 2017 24 April]; Available from: http://www.claysandminerals.com/sites/www.claysandminerals.com/files/22953_sh_4706.jpg.
166. Tavares, S.S.M., J.M. Pardal, J.L. Guerreiro, A.M. Gomes, and M.R. da Silva, *Magnetic detection of sigma phase in duplex stainless steel UNS S31803*. Journal of Magnetism and Magnetic Materials, 2010. **322**(17): p. L29-L33.
167. Helmut-Fischer, *Fischer Fischerscope MMS: Universal Coating and Material Property Measurement System*. 2005, Helmut Fischer GmbH: Germany.
168. Hao, L., S. Dadbakhsh, O. Seaman, and M. Felstead, *Selective laser melting of a stainless steel and hydroxyapatite composite for load-bearing implant development.* Journal of Materials Processing Technology, 2009. **209**(17): p. 5793-5801.
169. Zou, Y., R. Ueji, and H. Fujii, *Mechanical properties of advanced active-TIG welded duplex stainless steel and ferrite steel*. Materials Science and Engineering: A, 2015. **620**: p. 140-148.
170. ASTM, *Standard Test Method for Microindentation Hardness of Materials*, in *E 384 - 06*. 2006, American Society for Testing and Materials International: PA, USA. p. 33.
171. ASTM, *Standard Test Methods for Tension Testing of Metallic Materials*, in *E8/E8M – 09*. 2009, American Society for Testing and Materials International: PA, USA. p. 27.
172. Facchini, L., E. Magalini, P. Robotti, A. Molinari, S. Höges, and K. Wissenbach, *Ductility of a Ti-6Al-4V alloy produced by selective laser melting of prealloyed powders.* Rapid Prototyping Journal, 2010. **16**(6): p. 450-459.
173. Luecke, W.E. and J.A. Slotwinski, *Mechanical Properties of Austenitic Stainless Steel Made by Additive Manufacturing.* Journal of Research of the National Institute of Standards and Technology, 2014. **119**: p. 398-418.
174. Mumtaz, K. and N. Hopkinson, *Top surface and side roughness of Inconel 625 parts processed using selective laser melting.* Rapid Prototyping Journal, 2009. **15**(2): p. 96-103.
175. Singh, H., P. Singh, and J. Singh, *Analysis of surface roughness of 2507 super-duplex stainless steel during dry CNC turning using deep cryogenically treated ISO K313 Wc/Co inserts.* International Journal of Research in Mechanical Engineering & Technology, 2015. **6**(1): p. 27-32.
176. ISO. *ISO 4288:1996 - Geometrical Product Specifications (GPS) - Surface texture: Profile method - Rules and procedures for the assessment of surface texture*. ISO/TC 213 - Dimensional and geometrical product specifications and verification 2017 [cited 2017 26 April]; Available from: https://www.iso.org/standard/2096.html?browse=tc.
177. Lake-Shore-Cryotronics. *PMC MicroMag 3900 Series VSM*. 2017 [cited 2017 25 April]; Available from: http://www.lakeshore.com/products/Vibrating-Sample-Magnetometer/PMC-MicroMag-3900-Series-VSM/Pages/Overview.aspx.
178. BSSA. *Speeds and feeds for drilling and reaming stainless steels*. 2017 [cited 2017 15 May]; Available from: http://www.bssa.org.uk/topics.php?article=194.
179. Chen, W.-C. and X.-D. Liu, *Study on the various coated twist drills for stainless steel drilling.* Journal of Materials Processing Technology, 2000. **99**: p. 226-230.
180. Calliari, I., E. Ramous, and M. Pellizzari, *Thermal and mechanical treatments effects on phase transformation in duplex stainless steels.* Stainless Steel World, 2010.
181. Sathirachinda, N., R. Pettersson, S. Wessman, and J. Pan, *Study of nobility of chromium nitrides in isothermally aged duplex stainless steels by using SKPFM and SEM/EDS.* Corrosion Science, 2010. **52**(1): p. 179-186.
182. Bockelmann, M., J. Heather, and M. Knyazeva, *Solution annealing of thick walled large-diameter super duplex stainless steel pipes by induction heat treatment.* Stainless Steel World, 2012. **24**(9): p. 1-7.

183. Attar, H., M. Calin, L.C. Zhang, S. Scudino, and J. Eckert, *Manufacture by selective laser melting and mechanical behavior of commercially pure titanium.* Materials Science and Engineering: A, 2014. **593**: p. 170-177.
184. Yadroitsev, I., P. Bertrand, and I. Smurov, *Parametric analysis of the selective laser melting process.* Applied Surface Science, 2007. **253**(19): p. 8064-8069.
185. Rombouts, M., J.P. Kruth, L. Froyen, and P. Mercelis, *Fundamentals of Selective Laser Melting of alloyed steel powders.* CIRP Annals - Manufacturing Technology, 2006. **55**(1): p. 187-192.
186. Kruth, J.P., L. Froyen, J. Van Vaerenbergh, P. Mercelis, M. Rombouts, and B. Lauwers, *Selective laser melting of iron-based powder.* Journal of Materials Processing Technology, 2004. **149**(1-3): p. 616-622.
187. Yadroitsev, I., A. Gusarov, I. Yadroitsava, and I. Smurov, *Single track formation in selective laser melting of metal powders.* Journal of Materials Processing Technology, 2010. **210**(12): p. 1624-1631.
188. Spierings, A.B., K. Wegener, and G. Levy. *Designing material properties locally with additive manufacturing technology SLM*. in *23rd Solid Freeform Fabrication Symposium* 2012. Austin, TX.
189. Louvis, E., P. Fox, and C.J. Sutcliffe, *Selective laser melting of aluminium components.* Journal of Materials Processing Technology, 2011. **211**(2): p. 275-284.
190. Morgan, R., C.J. Sutcliffe, and W. O'Neill, *Density analysis of direct metal laser re-melted 316L stainless steel cubic primitives.* Journal of Materials Science, 2004. **39**(4): p. 1195-1205.
191. Su, X. and Y. Yang, *Research on track overlapping during Selective Laser Melting of powders.* Journal of Materials Processing Technology, 2012. **212**(10): p. 2074-2079.
192. Ilčík, J., D. Koutný, and D. Paloušek. *Geometrical Accuracy of the Metal Parts Produced by Selective Laser Melting: Initial Tests*. in *Modern Methods of Construction Design*. 2014. Liberec: Springer International Publishing.
193. Niendorf, T., S. Leuders, A. Riemer, H.A. Richard, T. Tröster, and D. Schwarze, *Highly Anisotropic Steel Processed by Selective Laser Melting.* Metallurgical and Materials Transactions B, 2013. **44**(4): p. 794-796.
194. Badrossamay, M. and T.H.C. Childs, *Further studies in selective laser melting of stainless and tool steel powders.* International Journal of Machine Tools and Manufacture, 2007. **47**(5): p. 779-784.
195. Muthupandi, V., P. Bala Srinivasan, S.K. Seshadri, and S. Sundaresan, *Effect of weld metal chemistry and heat input on the structure and properties of duplex stainless steel welds.* Materials Science and Engineering: A, 2003. **358**(1-2): p. 9-16.
196. Monroy, K., J. Delgado, and J. Ciurana, *Study of the Pore Formation on CoCrMo Alloys by Selective Laser Melting Manufacturing Process.* Procedia Engineering, 2013. **63**: p. 361-369.
197. Chawla, N. and X. Deng, *Microstructure and mechanical behavior of porous sintered steels.* Materials Science and Engineering: A, 2005. **390**(1-2): p. 98-112.
198. Dai, D. and D. Gu, *Thermal behavior and densification mechanism during selective laser melting of copper matrix composites: Simulation and experiments.* Materials & Design, 2014. **55**: p. 482-491.
199. Guo, L.Q., M.C. Lin, L.J. Qiao, and A.A. Volinsky, *Ferrite and austenite phase identification in duplex stainless steel using SPM techniques.* Applied Surface Science, 2013. **287**: p. 499-501.
200. Nowacki, J. and A. Łukojć, *Structure and properties of the heat-affected zone of duplex steels welded joints.* Journal of Materials Processing Technology, 2005. **164-165**: p. 1074-1081.
201. Tavares, S.S.M., J.M. Pardal, L.D. Lima, I.N. Bastos, A.M. Nascimento, and J.A. de Souza, *Characterization of microstructure, chemical composition, corrosion resistance and toughness of a multipass weld joint of superduplex stainless steel UNS S32750.* Materials Characterization, 2007. **58**(7): p. 610-616.

202. Song, B., S. Dong, Q. Liu, H. Liao, and C. Coddet, *Vacuum heat treatment of iron parts produced by selective laser melting: Microstructure, residual stress and tensile behavior.* Materials & Design, 2014. **54**: p. 727-733.
203. Teng, C., H. Gong, A. Szabo, J.J.S. Dilip, K. Ashby, S. Zhang, N. Patil, D. Pal, and B. Stucker, *Simulating Melt Pool Shape and Lack of Fusion Porosity for Selective Laser Melting of Cobalt Chromium Components.* Journal of Manufacturing Science and Engineering, 2016. **139**(1): p. 011009.
204. Gong, H., H. Gu, K. Zeng, J.J.S. Dilip, D. Pal, B. Stucker, D. Christiansen, J. Beuth, and J.J. Lewandowski. *Melt pool characterization for selective laser melting of Ti-6Al-4V pre-alloyed powder*. in *25th Solid Freeform Fabrication Symposium*. 2014. Austin, TX.
205. Yadroitsev, I., I. Yadroitsava, P. Bertrand, and I. Smurov, *Factor analysis of selective laser melting process parameters and geometrical characteristics of synthesized single tracks.* Rapid Prototyping Journal, 2012. **18**(3): p. 201-208.
206. Jia, Q. and D. Gu, *Selective laser melting additive manufacturing of TiC/Inconel 718 bulk-form nanocomposites: Densification, microstructure, and performance.* Journal of Materials Research, 2014. **29**(17): p. 1960-1969.
207. Vilaro, T., C. Colin, J.D. Bartout, L. Nazé, and M. Sennour, *Microstructural and mechanical approaches of the selective laser melting process applied to a nickel-base superalloy*. Materials Science and Engineering: A, 2012. **534**: p. 446-451.
208. Boegelein, T., S.N. Dryepondt, A. Pandey, K. Dawson, and G.J. Tatlock, *Mechanical response and deformation mechanisms of ferritic oxide dispersion strengthened steel structures produced by selective laser melting.* Acta Materialia, 2015. **87**: p. 201-215.
209. Song, B., S. Dong, P. Coddet, H. Liao, and C. Coddet, *Fabrication of NiCr alloy parts by selective laser melting: Columnar microstructure and anisotropic mechanical behavior.* Materials & Design, 2014. **53**: p. 1-7.
210. Zhou, X., K. Li, D. Zhang, X. Liu, J. Ma, W. Liu, and Z. Shen, *Textures formed in a CoCrMo alloy by selective laser melting.* Journal of Alloys and Compounds, 2015. **631**: p. 153-164.
211. Vrancken, B., L. Thijs, J.P. Kruth, and J. Van Humbeeck, *Microstructure and mechanical properties of a novel β titanium metallic composite by selective laser melting.* Acta Materialia, 2014. **68**: p. 150-158.
212. Thijs, L., M.L. Montero Sistiaga, R. Wauthle, Q. Xie, J.-P. Kruth, and J. Van Humbeeck, *Strong morphological and crystallographic texture and resulting yield strength anisotropy in selective laser melted tantalum.* Acta Materialia, 2013. **61**(12): p. 4657-4668.
213. Migiakis, K. and G.D. Papadimitriou, *Effect of nitrogen and nickel on the microstructure and mechanical properties of plasma welded UNS S32760 super-duplex stainless steels.* Journal of Materials Science, 2009. **44**(23): p. 6372-6383.
214. Niendorf, T., F. Brenne, and M. Schaper, *Lattice Structures Manufactured by SLM: On the Effect of Geometrical Dimensions on Microstructure Evolution During Processing.* Metallurgical and Materials Transactions B, 2014. **45**(4): p. 1181-1185.
215. Yagi, S. and D. Kunii, *Studies on effective thermal conductivities in packed beds.* AIChE Journal, 1957. **3**(3): p. 373-381.
216. Kruth, J.P., M. Badrossamay, E. Yasa, J. Deckers, L. Thijs, and J. Van Humbeeck. *Part and Material properties in selective laser melting of metals* in *16th International Symposium on Electromachining*. 2010. Shanghai, China.
217. Kolenič, F., L. Kovac, and D. Drimal, *Effect of laser welding conditions on Austenite/Ferrite ratio in duplex stainless steel 2507 welds.* Welding in the World, 2011. **55**(6-8): p. 19-25.
218. Yasa, E. and J.P. Kruth, *Microstructural investigation of Selective Laser Melting 316L stainless steel parts exposed to laser re-melting.* Procedia Engineering, 2011. **19**: p. 389-395.
219. Kruth, J.P., E. Yasa, and J. Deckers. *Experimental investigation of laser surface re-melting for the improvement of selective laser melting process*. in *19th Solid Freeform Fabrication Symposium*. 2008. Austin, TX.

220. Kell, J., J.R. Tyrer, R.L. Higginson, and R.C. Thomson, *Microstructural characterization of autogeneous laser welds on 316L stainless steel using EBSD and EDS.* Journal of Microscopy, 2005. **217**(2): p. 167-173.
221. Song, B., X. Zhao, S. Li, C. Han, Q. Wei, S. Wen, J. Liu, and Y. Shi, *Differences in microstructure and properties between selective laser melting and traditional manufacturing for fabrication of metal parts: A review.* Frontiers of Mechanical Engineering, 2015. **10**(2): p. 111-125.
222. Conde, A., R. Colaço, R. Vilar, and J. de Damborenea, *Corrosion behaviour of steels after laser surface melting.* Materials and Design, 2000. **21**(5): p. 441-445.
223. Kwok, C.T., K.H. Lo, F.T. Cheng, and H.C. Man, *Effect of processing conditions on the corrosion performance of laser surface-melted AISI 440C martensitic stainless steel.* Surface and Coatings Technology, 2003. **166**(2): p. 221-230.
224. Knyazeva, M. and M. Pohl, *Duplex Steels. Part II: Carbides and Nitrides.* Metallography, Microstructure, and Analysis, 2013. **2**(5): p. 343-351.
225. Pettersson, N., R.F.A. Pettersson, and S. Wessman, *Precipitation of Chromium Nitrides in the Super Duplex Stainless Steel 2507.* Metallurgical and Materials Transactions A, 2015. **46**(3): p. 1062-1072.
226. Tacke, G. and H.J. Kohler, *Precipitation behaviour of Ferritic-Austenitic stainless steels of high molybdenum content.* Steel Research International, 1987. **58**(3): p. 123-128.
227. Wischnowski, F., *Effect of microstructural modifications on the corrosion resistance of stainless ferritic-austenitic duplex steels*. 1995, Ruhr-Universität: Bochum, Germany.
228. Sathirachinda, N., R. Pettersson, S. Wessman, U. Kivisäkk, and J. Pan, *Scanning Kelvin probe force microscopy study of chromium nitrides in 2507 super duplex stainless steel—Implications and limitations.* Electrochimica Acta, 2011. **56**(4): p. 1792-1798.
229. Shifeng, W., L. Shuai, W. Qingsong, C. Yan, Z. Sheng, and S. Yusheng, *Effect of molten pool boundaries on the mechanical properties of selective laser melting parts.* Journal of Materials Processing Technology, 2014. **214**(11): p. 2660-2667.
230. Mourad, A.H.I., A. Khourshid, and T. Sharef, *Gas tungsten arc and laser beam welding processes effects on duplex stainless steel 2205 properties.* Materials Science and Engineering: A, 2012. **549**: p. 105-113.
231. Gong, H., K. Rafi, H. Gu, T. Starr, and B. Stucker, *Analysis of defect generation in Ti–6Al–4V parts made using powder bed fusion additive manufacturing processes.* Additive Manufacturing, 2014. **1-4**: p. 87-98.
232. Siddique, S., M. Imran, E. Wycisk, C. Emmelmann, and F. Walther, *Influence of process-induced microstructure and imperfections on mechanical properties of AlSi12 processed by selective laser melting.* Journal of Materials Processing Technology, 2015. **221**: p. 205-213.
233. Chlebus, E., K. Gruber, B. Kuźnicka, J. Kurzac, and T. Kurzynowski, *Effect of heat treatment on the microstructure and mechanical properties of Inconel 718 processed by selective laser melting.* Materials Science and Engineering: A, 2015. **639**: p. 647-655.
234. Sun, Y., A. Moroz, and K. Alrbaey, *Sliding Wear Characteristics and Corrosion Behaviour of Selective Laser Melted 316L Stainless Steel.* Journal of Materials Engineering and Performance, 2013. **23**(2): p. 518-526.
235. Saeidi, K., L. Kevetkova, F. Lofaj, and Z. Shen, *Novel ferritic stainless steel formed by laser melting from duplex stainless steel powder with advanced mechanical properties and high ductility.* Materials Science and Engineering: A, 2016. **665**: p. 59-65.
236. Devendranath Ramkumar, K., D. Mishra, M.K. Vignesh, B. Ganesh Raj, N. Arivazhagan, S.V. Naren, and S. Suresh Kumar, *Metallurgical and mechanical characterization of electron beam welded super-duplex stainless steel UNS 32750.* Journal of Manufacturing Processes, 2014. **16**(4): p. 527-534.
237. Wang, L.-z., S. Wang, and J.-j. Wu, *Experimental investigation on densification behavior and surface roughness of AlSi10Mg powders produced by selective laser melting.* Optics & Laser Technology, 2017. **96**: p. 88-96.
238. Gong, H., K. Rafi, H. Gu, G.D. Janaki Ram, T. Starr, and B. Stucker, *Influence of defects on mechanical properties of Ti–6Al–4V components produced by selective laser melting and electron beam melting.* Materials & Design, 2015. **86**: p. 545-554.

239. Mertens, A., S. Reginster, H. Paydas, Q. Contrepois, T. Dormal, O. Lemaire, and J. Lecomte-Beckers, *Mechanical properties of alloy Ti–6Al–4V and of stainless steel 316L processed by selective laser melting: influence of out-of-equilibrium microstructures.* Powder Metallurgy, 2014. **57**(3): p. 184-189.
240. Park, Y.-H. and Z.-H. Lee, *The effect of nitrogen and heat treatment on the microstructure and tensile properties of 25Cr-7Ni-1.5Mo-3W-xN duplex stainless steel castings.* Materials Science and Engineering: A, 2001. **297**(1-2): p. 78-84.
241. M, M.A., K.A. Shrikrishna, P. Sathiya, and S. Goel, *The impact of heat input on the strength, toughness, microhardness, microstructure and corrosion aspects of friction welded duplex stainless steel joints.* Journal of Manufacturing Processes, 2015. **18**: p. 92-106.
242. Najib, L.M., A. Alisibramulisi, N.M. Amin, I.A.A. Bakar, and S. Hasim, *The Effect of Rolling Direction to the Tensile Properties of AA5083 Specimen.* 2015: p. 779-787.
243. Carter, L.N., C. Martin, P.J. Withers, and M.M. Attallah, *The influence of the laser scan strategy on grain structure and cracking behaviour in SLM powder-bed fabricated nickel superalloy.* Journal of Alloys and Compounds, 2014. **615**: p. 338-347.
244. Guan, K., Z. Wang, M. Gao, X. Li, and X. Zeng, *Effects of processing parameters on tensile properties of selective laser melted 304 stainless steel.* Materials & Design, 2013. **50**: p. 581-586.
245. Vrancken, B., V. Cain, R. Knutsen, and J. Van Humbeeck, *Residual stress via the contour method in compact tension specimens produced via selective laser melting.* Scripta Materialia, 2014. **87**: p. 29-32.
246. Zhang, B., L. Dembinski, and C. Coddet, *The study of the laser parameters and environment variables effect on mechanical properties of high compact parts elaborated by selective laser melting 316L powder.* Materials Science and Engineering: A, 2013. **584**: p. 21-31.
247. Saeidi, K., *Stainless steels fabricated by laser melting*, in *Department of Materials and Environmental Chemistry*. 2016, Stockholm University: Stockholm, Sweden. p. 115.
248. Wang, D., C. Song, Y. Yang, and Y. Bai, *Investigation of crystal growth mechanism during selective laser melting and mechanical property characterization of 316L stainless steel parts.* Materials & Design, 2016. **100**: p. 291-299.
249. Mahmoudi, M., A. Elwany, A. Yadollahi, S.M. Thompson, L. Bian, and N. Shamsaei, *Mechanical properties and microstructural characterization of selective laser melted 17-4 PH stainless steel* Rapid Prototyping Journal, 2017. **23**(2): p. 280-294.
250. Badji, R., M. Bouabdallah, B. Bacroix, C. Kahloun, B. Belkessa, and H. Maza, *Phase transformation and mechanical behavior in annealed 2205 duplex stainless steel welds.* Materials Characterization, 2008. **59**(4): p. 447-453.
251. Lakshminarayanan, A.K. and V. Balasubramanian, *An assessment of microstructure, hardness, tensile and impact strength of friction stir welded ferritic stainless steel joints.* Materials & Design, 2010. **31**(10): p. 4592-4600.
252. Ilie, A., H. Ali, and K. Mumtaz, *In-Built Customised Mechanical Failure of 316L Components Fabricated Using Selective Laser Melting.* Technologies, 2017. **5**(1): p. 9.
253. Kubík, P., F. Šebek, and J. Petruška. *Ductile fracture criteria in prediction of slant fracture*. in *VII European Congress on Computational Methods in Applied Sciences and Engineering*. 2016. Crete Island, Greece: National Technical University of Athens (NTUA).
254. LeBrun, T., T. Nakamoto, K. Horikawa, and H. Kobayashi, *Effect of retained austenite on subsequent thermal processing and resultant mechanical properties of selective laser melted 17–4 PH stainless steel.* Materials & Design, 2015. **81**: p. 44-53.
255. Örnek, C., S. Idris, P. Reccagni, and D. Engelberg, *Atmospheric-Induced Stress Corrosion Cracking of Grade 2205 Duplex Stainless Steel—Effects of 475 °C Embrittlement and Process Orientation.* Metals, 2016. **6**(7): p. 167.
256. Sufiiarov, V.S., A.A. Popovich, E.V. Borisov, I.A. Polozov, D.V. Masaylo, and A.V. Orlov, *The Effect of Layer Thickness at Selective Laser Melting.* Procedia Engineering, 2017. **174**: p. 126-134.

257. Manfredi, D., F. Calignano, M. Krishnan, R. Canali, E. Paola, S. Biamino, D. Ugues, M. Pavese, and P. Fino, *Additive Manufacturing of Al Alloys and Aluminium Matrix Composites (AMCs)*, in *Light Metal Alloys Applications*, W.A. Monteiro, Editor. 2014, InTech: Rijeka, Croatia. p. 3-34.
258. Janssen, M., J. Zuidema, and R. Wanhill, *Fracture Mechanics*. 2 ed. 2004, Oxfordshire, UK: Spon Press.
259. Simonelli, M., Y.Y. Tse, and C. Tuck, *Effect of the build orientation on the mechanical properties and fracture modes of SLM Ti–6Al–4V.* Materials Science and Engineering: A, 2014. **616**: p. 1-11.
260. Herms, E., J.M. Olive, and M. Puiggali, *Hydrogen embrittlement of 316L type stainless steel.* Materials Science and Engineering: A, 1999. **272**: p. 279-283.
261. Brooks, C.R. and A. Choudhury, *Failure analysis of Engineering Materials*. McGraw-Hill professional engineering. 2002, New York: McGraw-Hill
262. Palousek, D., L. Pantelejev, T. Zikmund, and D. Koutny, *Processing of Nearly Pure Iron Using 400w Selective Laser Melting – Initial Study*. MM Science Journal, 2017. **2017**(01): p. 1738-1743.
263. Song, B., S. Dong, S. Deng, H. Liao, and C. Coddet, *Microstructure and tensile properties of iron parts fabricated by selective laser melting.* Optics & Laser Technology, 2014. **56**: p. 451-460.
264. Nave, C.R. *Ferromagnetism* 2017 [cited 2017 24 September]; Available from: http://hyperphysics.phy-astr.gsu.edu/hbase/Solids/ferro.html.
265. Fofanov, D. and S. Riedner. *Magnetic properties of stainless steels - applications, opportunities and new developments*. in *World Stainless Steel Conference & Expo*. 2011. Maastricht, The Netherlands.
266. O'Handley, R.C., *Modern Magnetic Materials - Principles and Applications*. 2000, USA: John Wiley & Sons, Inc. 740.
267. Sathirachinda, N., R. Pettersson, and J. Pan, *Depletion effects at phase boundaries in 2205 duplex stainless steel characterized with SKPFM and TEM/EDS.* Corrosion Science, 2009. **51**(8): p. 1850-1860.
268. Mészáros, I. and P.J. Szabó, *Complex magnetic and microstructural investigation of duplex stainless steel.* NDT & E International, 2005. **38**(7): p. 517-521.
269. Lai, J.K.L. and K.W. Wong, *An empirical model to describe the non-isothermal ageing behaviour of Feroplug materials.* International journal of pressure vessels and piping, 1995. **66**(1-3): p. 325-332.
270. Mumtaz, K., S. Takahashi, J. Echigoya, Y. Kamada, L.F. Zhang, H. Kikuchi, K. Ara, and M. Sato, *Magnetic measurements of martensitic transformation in austenitic stainless steel after room temperature rolling.* Journal of Materials Science, 2004. **39**(1): p. 85-97.
271. Zhang, B., N.-E. Fenineche, L. Zhu, H. Liao, and C. Coddet, *Studies of magnetic properties of permalloy (Fe–30%Ni) prepared by SLM technology.* Journal of Magnetism and Magnetic Materials, 2012. **324**(4): p. 495-500.
272. Zhang, B., N.-E. Fenineche, H. Liao, and C. Coddet, *Magnetic properties of in-situ synthesized FeNi3 by selective laser melting Fe-80%Ni powders.* Journal of Magnetism and Magnetic Materials, 2013. **336**: p. 49-54.
273. Mészáros, I., *Magnetic characterisation of duplex stainless steel.* Physica B: Condensed Matter, 2006. **372**(1-2): p. 181-184.
274. Tavares, S.S.M., P.D.S. Pedrosa, J.R. Teodósio, M.R. da Silva, J.M. Neto, and S. Pairis, *Magnetic properties of the UNS S39205 duplex stainless steel.* Journal of Alloys and Compounds, 2003. **351**(1-2): p. 283–288.
275. Lo, K.H. and J.K.L. Lai, *On the cryogenic magnetic transition and martensitic transformation of the austenite phase of 7MoPLUS duplex stainless steel.* Journal of Magnetism and Magnetic Materials, 2010. **322**(16): p. 2335-2339.
276. Landgraf, F.J.G., J.R.F. da Silveira, and D. Rodrigues-Jr, *Determining the effect of grain size and maximum induction upon coercive field of electrical steels.* Journal of Magnetism and Magnetic Materials, 2011. **323**(18-19): p. 2335-2339.

277. Tavares, S.S.M., M.R. da Silva, and J.M. Neto, *Magnetic property changes during embrittlement of a duplex stainless steel.* Journal of Alloys and Compounds, 2000. **313**(1-2): p. 168-173.
278. Nomani, J., A. Pramanik, T. Hilditch, and G. Littlefair, *Chip formation mechanism and machinability of wrought duplex stainless steel alloys.* The International Journal of Advanced Manufacturing Technology, 2015. **80**(5-8): p. 1127-1135.
279. BSSA. *Heat tint (temper) colours on stainless steel surfaces heated in air*. Process Plant & Furnaces 2017 [cited 2017 25 September]; Available from: http://www.bssa.org.uk/topics.php?article=140.
280. König, W., M. Klinger, and R. Link, *Machining Hard Materials with Geometrically Defined Cutting Edges — Field of Applications and Limitations.* CIRP Annals, 1990. **39**(1): p. 61-64.
281. Lin, T.-R. and R.-F. Shyu, *Improvement of Tool Life and Exit Burr using Variable Feeds when Drilling Stianless Steel with Coated Drills.* The International Journal of Advanced Manufacturing Technology, 2000. **16**(5): p. 308-313.
282. Çiçek, A., T. Kıvak, I. Uygur, E. Ekici, and Y. Turgut, *Performance of cryogenically treated M35 HSS drills in drilling of austenitic stainless steels.* The International Journal of Advanced Manufacturing Technology, 2012. **60**(1-4): p. 65-73.
283. Dolinšek, S., S. Ekinović, and J. Kopač, *A contribution to the understanding of chip formation mechanism in high-speed cutting of hardened steel.* Journal of Materials Processing Technology, 2004. **157-158**: p. 485-490.
284. Agapiou, J.S., G.W. Halldin, and M.F. DeVries, *On the Machinability of Ppowder Metallurgy Austenitic Stainless Steels.* Journal of Engineering for Industry, 1988. **110**(4): p. 339-343.
285. Dorofeev, Y.G., V.I. Ustimenko, and A.V. Skorikov, *Some features of cutting tool wear in finish machining of low-porosity alloy powder metallurgy steels.* Powder Metallurgy and Metal Ceramics, 1984. **23**(2): p. 153-156.
286. Pavel, R. and A.K. Srinivasan, *Investigations for safe grinding of Ti-6Al-4V parts produced by direct metal laser sintering (DMLS) technology.* ASME 2014 International Manufacturing Science and Engineering Conference collocated with the JSME 2014 International Conference on Materials and Processing and the 42nd North American Manufacturing Research Conference 2014. **2 - Processing**: p. V002T02A018-V002T02A018.
287. Esmailzadeh, M., M. Shamanian, A. Kermanpur, and T. Saeid, *Microstructure and mechanical properties of friction stir welded lean duplex stainless steel.* Materials Science and Engineering: A, 2013. **561**: p. 486-491.
288. Fang, Y.L., Z.Y. Liu, H.M. Song, and L.Z. Jiang, *Hot deformation behavior of a new austenite–ferrite duplex stainless steel containing high content of nitrogen.* Materials Science and Engineering: A, 2009. **526**(1-2): p. 128-133.
289. Saeid, T., A. Abdollah-zadeh, H. Assadi, and F. Malek Ghaini, *Effect of friction stir welding speed on the microstructure and mechanical properties of a duplex stainless steel.* Materials Science and Engineering: A, 2008. **496**(1-2): p. 262-268.
290. Sato, Y.S., T.W. Nelson, C.J. Sterling, R.J. Steel, and C.O. Pettersson, *Microstructure and mechanical properties of friction stir welded SAF 2507 super duplex stainless steel.* Materials Science and Engineering: A, 2005. **397**(1-2): p. 376-384.
291. Jorge, A.M., G.S. Reis, and O. Balancin, *Influence of the microstructure on the plastic behaviour of duplex stainless steels.* Materials Science and Engineering: A, 2011. **528**(6): p. 2259-2264.
292. Liu, F.C. and T.W. Nelson, *In-situ material flow pattern around probe during friction stir welding of austenitic stainless steel.* Materials & Design, 2016. **110**: p. 354-364.
293. Łabanowski, J. and M. Głowacka, *Heat tint colours on stainless steel and welded joints.* Welding International, 2011. **25**(7): p. 509-512.
294. Aumpiem, A. and A. Prateepasen. *The relation of oxygen value, heat tint and pitting corrosion in super duplex pipe*. in *3rd International Conference on Mechanical and Production Engineering*. 2017. Bangkok, Thailand.

295. Li, J., X. Liu, G. Li, P. Han, and W. Liang, *Characterization of the Microstructure, Mechanical Properties, and Corrosion Resistance of a Friction-Stir-Welded Joint of Hyper Duplex Stainless Steel.* Metals, 2017. **7**(4): p. 138.
296. Trent, E.M. and P.K. Wright, *Metal Cutting*. 4 ed. 2000, Woburn, MO, USA: Butterworth-Heinemann.
297. Sharif, S., E.A. Rahim, and H. Sasahara, *Machinability of Titanium alloys in drilling*, in *Titanium Alloys-Towards achieving enhanced properties for diversified applications*, A.K.M.N. Amin, Editor. 2012, InTech. p. 117-138.
298. Nomani, J., A. Pramanik, T. Hilditch, and G. Littlefair, *Stagnation zone during the turning of Duplex SAF 2205 stainless steels alloy.* Materials and Manufacturing Processes, 2017. **32**(13): p. 1486-1489.
299. Mateo, A., L. Llanes, L. Iturgoyen, and M. Anglada, *Cyclic stress-strain response and dislocation substructure evolution of a Ferrite-Austenite stainless steel.* Acta Materialia, 1996. **44**(3): p. 1143-1153.
300. Bhattacharyya, A., *Metal Cutting: theory and Practice*. Vol. 1. 2006, Kolkata, India: New Central Book Agency (P) Ltd.
301. Sidjanin, L. and P. Kovac, *Fracture mechanisms in chip formation processes.* Materials Science and Technology, 1997. **13**(5): p. 439-444.
302. Shaw, M.C., *Metal Cutting Principles*. 2 ed. 2005, New York, USA: Oxford University Press.
303. Watson, A.R., *Drilling model for cutting lip and chisel edge and comparison of experimental and predicted results. IV - Drilling tests to determine chisel edge contribution to torque and thrust.* International Journal of Machine Tool Design and Research, 1985. **25**(4): p. 393-404.
304. Boothroyd, G. and W.A. Knight, *Fundamentals of Machining and Machine Tools*. 3 ed. 2006, NW, USA: Taylor Francis Group, LLC.
305. O'Sullivan, D. and M. Cotterell, *Machinability of austenitic stainless steel SS303.* Journal of Materials Processing Technology, 2002. **124**: p. 153-159.
306. Sato, M., T. Aoki, H. Tanaka, and S. Takeda, *Variation of temperature at the bottom surface of a hole during drilling and its effect on tool wear.* International Journal of Machine Tools and Manufacture, 2013. **68**: p. 40-47.
307. Sushinder, K., P.R. Shivaram, S.B. Nivedh Kannaa, N. Gupta, and K.S. Vijay Sekar, *Investigation of Thrust Forces, Torque and Chip Microstructure during Drilling of Ti-6Al-4V Titanium Alloy.* Applied Mechanics and Materials, 2015. **787**: p. 431-436.
308. Rosa, P.A.R., O. Kolednik, P.A.F. Martins, and A.G. Atkins, *The transient beginning to machining and the transition to steady-state cutting.* International Journal of Machine Tools and Manufacture, 2007. **47**(12-13): p. 1904-1915.
309. Satyanarayana, V.V., G. Madhusudhan Reddy, and T. Mohandas, *Dissimilar metal friction welding of austenitic–ferritic stainless steels.* Journal of Materials Processing Technology, 2005. **160**(2): p. 128-137.
310. AK-Steel, *409 (UNS S40920) Stainless Steel*. 2007, AK Steel Corporation: Ohio, USA.
311. Selvaraj, D.P. and P. Chandramohan, *Influence of Cutting Speed, Feed Rate and Bulk Texture on the Surface Finish of Nitrogen Alloyed Duplex Stainless Steels during Dry Turning.* Engineering, 2010. **02**(06): p. 453-460.
312. Polishetty, A., M. Shunmugavel, M. Goldberg, G. Littlefair, and R.K. Singh, *Cutting Force and Surface Finish Analysis of Machining Additive Manufactured Titanium Alloy Ti-6Al-4V.* Procedia Manufacturing, 2017. **7**: p. 284-289.
313. Sultan, A.Z., S. Sharif, and D. Kurniawan, *Effect of Machining Parameters on Tool Wear and Hole Quality of AISI 316L Stainless Steel in Conventional Drilling.* Procedia Manufacturing, 2015. **2**: p. 202-207.
314. Drozda, T.J. and C. Wick, *Tool and Manufacturing Engineers Handbook*. 4 ed. Vol. 1 - Machining. 1983, Dearborn, Michigan, USA: Society of Manufacturing Engineers.

Appendices

Appendix I: Powder Conformity Certificate

SANDVIK

SANDVIK OSPREY LTD.,

RED JACKET WORKS,
MILLANDS ROAD,
NEATH SA11 1NJ,
UNITED KINGDOM.

Telephone: 01639.634121
Fax: 01639.630100
E-Mail: powders.osprey@sandvik.com

osprey

CERTIFICATE: 20049

Customer:	**SANDVIK NEW ZEALAND**
Customer Order:	30343
Customer Alloy Name:	SAF2507
Osprey Order Number:	140414/09
Osprey Alloy Name:	SAF2507
Dispatch Number:	14D0530
Weight:	22.00Kg (49lb)
Powder Size:	-45micron +10micron
Atomise Gas:	Nitrogen

Particle Size Data		**Powder Analysis** (weight %)			
		Element	Minimum	Actual	Maximum
+45µm	0.8%	Cr	24.6	**24.6 %**	25.4
-45µm +10µm	99.2%	Ni	6.8	**6.9 %**	7.2
-10µm	0.0%	Mo	3.76	**3.88 %**	4.24
		Mn	0.7	**0.9 %**	1.1
		Si	0.2	**0.5 %**	0.6
		N	0.26	**0.31 %**	0.31
		Cu	0.0	**0.0**	0.2
		Co	0.00	**0.04 %**	0.54
		Al	0.000	**0.020 %**	0.025
		C	0.00	**0.02 %**	0.02
		Sn	0.000	**0.010 %**	0.019
		Ti	0.000	**0.010 %**	0.025
		W	0.00	**0.01 %**	0.05
		P	0.000	**0.009 %**	0.025
		S	0.000	**0.005 %**	0.008
		B	0.000	**0.001 %**	0.003
		Fe	**BALANCE**		

Powder Tests		Min	Act	Max
Tap Density 4.3 g/cc	d10		22.8	µm
	d50		33.4	µm
Hall Flow 16.7 sec/50g				
	d90		49.1	µm
	-10 µm =			%
	Particle Size Distribution measured using Malvern 2000 instrument			

This certificate was produced electronically by KEITH CONSITT in accordance with Sandvik Osprey's Integrated Management System. No other signature is required to validate this document.

Printed on: 06/05/2014

Dispatch Group Ref: 14E0525

Page 2 c